THE UNIVERSITY *of* EDINBURGH

Investigating the internal structure of glaciers and ice sheets using ice penetrating radar

Richard John Delf

Submitted for the degree of Doctor of Philosophy

The University of Edinburgh

2020

Abstract

Ice penetrating radar (IPR) is a key tool in understanding the internal geometry and nature of glaciers and ice sheets, and has widely been used to derive bed topography, map internal layers and understand the thermal state of the cryosphere. Modern glacier and ice-sheet models facilitate increased assimilation of observations of englacial structure, including glacier thermal state and internal-layer geometry, yet the products available from radar surveys are often under-utilised. This thesis presents the development and assessment of radar processing strategies to improve quantitative retrievals from commonly acquired radar data.

The first major focus of this thesis centres on deriving englacial velocities from zero-offset IPR data. Water held within micro- and macro-scale pores in ice has a direct influence on radar velocity, and significantly reduces ice viscosity and hence impacts the long-term evolution of polythermal glaciers. Knowledge of the radar velocity field is essential to retrieve correct bed topography from depth conversion processing, yet bed topography is often estimated assuming constant velocity, and potential errors from lateral variations in the velocity field are neglected. Here I calculate the englacial radar velocity field from common offset IPR data collected on Von Postbreen, a polythermal glacier in Svalbard. I first extract the diffracted wavefield using local coherent stacking, then use the focusing metric of negative entropy to deduce a local migration velocity field from constant-velocity migration panels and produce a glacier-wide model of local radar velocity. I show that this velocity field is successful in differentiating between areas of cold and temperate ice and can detect lateral variations in radar velocity close to the glacier bed. The effects of this velocity field in both migration and depth-conversion of the bed reflection are shown to result in consistently lower ice depths across the glacier, indicating that diffraction focusing and velocity estimation are crucial in retrieving

correct bed topography in the presence of temperate ice.

For the thesis' second major component I undertake an assessment of automated techniques for tracing and interpreting ice-sheet internal stratigraphy. Radar surveys across ice sheets typically measure numerous englacial layers that can be often be regarded as isochrones. Such layers are valuable for extrapolating age-depth relationships away from ice-core locations, reconstructing palaeoaccumulation variability, and investigating past ice-sheet dynamics. However, the use of englacial layers in Antarctica has been hampered by underdeveloped techniques for characterising layer continuity and geometry over large distances, with techniques developed independently and little opportunity for inter-comparison of results. In this paper, we present a methodology to assess the performance of automated layer-tracking and layer-dip-estimation algorithms through their ability to propagate a correct age-depth model. We use this to assess isochrone-tracking techniques applied to two test case datasets, selected from CreSIS MCoRDS data over Antarctica from a range of environments including low-dip, continuous layers and layers with terminations. We find that dip-estimation techniques are generally successful in tracking englacial dip but break down in the upper and lower regions of the ice sheet. The results of testing two previously published layer-tracking algorithms show that further development is required to attain a good constraint of age-depth relationship away from dated ice cores. I make the recommendation that auto-tracking techniques focus on improved linking of picked stratigraphy across signal disruptions to enable accurate determination of the Antarctic-wide age-depth structure.

The final aspect of the thesis focuses on Finite-Difference Time-Domain (FDTD) modelling of IPR data. I present a sliced-3D approach to FDTD modelling, whereby a thin 3D domain is used to replicate modelling of full 3D polarisation while reducing computational cost. Sliced-3D modelling makes use of perfectly matched layer (PML) boundary conditions, and requires tuning of PML parameters to minimise non-physical reflections from the model-PML

interface. I investigate the frequency dependence of PML parameters, and establish a relationship between complex frequency stretching parameters and effective wavelength. The resultant parameter choice is shown to minimise propagation errors in the context of a simple radioglaciological model, where 3D domains may be prohibitively large, and for a near-surface cross-borehole survey configuration, a case where full waveform inversion may typically be used.

Lay Summary

Pulses of radio waves can travel through glacier ice, reflecting from objects inside and beneath the glacier, much like the echoes of sound from a wall. We can record the time of these echoes and layer them together to build an image of the interior of the glacier using an ice penetrating radar (IPR). It is important to understand the thickness and material properties of glacier ice in order to estimate the total volume of ice in the glacier. This can act as a starting point for modelling how glacier flow and extent will change in the future.

The first part of this thesis looks to improve how the shape (topography) of the bed is estimated using IPR. The conversion from echo time to bed depth depends on the velocity of radio waves. The velocity can change due to the presence of water within the ice, which can also influence the movement of the glacier. Typically, estimating this velocity relies on focused surveys that are difficult to carry out over large areas, so a constant velocity is often assumed. I develop an approach to estimating radio wave velocity using radar data that is quick and cheap to acquire, which allows us to improve both the shape of the bed retrieved from a survey, along with an improved understanding of the distribution of water within the ice. I applied this approach to data collected on Von Postbreen, a glacier in Svalbard, and show that the radar velocity changes across the glacier. As a result, it is important to estimate velocity to retrieve correct glacier bed shape.

The second chapter of this thesis focuses on radar data acquired from aircraft flying over Antarctica. This data often shows many layer reflections that are formed at the same time and can be used to estimate the age of ice within the ice-sheet, much like tree rings. These layers also allow us to understand the complex development and history of the Antarctic Ice Sheet. As so much

data has been collected over Antarctica, it is too time consuming to manually interpret so recently scientists have worked to automate this. I develop a test-bed for comparing these automated approaches by comparing their ability to retrieve the correct structure, as compared to manually-interpreted datasets.

The final chapter focuses on computer modelling of radar data, which is used to predict what a radar system would see when given an imagined underground structure. To simulate surveys realistically, large 3D models must be used, however these are very time consuming and expensive to run. I develop an approach to minimising the size of these models, reducing the time to run them. This requires changing how signals in the model respond to the edge of the model, which can introduce errors if not handled correctly. This is achieved by introducing an imaginary material that absorbs all energy. I present an approach to finding the best properties for this material to get the best possible absorption at the boundary. I demonstrate the improvement in model speed as a result of this approach and apply it to a glacier-type model.

Declaration

I declare that this thesis has been composed solely by myself, and that it contains only my work except where otherwise specified, or where the work is explicitly indicated in the text to have formed part of a jointly-authored publication. This work has not been submitted for any other degree or professional qualification.

Richard Delf

September 2020

Data are plural

Unknown

Acknowledgements

The work in this thesis was funded by a studentship through the NERC E^3 DTP (NE/L002558/1). Additional costs for fieldwork were sourced from a SIOS Pilot Project (990035) and an EDUCT fund fieldwork grant along with a NERC GEF equipment loan (1094). A research visit to Stanford University was funded through a SAGES PECRE grant, and funding to attend the IGS Symposium on Radioglaciology in California was obtained through the Trans-Antarctic Association. Thank you to all the funding sources that made this work happen.

This thesis would not have been possible without so many people who have contributed throughout my time at Edinburgh. I would first of all like to thank my main supervisor, Rob Bingham. His guidance through the last few years has been invaluable, from grant applications, fieldwork, conference presentations, writing papers and, eventually, this thesis. None of it would have been possible, or indeed intelligible, without his careful and dedicated support. I would also like to thank Antonis Giannopoulos and Andrew Curtis, my wider supervisory team, for their insight and advice into designing the studies, and feedback throughout. Thanks to Dustin Schroeder for hosting me at Stanford University in 2018 and his valuable contributions. And thank you to Ben Schwarz, of GFZ Potsdam, and Satyan Singh for their diffraction expertise.

Special thanks go to Penny How, who took me under her wing and looked out for me through the first few years of this project. I wouldn't have made it this far without your support in Edinburgh and on fieldwork. Thank you. Many people contributed further to fieldwork in Svalbard, not least Chris Borstad, whose navigation of logistics and support throughout helped no end. Thanks to Sara Mollie and Dag for being the approachable arm of UNIS Lo-

gistics. And thanks to the AG-825 crew for making my first time in the Arctic great fun.

I would also like to thank the team at Orbital Micro Systems, most notably Greg and Dave, for their patience in me as I worked (very) part-time while writing this thesis.

The last few years in Edinburgh and further afield have been incredibly enjoyable, and I'd like to thank all the friends I've spent time with, whether it's on the bike, in the hills, or in the pub; not least John, Damon, Lizzie, and Andy for showing me around and for the many great days out in the Highlands or Borders. I attribute an expensive taste in beers to Amit, Paul, Ash, and Conrad; both I and The Salt Horse would thank you for keeping us going, if not afloat. And cheers to the usual suspects: Frazer, Pete, Charlie, Anthony, Monika, Boris, Lauren, Laura, Rosie, Julian, Josh, Louis, and Warwick for the nights in Brass Monkey and making office life fun. Thanks to Tom, Rob, and Katie for the great baseball and camping trips in California, and particular thanks to Angus, Frazer, and Amit for putting up with living with me, and my bikes, over the years.

I would like to thank my parents for all of their support and understanding of, at times, why I put myself through it. It was worth it, honest.

And finally, I would thank my partner Lauren. Your love, support, perk, and plant buying has helped keep me going through the ups and downs, and especially through the last 6 months. Keep being you.

Contents

List of Figures

List of Tables

List of Abbreviations

CFS Complex frequency stretched.
CMP Common mid-point.
CReSIS Centre for Remote Sensing of Ice Sheets.
CSP Common source-point.
DGPS Differential global positioning system.
FDTD Finite Difference Time Domain.
GPR Ground-penetrating radar.
ILCI Internal Layer Continuity Index.
IPR Ice-penetrating radar.
MCoRDS Multichannel Coherent Radio Depth Sounder.
MO Multi-offset.
NSF National Science Foundation.
PASIN Polarimetric-Radar Airborne Science Instrument.
PML Perfectly matched layer.
RES Radio-echo Sounding.
SAR Synthetic aperture radar.
SNR Signal:Noise Ratio.
SPRI Scott Polar Research Institute.
TUD Technical University of Denmark.
UTIG Univeristy of Texas Institute for Geophysics.
WAIS West Antarctic Ice Sheet.

Chapter 1

Introduction

Understanding the geometry and internal nature of glaciers and ice sheets is fundamental in the ability to understand the long-term evolution of the cryosphere. Quantitative modelling to constrain and understand the timing and evolution of sea-level rise through the 21st century and beyond requires an understanding of the contemporary ice configuration and physical nature (Golledge et al., 2019), in addition to understanding historical evolution and responses to past climate events (Augustin et al., 2004).

Radioglaciology provides a solution to many of the key requirements associated with such modelling. While one aspect of ice sheet modelling, surface elevation, can be readily extracted from satellite measurements (e.g. Neumann et al., 2019), understanding of the nature of glacier and ice sheet interiors over large spatial scales has largely relied on radiophysical exploration from ground-based or airborne platforms (Schroeder et al., 2020).

In Antarctica, geophysical exploration as part of the International Geophysical Year (1957-58), and subsequent long-range airborne mapping through the 1970s (Drewry et al., 1982) fostered an understanding of the subglacial topography of the Antarctic Ice Sheet, including identifying the West Antarctic Ice Sheet (WAIS) as inherently unstable in a warming climate, due to the bed being largely grounded below sea level (Mercer, 1978). The internal structure

of Antarctica has been explored using Ice-Penetrating Radar (IPR) and can be used to target ice-core locations to enable climate reconstructions (Forieri et al., 2004), or understand regional ice palaeo-dynamics (e.g. Bingham et al., 2015; Wearing and Kingslake, 2019)

Glaciers in the High Arctic and mountain regions are known to respond faster to climate change relative to Antarctica and Greenland and are currently a major contributor to sea-level rise (Zemp et al., 2019). Many such glaciers are polythermal or temperate in nature; IPR surveys have been instrumental in understanding the contemporary structure and long-term evolution of such thermal structure (Gusmeroli et al., 2012; Sevestre et al., 2015), a key component of the system due to the strong influence of water content on glacier ice viscosity (Duval, 1977).

1.1 Definitions

The term Ice-Penetrating Radar (IPR) encapsulates the range of approaches to radioglaciological surveys with the same ultimate aim, yet different implementations and equipment. The following outlines the main distinctions, which will be reviewed further in Chapter 2:

- Radar (Radio Detection And Ranging); a general term, not restricted to radioglaciology, referring to the use of radio waves to detect and characterise anomalies.
- RES (Radio Echo Sounding); a term used in early literature referring to the general case of sounding ice with radio waves, although now more commonly used to describe sounding from airborne systems with a chirp signal waveform (e.g. Hélière et al., 2007)
- GPR (Ground-Penetrating Radar); used to refer to a system using dipole antennas, usually with a monopulse signal (consisting of one cycle of a wavelet; Daniels et al., 2003). The term is more commonly used in modern surveys, using a ground-based (snowmobile or on-foot) or airborne

(helicopter or small plane) platform, often using commercial systems (e.g. Murray et al., 1997) or custom-built systems with similar designs (e.g. the St Olaf's College-developed RES system, Welch and Jacobel (2003), or the Deep-Look Radio-Echo Sounder (DELORES), King (2009)).

- IPR (Ice-Penetrating Radar); an umbrella term referring to both monopulse GPR and chirp RES, recognising that while the details of approaches differ technically, the principles and results are comparable.

1.2 Outline of the thesis

The main aim of this thesis is to develop novel techniques for the processing and imaging of IPR data collected over polythermal glaciers and polar ice sheets. The thesis is structured as follows. Chapter 2 presents a review of radioglaciology, starting with origins and development from midway through the 20th century, and highlighting major progress and impacts of the field on the understanding of the cryosphere through to the present. Specific topics within the modern-day research field are introduced and gaps in the knowledge are highlighted, motivating the work of this thesis.

Chapters 3, 4, and 5 have been written for publication. At the time of writing, Chapter 3 is in preparation for submission, Chapter 4 has been published as a contribution to a special issue of *Annals of Glaciology* (Volume 81, April 2020, "Progress in Radioglaciology"), and Chapter 5 is currently in review. At the beginning of each chapter, a summary of author contributions is given, along with publication details.

Chapter 3 develops a diffraction focussing-based approach to velocity analysis, which is then applied to common offset, ground-based GPR data acquired over Von Postbreen, a polythermal glacier in Svalbard. The derived velocity field is then used to infer englacial water content distribution and investigate the effects of assuming a constant velocity on bed topography reconstruction.

Chapter 4 reviews algorithms and approaches to automated interpretation

of ice sheet internal-layer geometry, and develops a formalised methodology for intercomparison of automated approaches. Three algorithms for layer geometry extraction and three algorithms for characterising internal-layer structure are tested on two test datasets, and recommendations are made for future developments in internal-layer tracing.

Chapter 5 develops an approach to full-waveform modelling of GPR surveys using a finite-difference time-domain (FDTD) approach, while minimising the computational demand by optimisation of perfectly matched layer (PML) boundary conditions. Specific applications of a cross-borehole survey and glaciological GPR survey are used to demonstrate the improvements of the approach relative to typically used 2D models.

Chapter 6 presents a discussion on the limitations and future development opportunities for each of the specific topics presented in the preceding chapters, before discussing wider opportunities and the direction of future development of radioglaciology. Chapter 7 gives the final conclusions of the thesis.

Chapter 2

Radioglaciology

This chapter presents a summary of key progress in radioglaciology, focusing on the key areas and knowledge gaps which will form the basis of Chapters 3, 4, and 5 of the thesis. Section 2.1 opens by discussing the origins, motivations, and major landmarks of the research field for both polar and sub-polar glaciers and ice sheets. Section 2.2 introduces the typical approach to processing and interpreting ice-penetrating radar. Section 2.3 discusses the nature and importance of the subglacial and englacial structure of glaciers and ice sheets, motivating the work of chapters 3 and 4. Section 2.4 will introduce the key concepts of finite-difference time-domain forward modelling, setting up the research presented in Chapter 5. The chapter finishes by outlining the key knowledge gaps of the research field, before closing with a summary of the aims and objectives of the thesis.

2.1 A brief history of radioglaciology

The roots of modern-day radioglaciology can be found in the early 20th century. Early experiments used re-purposed aviation altimeters operating at 440 MHz (Waite and Schmidt, 1962), which were shown to map ice depths consistent with that of a seismic line (Steenson, 1951; Evans, 1963). The challenge of reliably sounding the bed, through scattering and attenuative media, spurred

the development of high power, lower frequency systems to provide penetration required to observe the basal reflection across the polar ice sheets. The first continuous radar-derived ice depth profile was taken in North-West Greenland in 1964 (Robin et al., 1969). A transmitter with central frequency 35 MHz, developed by the Scott Polar Research Institute (SPRI), was towed for a 96 km traverse between two U.S. Army research camps. A wheel odometer between astronomically-determined locations was used to locate traces. This was the first study to observe internal reflections within the ice and to discuss the effect of temperature on signal attenuation, laying the foundation for modern research into the cryosphere using IPR.

Over the coming decades, developments in the capability of airborne radar systems led to increased airborne surveying, allowing greater spatial coverage of the Antarctic Ice Sheet. Notably, between 1967 and 1979 of the Scott Polar Research Institute (SPRI), the U.S. National Science Federation (NSF), and the Technical University of Denmark (TUD) covered 50% of the Antarctic Ice Sheet in a comprehensive and systematic manner using an airborne platform (Drewry, 1983). Improvements in navigation, by use of an inertial navigation system, reduced positional errors to below 5 km for much of the ice sheet (Turchetti et al., 2008), and the first use of multiple radar systems on the same flight enabled multi-frequency observations of the bed and near-surface layers simultaneously at 60 and 300 MHz (Siegert, 1999). The SPRI-NSF-TUD collaboration eventually acquired 400,000 km of data over 13,500,000km^2 of the Antarctic Ice Sheet, providing an insight into the 3D bed topography of Antarctica for the first time (Drewry et al., 1982; Drewry, 1983).

IPR became a valuable tool in support of multi-disciplinary research programmes over the coming decades. In Antarctica, surveys were typically regional in scope, targeting specific research objectives; the US Support Office for Aerogeophysical Research (SOAR) spurred extensive surveys over the Western Antarctic Ice Sheet (WAIS) (Blankenship et al., 1993; Behrendt et al., 1994; Bell et al., 1998). International groups surveyed Lake Vostok and surrounding

subglacial lakes using IPR (Masolov et al., 2006), expanding on data collected by earlier surveys (Siegert et al., 1998). Airborne and ground-based surveys over the Siple Coast Ice Streams showed differences between layering and bed properties across ice streams and the intervening ridges (Retzlaff et al., 1993; Blankenship et al., 2001; Gades et al., 2000). Targeted radar surveys around the European Project for Ice Coring in Antarctica (EPICA) ice core site aided precise drilling location and provided estimates of the expected age of the deepest ice (Rémy and Tabacco, 2000; Forieri et al., 2004; Parrenin et al., 2007).

In the 21st century, more long-range surveys including Operation IceBridge (OIB) and the ICECAP projects acquired data over new regions not surveyed by the previous SPRI-NSF-TUD collaboration, including extensive and detailed surveys of the Thwaites catchment of the WAIS (Holt et al., 2006), surveys across the remotest parts of the East Antarctic Ice Sheet (Bell et al., 2011; Young et al., 2011) and over the South Pole (Jordan et al., 2018a), providing further valuable insight on bed topography and conditions at the ice-bed interface.

Greenland has similarly been widely explored using airborne systems, firstly in TUD-led efforts in the 1970s (Gudmandsen, 1975). Throughout the 1990s and 2000s extensive airborne surveys, principally led by CReSIS of the University of Kansas with OIB, covered much of the ice sheet. This included focused and systematic surveys over dynamic regions at the ice-sheet margin, notably over the Northeast Greenland Ice Stream (NEGIS) and the outlet of Jakobshavn Isbrae, and covering much of the west and south-eastern margin (Fahnestock et al., 2001). Continued surveys through the 21st century have enabled interpretation of ice-sheet-wide age-depth structure (MacGregor et al., 2015b), retrieval of subglacial topography, (Bamber et al., 2013; Morlighem et al., 2017), and imaging of englacial properties and subglacial hydrology and properties across much of the ice sheet (Jordan et al., 2018b).

Many of the aforementioned surveys have been over ice-sheet wide or re-

gional scales, using airborne platforms, yet ground-based surveys enable acquisition of higher-resolution grids and sounding on mountain or sub-polar glaciers. Over Antarctica, ground-based surveys have been used to investigate specific sites in greater detail; for example in investigating the structure of shear margins of Ice Stream C (Jacobel et al., 2000). High-resolution radar grids have been acquired to show the spatial variation of basal conditions of Rutford Ice Stream through amplitude analysis (Murray et al., 2008; King et al., 2009), and significant differences in basal roughness between regions (Bingham et al., 2017).

Radar has additionally been used extensively on smaller mountain and sub-polar glaciers. An inventory of ice thickness of Svalbard glaciers was undertaken throughout the first half of the 1980s (Macheret and Zhuravlev, 1982; Dowdeswell et al., 1984a; Drewry and Liestøl, 1985), using helicopter-mounted systems. A comparison of interpretations of this data to high frequency (440 - 840 MHz) Russian collected data revealed a strong scattering layer within many of Svalbard's polythermal glaciers (Dowdeswell et al., 1984a). Numerous radar surveys since acquired over polythermal glaciers have aided in understanding the structure through sounding of the englacial scatter (Jania et al., 1996), or derivation of englacial velocity (Björnsson et al., 1996; Murray et al., 2000) or water contents (Hamran et al., 1996; Pettersson et al., 2003). These have more commonly utilised ground-based, commercially-available systems such as PulseEKKO or Mälä rough terrain antennas systems.

These extensive studies covering much of the polar ice sheets have resulted in iterative improvements of understanding of Antarctic and Greenland bed topography (Drewry et al., 1982; Drewry, 1983; Lythe and Vaughan, 2001), most recently through the Bedmap2 collection for Antarctica (Fretwell et al., 2013) and BedMachine V3 products for Greenland (Morlighem et al., 2017) and Antarctica (Morlighem et al., 2020), although there remain many gaps in the record over regions of Antarctica (Pritchard, 2014). Approaches to estimating these gaps in the record differ between collections: the Bedmap2

approach to in-filling spatial gaps in the record uses alternate geophysical data sources, principally gravity, owing to the global spatial coverage from satellite data (Fretwell et al., 2013). Numerous mass-conservation (Morlighem et al., 2017; Farinotti et al., 2017) or geostatistical approaches (Goff et al., 2014; MacKie et al., 2020; Leong and Horgan, 2020) enable observation-consistent interpolation of bed topography of Antarctica and Greenland for ice-sheet modelling purposes. Similar collections have also been generated for Svalbard (Fürst et al., 2018) and the Himalaya and high-mountain Asia (Pritchard et al., 2020).

The radar-derived bed topography of glaciers and ice-sheets is commonly used to estimate subglacial flow paths (Rippin et al., 2003a; How et al., 2017) and subglacial water distribution through amplitude-based analysis of the bed return (Baelum and Benn, 2011). Further afield, radio-echo sounding has been undertaken on glaciers of the Canadian High Arctic on, for example, John Evans Glacier, where radar-derived basal topography (Copland and Sharp, 2001) was used to estimate basal water flow paths, which were later linked to seasonal velocity variations in the ablation area of the glacier (Copland et al., 2003; Bingham et al., 2008). The temporal characteristics of these systems have been explored through repeat and time-lapse surveys, relating the glacier motion, dynamics, and subglacial and englacial hydrology (Jacobel and Raymond, 1984; Jania et al., 2005).

The techniques and understanding gained through terrestrial radioglaciology have been applied beyond the terrestrial cryosphere; the NASA Mars Reconnaissance Orbiter carried a small radar system with the aim of imaging the near subsurface. The result was evidence of glaciated terrain (Phillips et al., 2008), and a full 3 dimensional model of the Martian polar ice caps (Putzig et al., 2018; Foss et al., 2017). The potential discovery of liquid water in the subglacial environment on Mars was reported in 2018 from orbital radar sounding (Orosei et al., 2018).

2.2 Theory and processing of IPR

Sounding vs. imaging IPR

Many of the advances described above can be categorised into the approaches of *imaging* and *sounding*. *Sounding* is generally considered to be the raw data acquisition, generating an understanding of the geometry of the subsurface structure, whereas *imaging* is the further processing of sounding data to generate data products. These products may be simply geometrically-corrected radargrams through the process of migration and depth conversion using an assumed constant velocity, or the derivation of other products such as the spatial variation of radar wave velocity, attenuation or basal reflectivity, hydrology, and melt.

There are a range of processing strategies applied to radar data collected over glaciers and ice sheets; the approach is generally dictated by the radar system used - either *incoherent* (impulse waveform) or *coherent* (usually using a chirp waveform) - and the scientific objective. Additional choices must be made to target specific objectives, for example sounding the internal structure or bed reflector of the ice. This section will introduce the processing approach for pulsed *incoherent* radar systems, followed by *coherent chirp* (frequency-modulated continuous wave, FMCW) radar processing.

2.2.1 Incoherent radar data processing

I first outline the standard processing steps usually taken for ground-based, pulsed radar data. This is generally considered to be *incoherent* radar in that phase data are not collected or used in the processing. This approach is used for the pre-processing of ground-based GPR data in Chapter 3. Figure 2.1 shows a flow-chart summary of this processing flow.

1. Assign trace geometries. GPS coordinates associated with the acquired data are often stored in a separate file to the radar data. On importing

data, trace coordinates are assigned. It is usually desirable to have a regular trace spacing, and this is achieved by interpolation or stacking of traces.

2. Dewow filter. The positioning of the receiver in the near-field of a transmitting antenna commonly results in a low-frequency or DC shift in trace amplitudes. As the geometry is generally stable throughout the survey, this can often be removed using a trace average subtracted from the data. Trace averaging additionally removes much of the direct arrival.
3. Bandpass filter. Aims to remove high-frequency noise and scatter. Exact frequency choices are dependent on the centre frequency of the antennas used.
4. Migration. Migration is the process by which diffraction hyperbolas are collapsed to their scattering location, and dipping reflectors are translated to their correct position within the radargram (Yilmaz, 2001). In general, this is applied using Stolt or Kirchhoff migration.
5. Amplitude correction. Scaling proportional to $\sqrt{t}$ to remove amplitude decay with two-way travel time.
6. Depth conversion. Data up to this point are in two-way travel time; this step uses the velocity of radar wave propagation in ice to convert to a depth. Similar to migration, a constant velocity is often used of 0.165-0.169 m/ns.

2.2.2 Coherent radar data processing

Coherent radars are generally processed through a synthetic aperture radar-based (SAR) approach, and this has been commonly applied for airborne systems in the 21st century. The following approach is an outline of Legarsky et al., 2001; Gogineni et al., 2001; Hélière et al., 2007; Peters et al., 2007, which have formed the basis of data processing for the long-range polar ice-sheet surveys carried out by the University of Texas, CReSIS and BAS. The

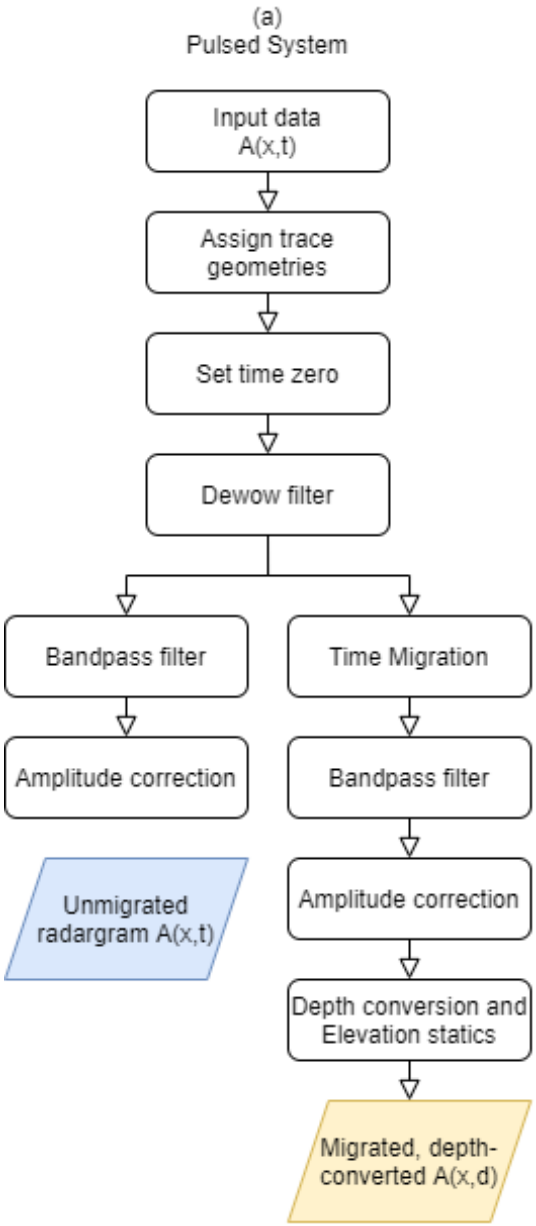

Figure 2.1: Processing flow for a pulsed radar system, as commonly used for ground-based studies over polythermal glaciers.

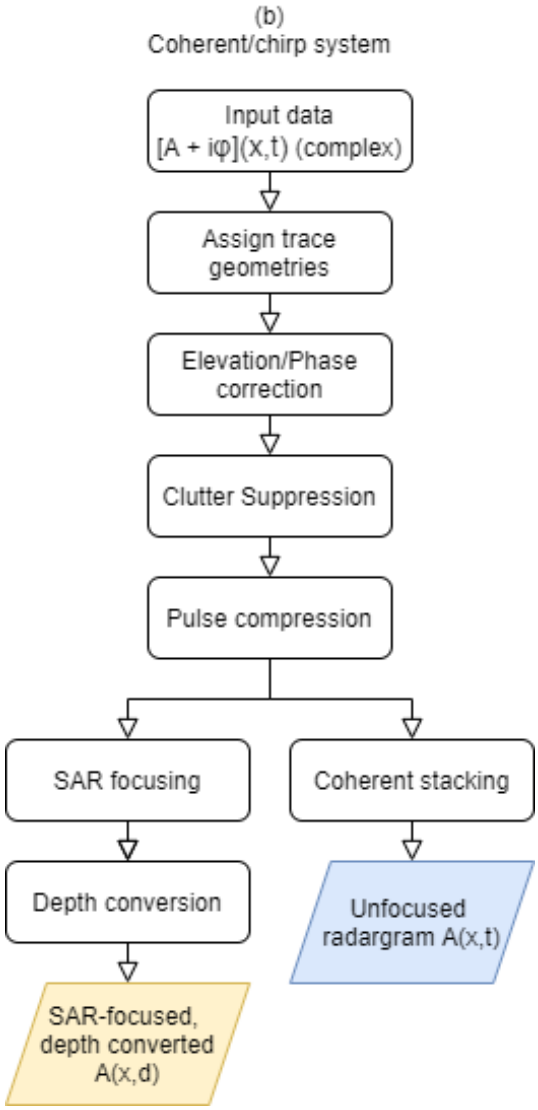

Figure 2.2: Processing flow for a coherent radar system, usually used for airborne radar systems over ice sheets.

process broadly fits into the steps of trace processing and along-track focusing, analogous to trace-by-trace filtering and migration steps of the incoherent processing described above. This approach is summarised in Figure 2.2

1. Data are acquired using a linear frequency chirp, defined by a chirp length and a bandwidth around a central frequency. The in-phase and quadrature components of the received waveform are digitised.
2. A phase correction, using the vertical component of the GPS trace, is applied to compensate for vertical aircraft motion.
3. Pulse compression using a tapered replica of the source waveform is applied; this generates an amplitude trace with a range resolution (at this point, layers and the bed return are interpretable).
4. Along-track coherent stacking, which may use phase information to generate coherent layers (Castelletti et al., 2019), can be applied at this point to increase SNR. This *unfocused* radargram is usually sufficient to pick layers in low-dip regions and can be considered equivalent to a pre-migrated radargram, where hyperbolas are present along the bed.
5. SAR focusing, analogous to Stolt (f-k) migration, is applied to collapse hyperbola along the bed reflection.

2.2.3 Multi-offset radar data

Radar wave velocity is often estimated through travel-time tomography of data acquired using multi-offset survey geometries; most commonly in the form of a common mid-point (CMP) or common source-point (CSP) survey. In a CMP survey, source-receiver offset increases symmetrically around a central point; CSP surveys use a single source location, with receiver offsets increasing from the source location. The general principle of multi-offset geometries was developed for seismic acquisitions (Green, 1938), where multi-offset surveys have long been the standard. In seismic exploration, multi-offset geometries enable assessment of seismic wave velocity, amplitude-versus-offset (AVO) analysis to

further characterise reflection properties (Yilmaz, 2001), assessment of attenuation (Reine et al., 2012), and full-waveform inversion (Virieux and Operto, 2009).

Velocity is derived through observing the relationship between two way travel time and source-receiver offset. The increasing travel time as a function of source-receiver offset can be described analytically through the moveout curve, known as the Dix NMO Equation (Dix, 1955),

$$t^2(x) = t_0^2 + \frac{x^2}{v_{NMO}^2}, \tag{2.1}$$

where $t(x)$ is the two-way travel time measured at a receiver offset x, t_0 is the two-way travel time at zero offset and v_{NMO} is the normal moveout velocity.

In early surveys and through the mid-20th century, assessment of v_{NMO} was by means of manual picking of the reflection moveout curve in data, and fitting of a straight line of best fit in the $x^2 - t^2$ domain (Robin et al., 1969). The modern approach, after Taner and Koehler (1969), uses the measure of semblance along a hyperbolic trajectory for all combinations of t_0 and v_{NMO} in Eq. 2.1, calculating semblance, S, by

$$S = \frac{\sum_{t=t_0}^{t_0+mdt} \left(\sum_{x=1}^{N} a_{t_x} \right)^2}{N \left[\sum_{t=t_0}^{t_0+mdt} \sum_{x=1}^{N} (a_{t_x}^2) \right]}, \tag{2.2}$$

where N is the maximum number of traces x, dt is the time discretisation of the recorded trace with data of amplitude a, m is the number of samples in the semblance window, and t_x is the two-way travel time at trace x. v_{NMO} is estimated from the peak of the semblance response, although for GPR corrections must be made for the mixed-phase nature of a GPR wavelet through back-shifting the pick of the semblance peak to match the first break two-way travel time (Booth et al., 2008a).

The CMP geometry has been widely utilised in near-surface GPR, in both

continuous surveys, and as sparse control-points within a wider common offset survey. Single CMP acquisitions can be integrated with common-offset datasets to improve interpretation through velocity analysis (Greaves et al., 1996) or amplitude versus offset analysis (Baker, 1998; Zeng et al., 2000). Continuous multi-fold (2D) data enable the application of more advanced seismic processing techniques to enhance data quality, including velocity analysis and stacking to improve SNR (Fisher et al., 1992a; Booth et al., 2008b). The logistics of continuous multi-fold acquisition are simplified for high-frequency systems, which can be easily managed due to the small size of antennas (e.g. at 500 MHz, Annan and Jackson, 2017). In many cases, however, acquisition must be through manual positioning of antennas (Forte and Pipan, 2017; Booth et al., 2008b) and continuous profiles become logistically challenging. The use of multi-offset surveys in glaciology will be revisited in section 2.3.3.

2.3 Radar for interrogating subglacial and englacial conditions

2.3.1 Radar for subglacial environments

The primary motivation of many radar surveys is to retrieve glacier thickness through picking of the bed reflector. Yet the subglacial topography of glaciers and ice sheets gives only a partial insight into the dynamics of ice flow. The flow of glacial ice can be considered as a force balance between the driving stress of ice with resisting forces of drag, including basal drag and buttressing. Frozen beds, where the bed is below the pressure melting point, allow only a small degree of sliding and flow is dominated by ice deformation processes, commonly described by Glen's relation (Glen, 1955). Basal sliding occurs predominantly where the bed is at the pressure-melting point, where regelation and enhanced creep allow ice flow over small obstacles, and cavitation reduces ice-bed coupling (Weertman, 1957, 1964; Lliboutry, 1968). As water is unable

to sustain shear stress, the effective basal stress is zero above a water cavity. The size and lateral extent of cavities is enhanced by pressurised basal water, which increases driving forces down-glacier, enhancing ice velocities (Iken et al., 1983; Bindschadler, 1983). In modern thermo-mechanical ice sheet models, the interaction of ice with the bed is often parameterised by a bed sliding friction including contributions of subglacial geology, bed roughness and wetness (Ritz et al., 2015). Understanding the spatial variation of such contributions is vital in understanding ice dynamics (Gasson et al., 2015; Nias et al., 2016).

The presence of water significantly increases the dielectric constant of a material and as such, radar is highly sensitive to the presence of water at the bed. Most work focusing on the characterisation of subglacial hydrology has taken advantage of this phenomenon. While borehole and surface seismic methods can give a good indication of basal hydrological conditions and the structural nature of subglacial sediments at specific locations (Blankenship et al., 1986; Smith, 1997; Anandakrishnan et al., 1998), their spatial coverage can be limited due to logistical constraints; seismic studies may require drilling to a depth of 10 to 20 m for each source and receiver (King et al., 2007). Radar enables acquisition and retrieval of the location of basal water over individual glaciers (Baelum and Benn, 2011) on regional scales (Shabtaie et al., 1987; Schroeder et al., 2014), and across ice-sheets (Jordan et al., 2018b) to interpret the presence of subglacial water or lakes (Robin et al., 1970; Wright and Siegert, 2012), characterised by a flat, specular reflector.

The ability to infer the precise dielectric nature of subglacial material is hampered by uncertainty in the propagation of radio waves through the overlying snow and ice, including the potential of scattering from the surface roughness and crevasses (Peters et al., 2005). Matsuoka (2011) argues that lateral variations in the bed return power can be directly influenced by englacial radar attenuation; therefore, given a lack of an accurate englacial attenuation model, the problem of estimating the subglacial dielectric constant is underdetermined. Investigation of the frozen state of the bed can nonetheless be

achieved through differentiation between frozen and thawed bed as the difference in reflection coefficient for the two cases is suitably large (Jordan et al., 2018b). Estimations for englacial attenuation can be made through a fit of radar amplitude as a function of depth (Matsuoka et al., 2010a; Matsuoka et al., 2010b), modelling based on ice-sheet model predictions (MacGregor et al., 2007; Ashmore et al., 2014; Matsuoka et al., 2012a), or through use of relative internal stratigraphy amplitude variations (MacGregor et al., 2015a).

2.3.2 Internal layers of polar ice sheets

Most radar surveys acquired over Antarctica and Greenland sound internal layers, methods for the detection of which form the central topic of the first research paper of this thesis (Chapter 3) They were observed in some of the earliest radar surveys, yet the exact nature of the reflections was uncertain. Robin et al. (1969) and Gudmandsen (1975) hypothesised that they represent isochrones within the ice, inferring that they could be attributed to changes in ice physical properties as a result of historic climate change and changes in the physical structure of the ice. Millar (1982), Moore (1988), and Fujita and Mae (1994) compared layers to the conductivity profiles from ice cores and concluded that these internal layers were most likely to be as a result of changes in internal conductivity, usually due to deposition of acidic volcanic ash layers at the ice sheet surface.

Three principal mechanisms are known to result in a reflection within ice sheets. Firstly, changes in density as a function of depth manifest as a change in the real part of the permittivity of ice as a result of the physical evolution of snow to firn, and then ice. Density variations are usually soundable to depths of less than 1000 m, below which changes in density are unlikely to occur (Siegert, 1999). The second is the aforementioned changes in conductivity due to the deposition of acidic layers at the surface (Moore et al., 1999; Fujita and Mae, 1994). Conductivity contrasts result in a change in the complex part

of dielectric constant and result in a frequency-dependent reflection coefficient with a phase change of $\frac{\pi}{2}$ on reflection. The final mechanism is through changes in the crystal orientation fabric, resulting in an anisotropy of dielectric constant (Eisen et al., 2007). Such fabric variations are rarely isolated and mapped across ice-sheet scales, and are more commonly derived through polarimetric surveys (Jordan et al., 2020). As the origins of internal layers are due to such ice-sheet wide surface processes, followed by compression and advection through ice flow (Vaughan et al., 1999), internal layers are usually considered to be isochronous in nature (Siegert, 1999).

Shallow Radiostratigraphy

Density contrasts in the upper ice column (10's of metres) are commonly sounded using snow radars operating in high-frequency ranges with, for example, the CReSIS snow radar operating at 2 - 18 GHz, enabling a vertical resolution of 5 cm to a depth of 40 m (Arnold et al., 2019). Such resolution enables studies of the very near-surface and picking of annual isochrones within the firn over ice-sheet scales. While the upper ice column is not the focus of this thesis, the study of isochrones near-surface nonetheless shares many of the same challenges as deep radiostratigraphy. Numerous high-resolution surveys have been undertaken with commercial pulsed (Anschütz et al., 2008) and custom-developed FMCW radar systems (Kanagaratnam et al., 2001; Arnold et al., 2019) to derive spatio-temporal variations in historical accumulation rates across Greenland and Antarctica. Large scale surveys include those by the International Trans-Antarctica Scientific Expedition (ITASE, 1998-99) and US-ITASE (2006-07), which revealed the internal structure of the megadunes of East Antarctica, developing the model of windward migration of the structures due to aeolian processes with pervasive katabatic winds (Frezzotti, 2002; Arcone et al., 2005), in addition to linking shallow ice cores across East Antarctica by isochrones in high-frequency GPR data (Frezzotti et al., 2005). Medley et al. (2013, 2014) used shallow internal layering to derive 30-year records of

accumulation over Thwaites and Pine Island glaciers, closely matching independent estimates from climate reanalysis and ice core estimates and concluding that the increased mass loss from the region has not been balanced by increased accumulation. Koenig et al. (2016) use high-frequency airborne data over Greenland to generate an ice-sheet wide, 3-year record of surface accumulation. Near-surface stratigraphy can commonly be dated by counting of stratigraphy assuming it is a result of seasonal temperature cycles, although this is commonly undertaken using isotope analysis (commonly, SO_4^{2-}), and by counting the seasonal cycles of relative geochemical concentrations (Steig et al., 2005; Eisen et al., 2008).

Deep Radiostratigraphy

Deep radiostratigraphy represents palaeoaccumulation over millennial timescales and greater. The dielectric contrast in the deeper ice column (in general, >1000 m depth) is usually a result of ice chemistry variations, often due to deposition of acidic aerosols from global volcanic activity (Millar, 1982), and can be more readily correlated to the conductivity profile of an ice core (Winter et al., 2017). In addition to the isotope analysis of near-surface ice-core dating, deep radiostratigraphy can be successfully dated using radiophysical (radioactive decay process-driven) processes (Pourchet et al., 2003; Eisen et al., 2008). The principal motivations for interpreting and tracing deep radiostratigraphy are to extrapolate knowledge of the age-depth structure of the ice sheets between and away from deep ice cores, to explore for the oldest ice for targeted drilling, to improve our understanding of contemporary and historical ice flow using isochrone geometry incorporated into ice flow models (Baldwin et al., 2003; Waddington et al., 2007), and to understand historical ice flow dynamics through observations of the continuity of isochrones (Rippin et al., 2003b; Bingham et al., 2007; Karlsson et al., 2012)

Continuity of internal layers

The continuity and character of deep radiostratigraphy can often be used as an indicator of ice flow dynamics and associated historical changes (Bell et al., 1998). Rippin et al. (2003b) and Siegert et al. (2003) qualitatively group radar stratigraphy into three main groups: continuous layers, suitable for tracking, disrupted layers (where undulations far exceed the scale induced by bed topography alone), and a lack of clear internal layers. They found that in general, disrupted layers originated in regions of higher balance velocity. By extension of this method, Rippin et al. (2006) inferred dynamic slow-down of Slessor Glacier, East Antarctica due to highly disrupted stratigraphy coincident with low surface velocities. Finally, this qualitative approach was furthered by Bingham et al. (2007) to use data acquired over the south pole, where satellite-derived surface velocities were unavailable, to evaluate the presence and extent of balance velocity model-derived enhanced flow from East Antarctica to the Filchner-Ronne Ice Shelf.

The manual nature and degree of subjectivity involved with this method motivated the development of quantitative metrics of internal layer disruption. The internal layering continuity index (ILCI) approach was developed by Karlsson et al. (2012) by calculating a mean of the absolute derivative,

$$\psi = \frac{1}{2\Delta r N} \sum_{i=n_1}^{n_N} |P_{i+1} - P_{i-1}|, \tag{2.3}$$

where r is the depth, n is the sample number within the selected section length N within the radargram. A smoothing operator is applied over a defined spatial range to reduce noise. An example from Karlsson et al. (2012) is shown in Fig. 2.3. In practice, it is a measure of total power reflected in a radargram, with regions of disrupted layering suffering from power loss relative to coherent layers due to non-specular reflection and incoherent stacking. ILCI can be readily applied over large-scale survey grids; it was successfully applied over

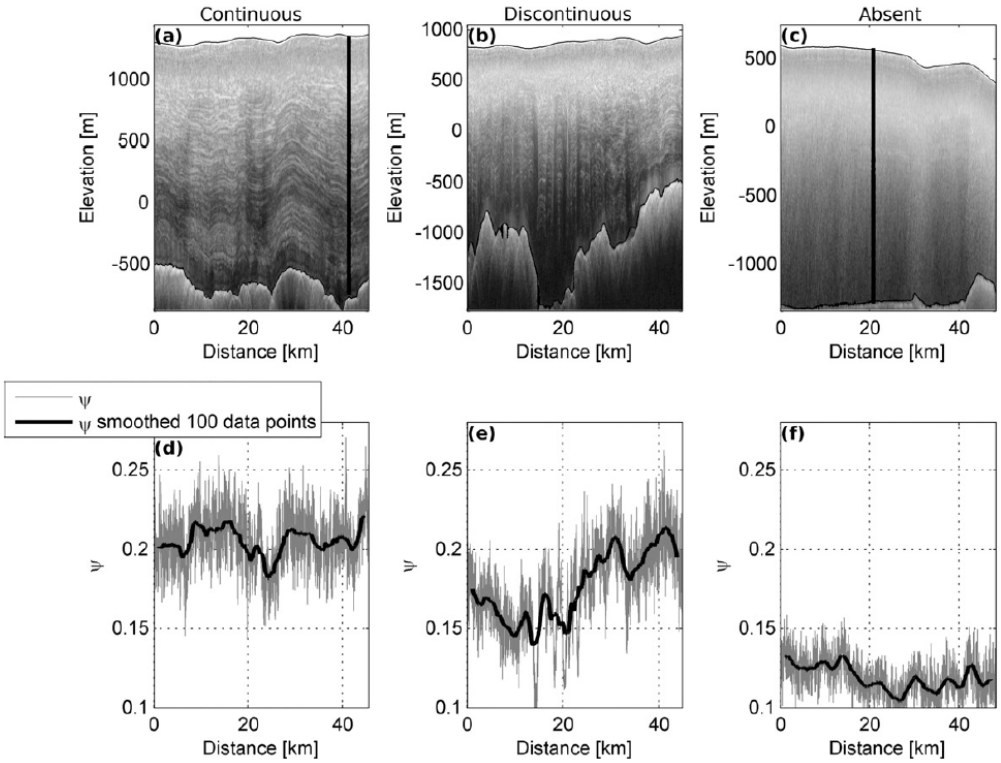

Figure 2.3: Example of internal layer continuity index (ILCI, ψ) showing the responses to (a) continuous, (b) discontinuous, and (c) absent layering, with associated plot of ψ in (d), (e), and (f). Figure from Karlsson et al. (2012).

Pine Island Glacier, West Antarctica, to delineate internal layer characteristics (Karlsson et al., 2012). Bingham et al. (2015) and Winter et al. (2015) use ILCI, in addition to extensive manual layer tracking, to understand the historical ice dynamics of Institute Ice Stream, showing instabilities of flow and supporting models of flow reconfiguration over the last 4000 years (Siegert et al., 2013). ILCI has since been further applied over Greenland to delineate shear margins of the North-East Greenland Ice Stream (NEGIS) (Keisling et al., 2014). Ashmore et al. (2020) show that ILCI can be used to inform regions where internal stratigraphy can be successfully traced, aiding subsequent interpretation and investigations into ice sheet age-depth structure, as will be discussed in the following section.

Radiostratigraphy for age-depth structures

The isochronal nature of internal layers permits the propagation of age-depth relationships away from ice-core locations. The chronologies of the Vostok and Dome C ice cores, separated by over 500 km, were linked by Siegert et al. (1998) by correlating amplitude peaks in A-scope (single trace) data at 50 km intervals, using data from the original 1970s SPRI-NSF-TUD surveys. By using the age-depth relationship derived at Vostok, an age-depth relationship at Dome C could be predicted, constrained by 6 layers apparent throughout the data. Many studies have since used similar methodologies of tracing individual internal layers through the ice sheet, away from ice cores. Cavitte et al. (2016) again linked Vostok and Dome C ice-cores, using modern and higher resolution McORDS data. Winter et al. (2019a) traced stratigraphy from Dome Fuji to the EPICA-DML (European Project for Ice Coring in Antarctica Dronning Maud Land) ice-core site to predict ages for oldest ice drilling targets. Ashmore et al. (2020) traced three horizons across the Institute and Möller ice streams of WAIS.

By far the most complete understanding of ice-sheet wide age-depth geometry has been compiled for Greenland, through field campaigns by the University of Kansas CReSIS and NASA Operation IceBridge (OIB) (Gogineni et al., 2001; Fahnestock et al., 2001; MacGregor et al., 2015b). Airborne campaigns over Greenland between 1993 and 2013 resulted in a collection of 479,595 km of 150 and 195 MHz coherent radar data sounding the bed, of which 158,091 km included traceable internal layers. The margins of the Greenland Ice Sheet consist of extensive firn aquifers (Forster et al., 2014; Chu et al., 2018) and regions of highly disrupted stratigraphy due to fast ice flow, precluding layer tracing across much of the margin. The challenge of manually tracing internal stratigraphy over an ice-sheet scale motivated the development of several techniques to aid the interpretation, bringing a degree of semi-automation to the process. While maximum peak and correlation auto-trackers had previously been

used to enhance manual approaches (Fahnestock et al., 2001), the Greenland project included several approaches to process the data beyond L1B products to improve pick success and minimise user intervention, generally through flattening layers using layer slope (MacGregor et al., 2015b). Typical horizontally coherent layers result in a smooth variation of phase which can be tracked to derive a rate of phase change $\frac{\Delta\phi}{\Delta t}$, which can be linked to slope by

$$\frac{\Delta t}{\Delta x} = \frac{1}{2\pi f_c}\frac{\Delta\phi}{\Delta t}, \tag{2.4}$$

where f_c is the central frequency of the radar system. Alternatively, a Doppler centroid approach, exploiting the peak of the response in a radon transform enabled automated extraction of layer dips. Both approaches were used for layer flattening, before manual and semi-automated picking were applied to flattened horizons.

Numerous challenges are encountered when attempting to re-create an age-depth model of Antarctica. As discussed in section 2.1, regions of Antarctica have been progressively surveyed using systems of numerous age, resolutions, frequencies, and noise levels. The challenge of reconciling system response was highlighted by Winter et al. (2017) by comparing five systems passing close to Dome C.

Internal layer dip

As a means of mitigating the challenges of tracing layers through multiple datasets across Antarctica, several studies have looked to develop automated methods to quantifying slopes within radargrams. This can be approached by means of moving window-based analysis of amplitude data (Sime et al., 2011; Panton, 2014; Holschuh et al., 2017) or phase-tracking of coherent data before horizontal stacking (Castelletti et al., 2019). Derived dip fields may also be used for layer flattening to simplify layer tracking (MacGregor et al., 2015b; Panton, 2014), and may be more robust in regions where isochrones

are obscured in regions of high noise (e.g. Holschuh et al., 2017).

Beyond its use as an aid for isochrone interpretation, the dip of internal stratigraphy enables assimilation of internal layer geometry with ice-sheet models. The geometry of internal layers has been used to infer palaeo-ice dynamics through integration with ice-sheet models (Ng and Conway, 2004; Catania et al., 2006; MacGregor et al., 2016). Examples include Leysinger Vieli et al. (2007) who used idealised modelling to show the impact of ice-flow on internal layer stratigraphy to aid interpretation of features intersected at multiple angles by a radargram. Holschuh et al. (2017) additionally presented a set of cases (idealised models) to aid the integration of englacial layer-dip data into interpretation to differentiate between the effects of topography, accumulation and basal processes.

2.3.3 Radar for sounding and imaging polythermal glaciers

Polythermal glaciers are characterised by the presence of both temperate and cold ice. There are multiple different forms of polythermal glacier (Irvine-Fynn et al., 2011), but for the following discussion I focus on a form typically found across the High Arctic, usually consisting of a two-layer structure, with cold ice overlaying temperate ice deep within the glacier which is at the pressure melting point (Irvine-Fynn et al., 2011). Improving our ability to image the internal structure of such glaciers forms the topic of the first research paper of this thesis (Chapter 3).

Radar surveys are highly sensitive to temperate ice as water inclusions result in a high degree of scatter; the nature of the scatter is dependent on the frequency of the survey used. Some of the first widespread surveys over the Svalbard archipelago were undertaken using a helicopter-borne platform with radar systems operating between 440 and 865 MHz, starting in 1974 (Macheret and Zhuravlev, 1982). Similar airborne surveys, starting in 1980 (Dowdeswell et al., 1984a) were undertaken using a system with a 60 MHz central fre-

quency, and comparison of the assumed bed reflection showed a significant underestimate from many of the earlier, higher-frequency surveys, with the newly derived bed topography closely matching that estimated by gravity surveys. Dowdeswell et al. (1984a) concluded that the higher frequency systems were sensitive to an internal reflecting horizon, which had been misinterpreted as the bed. This conclusion was corroborated by sparse estimations of gravity along the survey lines.

Widespread internal scatter within polythermal and temperate glaciers is usually the result of liquid water content held within the ice, and hence can often be considered an expression of the thermal state of the glacier. It is often referred to as the cold-temperate transition surface (CTS) (Blatter and Hutter, 1991), or, in recognising it as being a non-discrete surface, the cold-temperate transition zone (CTZ) (Irvine-Fynn et al., 2011).

A reflection-coefficient-based analysis of the scattering characteristics of these internal horizons placed estimates of the internal water content (approximately 3%, Bamber, 1987) for the CTS. Bamber (1987) also compared the topography of the upper scattering layer to the piezometric surface derived from a Röthlisberger channel using a range of channel roughness parameters to fit the observed topography (Röthlisberger, 1972). The Röthlisberger channel approach, however, assumes pressurised and distributed hydrological systems which may not apply for the general case of an internal scattering layer due to connectivity with low-pressure channels (Murray and Clarke, 1995; Fudge et al., 2008; Walder, 2010).

The link between glacier thermal state and englacial scatter was further developed by Björnsson et al. (1996). By comparing the position of the upper scattering layer with down-borehole temperature measurements across Kongsfjorden, Svalbard, pervasive englacial scatter in radargrams was linked to the presence of temperate ice, often overlain by a layer of cold ice. The deep temperate ice was at the pressure melting point and believed to be advected down-glacier from the accumulation area, where summer meltwater refreezes

within the firn, releasing latent heat within the firn. Similar studies with borehole-derived temperature profiles and radar have shown the radar-derived CTS matches the transition to temperate ice at Finsterwalderbreen, Svalbard (Ødegård et al., 1997), Storglaciären, Arctic Sweden (Pettersson et al., 2003) and in the European Alps (Ryser et al., 2013).

The lateral extent and topography of the internal scattering layer is therefore interpreted as indicative of the glacier thermal state. Manual interpretation of CTS topography has been widely used to derive the glacier thermal state across Svalbard (Dowdeswell et al., 1984a; Bamber, 1987; Jania et al., 1996; Sevestre et al., 2015) and to interpret the presence and dynamics of cold ice within temperate glaciers (Pettersson et al., 2003; Reinardy et al., 2019). Schannwell et al. (2014) present a radar amplitude-based approach to automate the interpretation of this upper scattering layer, although issues with noise or surface-related scatter in the upper regions of the glacier hamper such efforts.

Scattering within glaciers is not exclusively a result of internal water content. Debris can be entrained within glaciers by a range of mechanisms; predominantly basal freeze-on, folding, crevasse filling of supraglacial sediment and thrusting (Hambrey and Glasser, 2011). Numerous studies in Svalbard have observed internal scatter as a result of sediment entrainment in thrust structures close to the glacier front. These have typically been as a result of historic surges, where a surge front has approached a cold frontal region with a frozen bed. The subsequent thrust faults with entrained sediment have been imaged by radar using 2D (Murray et al., 1997; Sevestre et al., 2015) and 3D surveys (Murray and Booth, 2010), and correlated with outcropping sediments at a nearby ice cliff (Woodward et al., 2003). These features are commonly identified as low-dip, connected to the bed and consisting of a continuous reflector; this is in contrast to englacial water content, which is often chaotic in nature with multiple single diffraction hyperbolae, bounded by an undulating upper layer. Debris entrainment has also been observed in the Weddell

Sea sector of the West Antarctic Ice Sheet by ground-based GPR, reaching the surface in blue-ice regions of negative surface mass balance (Winter et al., 2019b).

Three principal approaches have been used in efforts to further quantify the englacial water content of polythermal glaciers from surface radar surveys: scattering-based approaches, multi-offset based approaches, and common-offset diffraction focusing approaches. These will be outlined in the following section.

Backscatter amplitude-based approaches

These approaches generally exploit the backscatter amplitude from the upper reflecting interface from common-offset surveys (Hamran et al., 1996; Pettersson et al., 2004). The received backscatter power P_r of a target with scattering cross-section σ can be described by the radar range equation (Ulaby et al., 1981)

$$P_r = \frac{P_t G^2 \lambda^2 \sigma}{(4\pi)^3 R^4} e^{-4\alpha R}, \tag{2.5}$$

where P_t is the transmitting power, G is the antenna gain, λ is the signal wavelength, α is the attenuation coefficient and R is the depth of the target. The scattering cross-section σ can most simply be described by

$$\sigma = \rho \sigma_1 V, \tag{2.6}$$

where ρ is the particle density in a volume V and σ_1 is the scattering cross-section from one particle. In principle, P_r can be used to estimate σ and hence place estimates on the density of scattering particles. In practice the radar power, attenuation and antenna coupling with the surface are unconstrained, requiring use of a borehole-derived water content profile as a calibration target (Hamran et al., 1996). An estimate of glacier-wide englacial water content can be made relative to this borehole location. The same process was used by Pettersson et al. (2004) to estimate water content at Storglaciären from a

dense common offset survey.

Backscatter-power approaches make the assumption of a constant attenuation factor α, which includes attenuation induced by scattering, and a constant particle size. The approach is most reliable at the CTS and the accuracy reduces deeper in the ice column, where uncertainties in attenuation increase, where scatterer radius may change, and where the depth of the CTS changes relative to the control point. Hence, backscatter based approaches are strongly dependent on the location of the borehole being representative of englacial water glacier-wide. The scattering cross-section σ_1 in equation 2.6 is a function of particle size, hence changes in size introduce a bias in volume estimation. They are additionally highly sensitive to the presence of out-of-plane scatterers, which may be surveyed multiple times in a closely spaced grid as in Pettersson et al. (2004), and contribute to a possible overestimate in water content.

Multi-offset radar approaches

The earliest uses of the multi-offset approach in glaciology were in the late 1960s and 1970s over Greenland and Antarctica, in efforts to quantify dielectric constant of ice in-situ. Prior to these studies, velocity used for depth estimation was inferred from ties to seismic data (Waite and Schmidt, 1962), boreholes (Glen and Paren, 1975; Robin, 1975), or laboratory studies (Johari and Charette, 1975). Robin et al. (1969) detail the acquisition challenges and early experiments near Thule base in north-west Greenland, where 7 source-receive offset pairs were utilised to estimate a velocity in ice of 0.166 m/ns. Numerous other early studies over McMurdo and Ross ice shelves (Jiracek and Bentley, 1971; Jezek et al., 1978) and in East Antarctica (Bogorodskiy et al., 1970) refined the technique for polar ice sheet studies, although until the late 1990s few were taken over temperate and polythermal glacier ice.

Macheret et al. (1993) calculated the englacial radar velocity on Fridtjovbreen and Hansbreen, Svalbard, by means of fitting lines to manual picks of the bot-

tom and near-surface reflectors on a $t^2 - x^2$ plot; considerations for bed and surface dip were made through coarse estimations from an along-glacier common offset dataset. Murray et al. (2000) applied semblance analysis to CMP data acquired over Falljökull, Iceland. Out-of-plane reflections were discounted in the semblance scan, based on the peak velocity being above that expected. Borehole-derived near-surface radar wave velocities agreed well with the CMP-derived results.

On glacier scales, the acquisition of a continuous multi-offset GPR dataset is highly challenging; the sole example in the literature was undertaken by Bradford et al. (2009) along a 3.5 km long profile on Bench Glacier, Alaska. Five passes along the profile with an array of 4 antennas (1 transmitter, 3 receivers) enabled the application of velocity analysis, dip-moveout processing and pre-stack depth migration to retrieve a continuous long profile of englacial radar velocity and hence an estimate of water content.

Common-offset diffraction approaches

Diffractions are a common feature in both seismic and common-offset IPR data, and their geometries present an opportunity to sample radar velocity from common-offset datasets. In general, we can consider there to be two approaches to diffraction imaging: those estimating a focusing velocity from the point at which the diffraction focuses in a constant-velocity migration, or by fitting to the hyperbolic shape in unmigrated data. Both can be approached manually or through semi- or fully-automated approaches. These will be referred to as focusing and geometric approaches in the following.

The general principle of focusing approaches is to apply a series of common-velocity migrations to a radargram to identify the point at which hyperbolas collapse fully. This principle was first applied to seismic data by Harlan et al. (1984) and De Vries and Berkhout (1984) by estimating the measure of focus for the full dataset. Negative entropy, a measure of focusing after Shannon

(1948), was used, which defines the focusing measure V as

$$V = \frac{1}{N} \sum_{i=1}^{N} a_i \log a_i, \tag{2.7}$$

calculated across the constant-velocity panel with data amplitude a_i. This approach included planar reflections which hamper the ability to accurately derive focusing velocity. Fomel et al. (2007) developed the approach further by firstly applying a plane-wave destruction filter (Fomel, 2002) to enhance diffractions, and using semblance (equation 2.2) to derive a local estimate of focusing, before deriving a continuous velocity field through picking on semblance panels.

Geometric approaches seek firstly to identify hyperbolas within the data, then estimate the focusing velocity from hyperbola geometry. Identifying hyperbolas may be by means of machine learning or pattern matching (Gamba and Lossani, 2000; Pasolli et al., 2009; Maas and Schmalzl, 2013; Mertens et al., 2016), which enables rapid identification of features for near-real-time velocity model building (Dou et al., 2017). These methods are fast to employ, yet struggle in regions of high signal noise and can have significant false alarm rates (Mertens et al., 2016).

The use of diffractions in velocity model building is more limited in glaciology. Moore et al. (1999) used a manual approach to geometric fitting to derive the velocity field and hence distribution of water content within Hansbreen, Svalbard, identifying areas of higher water content in the vicinity of surface crevassing and moulins. A similar approach was used by Navarro et al. (2005). The exact workflow used is not detailed in these studies though is likely to be through interactive fitting, whereby a synthetic hyperbola is matched with the shape of a hyperbola in data, (for example as used in ReflexW radar processing software, Sandmeier, 2020) as opposed to manual picking of diffraction focusing points. Bradford (2005) applies the latter by means of wavefield migration with data from temperate Bench Glacier, Alaska, selecting the peaks

of focusing manually from common image gathers across the radargram.

Water content mixing models

Multi-offset and diffraction focusing approaches derive a velocity model for the glacier. The transformation between velocity model and water content distribution usually assumes that the velocity can be regarded as representative of the bulk permittivity, consisting of ice with water and often air inclusions. The most commonly used approach is the Looyenga 2-phase model (Looyenga, 1965) where the fraction of water n_L is defined as

$$n_L = \frac{\left(\frac{c}{v}\right)^{2/3} - \epsilon_i^{1/3}}{\epsilon_w^{1/3} - \epsilon_i^{1/3}} \tag{2.8}$$

where ϵ_w and ϵ_i is the relative permittivity of water and ice, respectively. This approach makes no assumption of the shape of internal scatterers, and has been used by several studies (Macheret et al., 1993; Navarro et al., 2005; Murray et al., 2000; Benjumea et al., 2003), mainly as it was one of the first models available (Barrett et al., 2007).

Alternatively, the complex refractive index method (CRIM) uses a weighted summation for an arbitrary number of constituent materials in the generalised form

$$\frac{c}{v} = \sum_{i=1}^{k} n_k \sqrt{\epsilon_k} \tag{2.9}$$

which for a two-phase system reduces to a volumetric fraction n_{CRIM} of

$$n_{CRIM} = \frac{\left(\frac{c}{v}\right) - \sqrt{\epsilon_i}}{\sqrt{\epsilon_w} - \sqrt{\epsilon_i}} \tag{2.10}$$

The CRIM equation readily enables incorporation of a higher number of contributions, which was exploited by Bradford et al. (2009) to incorporate a contribution of air pockets as a function of depth. The two-phase CRIM method was used by Bradford (2005) and Brown et al. (2017). Comparisons by Barrett

et al. (2007) and Brown et al. (2017) note that the CRIM approach yields more conservative values for volumetric water content.

Multi-offset geometry errors

The multi-offset approach makes numerous assumptions regarding the nature of the internal reflecting horizons; these are often violated in the case of polythermal glaciers. CMP studies in glaciology commonly violate the main assumptions of the CMP technique, namely the short-spread assumption, the horizontal planar reflector assumption. Barrett et al. (2007) quantify the error budget as a result of these contributions for a general case GPR CMP survey, which is used to quantify the error on temperate ice by Murray et al. (2000). Bradford (2005) argue that CMP datasets over scattering produce a overestimate in derived velocity, as the location of englacial scatterers cannot be known to be directly below the centre of the CMP. The technique makes the assumption of flat-lying reflectors (Yilmaz, 2001), an assumption that is often violated in the case of glacial CMP survey due to the complex reflected wavefield originating from point scatterers located 3-dimensionally around the survey (Barrett et al., 2008). For point scatterers, this corresponds to the case where all scatterers are directly below the mid-point. Such an error can be quantified by equating the offset between CMP mid-point and point scatterer in the survey plane to a specular layer reflection with an effective dip ϕ (Yilmaz, 2001).

If we consider the simple case of a flat, specular reflector the geometry of the resultant moveout curve can be described by the typical moveout equation

$$t^2 = t_0^2 + \frac{x^2}{v_{stk}^2}. \tag{2.11}$$

In this case, v_{stk}, the velocity derived from semblance analysis can be considered equivalent to v_{RMS}. Introducing a dip of ϕ° to the reflector results in a

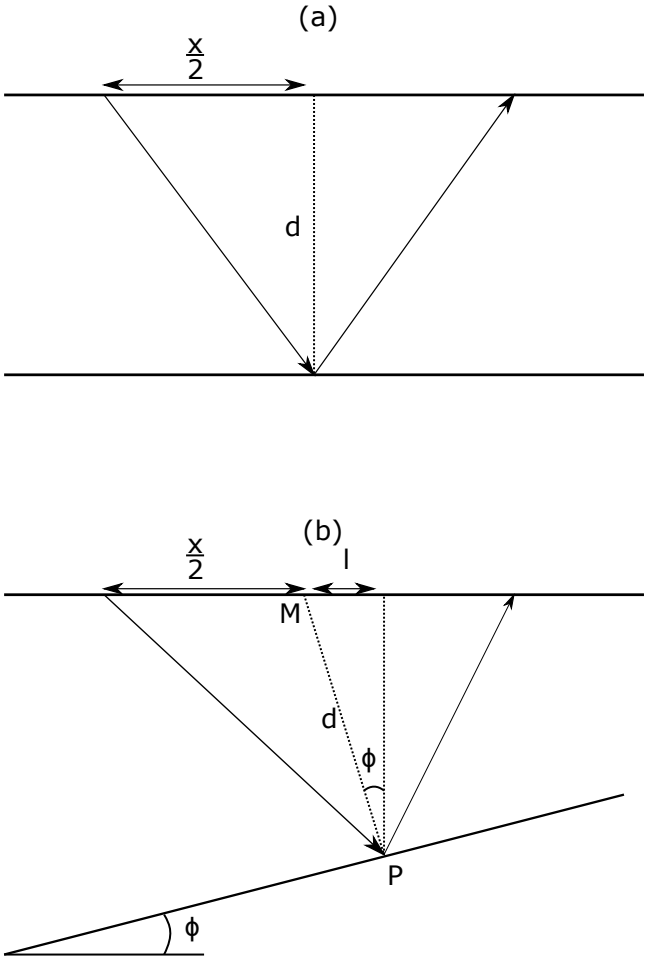

Figure 2.4: Geometry associated with CMP acquisition. (a) The simple case of a CMP acquisition geometry with flat reflectors. (b) The CMP geometry with a dipping reflector.

modified moveout equation, known as the dip-moveout equation (DMO),

$$t^2 = t_0^2 + \frac{x^2 \cos^2\phi}{v_{stk}^2}, \tag{2.12}$$

which, when used uncorrected to estimate velocity through NMO corrections, produces the stacking velocity

$$V_{NMO} = \frac{v_{stk}}{\cos\phi}. \tag{2.13}$$

In seismic exploration DMO correction can be applied to correct the stacking velocity for the effects of dip, hence reconstructing v_{RMS} to a reflector, yet this requires a continuous multi-fold survey, whereas in glaciology, sparse single CMP surveys are the norm.

If we consider the geometry of Fig. 2.4, for a scattering point P, at a depth of d and a distance l from the CMP mid-point M, the angle ϕ can be found by $\cos\phi = \frac{d}{h}$, where h is the shortest travel time between the M and P. As $h = \sqrt{d^2 + l^2}$, the error in velocity then becomes

$$V_{NMO} = \frac{Vh}{d} = \frac{V\sqrt{d^2 + l^2}}{d} \tag{2.14}$$

Hence, as $h > d$, the velocity structure of a glacier is systematically overestimated when a CMP dataset is not directly over each scattering point producing a moveout curve. Such an error may explain overestimates in interval velocity derived by Jania et al. (2005), which record an interval velocity < 0.170 m/ns on Hansbreen, with one internal layer at 91 m depth giving an apparent velocity of 0.183 m/ns. This is infeasible without a significant proportion of air by volume at depth. Murray et al. (2000) note that semblance peaks with a high velocity were discounted from velocity picking, yet this assumes incorrect velocities are distinguishable from correct velocities, which may not be the case if the offset (I in Fig. 2.4) is small.

Assessment of approaches and summary

Scattering approaches, such as the approaches of Hamran et al. (1996), give an instantaneous and highly-localised estimate of the density of scattering particles to estimate water content. Reflection and diffraction focusing approaches sample the overburden to a reflecting event to derive a bulk radar velocity, and a prediction of water content is then dependent on a material mixing model for estimation of internal water content. Backscatter approaches additionally require a borehole calibration point, and assume that the size and nature of the scattering particles are invariant, whereas reflection focusing approaches assume point scatterers of any size less than the radar wavelength, with assumptions on geometry required when inferring a water content from radar wave velocity. While widely used across polythermal glaciers, multi-offset approaches present several issues to obtaining glacier-wide estimations of ice properties, not least the logistical challenges of obtaining the data. Diffraction focusing approaches on the other hand present an opportunity for deriving the glacier-wide internal water content from a single pass of a common offset radar survey.

2.4 FDTD Modelling of GPR

All of the above discussion has focussed on 2D radar acquisition and analysis, appropriate to the vast majority of IPR data collection to date. Looking to the future, it is a clear aspiration to develop more advanced IPR systems and inversion techniques with a glaciological application, with many themes such as full-waveform inversion (FWI) shared with developments in the near-surface and cross-borehole GPR research field. This is the challenge that motivates the third research paper of this thesis, presented in Chapter 5, which explores the use of finite difference time domain (FDTD) modelling for glaciological and near-surface applications. This section provides some background on the topic.

FDTD modelling of GPR datasets represents an opportunity to numerically obtain the response of a controlled environment to a synthetic survey. In this section, I will first outline the algorithm used for FDTD modelling, discuss the uses and applications of FDTD modelling, before discussing the motivation for Chapter 5.

2.4.1 The Yee algorithm in 2D and 3D

FDTD modelling is generally undertaken using the Yee algorithm (Yee, 1966). The formal derivation of this approach is included in Appendix A and detailed further in Taflove and Hagness (2005). Fundamentally, the Yee algorithm is a discretisation of Maxwell's equations of electrodynamics, replacing the integrals in Faraday's and Ampere's laws with finite differences. At each step, the unknown *future* fields are calculated for every location grid representing the model domain. This is repeated for the required duration of the simulation. The amplitude of any field at any location in the domain can be output directly and analysed without any post-processing required. This algorithm can be followed in 3D, or, given the simplification and removal of z-components to the E and H fields, in 2D.

FDTD modelling is widely applied in the field of near-surface geophysics. Modelling of near-surface targets has been used by many studies as an aid to interpretation of the results of field surveys (Booth et al., 2008a). Imaging methods such as reverse time migration (RTM) require an FDTD model, built using data-derived velocity (Fisher et al., 1992b; Yilmaz, 2001; Leuschen and Plumb, 2001; Church et al., 2018). In recent years, FDTD modelling has become a vital step in the training of machine learning and neural network approaches to automated interpretation, requiring the generation of many independent models contributing to training datasets for, e.g., utility and landmine detection (Pasolli et al., 2009; Dou et al., 2017; Giannakis et al., 2019). It is widely use in full-waveform inversion, requiring multiple runs of an FDTD

model per iteration (Meles et al., 2010; Yang et al., 2013; Jazayeri et al., 2018; Klotzsche et al., 2019; Busch et al., 2012; Mozaffari et al., 2016).

In glaciology, several authors have used FDTD modelling to aid the interpretation of field data. Eisen et al. (2003) used a 2D FDTD model to match the dielectric profile-derived stratigraphy of an ice core in Dronning Maud Land to a coincident radar line, showing that the reflections seen in IPR data were principally a result of permittivity variations in the upper 100 m. Catania et al. (2008) compared the synthetic response of water-, air-, and ice-filled moulins to features observed in field data acquired in the ablation zone of Greenland to aid differentiating between the moulin fill levels. Langhammer et al. (2017) investigated the bed reflection amplitude as a function of antenna orientation to aid the design and processing of a dual-polarisation helicopter-mounted radar over a temperate alpine glacier in Switzerland. As the aim of the study was to investigate the effects of polarisation, a full 3D model with 160 cells cross-line was required, despite the geometry of the problem being 2D. In general, however, the application of FDTD modelling in glaciology has been hampered by computational demands due to the large model domains required. Such demand is a function of model size and resolution, required to avoid numerical dispersion (typically $dx < \frac{\lambda}{10}$, see Appendix A). Computational demand is lessened in small models of the near-surface approaches, where forward modelling has been routinely implemented in iterative inversion techniques, such as full-waveform inversion.

To reduce the computational requirements of FDTD modelling, models can often be undertaken in 2D by assuming invariance in the fields of the cross-line domain. 2D simulations are a computationally quick method of modelling the response of the model equivalent to using ideal z-polarized source stretching to infinity in the cross line orientation. However, real-world sources may not be solely polarized in this orientation and this does not allow simulation of cross-polarisation antenna orientations. This limits the use of FDTD modelling for survey design however, as several authors have noted the significance of an-

tenna orientation in both near-surface applications (Roberts and Daniels, 1996; Daniels et al., 2003) and glacial GPR surveys (Moran et al., 2000; Langhammer et al., 2017). Additionally, the 2D FDTD approach results in an incorrect scaling in amplitude and a phase-shift of $\pi/4$, which must be corrected in post-processing of synthetic data using a Bleistein filter (Bleistein, 1986), although residual amplitude errors are hard to compensate for in the case of heterogeneous velocity models commonly required for near-surface GPR modelling (Auer et al., 2013).

2.5 Summary

Sections 2.2.3 and 2.3.3 discussed the approaches used to investigate the internal thermal structure of polythermal glaciers, the need for a greater understanding of the lateral variation in ice properties, and the issues and challenges associated with using multi-offset CMP surveys to retrieve understanding polythermal glacier hydrology. Section 2.3 also discussed approaches to diffraction imaging, developed to estimate seismic velocity, yet these approaches have yet to be applied to a glacier setting to aid interpretation of glacier hydrological and thermal state.

Section 2.3.2 discussed the uses of internal stratigraphy of the Antarctic and Greenland ice sheets and approaches to interpretation. Interpretation of internal stratigraphy over large survey scales is limited by the labour-intensive nature of manual interpretation. Several studies using automated approaches to the interpretation of internal stratigraphy have been published, yet the validity of the resultant layer geometries for use in ice-sheet wide age-depth structure retrieval is unclear. There has yet to be a formalised assessment of the impacts of automated interpretation techniques available for IPR data over ice-sheets, which limits the ability of the community to assess and improve on approaches to automated and semi-automated interpretation.

Section 2.4 summarised the approach to and applications of FDTD mod-

elling. FDTD modelling is often undertaken in the computationally cheap 2D domain, where we assume that the dipole source is infinite in the cross-line direction. The computational demands of FDTD modelling are significant; reducing the requirements for generating 3D polarisation modelling may enable wider uptake for glaciological FDTD modelling to aid survey design, in addition to improving the performance of FWI and RTM algorithms in near-surface geophysics.

2.6 Research Aims

The above discussion has provided an overview of the state of knowledge across key areas of radioglaciology. I have subsequently highlighted some areas with potential for further development, which make up the main research aims of this thesis, and will form the basis of Chapters 3, 4, and 5, as follows:

1. To investigate and develop methods to enable tracking of englacial stratigraphy and structure across polar ice sheets.
2. To develop methods for quantifying the internal structure and refining the approach to bed topography retrieval in polythermal glaciers.
3. To improve approaches to generating full-polarisation and true-amplitude models from the FDTD technique to aid development in near-surface geophysics and radioglaciology.

Chapter 3

Reanalysis of polythermal glacier thermal structure using radar diffraction focussing

This chapter develops an approach to estimating the englacial radar-wave velocity of a polythermal glacier in Svalbard using common-offset radar data. Fieldwork for this chapter was supported by a Svalbard Integrated Arctic Earth Observing System (SIOS) pilot project, and equipment was loaned through the NERC Geophysical Equipment Facility (GEF).

Publication details This chapter is currently in preparation for submission as follows: Delf, R., Bingham, R.G., Curtis, A., Singh, S., Giannopoulos, A., Schwarz, B. and Borstad, C. (in preparation) Reanalysis of polythermal glacier thermal structure using radar diffaction focussing. *Journal of Geophysical Research - Earth Surface.*

Author contributions I led the study design, data acquisition, processing and wrote the manuscript, Robert Bingham helped with data acquisition and advised throughout, Andrew Curtis and Satyan Singh helped in developing the data processing flow, Benjamin Schwarz provided code for coherent diffraction

stacking, and Chris Borstad helped with fieldwork logistics. All co-authors contributed feedback and edits on the manuscript.

3.1 Abstract

Ground Penetrating Radar (GPR) is widely used on polythermal and temperate glaciers to image bed topography and to detect internal scatter as a result of temperate ice. The motivation for this is two-fold. Firstly, water held within micro- and macro-scale pores in ice significantly reduces ice viscosity and hence impacts the long-term evolution of polythermal glaciers. The presence of water has a direct influence on radar velocity; efforts to quantify the presence of water by radar velocity analysis usually requires multi-offset common mid-point or common source-point surveys, yet these are logistically challenging and expensive to acquire. Secondly, knowledge of the radar velocity field is additionally essential to retrieve correct bed topography from depth conversion processing. As a result of the difficulties in acquiring spatially-variant radar velocities, bed topography construction is often undertaken using an assumed or representative constant velocity, and because lateral variations in the velocity field are unaccounted for, errors in topography are likely.

We calculate the englacial radar velocity field from common offset GPR data collected on Von Postbreen, a polythermal glacier in Svalbard. We first separate and enhance the diffracted wavefield by systematically assessing data coherence. We then use the focusing metric of negative entropy to deduce a local migration velocity field from constant-velocity migration panels and produce a glacier-wide model of local (interval) radar velocity. We show that this velocity field is successful in differentiating between areas of cold and temperate ice and can detect lateral variations in radar velocity close to the glacier bed. The effects of this velocity field in both migration and depth-conversion of the bed reflection are shown to result in consistently lower ice depths across the glacier, indicating that diffraction focusing and velocity estimation are crucial

in retrieving correct bed topography in the presence of temperate ice.

3.2 Introduction

In this chapter, we apply common-offset velocity analysis to conventional glaciological ground penetrating radar (GPR) data acquired across an Arctic polythermal glacier. Our motivation is to improve constraints on the englacial temperate-cold ice distribution and to improve the accuracy of picked basal topography, which is often degraded beneath polythermal ice masses. The importance of this approach is two-fold. The englacial radar velocity field is strongly indicative of the presence of interstitial water within ice (Björnsson et al., 1996; Copland and Sharp, 2001; Benjumea et al., 2003; Murray et al., 2007; Bradford et al., 2009; Brown et al., 2017) and hence constraining glacier-wide variations in radar velocity leads to a more complete understanding of the water content and temperate ice distribution within the glacier. Additionally, the application of GPR processing strategies to retrieve correct bed depth and topography is dependent on an accurate radar velocity field, yet this is often overlooked or poorly understood in studies retrieving ice volume or bed topography of polythermal and temperate glaciers (Lapazaran et al., 2016).

Several approaches have previously been used to investigate the englacial radar velocity distribution of polythermal ice, including multi-offset (Murray et al., 2007; Bradford et al., 2009; Brown et al., 2017), common-offset approaches (Moore et al., 1999; Benjumea et al., 2003; Navarro et al., 2005; Bradford, 2005; Forte et al., 2014) and down-borehole surveys (Gusmeroli et al., 2010). Common-offset data have also enabled direct estimation of englacial water content through radar backscatter amplitudes, yet these do not resolve velocity structure (Bamber, 1987; Hamran et al., 1996; Pettersson et al., 2004). Multi-offset approaches to velocity analysis rely on logistically challenging acquisition geometries to achieve suitable velocity precision (Murray et al., 2007; Barrett et al., 2007) and consequently do not presently offer a viable solution for most

field acquisitions. To extract an englacial velocity field from common-offset data, however, has required users either to fit diffraction hyperbolae manually along the radar profiles (Moore et al., 1999; Benjumea et al., 2003; Navarro et al., 2005) or to retrieve the focusing velocity from migration velocity analysis (Bradford, 2005), which are significant resource- and time-consuming operations.

Here, we present a method for estimating a 2D englacial radar velocity field to provide an improved understanding of the temperate-ice distribution within a polythermal glacier using a series of 2D, common offset GPR datasets. The underpinning method of inverting from diffractions in common-offset data has been developed in seismic applications (Fomel et al., 2007; Schwarz and Gajewski, 2017; Preine et al., 2020), but has not previously been applied to radioglaciological data. We apply the workflow to field data collected on a polythermal glacier in Svalbard, and detect areas of low radar-wave velocity coincident with high signal scattering within the data, in accordance with previous studies on similar polythermal glaciers (Murray et al., 2007). These areas of low radar-wave velocity are interpreted as indicative of liquid water present interstitially within temperate ice, and the resultant inversion for water content distribution provides insights beyond the simple temperate-cold ice transition interpretation. We then use the resultant radar-wave velocity field to estimate the improvements in glacier bed topography, compared to the assumption of a constant, cold ice velocity. We demonstrate that to determine the bed topography, and hence glacier volume, accurately in the presence of temperate ice, understanding lateral variations of englacial radar velocity is essential.

3.3 Field Data and Acquisition

3.3.1 Physical Setting

Von Postbreen (78°25.07 N 17°43.27 E) is a polythermal glacier located in the Tempelfjorden region of Svalbard. It is approximately 15 km in length and has an area of 168 km^2 (König et al., 2014). The upper tributaries include Fimbulisen to the south, Potpeschniggbreen to the North-East and Phillippbreen to the north. The lower ablation area consists of two tongues, the southernmost of which is the widest at 2 km width on average and forms the focus of this study. The glacier is classed as surge-type and is currently in a long quiescent phase, typical of many Svalbard glaciers (Dowdeswell et al., 1991), having last surged in 1870 (De Geer, 1910). Crevasse-squeezed ridges are present in the modern-day forefield and are noted as a sign of historic surging (Farnsworth et al., 2016). The glacier was historically confluent with Tunabreen with a continuous calving front in Tempelfjorden, but has steadily retreated throughout the 20th century and is now entirely land-terminating (Sweeting and Groom, 1956; Flink et al., 2015). While Von Postbreen has been long quiescent, neighbouring Tunabreen has surged regularly and is well-studied (How et al., 2019), and the confluent minor glacier Bogebreen surged in 1980 (Dowdeswell et al., 1984b).

Geophysical surveys on Von Postbreen were first undertaken in 1980 using an airborne radio-echo sounding system using a central frequency of 60 MHz (Drewry et al., 1980), sounding both the bed and internal scatter within the ice as part of extensive surveys over the archipelago (Dowdeswell et al., 1984b). Bamber (1987) undertook a reflection coefficient-based analysis of the uppermost internal scattering horizon on similar glaciers across Svalbard from the same surveys and concluded that it represents a layer of temperate ice with a water content of approximately 3%. In 2012 and 2015, Sevestre et al. (2015) undertook an extensive GPR campaign at 100 MHz, successfully

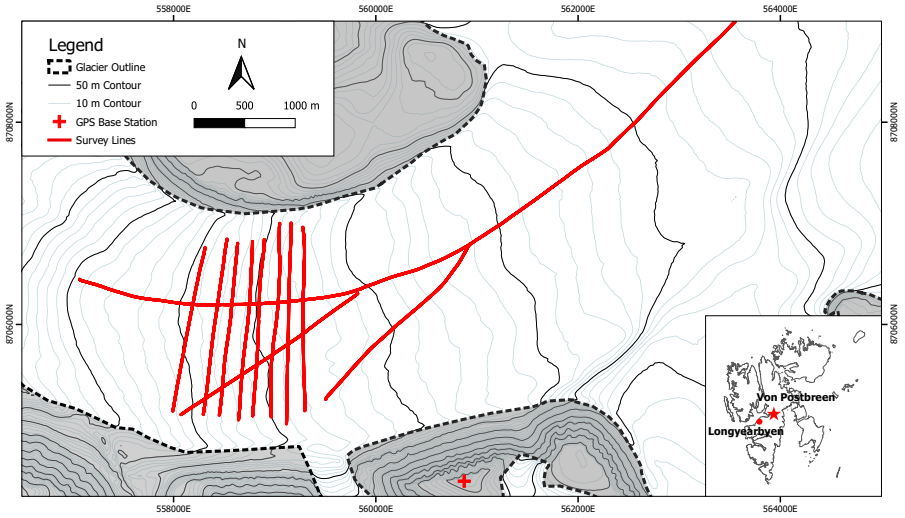

Figure 3.1: Map of GPR lines collected in 2018 on the lower region of Von Postbreen, with location within Svalbard (inset). Tempelfjorden is to the west of the glacier front. The GPS base station was situated to the south of the glacier on Przybyllokfjellet. Contours are derived from Norwegian Polar Institute S0 DEM.

mapping the distribution of temperate ice within the glacier, but encountering strong scattering throughout the deepest ice, precluding the ability to pick the bed confidently throughout.

3.3.2 Data Acquisition

Data were collected on the 13th and 15th March 2018, using a 25 MHz PulseEkko Pro GPR system mounted on plastic pulks towed behind a snowscooter. We acquired eight transverse profiles across the ablation zone, each 2km long and spaced by 200m, and a 13 km longitudinal profile extending to the upper accumulation zone (Figure 3.1). Antennas were mounted in a parallel endfire configuration in line with the direction of travel; antenna dipole centres were separated by an offset of approximately 5 metres, which in this study we refer to as a common-offset acquisition. A 4 ns sample interval was used with a trace length of 1125 samples. The snowscooter was driven at 10 - 15 km/h, giving

an average trace spacing in the raw data of 0.5 m. Traces were located with a differential GPS rover feeding real-time kinematic (RTK) corrections directly to the GPR system, the base station for which was located on Przybyllokfjellet to the south of the glacier at an elevation of 720 m above sea level. The base station location was corrected using the Canadian Spatial Reference System Precise Point Positioning (CSRS-PPP) service following a 30 minute static recording time on a previous day.

3.4 Methodology

Following an approach previously developed and applied by Fomel et al. (2007) to assess the velocity from a post-stack seismic dataset, we apply diffraction focusing to the radar profiles to generate time-domain englacial radar-wave velocity fields. We modify this approach to enhance the retrieval of diffractions at depth, and by applying a novel focusing measure of the local signal entropy as a function of focusing velocity. We then undertake parameter testing on shaping regularisation of the radar-wave-velocity field to assess the tradeoff between overfitting, with associated non-physical local velocities, and oversmoothing, whereby local anomalies are lost.

3.4.1 Pre-Processing

Data pre-processing was required before application of the velocity analysis algorithm. Traces were re-sorted to 1 m intervals using associated GPS locations. A static time shift was applied such that $t = 0$ ns at the first break of the direct arrival, followed by a 2 MHz high-pass (*dewow*) filter to remove low frequency or static, DC noise.

Due to the small offset between transmitter and receiver, imposed by logistical constraints, significant ringing was experienced through approximately the first 300 ns of each trace. To remove this noise, we used a modification

of the singular value decomposition (SVD) filter, developed by Freire and Ulrych (1988) for seismic data and applied to helicopter-borne radar data over Glacier de la Plaine Morte, Switzerland, by Grab et al. (2018). This approach decomposes the radargram $\mathbf{D}$ of m traces and n data points to

$$\mathbf{D} = \mathbf{U}\mathbf{S}\mathbf{V}^T = \sum_{i=1}^{m} \sigma_i \mathbf{u}_i \mathbf{v}_i^T \tag{3.1}$$

where $\mathbf{U}$ is a $m \times m$ orthogonal matrix consisting of the eigenvectors $\mathbf{u}_i$ of the covariance matrix of $\mathbf{D}\mathbf{D}^T$, (the *left* singular vectors), $\mathbf{S}$ is a diagonal matrix whose diagonal elements are the singular values σ_i of $\mathbf{D}$ in descending order, and $\mathbf{V}$ is a $n \times n$ matrix of the eigenvectors $\mathbf{v}_i$ of $\mathbf{D}^T\mathbf{D}$ (the *right* singular vectors). Equation 3.1 shows that $\mathbf{D}$ can be reconstructed by a σ_i-weighted summation of the orthogonal eigenimages $\mathbf{u}_i\mathbf{v}_i^T$. The ringing noise constitutes a highly-correlated signal between traces which can be described well by a low number of high-amplitude eigenvalues σ_i. Filtering is applied over $\mathbf{S}$, scaling high-amplitude values of σ_i and retaining low values of σ_i which constitute the uncorrelated internal reflections. To generate a modified vector $\hat{\mathbf{S}}$, and the filtered radargram is reconstructed by

$$\mathbf{D}_{\text{filt}} = \mathbf{U}\hat{\mathbf{S}}\mathbf{V}^T \tag{3.2}$$

This approach is successful in removing near-surface ringing, yet in the case of a flat or low-dip bed reflection, it can result in an additional attenuation of the bed reflection amplitude. We therefore modify this approach by applying a smooth amplitude taper to the data between $t = 0$ ns and a user-defined two way travel time (twtt), such that we generate two matrices $\mathbf{D} = \mathbf{D_{ns}} + \mathbf{D_{bed}}$, where $\mathbf{D_{ns}}$ captures the near-surface and upper scattering layer and $\mathbf{D_{bed}}$ represents the deeper radargram including the bed, with data partitioned in twtt by a tapered transition. SVD filtering (equations 3.1 and 3.2) is applied to $\mathbf{D_{ns}}$, and the output radargram is reconstructed by $\mathbf{D_{out}} = \mathbf{D_{ns_{filt}}} + \mathbf{D_{bed}}$.

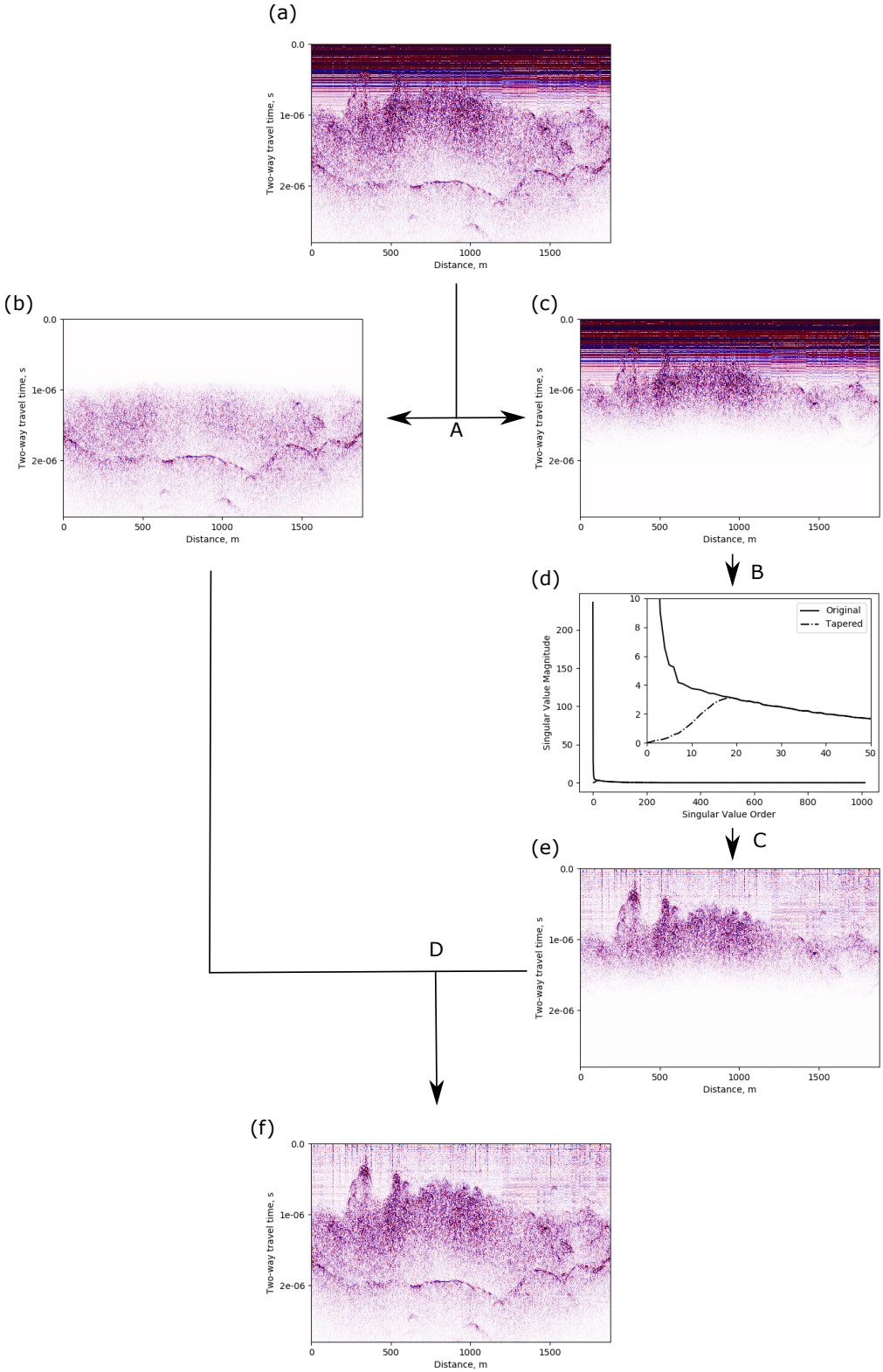

Figure 3.2: Caption on next page

Figure 3.2: Flow chart of the steps and output of SVD filtering. (a) Starting data $\mathbf{D}$. Step A represents splitting to (b) $\mathbf{D_{bed}}$, (c) $\mathbf{D_{ns}}$. Step B is application of SVD to generate (d) the singular values S, the low values of which are scaled using a taper over the first 20 values. Step C generates (e), the filtered near-surface data $\mathbf{D_{nsfilt}}$. (f) shows the final, filtered product $\mathbf{D_{out}} = \mathbf{D_{nsfilt}} + \mathbf{D_{bed}}$.

Parameter testing is required on the scale of the pre-filter data partition (separating $\mathbf{D_{ns}}$ and $\mathbf{D_{bed}}$) which we generally define as a 100-sample plateau with a 200-sample cosine taper, and the filter of eigenvalues, which we scale from zero using a cosine taper over the first 20 values. The steps of the SVD filtering algorithm applied to an example dataset are shown in Figure 3.2.

3.4.2 Retrieving the diffracted wavefield

Estimation of a full-ice-depth velocity field requires retrieval and focusing of diffractions close to the bed. The bed reflection is high-amplitude and specular in nature relative to diffractions within the ice. As such, there is little change with migration velocity perturbation, hence little variation in a time-velocity-domain common image gather (CIG). Suppression of the bed reflection is therefore essential to see the diffracted signals clearly, and thus enable retrieval of a full-depth average velocity and interval velocity of the deepest regions of ice.

We use a coherent summation and subtraction scheme (Schwarz, 2019) to extract diffraction-only data from the pre-processed radar lines. This is a three-step process: first, the coherence of arriving wavefronts is estimated as a directional stacking optimisation problem. For every data point (x_0, t_0), an estimation of the inclination of the most coherent arrival can be phrased as an optimization problem using the semblance norm (Neidell and Taner, 1971), in which the linear moveout Δt acts as the optimization parameter

$$\max_{\Delta t_k} \frac{1}{n} \frac{\sum_{\delta t} \left(\sum_{i=1}^{n} \mathbf{D}[x_0 + \Delta x, t_0 + \Delta t] \right)}{\sum_{\delta t} \left(\sum_{i=1}^{n} \mathbf{D}^2[x_0 + \Delta x, t_0 + \Delta t] \right)} \tag{3.3}$$

where δt is a time window over which summation is performed. To ensure reliable convergence even in the case of strong interference and noise contamination, the problem expressed in equation (3.3) is solved within a local aperture spanning n traces using a global differential evolution optimizer that is constrained to low wavenumbers (Storn and Price, 1997). Directional stacking on the original data is then applied using the resultant slope field, leaving strong, near-planar reflections which are subtracted from the raw data to leave high slope angle arrivals (Schwarz and Gajewski, 2017). Used alone, this step is sufficient to obtain an approximately diffraction-only dataset, although this still retains much of the high-frequency scatter which is found in the case of temperate ice, and hyperbolas are imperfect and noisy. In addition, the derived low-wavenumber wavefield may encode sufficiently accurate waveforms, but is likely to suffer from amplitude deviations and temporal offsets, which can compromise the subsequent step of noise attenuation.

To enhance the diffracted wavefield further and suppress high-frequency scatter, we follow Schwarz (2019) in applying a least-squares optimisation approach to subtract the previously obtained low-wavenumber estimate from the input data. The optimisation for the local amplitude scaling α_0 and a local time shift τ_0 minimises the misfit

$$\min_{\alpha_0,\tau_0} \left[\sum_{\delta t} \sum_{i} \mathbf{D}(x,t) - \alpha_0 \mathbf{D}_{low}(x_i, t_i + \tau_0) \right]^2 \tag{3.4}$$

where $\mathbf{D}_{low}$ is the coherent reflection model estimated in the previous step, $\mathbf{D}$ is the raw input data, and the index i, as in equation 3.3, refers to the i-th trace within a spatial aperture. To remove planar wavefronts and estimate the local slope, we used an aperture of 20 m, a coherence window of 20 ns and a maximum angle of incidence of 3°. Diffraction separation and coherent stacking were then performed with a wider aperture of 100 m, with a temporal adaptation window of 100 ns (δt in equation (4)). The result can be considered to be a diffraction-only dataset with contaminating noise and planar reflections

suppressed. We apply this approach to our data, and use this diffraction-only dataset going forward for velocity analysis.

3.4.3 Time Migration Velocity Analysis

We follow the approach of Fomel (2003) to estimated time-migration velocity field using local focusing velocities for each hyperbola in the dataset. An initial Stolt F-K migration is applied using a velocity of 0.1 m/ns, which is below the minimum expected value for radio-wave transit through glacier ice. We then apply velocity continuation using a velocity interval of 0.005 m/ns up to 0.2 m/ns to produce a 3D data volume $\mathbf{D}(t, x, v)$. To constrain the focusing function, we chose a velocity discretisation of 0.005 m/ns as a balance between velocity precision and computational demand; this follows the discretisation used in the manual migration velocity analysis approach of Bradford (2005).

We measure the level of local focusing through use of the statistical measure of negative entropy. First introduced by Shannon (1948) as a measure of information order in communications technology, the concept of negative entropy as a measure of signal focusing was extended and subsequently applied to diffraction imaging by De Vries and Berkhout (1984) by calculating the measure of focusing for a constant-velocity migrated dataset to estimate a constant migration velocity for the whole dataset. The concept can be extended to a 2D $v(x, z)$ problem through the use of moving windows. This can be achieved by firstly applying a Hilbert transform to generate amplitude data a_{ij} of amplitude a at pixel i, j, and calculating negative entropy focusing (S) by

$$S = \frac{1}{N} \sum_{i=1}^{N1} \sum_{j=1}^{N2} (a'_{ij}) log(a'_{ij}) \tag{3.5}$$

for each location throughout the data, where

$$a'_{ij} = \frac{a_{ij}}{\frac{\sum_{i,j} a_{ij}}{N}} \tag{3.6}$$

is the data amplitude normalised by the mean over an $N1 \times N2$ moving window, and $N = N_1 N_2$, the number of cells in the moving window. Each window is tapered with a Gaussian kernel such that only the central pixels of the window are equal to the input data. This approach using moving windows is highly computationally intensive, and we therefore calculate S using an alternate approach, by scaling all-positive amplitude data using a 2D automatic gain control (AGC) filter on which we calculate local negative entropy by

$$S = ag(x,t)\log(ag(x,t)) \tag{3.7}$$

where $g(x,t)$ is the AGC gain function (Yilmaz, 2001)

$$g(x,t) = \frac{1}{\sqrt{\frac{1}{N}\sum_{i=1}^{N} a_i^2}} \tag{3.8}$$

and a is the Hilbert-transform derived amplitude as previously. This results in one calculation to estimate $g(t)$ within a moving window, followed by a point-wise calculation of S (equation 3.7), and is significantly more computationally efficient. The result is a statistical measure of the degree of signal focussing for each location within the data; this metric is calculated for each constant migration panel.

Figure 3.3 compares the performance of negative entropy to the continuous and windowed negative entropy function, semblance, and kurtosis measures of focusing. The diffraction is modelled at a depth of 100 m within a homogenous medium of $v = 0.165$ m/ns, representing an anomaly within a cold ice background medium. The diffraction is focussed using a velocity range of 0.13-0.19 m/ns. We find that the negative entropy measure gives an improved metric of focusing, as semblance and kurtosis measures of focusing are susceptible to the presence of side-lobes as a result of multiple wavelet cycles present in the typical GPR dataset, as discussed by (Booth et al., 2010). This is beneficial in the application of automated picking algorithms, as in the subsequent step,

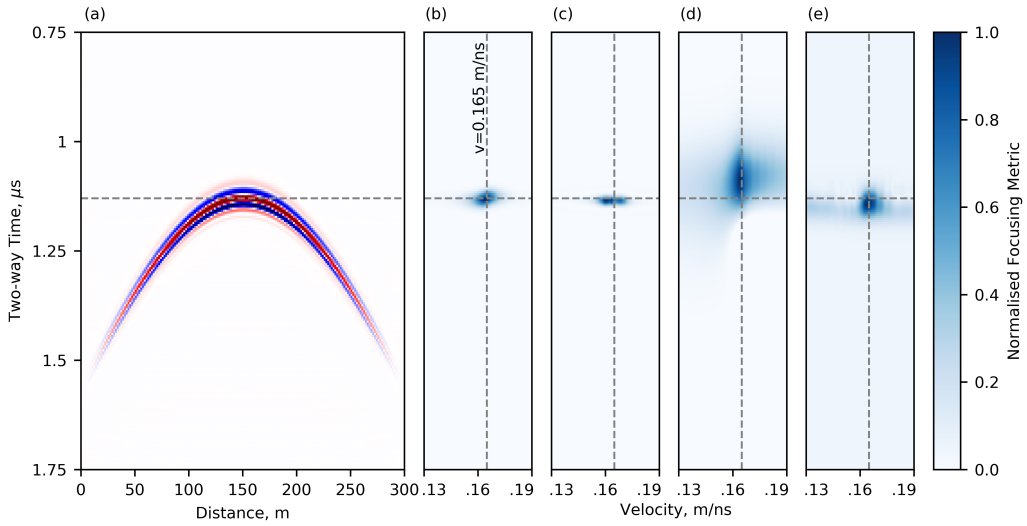

Figure 3.3: Comparison of focusing functions on a semblance-like time-velocity panel for a synthetic single diffraction (a). Panels are extracted for the centre point of the diffraction and normalised. (b) Negative entropy calculated as a continuous function. (c) Negative entropy calculated using moving windows. (d) Semblance and (e) Kurtosis, as used in Fomel (2003).

where the focussing metric is used as an objective function to maximise (Toldi, 1989), as it avoids the potential of local maxima which may lead to an incorrect velocity pick in the case of semblance or kurtosis (Figure 3.3 (c) and (d) respectively).

Automated velocity picking from focusing image gather panels is undertaken by maximising the function

$$P[v(t)] = \int_{t_{min}}^{t_{max}} S(t, v(t))dt, \tag{3.9}$$

(Toldi, 1989; Fomel, 2003). The picking algorithm is undertaken in a 2-step process. The first step maximises the function in equation 3.9 for each trace to give a coarse, strongly laterally-variant velocity field. The vertical gradient of the picking surface is dictated by defining the picking gate, a maximum variation in velocity between time samples. A second step undertakes smoothing through shaping regularisation in trace and time coordinates (Fomel et al., 2007), to limit the gradient. We then apply a time backshift $\Delta t = 5.6 \times 10^{-9} s$

to the data, to account for the time difference between the wavelet maximum and first break (Booth et al., 2010). The derived velocity field is considered to be an average between the surface and the scattering point, which we henceforth refer to as V_{RMS}. A smooth Dix inversion is then applied to V_{RMS} to derive the local velocity, which we refer to as interval velocity or V_{local}.

3.4.4 Migration and Depth Conversion

With the assumption of a constant velocity field, Stolt (Hambrey et al., 2005; Murray et al., 1997; Saintenoy et al., 2013; Navarro et al., 2014) or Kirchhoff migrations (Arcone et al., 1995; Schannwell et al., 2014; Sevestre et al., 2015) have been commonly applied to similar glacier GPR surveys on polythermal glaciers. In exploration seismic imaging, depth migration or reverse time migration (RTM) is undertaken when there are lateral variations in interval velocity due to the effect of energy refraction with depth (Yilmaz, 2001). Some studies have used RTM with airborne GPR data over temperate ice to reconstruct bed topography, where two constant velocity layers are required due to the elevated platform (Grab et al., 2018; Langhammer et al., 2019), yet this approach is not widely implemented due to the wavelength and model scales required. Assuming a migration aperture of 200 m, while we expect a degree of lateral variation in the velocity field, the magnitude and scale of velocity variations are minimal on the scale of the migration algorithm aperture as a result of the regularisation used in the velocity picking step. For this reason, we apply Kirchhoff time migration followed by a 1D, trace-by-trace depth conversion, both using the derived V_{RMS} model.

3.4.5 Water content inversion

Inversion for water content requires the assumption of a geophysical mixing model. Previous studies have used the Looyenga mixing model (Macheret et al., 1993; Murray et al., 2007), which makes the assumption of isotropic

and spherical inclusions in a two-phase mixture, or the Complex Refractive Index Model (CRIM) (Bradford et al., 2009; Brown et al., 2017)) which allows the inclusion of an arbitrary number of phase contributions by estimating a time-averaged slowness weighted using the relative volumetric contributions of each phase (Greaves et al., 1996). More advanced mixing models include the formulation of Giordano (2005), which considers the case where water is held within disc-shaped inclusions with a preferred orientation resulting in an anisotropy in velocity. This was used by Bradford et al. (2013) to quantify anisotropy on Bench Glacier, Alaska, yet our data collected on Von Postbreen show little evidence of significant anisotropy at survey line intersections, hence we use the CRIM equation.

We treat the glacier as a three-phase material whereby pore spaces are made up of water or air pockets, and as such the water content by volume can be estimated by

$$\phi_w = \frac{\frac{1}{v} - \frac{1}{v_i} - \phi_a\left(\frac{1}{v_a} - \frac{1}{v_i}\right)}{\frac{1}{v_w} - \frac{1}{v_i}} \tag{3.10}$$

where ϕ_w and ϕ_a are the proportion by volume of water and ice respectively, v is the estimated local velocity, and v_i, v_w and v_a are the velocity of propagation through ice, water and air.

The fraction of air in glacier ice, held within pockets and bubbles, decreases as a function of depth due to closure as a result of overburden pressure (Cuffey and Paterson, 2010), and must be estimated for equation 3.10 to remove a possible depth-dependent bias in water content. Using the assumption of zero deviatoric stress, Bradford et al. (2009) balance the gas pressure within bubbles with the hydrostatic pressure due to an ice overburden to show that the volumetric air fraction ϕ_a as a function of depth z, calculated at a depth discretised by Δz, is

$$\phi_{a(n+1)} = \frac{KT_0}{\left[g\rho\Delta z \sum_{k=1}^{n}(1 - \phi_{a(k)})\right] + P_0} - K\beta' \tag{3.11}$$

where g is acceleration due to gravity (9.81 ms^{-2}), ρ the density of ice (918 kg/m^3) and $K = \phi_0 R/M$, the volumetric contribution of air in ice at the surface scaled by R, the ideal gas constant and M, the molar volume of air at atmospheric pressure. $\beta' = 9.8 \times 10^{-8}$ K Pa^{-1} is a constant representing the rate of change of melting point with pressure, and P_0 is the atmospheric pressure at the surface. $\phi_{a(0)}$ is the air fraction at the surface, which is assumed to be 0.1.

3.4.6 Uncertainty analysis

Uncertainty in water content can be estimated with propagation of errors using partial derivatives (Bradford et al., 2009). We consider contributions from uncertainty in air fraction σ_a, uncertainty in Dix-inverted interval velocity σ_v, and uncertainty in cold ice velocity σ_{v_i}. σ_a and σ_v are estimated through partial differentiation of the CRIM equation (equation 3.10);

$$\sigma_v = \delta\phi_{w,v} = \frac{\frac{\delta v}{v^2}}{\frac{1}{v_i} - \frac{1}{v_w}} \tag{3.12}$$

$$\sigma_a = \delta\phi_{w,\phi_a} = \frac{\delta\phi_a\left(\frac{1}{v_a} - \frac{1}{v_i}\right)}{\frac{1}{v_i} - \frac{1}{v_w}} \tag{3.13}$$

and

$$\sigma_{v_i} = \delta\phi_{w,v_i} = \frac{\delta v_i(\phi - 1)}{v_w\left(\frac{v_i}{v_w} - 1\right)^2} \tag{3.14}$$

and the total error, assuming the error in v and error in ϕ_a are uncorrelated, is

$$\sigma_w = \sqrt{\sigma_v^2 + \sigma_a^2 + \sigma_{v_i}^2} \tag{3.15}$$

The contributions of uncertainties in radar velocity of water v_w and air v_a are negligible and can be ignored. The velocity of cold ice v_i is estimated using the derived velocity above the scattering region and below 50 m depth (where $\phi_a < 0.02$, and we assume the contributions of air bubbles to radar velocity is negligible) and δ_{v_i} is estimated from the distribution of the derived velocity.

Consistent with the uncertainty estimations of ϕ_a from Bradford et al. (2009), we hold the uncertainty in air fraction as $\delta_{\phi_a} = 0.5\phi_a$ which allows a significant variation in air fraction estimation given the simplified nature of ϕ_a estimation.

We estimate uncertainty in local velocity (σ_v) by firstly estimating the uncertainty in V_{RMS} as a result of picking on panels of negative entropy. We do so by assessing the width at half maximum of the negative entropy peaks derived from equation 3.7. The negative entropy response in Figure 2 (b) shows a width at half maximum of ± 0.07 m/ns, which we use as an uncertainty going forward. Note that, as this is an uncertainty in V_{RMS}, this can be used directly as an estimate of the uncertainty in bed topography correction. To estimate the uncertainty in interval velocity we must consider the implications of propagating this error in V_{RMS} through a smooth Dix inversion algorithm. To do so, we use a Monte Carlo approach to velocity analysis using an example trace, similar to Booth et al. (2011), but using a continuous function of V_{RMS}. We generate an ensemble of 100,000 traces with added random Gaussian noise with a standard deviation $\sigma = 0.75$ mns^{-1}, matching that of the V_{RMS} range estimated above, smoothed over a scale factor of 10 pixels. We then undertake Dix inversion on all 100,000 noisy V_{RMS} trajectories independently and calculate a 1D depth-dependent estimate of ensemble standard deviation. Due to the computational cost of this approach in 2D, we repeat this in 1D for a single trace and use the standard deviation in local velocity as representative for the wider dataset.

3.4.7 Manual validation of velocity field

We validate the results of velocity estimation by manually estimating the V_{RMS} for survey line 5, taken across the glacier. We use the approach of Booth and Pringle (2016) for calculating the semblance response of individual hyperbolas and picking the semblance response of the first peak of the wavelet. Uncertainties on velocity are estimated using the width of the semblance response at 50

% of the semblance peak. We pick semblance peaks for clear hyperbolas at or immediately above the ice/bed interface with no clear hyperbolas immediately above, which may indicate multiples from sub- or englacial channels (Stuart, 2003) and hence focus at a lower V_{RMS} than primary diffractions. We use the coherence-enhanced diffraction-only dataset, as data with only pre-processing applied do not contain sufficient diffraction hyperbolas to enable this approach.

3.5 Results

3.5.1 Diffraction Focusing

We apply the preprocessing, SVD filtering, and coherent wavefield separation and stacking to each line and present the results from a radargram taken across-glacier in Figure 3.4. Figures 3.4 (a) and (b) show the significant near-surface ringing in the pre-processed data, which was effectively removed by SVD filtering (Fig. 3.4 (c)) without lateral smearing or degradation of near-surface hyperbolas ('A' in Fig. 3.4 (b) and (d)). The SVD approach additionally handled changes in the noise characteristics along the survey line well (annotated 'B' in Fig. 3.4 (b) and (d)), and was successful in preserving the bed reflection throughout.

Coherent wavefield separation and stacking enhanced diffractions at the bed while removing planar bed returns, enabling estimation of V_{RMS} for the full ice depth throughout much of the survey area. Figures 3.4 (e) and (f) show the resultant diffracted wavefield. Coherent diffractions can be detected throughout much of the deeper regions of ice, and planar reflections have been removed. Some residual noise in the near-surface is additionally further suppressed in the diffraction-only dataset.

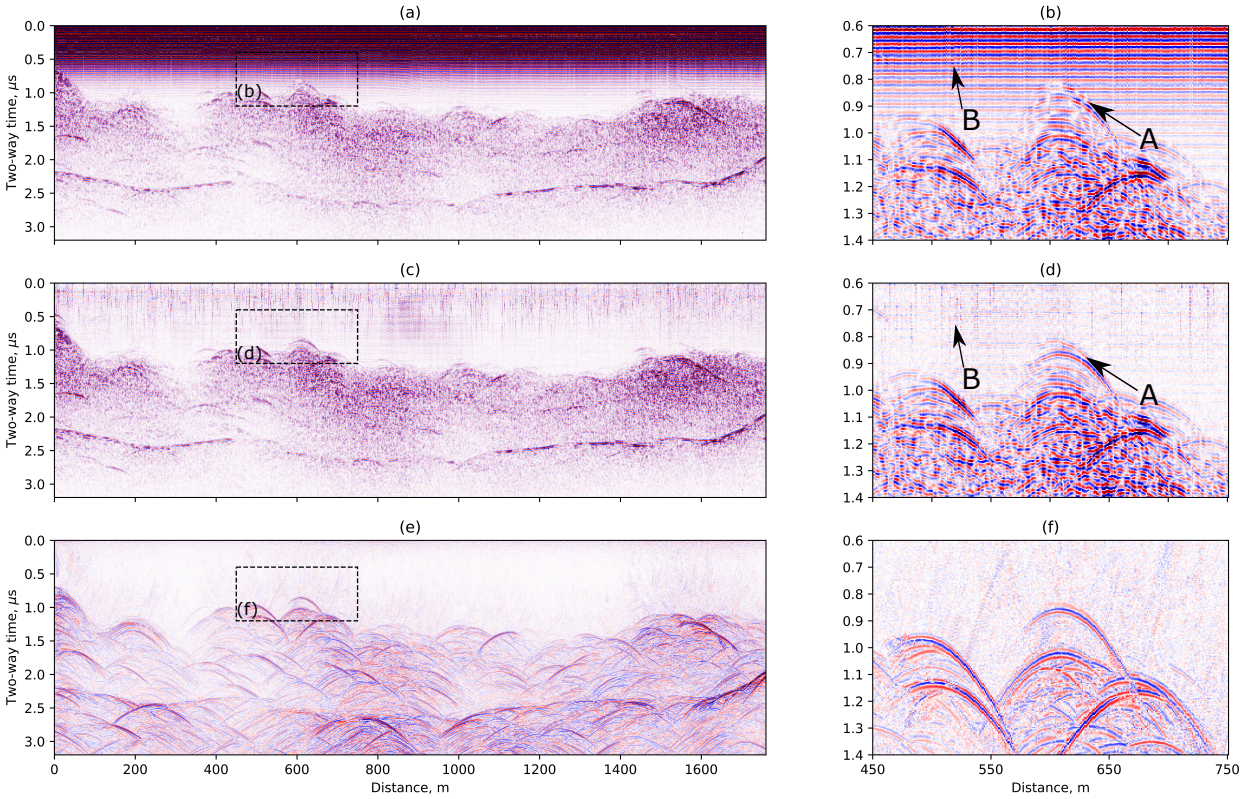

Figure 3.4: (a) Raw data from line 02 with only trace spacing corrections and *dewow* filter applied, showing significant ringing in the near surface (b) sub-set of data from the rectangle in (a). (c) and (d) show data following SVD pre-processing, with much of the near surface ringing suppressed (highlighted by B), while diffractions are retained (highlighted by A). (e) and (f) show data after the coherence-based extraction of diffractions (Schwarz, 2019). Planar reflections are removed and the diffracted wavefield is enhanced.

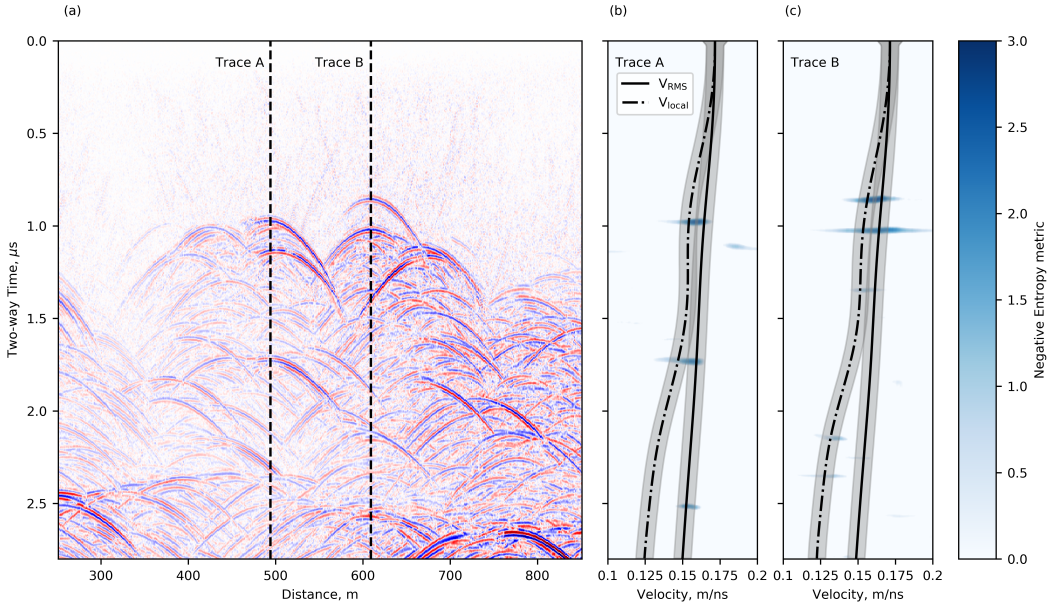

Figure 3.5: Application of the focusing function and automated picking algorithm to data after coherent diffraction retrieval. (a) Data from line 05. (b) Negative entropy metric estimated for the range of velocities 0.1 - 0.2 m/ns, for trace A in (a). (c) The same as (b) for Trace B. V_{RMS} and V_{local} extracted for each trace are overlaid in (b) and (c).

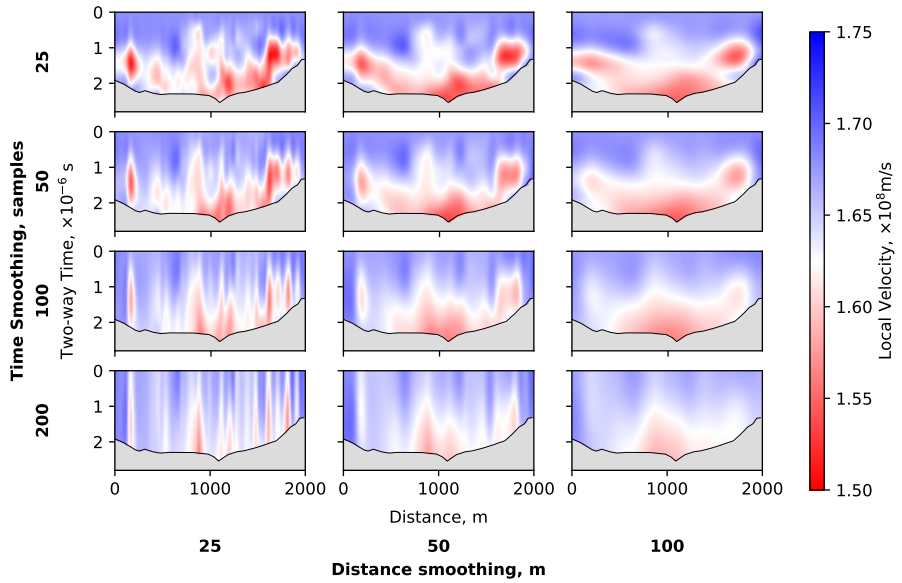

Figure 3.6: Testing picking regularisation parameters using an example cross-line dataset. A low distance smoothing results in physically infeasible velocity models. A low time smoothing parameter increases the chance of velocity spikes outside the expected range of 1.4-1.7 $\times 10^8$ m/s. Data are clipped before the bed reflection to avoid fitting to subglacial diffractions.

3.5.2 Velocity picking and validation

Figure 3.5 shows two example negative entropy panels from a segment of line 05 across the glacier, showing the correspondence of negative entropy peaks to prominent diffractions throughout the data. Note that due to smoothing across traces, the picked V_{RMS} profiles do not pass through all peaks in the panel but nevertheless provide a representative V_{RMS} across the regularisation aperture.

We undertake a sensitivity analysis on the picked and Dix-inverted velocity field to select regularisation scales by testing the results of a range of distance and two-way time smoothing windows, after Nicolson et al. (2014). Figure 3.6 shows the result of testing a range of regularisation windows for a single cross-line dataset. Small regularisation radii result in overfitting of Dix-inverted radar velocity (to the upper left of Figure 3.6). Cases with velocities below 0.1

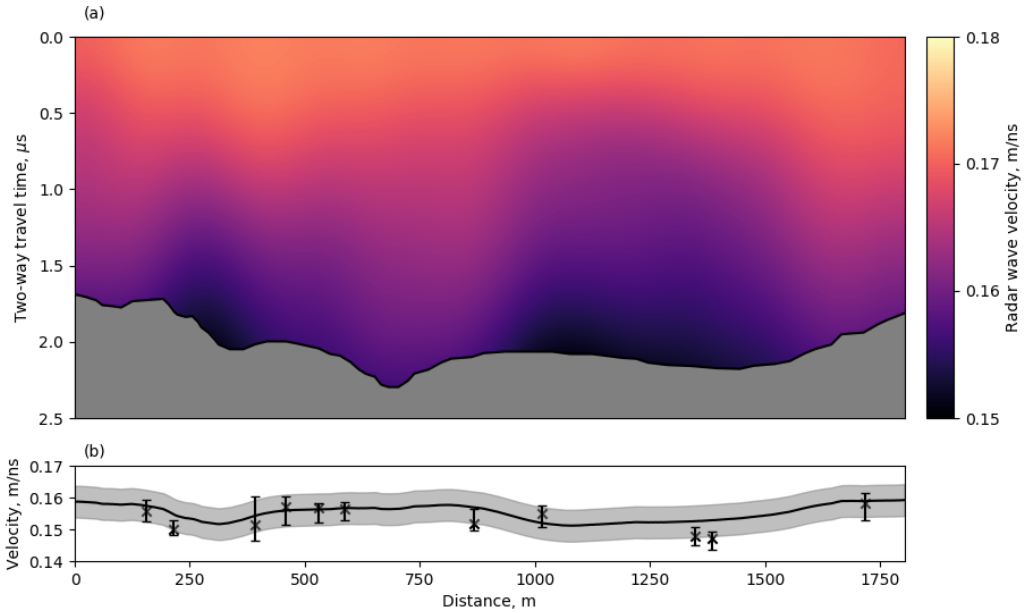

Figure 3.7: (a) V_{RMS} field for line 5 across the lower ablation zone of the glacier (b) V_{RMS} extracted from (a) along the bed, with uncertainty in V_{RMS} in grey. Crosses show manually-picked V_{RMS} along the bed, with uncertainties estimated from the width at half maximum of the semblance response.

and above 0.18m/ns are rejected as these correspond to physically infeasible velocities and are likely to be as a result of overfitting, and rapid transitions in average englacial water content are unlikely over short length scales. At large regularisation scales, the velocity of the upper ice column reduces indicating an oversmoothing of low velocities into the higher-velocity upper layer, and a loss of distinctive cold/temperate ice distribution. In general, we find that a large smoothing radius is required to minimise rapid local transitions in velocity, which resulted in extreme local velocities. We used a window size of 100 m laterally and 50 samples in time (0.2μs) across all lines for consistency.

We manually pick the location of the apex of 11 diffractions at or immediately (<100 ns twtt) above the bed throughout the data. Figure 3.7 shows the extracted V_{RMS} from the bed pick compared to the manually-derived velocities. The uncertainty in Figure 3.7 is the uncertainty in V_{RMS} as derived in section 3.4.6. The manually-derived picks do show some variations on short

length scales which are not fully resolved by the automated approach (such as at 200 m in 3.7(b)) but in general, the diffraction focussing-derived velocity field closely matches the manually-derived picks to within the estimated uncertainty.

3.5.3 The thermal structure of Von Postbreen

Figure 3.8 (a) presents an elevation-corrected radargram, produced assuming a constant englacial velocity field, along the full 13 km centreline profile through Von Postbreen. The profile excludes only the uppermost 900 m and lowermost 1.1 km of the glacier, where we could not gather data. Onto this, we have marked a manually-picked upper surface of the scattering zone, a surface that elsewhere has been taken as the interface between cold and warm ice (Bamber, 1987; Irvine-Fynn et al., 2011; Schannwell et al., 2014) and hence is hereafter termed the Cold/temperate-ice Transition Zone (CTZ). This shows that the glacier has a typical Svalbard- or Scandinavian-type thermal structure, whereby temperate ice makes up much of the ice column in the accumulation area and is advected down-glacier to the ablation zone, where a layer of cold ice mantles the surface across the ablation zone (Blatter and Hutter, 1991; Irvine-Fynn et al., 2011).

Data collected in the upper accumulation area depict scattering up to between 50 and 100 m below the surface across the upper 2 km of Von Postbreen. We are unable to determine if this extends to the surface as ringing in the near-surface has resulted in data clipping, hence SVD filtering in preprocessing would be unable to retrieve this near-surface scatter. Such scattering is expected in the near-surface however due to snow and firn layers in the accumulation zone and was present in surveys undertaken by Sevestre et al. (2015). The lower ablation region consists of a layer of cold ice of approximately 80 m thickness overlying temperate ice in the lower ablation zone (up to 2 km in Fig. 3.8). Our centreline does not capture the glacier front, which

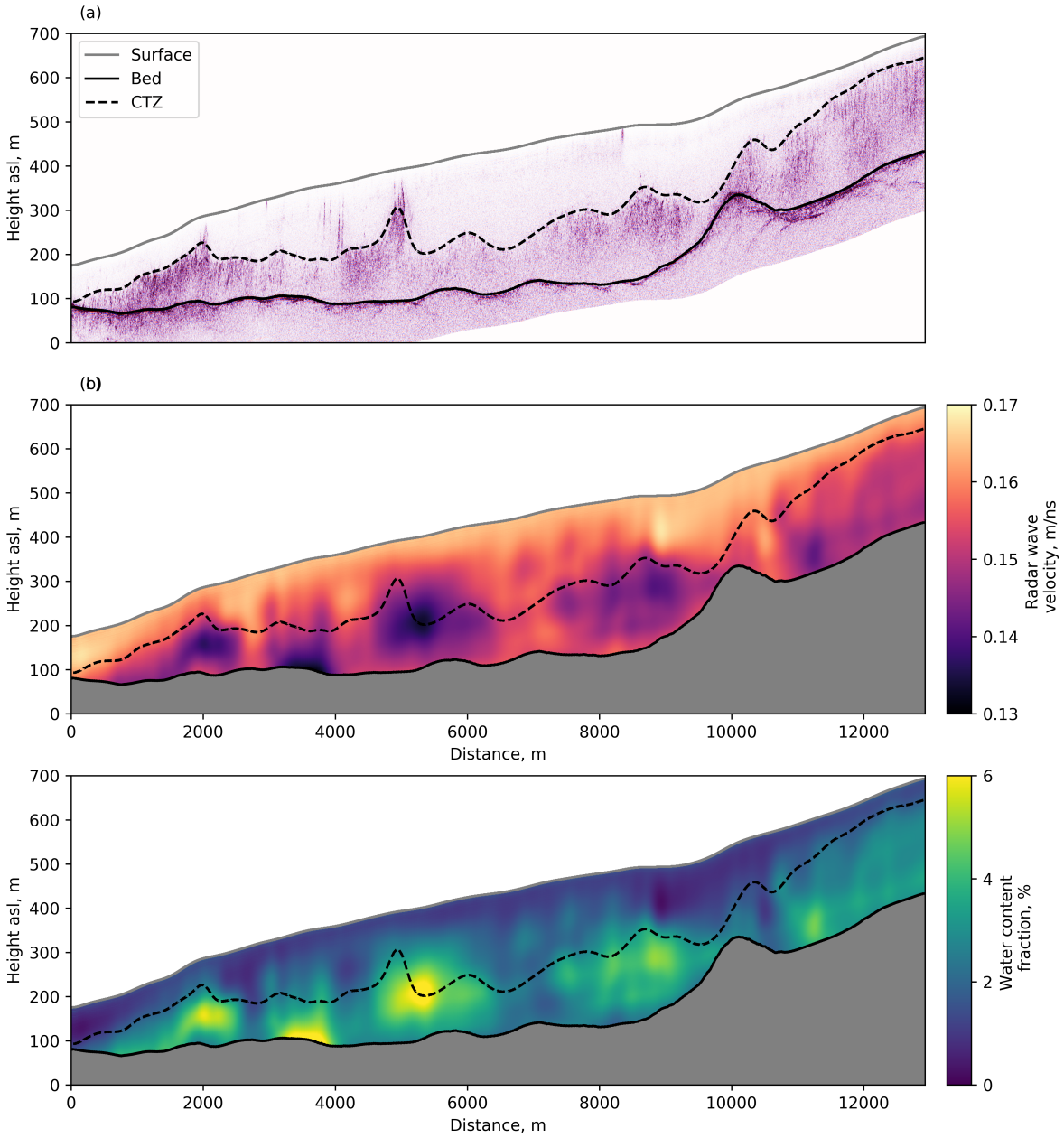

Figure 3.8: (a) Elevation-corrected centreline radar profile through Von Postbreen assuming constant englacial velocity of 0.165 m/ns. Dashed black line marks manually picked Cold/temperate-ice Transition Zone (CTZ). Data are presented after pre-processing and SVD filtering. (b) Englacial velocity field derived by diffraction focussing. (c) Englacial water-content derived from the velocity field in (b), using equations 3.10 and 3.11.

is approximately 1.1 km from the survey start point. Figure 3.8 (a) shows the CTZ to be coincident with the bed at the survey start point, and it is likely therefore that the glacier is cold-based for the lowermost 1 km.

There is significant topography in the CTZ along the glacier centreline, with high-amplitude scattering reaching close to the surface at 2 and 5 km in Fig. 3.8 (a). These are likely to correspond to crevasses or moulins whereby surface meltwater is able to access the englacial hydrological system during the summer melt, potentially enhancing local englacial melt. No clear surface features were apparent when undertaking the survey. Further topography is seen at approximately 10 km, where a small high in CTZ topography is seen up-glacier of a significant bed topography high.

The diffraction focussing-derived radar-wave interval velocity field (V_{local}) along the same profile (Figure 3.8(b)) resembles structurally the contrasts in scattering depicted by Figure 3.8(a). The upper ice column is characterised by higher velocities, generally 0.16 m/ns, while the lower ice column consists of lower velocities, generally ranging between $0.14 - 0.15$ m/ns. The distribution of velocities above and below the manually-derived CTZ is shown in Figure 3.9, reflecting the ability of the approach to differentiating the radar-wave velocities in the respective thermal regimes. Several regions of very low velocity (down to 0.13 m/ns) are found in the lower glacier (at approximately 3.8 and 5.4 km). The mean velocity below the scattering interface is 0.150 ± 0.004 m/ns, with the mean above being 0.159 ± 0.006 m/ns, although with a significant negative skew with a peak at 0.165 m/ns. This peak corresponds well with typical values for cold ice of 0.165 - 0.168 m/ns (Bradford et al., 2009; Navarro et al., 2014)

Figure 3.8 (c) shows the englacial water content distribution derived from Figure 3.8 (b). We estimate the uncertainty in englacial water content, following equation 3.15, to be $\pm 1.6\%$. Some regions of cold ice within the upper ice column have non-zero water content estimated, which may be a reflection of this uncertainty.

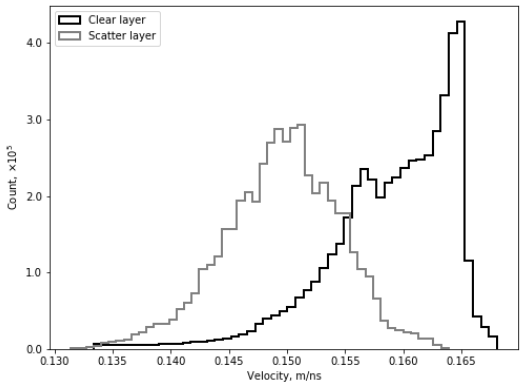

Figure 3.9: Histogram of derived local velocities for above and below the manually-interpreted CTZ across the full survey, labeled as the clear layer and scattering layer, respectively.

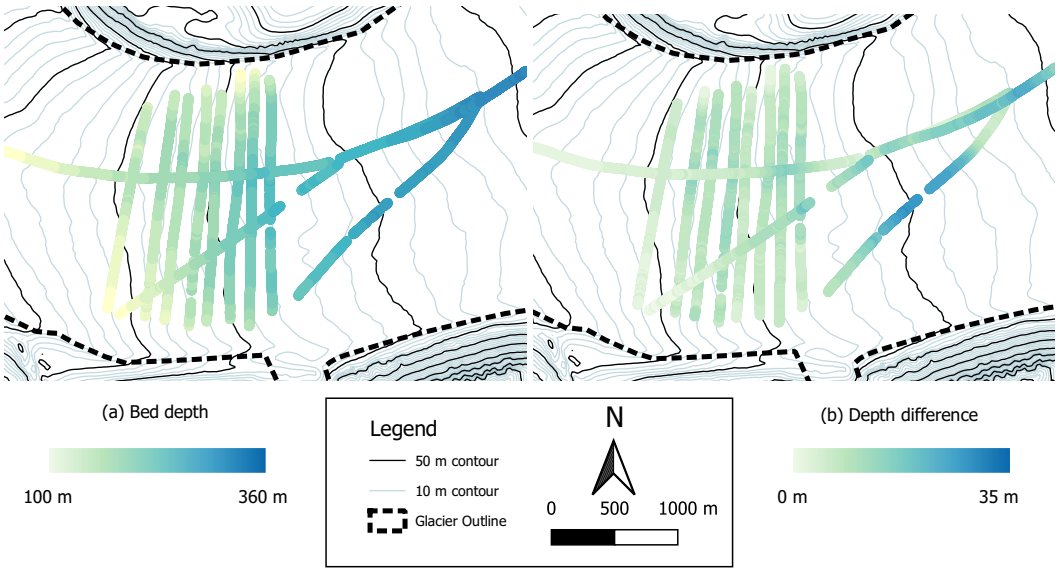

Figure 3.10: (a) bed depth estimated using the diffraction-focussing velocity field over the main survey area. (b) Difference between bed topography using depths estimated with a constant velocity $v = 0.165$ m/ns minus depths using diffraction-focussing-derived V_{RMS}.

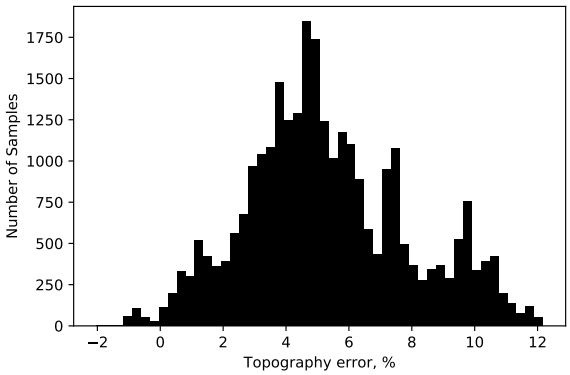

Figure 3.11: Histogram of percent error between constant velocity and picked velocity-derived bed topography.

3.5.4 Glacier bed topography reconstruction

We compare the results of undertaking bed topography estimation using an assumed englacial velocity of 0.166 mns^{-1}, as used by Navarro et al. (2014) to our newly derived radar velocity. Figure 3.10 (a) shows the glacier-wide retrieved bed depth using picked velocities. Figure 3.10 (b) shows the difference between the bed topography of Fig. 3.10 (a) and bed topography retrieved using the constant velocity approach. The histogram in 3.11 shows the distribution of differences between bed topography reconstructions across the glacier. We observe an average difference of $4.9 \pm 2.5\%$, equivalent to 12.0 ± 8.4 m between constant- and picked-velocity bed topography.

3.6 Discussion

3.6.1 The velocity structure of Von Postbreen

In Figure 3.8, we show the retrieved velocity structure with the interpretation of the upper scattering layer, which is representative of the interface between cold and temperate ice in a polythermal glacier. The velocity field below the scattering layer shows much variation along the length of the centreline profile. This is representative of lateral variations in water content through the glacier.

Of particular note are areas of very low velocity at or down-glacier of regions of enhanced scattering (approximately 2 and 5 km in Figure 3.8 (a)), where the upper scattering layer extends into the upper ice column. Given the low prevalence of crevassing across much of the glacier surface, this is likely to be a small moulin whereby water is accessing the glacier interior over the summer melt season and either (a) being held within the ice as part of a disconnected englacial drainage system or (b) enhancing local melt through the release of latent heat. Our data were collected in spring before significant seasonal melt began, hence this enhanced englacial scatter is likely to have been persistent through winter and represent seasonal storage of water. Similar undulations in the upper surface of the scattering zone have been observed in the presence of surface crevassing and moulins at Hansbreen, Svalbard (Moore et al., 1999), and seasonal changes in the vertical distribution of water content have been observed, whereby a decreased scattering intensity at the CTZ may be attributed to enhanced drainage through the summer melt season (Jania et al., 2005). A similar conceptual model of overwinter englacial water storage is proposed by Irvine-Fynn et al. (2006) using repeat GPR surveys over the polythermal Stagnation glacier, Canada, suggesting that the englacial piezometric surface is elevated in the early melt season due to an inefficient englacial drainage system. This may be consistent with observations of Hodson et al. (2005), who hypothesise that over-winter subglacial storage of water is necessary to complete the annual runoff and mass balance budget of Midre Lovenbreen, a smaller polythermal glacier with a low relative proportion of temperate ice by depth (Sevestre et al., 2015).

The presence of enhanced scattering through much of the middle ice column may indicate a low hydraulic connectivity with the deeper subglacial hydrological network. At several locations in Figure 3.8, the inferred water content close to the bed is lower than in the overlying mid-ice column (for example, at approximately 2, 6 and 8 km in Figure 3.8 (b) and (c)). Such a multi-layer structure has previously been observed using temperature pro-

file measurements (Jania et al., 1996) and from GPR CMP velocity analysis (Murray et al., 2000), both inferring a 4-layer structure with temperate ice of water content of $3-5\%$ overlying a low water content region close to the bed. Our results partly follow this structure, but not continuously throughout the glacier, breaking down in some regions of low scattering intensity (e.g. at 7 km in Figure 3.8 (b)). The wider variations in water content imply that the glacier thermal structure may not be well-represented by sparse CMP-derived estimates of 1D velocity profiles.

3.6.2 The nature of scattering bodies

Having elected to use the CRIM methodology of calculating englacial water content (Bradford et al., 2009; Brown et al., 2017), we assumed a 3-phase isotropic internal structure of englacial water content. The precise nature of englacial water is likely to be more complex than this. Some previous studies have assumed that water held within ice does so within intra-ice crystal veins, yet time-domain reflectometry of temperate glacier ice cores has shown that such veins only have a low capacity to store water, with an inferred upper bound of storage of $< 0.03\%$ at 2° (West et al., 2007). Much water has instead been hypothesised to be stored predominantly in hydraulically disconnected macroscale pores, or voids, such as those imaged in the upper temperate ice of Storglaciaren using borehole video (Fountain et al., 2005). There, the majority of water storage and flow was found to be through fractures in the lower regions of ice, generally in the form of subglacial crevasses, at a similar orientation to the surface strain-related features and at sub-vertical ($> 70^{\circ}$) angles. This is consistent with Bradford et al. (2013), who showed through azimuthal GPR CMP surveys that velocity anisotropy is possible close to the bed of the glacier as a result of such subglacial features. Velocity anisotropy can be described by the retrieval of two dielectric constants in the ordinary and extraordinary axes, $\epsilon_{\parallel}$ and $\epsilon_{\perp}$, respectively. This approach suggests an anisotropic mixing model

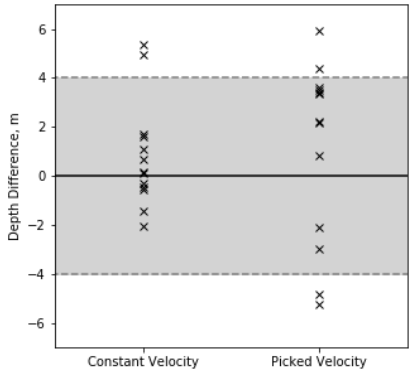

Figure 3.12: Scatter plot showing the difference between bed pick depth using a constant and picked velocity. This is calculated by $d_{\parallel} - d_{\perp}$, where $d_{\parallel}$ is the depth derived from surveys along flow and $d_{\perp}$ is derived from lines perpendicular to flow. Grey dashed lines show the average depth uncertainty, derived from the global average depth uncertainty.

should be used, for example as developed by Giordano (2005), which enables estimation of a $\epsilon_{\perp}$ and $\epsilon_{\parallel}$ for a distribution or arbitrarily oriented bodies of defined aspect ratio.

We can test for anisotropy by considering the differences in two-way travel time at survey line crossovers. Our survey grid gives a total of 16 crossover locations, with 8 at near-perpendicular and 8 at approximately 50° intersection angles. Figure 3.12 shows the results of crossover analysis on depth-converted data for all 16 locations using both constant and picked velocity fields. Our results show very little anisotropy at radar line crossover points. Average mis-tie between crossovers for data with constant velocity migration applied is 16 ± 32 ns, with all mis-ties below 61 ns, showing no systematic bias, suggesting a low anisotropy between orientations. This implies that water may be held in three possible configurations: a) within macroscopic, disconnected pores, as predicted by West et al. (2007), with isotropic behaviour, b) within a series of subglacial fractures with a near-random distribution relative to the survey line such that the bulk dielectric constant has no azimuthal variation, or c), within fractures intersecting the survey lines by $\approx 45°$ such that $\epsilon_{\parallel} \approx \epsilon_{\perp}$. Of

these, (a) would support the use of a spherical inclusion mixing model such as Looyenga or the CRIM model, and (b) and (c) would support treating the inclusions as fractures or disks as in Giordano (2005) with different distributions of orientations. Of these, (b) is unlikely as crevasses will generally be uniform in orientation (perpendicular to the direction of bulk ice deformation, Cuffey and Paterson (2010)), and (c) is unlikely given that anisotropy is not observed for profiles intersecting at both $\sim 90°$ and $\sim 50°$. Brown et al. (2017) interpret a similar result with TMz and TEz oriented common offset surveys in Greenland, and as such use isotropic mixing models. Air voids or pockets are unlikely to be a source of scattering within the deeper ice as they would be likely to close rapidly due to overburden pressure (Cuffey and Paterson, 2010), and scattering is unlikely to be debris-induced due to the lack of surface debris.

3.6.3 Radar-wave velocity and bed topography

Our derived velocity structure results in a consistently reduced bed depth compared to the assumption of a cold ice glacier with a velocity of 0.166 mns^{-1} (Figure 3.10). This is expected in the sense that other authors have shown bed depths can be overestimated when assuming constant englacial velocities in polythermal ice (e.g. Murray et al., 2000). For many such glaciers, a practical workaround based on CMP-derived velocities from warm ice, cold ice and firn has been to assume that high radio-wave velocities in the firn counteract the lower radio-wave velocities through the warm ice, such that a constant velocity can be applied in most instances (Jania et al., 2005; Navarro et al., 2014). While absolute glacier volume estimates are within a suitable error range using this approach, the relative error in bed depth along the glacier profile remains unconstrained, resulting in possible underestimates where firn/cold ice dominates and overestimates in regions of predominantly temperate ice (Lapazaran et al., 2016). The effect of such a systematic error is unclear when mass-conservation approaches to glacier volume estimation are used, such as

in retrieving archipelago-wide bed topography estimates in Svalbard by Fürst et al. (2018). Our data from Von Postbreen show a consistently lower velocity due to temperate ice through the full accumulation zone ice depth, similar to previous observations at this site (Sevestre et al., 2015), in addition to Kongsvegen (Björnsson et al., 1996) and Hansbreen (Jania et al., 2005). As such we cannot assume that the higher velocities expected within snow and firn will be sufficient to counter low velocities of temperate ice.

3.7 Conclusions

We have for the first time applied a coherent diffraction extraction and focusing technique to the study of water content within glaciers, and derived a continuous profile of englacial radar velocity from a common-offset GPR data. Previous attempts at retrieval of englacial water content have focused on the use of common mid-point or common source-point surveys, which are logistically challenging, hence only a sparse representation of spatially-variant glacier-wide water content distribution can be achieved. Common-offset data are far more readily available and can be acquired over a sufficient spatial scale to well-represent the glacier-wide distribution of water content.

We have shown that the spatial distribution of low radar-wave velocity regions and the corresponding volumetric contributions of englacial water content are more complex than can be typically described by interpretation of the cold-temperate transition zone alone. For example, regions of high englacial water content can be found in the vicinity of near-surface scatter, which may represent enhanced local melt or seasonal storage. This lateral variation in radar velocity, in turn, results in deviations of bed topography from that derived using a constant, representative radar velocity for the region.

Chapter 4

A comparison of automated approaches to extracting englacial-layer geometry from radar data across ice sheets

This chapter investigates automated approaches to internal layer geometry extraction from airborne RES data collected over Antarctica. The work was stimulated by the AntArchitecture project, an Edinburgh-led SCAR project to collate internal-layer geometries from surveys across Antarctica to generate a continent-wide age-depth model. This work was the result of a post-doctoral and early career researcher (PECRE) grant from the Scottish Alliance for Geoscience, Environment and Society (SAGES), which facilitated a research visit hosted by Dustin Schroeder at Stanford University in 2018. This work was presented at the *IGS Symposium on 50 years of Radioglaciology* at Stanford University in July 2019, and published in the associated *Annals of Glaciology* volume. The formatted *Annals* paper can be found in Appendix B.

Paper Details Delf, R., Schroeder, D., Curtis, A., Giannopoulos, A., and Bingham, R. (2020). A comparison of automated approaches to extracting

englacial-layer geometry from radar data across ice sheets. *Annals of Glaciology*, 61(81), 234-241. doi:10.1017/aog.2020.42.

Author Contributions I collated the datasets, processed the data and wrote the manuscript. Dustin Schroeder and Robert Bingham helped design the study and all co-authors contributed to editing the manuscript.

4.1 Abstract

Radar surveys across ice sheets typically measure numerous englacial layers that can be often be regarded as isochrones. Such layers are valuable for extrapolating age-depth relationships away from ice-core locations, reconstructing palaeoaccumulation variability, and investigating past ice-sheet dynamics. However, the use of englacial layers in Antarctica has been hampered by underdeveloped techniques for characterising layer continuity and geometry over large distances, with techniques developed independently and little opportunity for inter-comparison of results. In this paper, we present a methodology to assess the performance of automated layer-tracking and layer-dip-estimation algorithms through their ability to propagate a correct age-depth model. We use this to assess isochrone-tracking techniques applied to two test case datasets, selected from CreSIS MCoRDS data over Antarctica from a range of environments including low-dip, continuous layers and layers with terminations. We find that dip-estimation techniques are generally successful in tracking englacial dip but break down in the upper and lower regions of the ice sheet. The results of testing two previously published layer-tracking algorithms show that further development is required to attain a good constraint of age-depth relationship away from dated ice cores. We recommend that auto-tracking techniques focus on improved linking of picked stratigraphy across signal disruptions to enable accurate determination of the Antarctic-wide age-depth structure.

4.2 Introduction

Ice-sheet englacial stratigraphy is prevalent throughout radar-sounding data collected over Antarctica and Greenland (e.g. Bailey et al., 1964; MacGregor et al., 2015b; Schroeder et al., 2019). Due to the isochronous nature of most englacial layers (Siegert, 1999) such stratigraphy has been used to extrapolate age-depth relationships away from deep ice cores (Siegert et al., 2003; Siegert and Payne, 2004; MacGregor et al., 2015b; Cavitte et al., 2016) to calculate palaeoaccumulation rates and variability (Fahnestock et al., 2001; Koutnik et al., 2016; Hindmarsh et al., 2009; Karlsson et al., 2014; Cavitte et al., 2018) and to make inferences concerning historical and contemporary ice dynamics (Nereson et al., 2000; Rippin et al., 2003b; Siegert et al., 2003; Leysinger Vieli et al., 2007; Parrenin and Hindmarsh, 2007; Carter et al., 2009; Bingham et al., 2015; Holschuh et al., 2017).

To date, most studies exploiting ice-sheet englacial stratigraphy have employed manual tracing approaches, which can be prohibitively slow. After five decades of radioglaciology, and many thousands of radar profiles already in the archive and, in principle, available for ice-sheet modelling applications, it is imperative to develop automated and semi-automated approaches to trace englacial layers and/or characterise englacial-layer dip. This is far from straighforward, with surveys across Antarctica especially having been undertaken using a wide range of radar systems with different performance characteristics (Winter et al., 2017).

In this paper, we present a scheme for assessing the relative effectiveness of automated interpretation algorithms in a range of englacial stratigraphic settings. We apply each algorithm to a set of control radargrams from East Antarctica that cover the full range of englacial-layering geometries from continuous (typically associated with steady ice flow) to buckled/discontinuous (typically associated with fast or variable flow (Karlsson et al., 2012)). We focus on two sets of algorithms: those that focus on tracing layers or layer

continuity; and those that extract the slope, or dip, of englacial layers. The former are, in principle, of primary value for extracting age-depth information across ice sheets (e.g. MacGregor et al., 2015b), while the latter have been advocated as a more practical alternative input for ice-sheet modelling (Holschuh et al., 2017). Our principal objective is to present a set of performance metrics for the intercomparison of algorithms as applied to future datasets. We use our results to highlight the principal shortcomings of current implementations of layer autotracking algorithms, and make recommendations for future development of automated interpretation algorithms to facilitate continent-scale interpretation.

4.3 Data and Methodology

4.3.1 Reference data

We focus on two reference datasets from the CReSIS data archive (CReSIS, 2016). The datasets were chosen to present variable levels of challenge to automated picking algorithms. Example 1 was acquired across the Vostok region of East Antarctica on 27/11/2013 (frames 01_034-036, 77.0825° S 111.1064° E to 76.4341° S 116.3196° E), and represents a set of relatively low-dip, continuous englacial layers throughout much of the ice depth (Figure 4.1). Example 2 (Figure 4.2) was obtained over Antarctica's Gamburtsev Mountain Province on 25/12/2008 (frames 04_002-005, 83.7551° S 75.0735° E to 82.4212° S 75.9330° E), and includes numerous reflector terminations and conflicting dips throughout. We begin with data lodged in the archive from processing stage L1B, after pulse compression, coherent channel averaging and SAR focusing through f-k migration (CReSIS, 2016). We firstly applied a simple high-pass filter by convolving the data with a Gaussian kernel in time and subtracting this from the original data to remove the trend of decreasing amplitude with depth, as in Panton (2014), which balances the amplitudes of near-surface, high ampli-

tude reflections and deeper, low amplitude reflections. To generate reference englacial-layer picks, against which to test the further algorithms explored in this study, we imported the radargrams into Schlumberger Petrel, wherein we then traced layers using a combination of semi-automated local maxima peak tracking, guided tracking and fully manual tracking. For Example 1 we were able to pick 35 layers, mostly continuously traversing the 147 km radar profile; for example 2, we picked 41 layers across a 145 km radar profile as a greater number of reflector terminations are observed.

4.3.2 Automated isochrone picking

To our reference radar datasets we applied three algorithms designed to trace layers automatically, which, for simplicity, we will hereafter term the ARESELP, Steger, and Sobel-Feldman algorithms. The Automated Radio-Echo Sounding Englacial Layer-tracing Package (ARESELP) autotracker algorithm was developed by Xiong and others (2018) to autotrace englacial layers. It uses a continuous wavelet transform (CWT) peak detection algorithm with an assumed Ricker or Morlet wavelet, combined with local Hough transform, to estimate local dip and propagate picks away from peak CWT response (seed) points. Initial tests showed that optimum performance was attained using a Morlet wavelet for the CWT and a block size of 20 pixels, approximately 50 m (depth) x 1500 m (along track) (assuming $v_{ice} = 1.68 \times 10^8 \mathrm{ms}^{-1}$). We found that the Ricker wavelet applied by Xiong et al. (2018), while suppressing noise in regions of high amplitude stratigraphy, failed to generate picks in lower amplitude regions (for example, between 90 and 120 km in Fig. 4.1(a)).

The Steger algorithm is an image-processing technique that follows Ferro and Bruzzone (2013) in applying a pre-conditioning block-matching and 3D-filtering process (BM3D filter) (Dabov et al., 2007), followed by a Steger filter ridge detection algorithm (Steger, 1998) to enhance and detect englacial layering. In this image-processing context, the "ridges" being detected equate

to sets of amplitude peaks in adjacent traces, that represent englacial layers on radargrams. Ferro and Bruzzone (2013) applied this technique to extract layering in Mars' North Polar Ice Cap, but it has not previously been applied to terrestrial radar data. To our reference data we firstly applied the BM3D filter followed by a stretch to the range [0,255] and application of the Steger ridge detector, filtering to a minimum line length of 50 pixels with an upper and lower threshold of 0.5 and 1, respectively.

Finally, the Sobel-Feldman algorithm is an image-processing edge-detection tool that identifies peak gradients in image brightness (Sobel, 1990). We apply this to the reference data wherein the edges equate to englacial layers, then skeletonise the results to binary images of the detected lines, filtered to remove lines below a minimum size of 50 pixels. This approach is the most simplistic but has the lowest computational cost.

4.3.3 Age-depth relationship propagation

One means of assessing layer-tracking performance is to test the effect each imposes on the propagation of an age-depth relationship through the ice sheet. To gauge this, we deployed a technique similar to MacGregor et al. (2015b), but using a synthetic age-depth profile. We generated a synthetic age-depth relationship using a 1-dimensional Nye model of reflector depth (Nye, 1963), as implemented in Leysinger Vieli et al. (2011) by

$$A = \frac{H}{a} \ln \left(\frac{z - b}{H} \right), \tag{4.1}$$

where A is the age (years), H, z and b are ice thickness, elevation in the ice column, and bed elevation respectively (all in m), and a is the mean accumulation rate (m a^{-1}). We use a representative average accumulation rate of 0.05 m a^{-1}, typical of East Antarctica (e.g. Leysinger Vieli et al., 2004), although only the relative amplitudes of errors reported here are of interest and the findings are independent of this rate. This approach makes the assumption of steady-state

flow with zero horizontal advection and that all motion is due to basal sliding. We intersect picked isochrones (henceforth referred to as picks) at location A (Fig. 4.1(a)) with this age-depth relationship, which can be considered to be similar to a synthetically generated ice core with a known age-depth profile, and assign an age to each pick. We then propagate this age-depth relationship away from A. For each trace, we generate a 1-dimensional age-depth relationship from previously dated picks using a spline interpolation, then assign an age to each un-dated pick with the generated profile. All dated picks are then used to generate the age-depth relationship for the subsequent trace. We then extract the interpolated age-depth profile at a second location A' (Fig. 4.1 (a)).

A principal benefit of manual interpretation is the ability to match layers through regions of discontinuous reflectors by recognising patterns or packages of reflections (see, for example Karlsson et al., 2014). For each picked isochrone we calculate the degree of connectivity between that pick and the starting age-depth profile at A (Fig. 4.1 (a)). Uninterrupted picks intersecting A are assigned a score of 0 as they present the lowest age uncertainty, assuming the pick is correctly aligned with an isochrone. For each interpolation required to assign a date to a new pick, the connectivity increases by one. The newly dated pick is assigned this score of connectivity, and used for subsequent pick dating. This approach to assessing uncertainty highlights when the interpretation consists of a high number of disconnected isochrones, potentially indicating a high sensitivity to low amplitude signal anomalies.

4.3.4 Englacial dip estimations

To extract dip fields through the reference data, we applied three approaches, which we will hereafter term Panton, ARESP and PWD. The Panton algorithm is described as Step 2 in Panton (2014). We convolve the radar data with a variably-slanted Gaussian kernel to derive the maximum stacking amplitude

as a function of dip. The dip field is then filtered to remove noise caused by regions of low signal amplitude, characterised by bands of dip noise between layers, by using an amplitude-weighed spline filter of dip. In Panton (2014) this procedure was presented mainly as pre-processing for englacial-layer tracing, but for this paper we treat it as one of the direct methods that can be used to extract englacial-layer dip fields across wide swathes of ice sheets.

The Automated Radio Echo Sounding Processing (ARESP) algorithm (Sime et al., 2011) firstly applies horizontal stacking to reduce SNR, followed by a binarisation of layers and estimation of local dip of high amplitude signals using a moving window approach.

The plane wave destruction (PWD) algorithm follows Fomel (2002) in minimising the convolution of a predicted texture with the data to derive local slope. While the Panton and ARESP algorithms have previously been applied widely to radar surveys in Greenland (Sime et al., 2014; Panton and Karlsson, 2015), the PWD method, used routinely in seismic-data processing, is yet to be applied in radioglaciology.

To assess the performance of each algorithm in deriving englacial-layer dip, we use the synthetic age-depth profiles derived previously and consider that the dip of an isochronous reflector will be perpendicular to the angle of maximum gradient. The dip field relative to the surface can therefore be calculated as:

$$\theta = \tan^{-1} \frac{g_y}{g_x} - 90 \tag{4.2}$$

where $g_x = \frac{dA}{dx}$ and $g_y = \frac{dA}{dy}$ and $A(x, y)$ is the inferred age-depth structure as a function of trace x and depth y. We then propagated a streamline through the data, which represents an integral across the dip field, starting from the location of the synthetic ice core described previously. This highlights the variation in algorithm performance as a function of depth through the radargram.

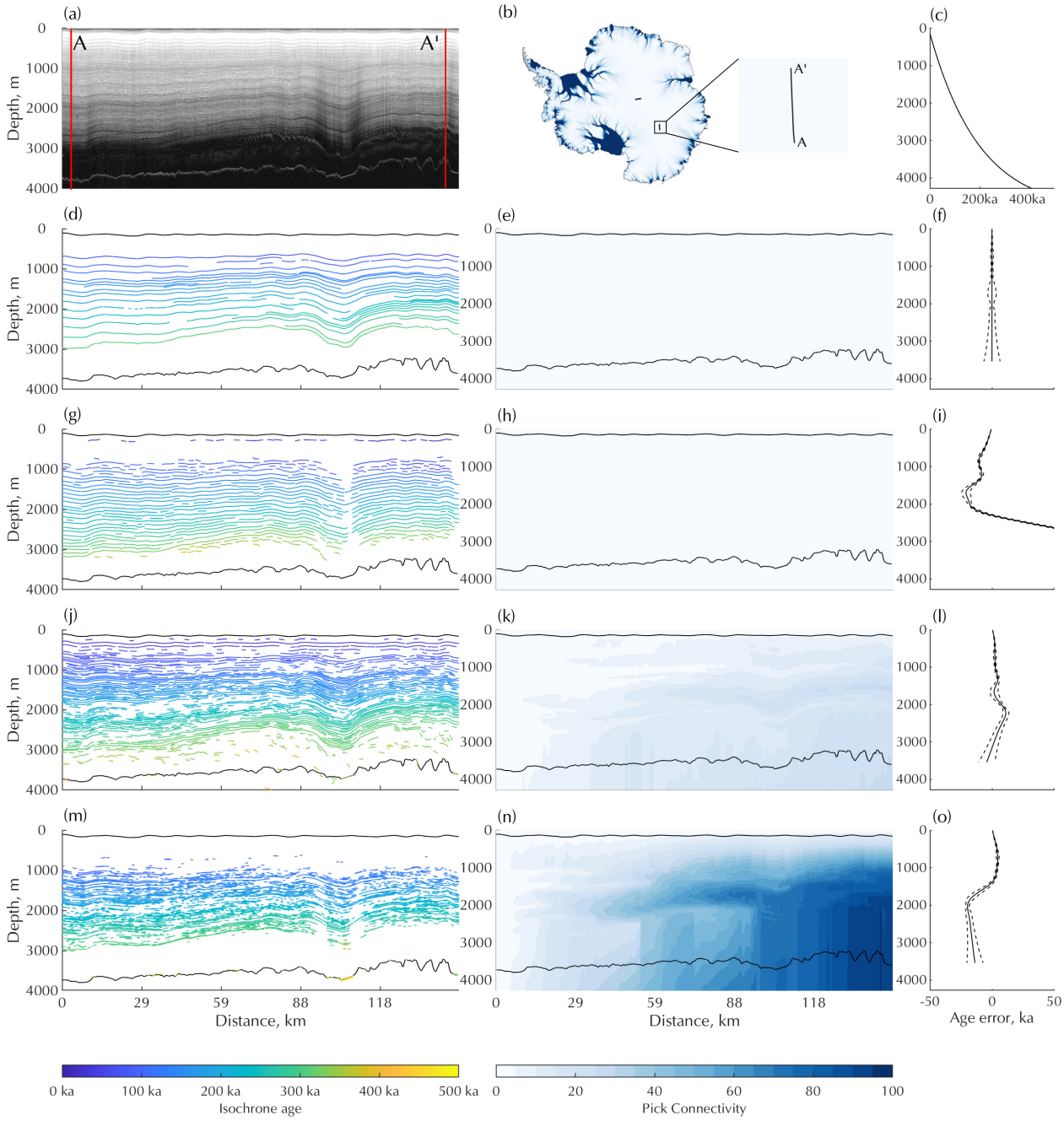

Figure 4.1: Comparison of age propagation through auto-tracked isochrones. (a) The raw radar data showing coherent, low-dip layers. (b) Location within Antarctica. (c) Synthetic age-depth relationship applied at location A. (d) Manually-picked reference dataset with (e) isochrone connectivity metric and (f) profile of misfit between reference picks age-depth relationship with uncertainties propagated through the picks. (g) Englacial picks, (h) isochrone-connectivity metric and (i) misfit profile for ARESELP algorithm. (j) Englacial picks, (k) isochrone-connectivity metric and (l) misfit profile for Steger algorithm. (m) Englacial picks, (n) isochrone-connectivity metric and (o) misfit profile for Sobel-Feldman algorithm.

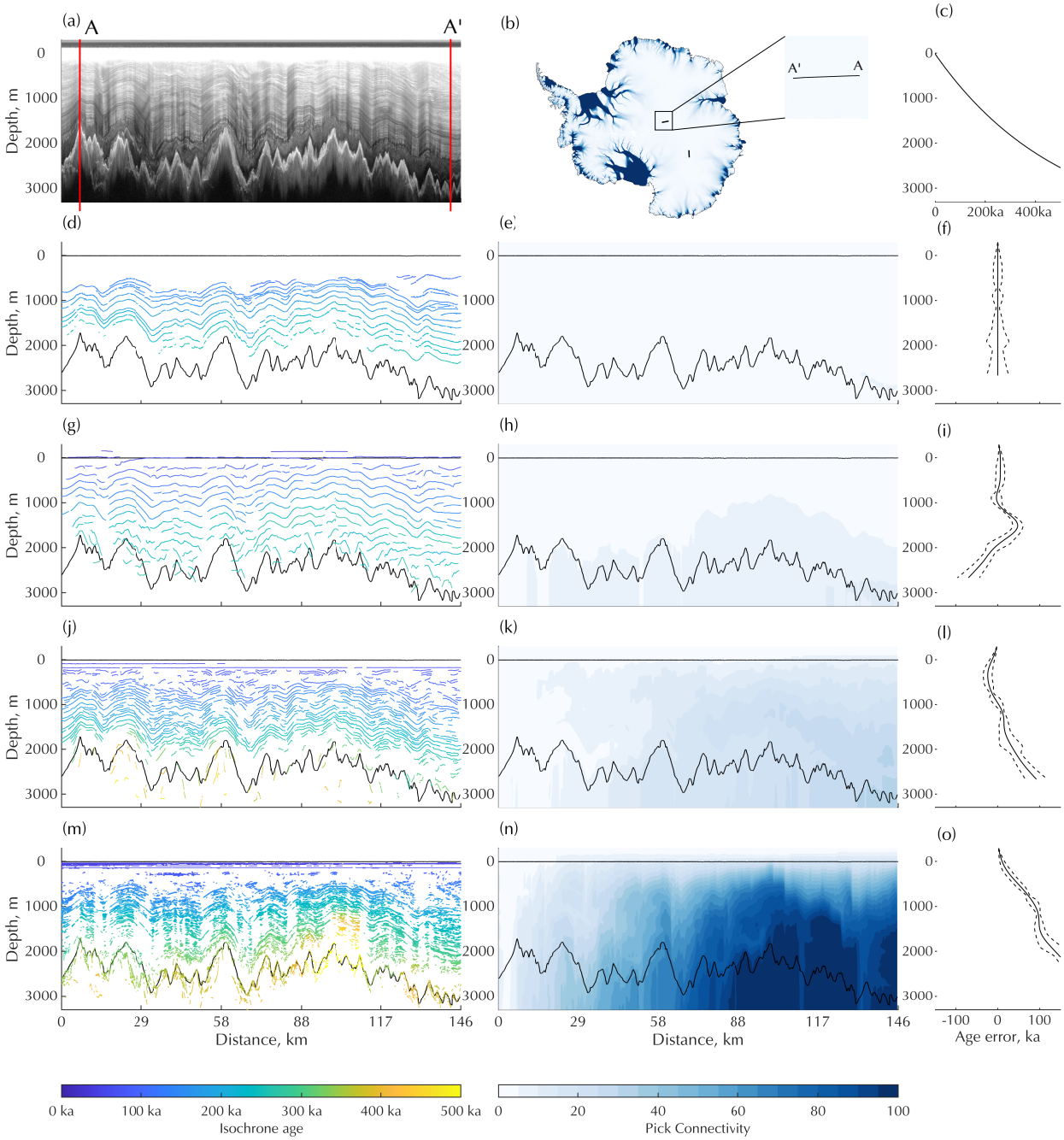

Figure 4.2: Application of auto-tracking algorithms to the second of the example datasets, similar to Fig. 4.1 in the main text. (a) Profile from A to A', with (b) location in Antarctica and (c) starting age-depth profile at A. (d) Manually-picked reference dataset with (e) isochrone connectivity metric and (f) profile of misfit between reference picks age-depth relationship with uncertainties propagated through the picks. (g) Englacial picks, (h) isochrone-connectivity metric and (i) misfit profile for ARESELP algorithm. (j) Englacial picks, (k) isochrone-connectivity metric and (l) misfit profile for Steger algorithm. (m) Englacial picks, (n) isochrone-connectivity metric and (o) misfit profile for Sobel-Feldman algorithm.

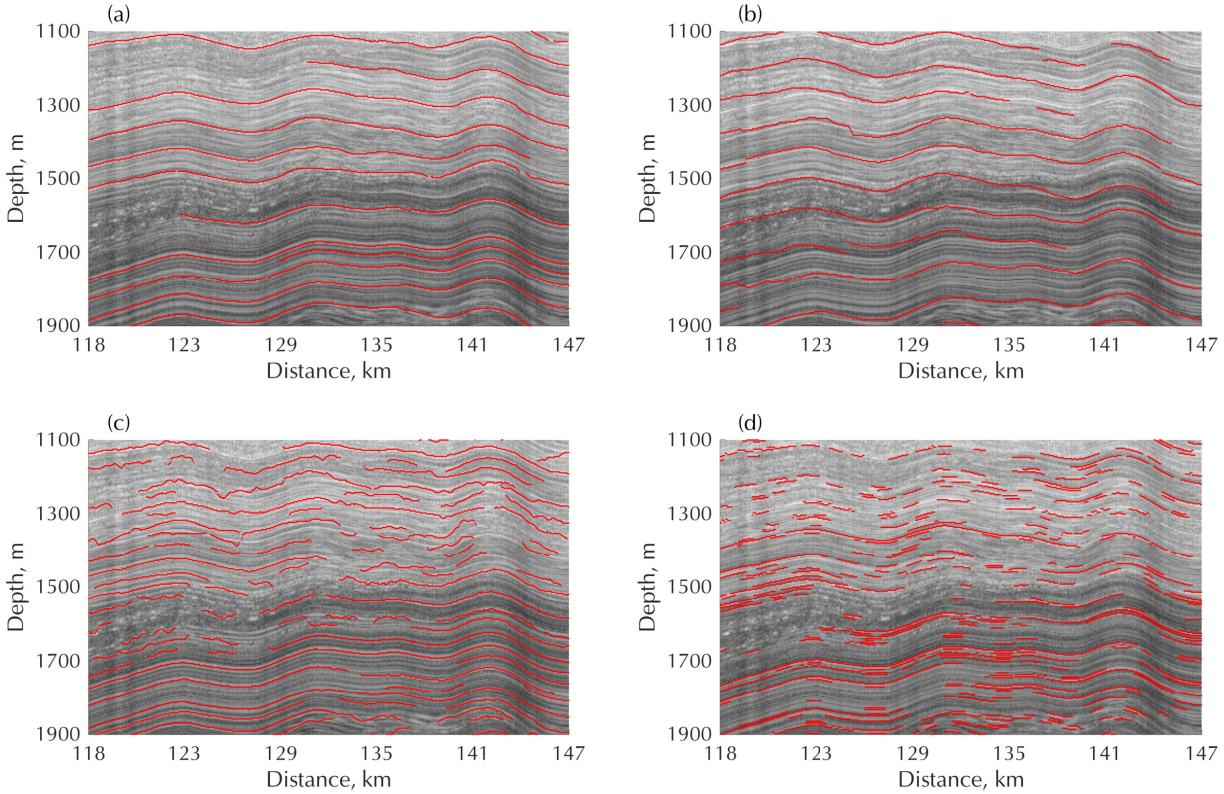

Figure 4.3: Detail of each isochrone tracking methodology applied to data from Fig. 4.1 showing different failure points for each algorithm (a) Manually-picked reference dataset (b) ARESELP (c) Steger filter and (d) Sobel edge detection.

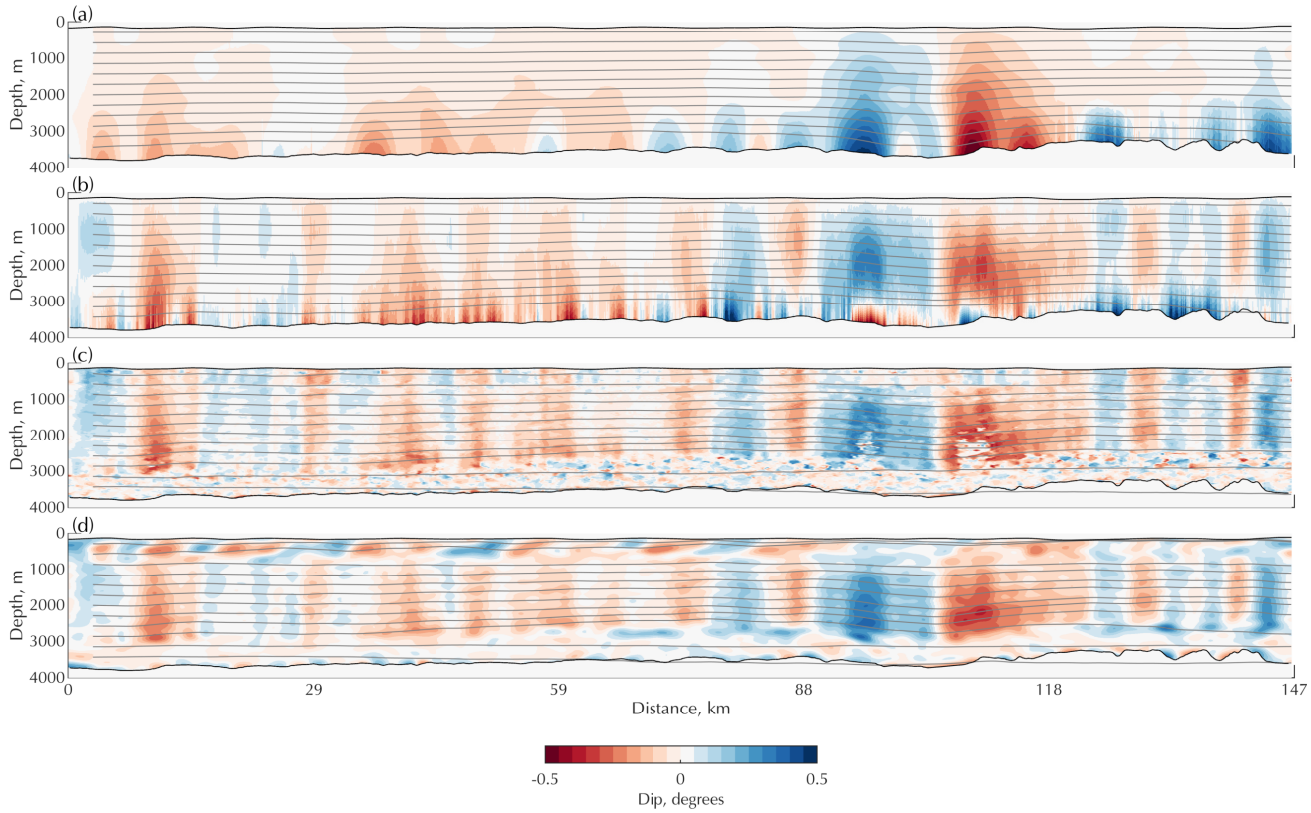

Figure 4.4: Propagation of a streamline through dip fields derived from (a) reference picks, (b) Panton slope-extraction step, (c) ARESP, and (d) using PWD.

4.4 Results

4.4.1 Isochrone tracking

Figure 4.1 presents the application of our workflow to our reference data (frames 01_034-036 collected 27/11/2013, Fig. 4.1 (a)), from East Antarctica's Vostok region, characterised by low dip, continuous reflectors. Parallel results for the more disrupted radar profiles across the Gamburtsev Mountains are presented in Figure 4.2. The numerical results for isochrone tracking algorithms are summarised in Table 1. Englacial layers extracted using ARESELP indicated a high degree of continuity along the section (Fig 4.1 g). This approach took 4 minutes 56 seconds for the example 1 dataset. We extracted 66 individual elements, that in effect pick out most of the englacial layers that we had picked manually, yet the error between reference age-depth profile at A' shows a significant deviation of up to -25 ka in the upper 50 % of the ice column with a significant swing to positive errors >100 ka deeper in the ice column (Fig. 4.1 h,i). This error can be traced to breaks in the englacial layers in two ways. Firstly, the algorithm fails to constrain multiple isochrones crossing the amplitude low at 90-120 km, resulting in a region over which the age-depth profile is continued unconstrained in the deeper ice. Secondly, there are additional breaks in layer continuity in the upper layers across which the linking stage of the algorithm has mismatched wavelet peaks between seed points of the layers either side of the breaks.

The Steger approach shows improvements in some areas (Fig 4.1 j-l) over the ARESELP algorithm. The retrieved age-depth profile shows a maximum error of 10 ka in the deepest regions of ice (Fig 4.1 l), but there is a greater degree of disconnectivity between A and A' than for ARESELP (compare Fig. 4.1 l with Fig. 4.1 i). This approach took 48 s per radargram for the BM3D filter, and 23 s for the picking and isochrone linking. We undertook parameter testing to increase the sensitivity to cross the amplitude low at 90-

Method	N	$\langle L \rangle$ (traces)	Median age error (ka)	Max age error (ka)	Max Connectivity
			Example 1		
Manual	33	2425	N/A	N/A	4
ARESELP	66	1652	14.9	101.2	5
Steger filter	1076	185	2.7	11.1	27
Sobel-Feldman	3210	57	13.8	19.7	95
			Example 2		
Manual	36	1222	N/A	N/A	5
ARESELP	95	885	6.4	70.0	11
Steger filter	641	134	19.3	92.4	34
Sobel-Feldman	6391	28	97.1	207.0	127

Table 4.1: Summary of quantitative assessment of auto-tracking algorithms. N is the number of elements (picks) generated by the algorithm, $\langle L \rangle$ is the average length of these picks in number of traces, *Median age error* and *Max age error* are the median and maximum difference between interpreted and reference age-depth profiles at A' (Fig. 4.1(a)), and *Max Conn.* is the maximum value of the connectivity index at A'

120 km, which led to an increase of picking success, but with an increase of false alarms in the deepest regions of ice. Overall, the Steger algorithm was able to identify 1076 elements in the radargram, compared with 66 from ARESELP, comparatively identifying more isochrones but with more disconnectivity. Up to 35 interpolations were required to constrain the age model throughout (Fig. 4.1 k).

The Sobel-Feldman edge-detection algorithm extracted the highest number of individual elements (3210) throughout the data (Fig. 4.1m), showing a high sensitivity to low-amplitude signals. This is also highlighted through the degree of connectivity between A and A', where the maximum number of interpolations reaches 91 at the bed (Fig. 4.1n). This approach typically took under 1 s for the each radargram. This experiment serves to highlight that although a good constraint on age-depth relationship can be achieved

using simple edge-detection implementations, the uncertainties associated with propagating age between a high number of low-quality picks suggest that such approaches should be avoided.

Figure 4.3 shows a detailed sub-set of the data shown in Fig. 4.1 to better highlight the relative strengths and weakness of each of the three tracing approaches. The ARESELP algorithm shows the most continuity and smoothest reflector dip throughout the data. In regions of good signal to noise ratio, the Hough transform approach to isochrone linking generally performs well, but dips deviate from the radargram structure for numerous internal layers (for example, the layer starting at 1550 m depth). There are also numerous picks where the interpretation fails to trace reflector peaks successfully or, more significantly, jumps at a high angle (e.g., depth $\approx$ 1400 m in Fig. 4.3b). This can give rise to substantial deviations in the age-depth profile propagated along profiles. This behaviour reflects the results of Fig. 4.1 (g,h and i), where the ARESELP algorithm shows that a low degree of connectivity (Fig 4.1.(h)) can be achieved between A and A', but large errors in age-depth relationship are obtained when comparing to the reference dataset (Fig. 4.1 (i)).

The Steger filter gives much more variability and a rougher pick as each ridge is picked independently of the previous one; there is only limited local directional guidance between traces. As such, in regions of strong signal with continuous isochrones the ridge tracking performs well in estimating the dip of structures within the radargram (in general, in the deeper regions of Figure 4.3 (c)). Increasing noise levels in the upper region of the figure (depths $<$ 1400 m) result in a larger number of noisy, conflicting-dip picks which do not track the radargram structure well. From Fig. 4.1 (j,k and l), the general ability of the Steger filter to track the dip of continuous reflectors results in results in a better age-depth error compared to the ARESELP algorithm, but with more age interpolations required to connect A and A'.

The Sobel-Feldman edge detection algorithm is similar in that the linking is unguided by dip and shows similar variation and susceptibility to the variation

of reflection amplitude to the Steger pick. The sensitivity of the Sobel-Feldman technique is higher to low-amplitude signals, resulting in the higher number of picks, but should be noted that despite this, the Sobel-Feldman shows a much lower susceptibility to crossing radargram layers in Fig. 4.3 (d) compared to both the Steger filter and ARESELP algorithms. This results in a much larger number of interpolations required to propagate the age-depth structure, which is reflected in Fig. 4.1 (n).

4.4.2 Dip estimation techniques

Figure 4.4 presents englacial-dip fields along profile AA' derived directly from the manual englacial-layering picking (panel a) then from the three automated approaches. The Panton approach to dip estimation (Fig. 4.4b) shows a good agreement with the reference dataset. This approach includes a step to remove noise in regions of low amplitudes and applies an interpolation across such regions. There is also little differentiation between noise and englacial-layer dips, such that incorrect dips are propagated across the echo-free zone, shown for example by a reversal of the dip at the deepest regions of ice at approximately 110 km along the profile and small-scale variations close the lowest streamline in Fig. 3b.

The ARESP approach exhibits higher sensitivity to lower-SNR regions, highlighted in the middle of the ice column at 110 km (Fig. 4.4c). Beneath the lowest traced englacial layer the average dip is zero, although slight noise in dip amplitude is observed.

Finally, the PWD method yields a higher degree of smoothing than ARESP, and has a flat streamline through the deepest ice. It is, however, sensitive to non-zero dips in the near surface that are not present or detected by the other techniques, and the uppermost streamlines deviate towards the surface as a result.

4.5 Discussion

4.5.1 Isochrone tracking intercomparison

Xiong et al. (2018) compared their ARESELP results to the picks from the manually-constrained interpretation of MacGregor et al. (2015b) using a direct overlay of extracted isochrones, which enabled only a limited degree of inter-comparison and quantitative assessment. Ferro and Bruzzone (2013) similarly used a manually-picked dataset as a reference against which to compare their application of the Steger algorithm, but further compared their results in terms of false alarms and missed layers to guide optimal parameter selection. Critically, neither of these approaches facilitated quantitative insights into the glaciological implications of incorrect picking in an automated algorithm, which we can gain from the age-depth relationship propagation.

The results of this comparison show that significant errors in age-depth structure can result from isochrone tracking algorithms. On our least complex dataset, the best algorithm resulted in a 11.1 ka error, but with large uncertainties due to the low number of continuous reflections between A and A'. Cavitte et al. (2016) model the age uncertainty from manual layer tracking as a combination of ice core age uncertainty and the radar range resolution and estimate an upper bound of uncertainty of 3.73 ka. Winter et al. (2019a) similarly estimate typical errors < 2 ka, but up to 3.7 ka. Hence, none of the isochrone-tracking methods trialled in this study is yet able to rival the accuracy of picking englacial layers manually. However, manual interpretation of multiple layers takes of the order of days per 100 km, especially where the layering structure is disrupted or broken. Expanding this across the Antarctic data record, with ongoing surveys with ever-improving resolution rapidly becomes a considerable effort, which motivates the further development of auto-tracking algorithms.

The approach to age-depth propagation used here comprises a simpler im-

plementation of the effective-strain estimation approach of MacGregor et al. (2015b), giving an interpolated fit rather than a physically-derived age-depth profile between isochrones. We found that due to the noisy and potentially converging layer picks from the automated approaches tested here, effective-strain estimations can be highly variable resulting in rapid deviations away from the expected ages. As algorithms improve, age propagation through a local strain estimation should be used. Despite ours being an approximate approach, it nonetheless gives insights into the performance of age-structure propagation through picked isochrones beyond a direct comparison of picked horizons.

Our approach to age-depth uncertainty using synthetic ice-core connectivity also highlights further issues that may be encountered with auto-tracking techniques. When manual picking is used, isochrones may be tracked across discontinuous regions in the absence of intersections with other interpreted profiles through recognising similar packages of reflections on either side of the noisy region (Cavitte et al., 2016; Ashmore et al., 2020), similar to practice in the seismic interpretation workflow (Nanda, 2016). However, none of the automated layer-tracking algorithms investigated here have implementations that allow the recognition, and matching, of similar packages of layers across gaps in the records. Such shortcomings that have challenged wider layer-tracing efforts have indeed been one of the major motivations for developing dip tracking as an alternate approach. Matching layer packages has long been a challenge in the field of automated seismic interpretation, where discontinuities are prevalent as faults. Discontinuities could potentially be overcome using artificial neural networks (Harrigan et al., 1992) or through global interpretation (Hoyes and Cheret, 2011) but these approaches have yet to be applied to ice-sheet radiostratigraphy.

Future automated interpretation techniques need to target automated linking of interpreted horizons to match disconnected isochronal picks derived from the local peak tracking. The principal issue experienced with implementations

tested here relates to trackers deviating from the target reflection. The ARESELP algorithm overcomes this to an extent as a result of the use of a Hough transform, yet still results in errors of age-depth profile as a result of deviations away from the data stratigraphy. Such linking may further be enhanced using correlation or artificial neural network approaches to signal matching, or through tracking along multiple trajectories using a confidence-based metric. The example and approach of age propagation testing presented here could be used to test these approaches.

4.5.2 Isochrone dip estimation

Each of the tested dip-retrieval algorithms worked well in the case of high-amplitude, high-SNR regions of the radargram. Failures occurred at three major locations; the deepest regions of ice with weaker or absent echoes; where englacial layers dip most steeply and SNR drops; and in the near surface. These are each where the signal power drops, or where local amplitudes vary rapidly as in the near surface. To combat this, operational use of algorithms could limit dip estimation to the middle of the ice column, following an approach commonly adopted for estimating layer continuity where the upper and lower 20% of the ice column are not used (Karlsson et al., 2012; Bingham et al., 2015). The Panton approach tested here did attempt to remove such low-amplitude regions by removing high spatial-frequency noise, but the drawback of this approach is the interpolation and associated loss of information from regions where dip is high, e.g. in the lower ice. This compares to Holschuh et al. (2017), who used signal-amplitude thresholding within a moving window to reduce the impact of low-amplitude areas, returning a zero dip field in these regions.

Modern SAR processing of airborne phase-coherent data offers opportunities for direct estimation of englacial-layer dip. Castelletti et al. (2019) presented a process to derive englacial-layer dips using retrieved phase before

stacking in phase-coherent systems to reduce the effects of destructive stacking described in Holschuh et al. (2014). Such an approach shows promising results in retrieving a dip field and enhancing layer coherence from complex data, but has yet to be applied to a larger region of Antarctica to aid a wider interpretation of ice-sheet stratigraphy.

4.6 Conclusions

We have undertaken an intercomparison of three isochrone auto-tracking and three englacial-dip estimation algorithms which may be used for wider exploration of the englacial radio-stratigraphic structure of the Antarctic Ice Sheet. We have presented a formal procedure for evaluating these approaches relative to a manually-picked reference dataset to give a reliable indication of the benefits and shortcomings of each isochrone tracking technique. Of the automated isochrones trackers tested here, there is only limited success in linking the age-depth profile between two locations along a relatively simple isochrone geometry. Of the three algorithms tested, the ARESELP procedure (Xiong et al., 2018) is best at retrieving substantial lengths of isochrones, yet can be prone to deviations in dip. While the Steger algorithm (Ferro and Bruzzone, 2013) shows a greater uncertainty in propagated ages, it shows an improvement in tracking general dip and a lower error in propagated age profile. Supplementing this approach with more advanced pattern-matching using, for example, neural networks to improve isochrone pick continuity is recommended.

The three different approaches to dip estimation that we tested all performed relatively well on our reference datasets, although all are challenged in the deepest ice and at the near-surface. All have the potential for higher performance by adopting improved data preprocessing, application of tapered windows or thresholding (e.g. Holschuh et al., 2017). Future developments in automated tracking should focus on the ability to automate linking of interpreted isochrones and use a similar approach to age propagation to demon-

strate successful implementation. We propose that the methodology developed here, and the two datasets from East Antarctica presented in this study, covering a range of englacial conditions, may be used as a standard validation approach for future algorithm developments.

Chapter 5

A sliced-3D approach to GPR FDTD modelling by optimising perfectly matched layers

This chapter details an approach to modelling 3D polarisation GPR data using a sliced-3D approach to FDTD modelling. An early version of this work was published as a conference submission for the International Workshop on Advanced Ground Penetrating Radar (IWAGPR) 2017, hosted in Edinburgh. This version is attached in Appendix C, although the work has been greatly extended for this chapter. A version of this chapter is currently in review for publication in *Geophysics*.

Conference paper Delf, R., Giannopoulos, A., Bingham, R. G., Hulton, N. R. J. and Curtis, A (2017). A Sliced-3D FDTD approach as an alternative to 2D Ground Penetrating Radar modelling, *9th International Workshop on Advanced Ground Penetrating Radar (IWAGPR), Edinburgh, 2017* pp. 1-5, doi: 10.1109/IWAGPR.2017.7996038.

Author contributions I generated and processed the data and wrote the manuscript. Antonis Giannopoulos contributed to the design of the study, and

all co-authors contributed edits to the final manuscript.

5.1 Abstract

Finite-Difference Time-Domain (FDTD) forward modelling is often used to gain a more quantitative understanding of the interactions between electromagnetic fields and targets. To undertake full 3D simulations the computational demands are challenging, so simulations are often undertaken in 2D where assumptions in the propagation of electromagnetic fields and source type can result in errors. Here, we develop the concept of a sliced-3D simulation, wherein a thin slice of a 3D domain with strictly 2D geometry is used to minimise computational demands while obtaining synthetic waveforms that contain full 3D propagation effects. This approach requires optimisation of perfectly matched layer (PML) boundary condition parameters so as to minimise the errors associated with the source being located close to the boundary, and as a result of grazing-incident angle wave conversion to evanescent energy. We explore the frequency dependence of PML parameters, and establish a relationship between complex frequency stretching parameters and effective wavelength. The resultant parameter choice is shown to minimise propagation errors in the context of a simple radioglaciological model, where 3D domains may be prohibitively large, and for a near-surface cross-borehole survey configuration, a case where full waveform inversion may typically be used.

5.2 Introduction

Finite-Difference Time-Domain (FDTD) forward modelling has been used in many areas of exploration and near-surface geophysics to test the performance of novel processing algorithms and acquisition (Versteeg, 1993; Langhammer et al., 2017), in data processing directly for finite difference and reverse time

migration (Fisher et al., 1992b; Yilmaz, 2001; Leuschen and Plumb, 2001; Church et al., 2018), and as a part of inversion algorithms including full waveform inversion (FWI) (Virieux and Operto, 2009; Busch et al., 2012; Mozaffari et al., 2016). In electromagnetic applications, 2D formulations of the Yee algorithm (Yee, 1966) are generally used, which make the implicit assumption of lateral model invariance. The resultant synthetic 2D data have an incorrect amplitude scaling with travel time for which a correction must be made. Many studies have employed a Bleistein filter (Bleistein, 1986; Auer et al., 2013) in pre-processing of field data to enable comparison with 2D models (Mozaffari et al., 2016; Klotzsche et al., 2019), but it has been demonstrated that this can result in errors after the first break or in complex velocity models (Auer et al., 2013).

Reduction to 2D requires the operator to assume that the radar antennas are either cross-line or in-line, modes that are typically and hereafter denoted TMz and TEz respectively. The most commonly-used modelling platforms apply TMz reduction from the principle that cross-line antennas are more widely used in many fields. However, the importance of source polarisation has been noted in several areas of the literature, including in glaciology (Langhammer et al., 2017), where the TEz mode is more commonly applied in ground-based studies (e.g., Bingham et al., 2017).

To address the issues outlined above, 3D modelling must be developed, yet the computational demands are intense. Here we present a new method for minimising domain size and hence the computational cost of full polarisation FDTD modelling of 2D geometries using a sliced-3D approach in gprMax, an open-source software GPR modelling package (Warren and Giannopoulos, 2016). We demonstrate the improvements in noise attenuation that can be achieved through optimisation of boundary conditions surrounding the model domain to minimise the effect of evanescent waves. We then investigate the frequency dependence of these optimum parameters, and demonstrate the effectiveness of the approach by applying the technique to two synthetic exam-

ples. We use a cross-borehole synthetic scenario, similar to FWI examples in the published literature (Klotzsche et al., 2010; Mozaffari et al., 2016), and a synthetic glacier study, two cases where full 3D models can be prohibitively large and where assumptions about the source and propagation mechanisms, that are implicit in 2D modelling, do not hold.

5.3 Theoretical Background

5.3.1 Approaches to modelling 2D geometries

FDTD modelling is generally undertaken using Yee's algorithm (Yee, 1966; Taflove and Hagness, 2005). In brief, the algorithm involves a discretisation of Maxwell's equations of electrodynamics, and an iterative propagation of a source term through time steps. The algorithm can be implemented in 3D or simplified to 2D in the TMz mode by assuming an infinitely long z-polarized dipole antenna (i.e. a line source) and cross-line geometry invariance to remove invariant E and H field components (Taflove and Hagness, 2005) (Figure 1). 2D simulations comprise a computationally quick method of modelling the response of a laterally invariant model. In practice, however, the assumption of an infinite z-polarised source is often violated due to the field logistics imposed on many GPR surveys. For example, due to the low frequencies often used in ground-based glaciological radio-echo sounding (Scott et al., 2010; Sevestre et al., 2015; King et al., 2016), lengthy dipole antennas are often towed in-line to the survey direction and as such cannot be modelled accurately using these implementations.

Additional issues are encountered in the scaling of amplitude with travel time. In a 3D domain with a point source, $A \propto \frac{1}{r}$, where A is amplitude and r is distance, but in 2D the source becomes an infinite dipole and the relationship becomes $\frac{1}{\sqrt{r}}$ (Bleistein, 1986; Auer et al., 2013). Because of this, when 2D modelling is employed the results need to be post-processed to obtain

amplitudes that quantitatively match field data. In seismic FDTD modelling the 2D Green's function can be transformed between 2D and an equivalent 3D function through a $\frac{\pi}{4}$ phase shift and an amplitude scaling using the Bleistein filter (Bleistein, 1986), expressed in the frequency domain as

$$G^{3D}(\omega) = G^{2D}(\omega)\sqrt{\frac{|\omega|}{2\pi\sigma}}\exp\Big(-\mathrm{sgn}(\omega)\frac{j\pi}{4}\Big) \tag{5.1}$$

where G^{2D} and G^{3D} are the 2D and 3D Green's functions, ω is angular frequency, $j = \sqrt{-1}$ and $\mathrm{sgn}(\omega)$ is the signum function of ω. σ is a scaling factor $\sigma = cr$, where r is distance (m) and c is velocity of propagation (ms^{-1}). This widely used function (e.g. Deregowski and Brown, 1983; Vidale et al., 1985; Esmersoy and Oristaglio, 1988; Yang et al., 2013) comprises an important correction when implemented in amplitude-sensitive imaging algorithms such as Marchenko methods (Lomas and Curtis, 2019).

Equation 5.1, however, is an asymptotic solution making the far-field assumption that distance $r \gg \lambda$, the wavelength of the signal, hence the near-field phase corrections are incorrect. Additionally, the scaling function σ is commonly estimated for the first break arrival, yet in the presence of heterogeneous media where the velocity field is not known the raypath distance r and velocity c cannot be accurately calculated. Later arrivals are not considered and hence not correctly scaled. Errors at pre-processing stage are propagated through the forward model and then reduce the accuracy of FWI results (Auer et al., 2013). Errors in such an approach are particularly prevalent in the case of largely heterogeneous velocity models; more complex approaches requiring a good starting velocity model are therefore required (Van Vorst et al., 2014).

To overcome issues of amplitude scaling and to retrieve EM polarisations in the in-line survey orientation using a 2D modelling domain, several authors have used 2.5D implementations of the Yee algorithm. These project the 3D algorithm onto a 2D plane by assuming a series of constant wavenumbers k_z and iterating over multiple values of k_z (e.g. Stoyer and Greenfield, 1976; Moghad-

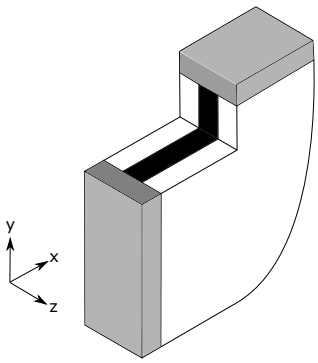

Figure 5.1: Design of a sliced 3D model: grey represents standard PMLs bounding the model, for which advanced optimisation is not required. Black represents the model domain and white is the bounding PML required to attenuate grazing waves. Image size truncated by the curved boundary for clarity.

dam et al., 1991; Xu and McMechan, 1997). Although computationally cheap, as it involves multiple easily parallelisable 2D syntheses, 2.5D implementations require a reformulation of the Yee algorithm and post-processing of results and are therefore not readily implemented in available FDTD software packages.

While the above approaches to data pre-processing are effective in converting processing to a 2D problem, full 3D FDTD modelling of 2D geometries remains the optimal solution for generating full 3D polarisation and propagation effects, even in the case of strictly 2D geometries of data acquisition or subsurface heterogeneity (e.g. Mozaffari et al., 2016; Langhammer et al., 2017). The computational demands of such an approach can be significant and as such it is preferable to minimise the width of the domain, as, for example, in Figure 5.1. This is, however, not simple to solve because moving the grid boundaries closer to source and receiver points results in an increase in grazing-incidence energy on the boundary and associated spurious reflections (Berenger, 1999; Drossaert and Giannopoulos, 2007; Feng et al., 2017).

5.3.2 Perfectly Matched Layer Theory

The boundaries of an FDTD grid can be terminated using a perfectly matched layer (PML), a boundary of cells designed to attenuate energy, lined with a

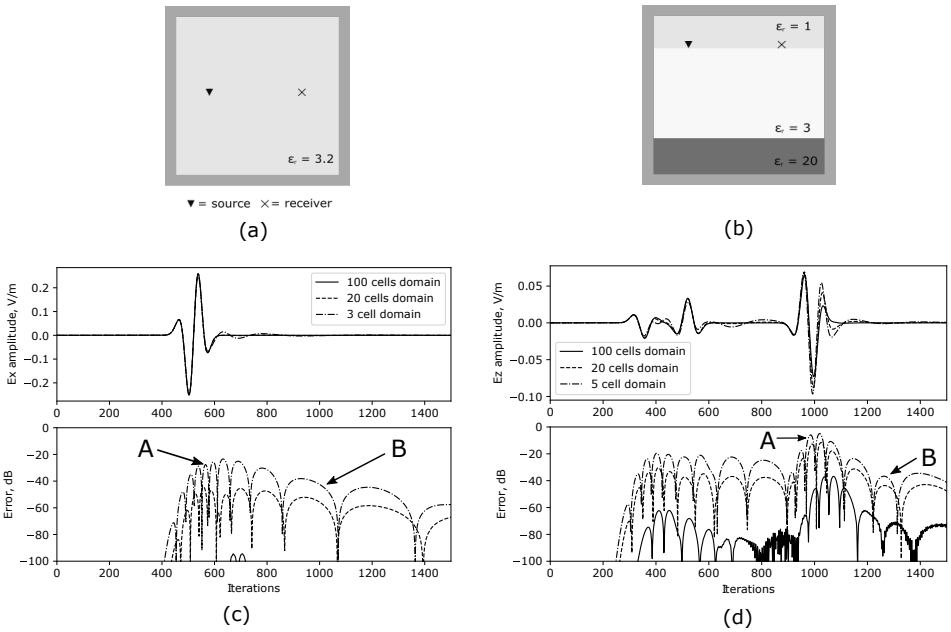

Figure 5.2: Comparison of the effects of cross-line domain size (in/out of the page), for (a and c) a homogeneous ice ($\epsilon = 3.2$) model with a Gaussian wavelet and a standard PML, and (b and d) a 3-layer model with a homogeneous ice layer overlying flat bedrock with a free-space layer above the surface. Two sources of noise can be noted for each. 'A' shows high frequency noise as a result of normal incidence reflections through the PML. The arrival time of this noise is delayed in wider implementations, as the two way travel time between boundaries (out of the plane in (a) and (b)) increases. 'B' shows low-frequency, evanescent noise as a result of grazing wave interactions between the signal and PML boundary. A wider model results in minimisation of this noise, as the incidence angle increases with increasing width.

perfect electrical conductor (PEC) sheet at the outermost layer. The ideal PML will attenuate incident energy and not produce acausal or spurious, non-physical reflections. Within the PML region we can consider a complex stretched coordinate system such that the x-projection of Maxwell's equations in the frequency domain become

$$j\omega\tilde{D}_x = \frac{1}{s_y}\frac{\partial\tilde{H}_z}{\partial y} - \frac{1}{s_z}\frac{\partial\tilde{H}_y}{\partial z} \tag{5.2}$$

$$j\omega\tilde{B}_x = \frac{1}{s_z}\frac{\partial\tilde{E}_y}{\partial z} - \frac{1}{s_y}\frac{\partial\tilde{E}_z}{\partial y} \tag{5.3}$$

where s_y and s_z are the PML stretching functions (Taflove and Hagness, 2005; Giannopoulos, 2018).

Early implementations of the PML used s_u as

$$s_u = \kappa_u + \frac{\sigma_u}{j\omega_u} \tag{5.4}$$

where u is the orientation perpendicular to the model boundary. In general and in this chapter we assume that the PML parameters are the same in each orientation, so we will refer to s_u, κ_u and σ_u as s, κ and σ, respectively. Conceptually, κ dictates a real coordinate stretch, and $\frac{\sigma}{j\omega}$ introduces an imaginary spatial coordinate stretch mainly responsible for signal attenuation. Minimising the z-dimension of a 3D model necessarily results in energy propagating within the model domain at grazing (low-incidence) angles to the PML boundary. Such propagation has been reported to result in significant spurious reflections through evanescent energy in the case of the standard PML (Berenger, 1999; Drossaert and Giannopoulos, 2007; Feng et al., 2017), and this can be seen in equation 5.4 as $s \to -j\infty$ as $\omega \to 0$, resulting in a pole at large wavelengths due to the rapid transition to a highly stretched imaginary coordinate system.

Enhanced attenuation of evanescent energy through a model can be undertaken using a complex frequency shifted PML (hereafter, CFS-PML) stretching

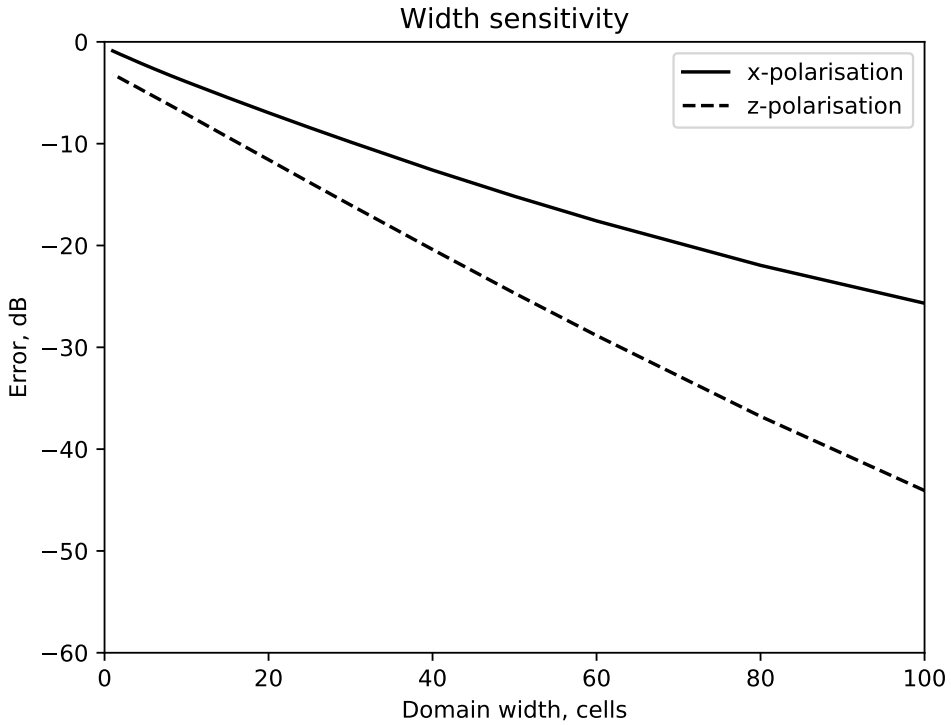

Figure 5.3: Plot of maximum error as a function of domain width for a homogeneous ice model shown in Figure 2(a). Decreasing model width results in an increased error as a result of interactions with grazing-angle incident energy.

function. The CFS-PML is a modification of the standard stretching s through addition of a shift function $\alpha \geq 0$ in equation 5.4, such that

$$s = \kappa + \frac{\sigma}{\alpha + j\omega\epsilon_0}. \tag{5.5}$$

This removes the pole at $\omega = 0$, and since $s \to \kappa + \frac{\sigma}{\alpha}$ as $\omega \to 0$, results in improved attenuation of low-frequency energy as the smooth transition to a stretched coordinate system is maintained (Roden and Gedney, 2000; Berenger, 2002; Giannopoulos, 2008).

The CFS-PML parameters can be tuned to improve performance over a frequency range and reduce non-physical reflections from the PML boundary. This is done by scaling parameters α, κ and σ through the PML, usually using

an integer polynomial m. σ is scaled from 0 to σ_{max} as

$$\sigma(x) = \sigma_{max}\left(\frac{x}{d}\right)^m, \tag{5.6}$$

where d is the depth of the PML in cells and $0 < x < d$ is the location within the PML so as to avoid sudden changes in σ and associated non-physical reflections. κ is similarly scaled from 1 to κ_{max} by

$$\kappa(x) = 1 + (\kappa_{max} - 1)\left(\frac{d-x}{d}\right)^m, \tag{5.7}$$

such that $\kappa = 1$ (no coordinate stretch) at the model/PML interface and $\kappa = \kappa_{max}$ at the grid boundary.

The scaling of α is less physically intuitive. Taflove and Hagness, 2005 show that in a 1st order CFS-PML there exists a cutoff frequency

$$f_{cutoff} = \frac{\alpha_x}{2\pi\epsilon_0} \tag{5.8}$$

whereby for incident wavefields $f_{app} \ll f_{cutoff}$, there is little absorption for travelling waves within the PML. Conversely, for $f_{app} \gg f_{cutoff}$ there is a high absorption. A similar result is obtained in Berenger, 2002, who calculate analytically a value for α_{max} in the case of a waveguide terminated by a PML. If α varies throughout the PML, a broader frequency band can be attenuated by the PML. Additionally, the reflection coefficient at the model/PML boundary, Γ can be approximated by

$$\Gamma \approx \frac{\sigma}{4\alpha} \tag{5.9}$$

(Taflove and Hagness, 2005). As such, α is generally scaled from a maximum at the model/PML boundary to zero at the outermost grid boundary, such that

$$\alpha(x) = \alpha_{max}\left(\frac{1-x}{d}\right)^m. \tag{5.10}$$

Higher order CFS-PMLs operate via a product of multiple contributions,

by

$$s = \prod_{i=1}^{N} s_i \tag{5.11}$$

where N is the number of terms, i is the order, and s_i is defined in equation (5.5), with the aim of combining the characteristics of improved attenuation within the PML compared to the standard PML with the attenuation of evanescent energy of the CFS-PML. Typically, two terms ($N = 2$ in equation 5.11) are used for a higher order PML, but more terms are possible by introducing further terms of s_i. Feng et al., 2017 undertook an optimisation of the higher order PML for the application of broadband seismic modelling and showed a reduction in the error as a result. However, it is clear from inspection that such implementations introduce cross-terms in addition to the desired terms as, for a 2nd order CFS-PML,

$$s = \left(\kappa_1 + \frac{\sigma_1}{\alpha_1 + j\omega\epsilon_0}\right)\left(\kappa_2 + \frac{\sigma_2}{\alpha_2 + j\omega\epsilon_0}\right) \tag{5.12}$$

(Giannopoulos, 2018). What remains unclear is what impact these additional cross-terms have in an optimisation process. Along with the higher number of degrees of freedom associated with multiple stretching functions, this results in the process becoming a cumbersome problem for the general case, and hence will not be considered in this study.

5.3.3 Optimum CFS-PML parameters

Several studies have demonstrated improved implementations of PMLs in both seismic and GPR FDTD modelling, but few have proposed generally applicable optimal parameter selections. An optimally defined PML can be considered one where the amplitude of the misfit between the model and some reference is minimised, and the performance is often compared through the maximum error in dB across the full domain (Roden and Gedney, 2000; Berenger, 2002; Giannopoulos, 2008; Taflove and Hagness, 2005; Feng et al., 2017). Gedney and

Zhao, 2010 undertook a parameter search over σ_{opt}, α and κ for specific cases and recommend for application to simulations of a 1 cm thick waveguide and of a thin perfect electrical conductor plate model. Drossaert and Giannopoulos, 2007 recommend parameters for an elongated seismic FDTD grid through such an approach. This approach showed a stronger error dependence on κ_{max} than on α_{max}, and that the optimum values depend on the location in the domain and on travel time. As these results pertain to a different problem, they will not be considered for comparison to our results, but the methodology will be adapted and followed for our particular optimised CFS-PML results.

Gedney, 1996 showed through numerical testing of standard PMLs (equation 5.4) that the optimum value for σ_{max} can be estimated through

$$\sigma_{max} \approx \frac{m+1}{150\pi dx\sqrt{\epsilon_r}}, \tag{5.13}$$

where m is a polynomial scaling, dx is the spatial resolution, and ϵ_r is the relative dielectric constant. In general, this approximate value has been adopted widely for both standard PML and CFS-PML (Gedney and Zhao, 2010; Giannopoulos, 2012) and will be used throughout this study.

Feng et al., 2017 undertook a parameter search for a higher order, 2-term CFS-PML. In the case of a higher order CFS-PML implementation, terms $\kappa_{i_{max}}$ define the maximum values for κ for the i^{th} term in the product series in equation 5.11. Feng et al., 2017 recommended that the optimum values are $\kappa_{max1} = 1$ and $\kappa_{max2} = \frac{2PPW_{f_{max}}}{PPW_{FD}}$, where $PPW_{f_{max}}$ (points per wavelength) is the number of grid cells per wavelength at the maximum modelled frequency f_{max}, and PPW_{FD} is the number of grid cells per wavelength required by the algorithm, in this case $PPW_{FD} \approx 10$ for the central finite difference algorithm. We follow Feng et al., 2017 in using

$$PPW_{f_{max}} = \frac{v}{dx f_{max}}, \tag{5.14}$$

and estimate f_{max} from the maximum contributing frequency for the wavelet used. Additionally, $\alpha_{max1} = 0, \alpha_{max2} = \frac{\epsilon_0 \times f_{max}}{8}, \sigma_{max1} = 0.4\alpha_{max2}$ and $\sigma_{max2} = 3\sigma_{opt}$, where σ_{opt} is given by equation 5.13. As this approach gives a general case solution to estimate optimum parameters, these recommendations will be used for comparison in this study to compare the performance to an optimised CFS-PML.

5.4 Methodology

We initially explore the impact of cross-line domain size on signal error as a result of evanescent energy. We firstly assess the effect of reducing the cross-line domain size for both a homogeneous ice ($\epsilon_r = 3.2$) model (Figure 5.2a), and a layered model of homogeneous ice overlying a bedrock layer ($\epsilon_r = 20$) (Figure 2b) following a modified methodology of Delf et al., 2017.

Then, for a sliced-3D model with a fixed domain size of 5 cells and a PML thickness of 15 cells, we undertake a series of sensitivity experiments with uniform models to investigate the performance of PMLs in attenuating grazing wave energy on the boundary of the sliced-3D model. The experiments were performed at (a) 25 and (b) 50 MHz using a Ricker wavelet. We use a similar approach to Taflove and Hagness, 2005 and Drossaert and Giannopoulos, 2007 in testing parameter pairs over an expected range to derive the optimum values because, although this is a computationally intensive option, it allows a clear assessment of the sensitivity to different parameters. We initially do this using a κ scaling polynomial $m = 2$ and α polynomial $m = 1$ (see eqs. 5.7 and 5.10). The model was discretized at 0.1m to give a model domain size of 24 x 24 x 3.5 m. The PML thickness was extended compared to a typically used 10-cell implementation, with the intention of reducing errors due to normal incidence energy at the bounding edges, which may not be attenuated as effectively when optimisation is undertaken to reduce evanescent energy. We then repeat this approach to investigate the impact of polynomial order m for κ and α, running

this test for all combinations between $m = 0$ (constant value) and $m = 6$.

For each case, a reference solution of a 3D model, $\mathrm{E}(x, y, t)_{\mathrm{ref}}$, is calculated using a large 3D model with an identical 2D geometry, to give the response where there is no interaction with bounding PMLs normal to the z orientation. The 3D model consists of identical geometry in the x- and y-orientation, with a 120-cell model width in the z-orientation and a 20-cell PML. As a result of this larger width there is no grazing-wave interaction with the model-PML interface, and we can assume this to be the best-case scenario with minimum error response. Errors are reported relative to this reference solution as in Roden and Gedney, 2000; Berenger, 2002; Giannopoulos, 2008; Taflove and Hagness, 2005; Feng et al., 2017 as

$$error(x, y, t) = 20\log_{10}\frac{\mathrm{E}(x, y, t) - \mathrm{E}(x, y, t)_{\mathrm{ref}}}{\mathrm{E}_{\mathrm{ref}_{\mathrm{max}}}}, \tag{5.15}$$

where $\mathrm{E}(x, y, t)$ is the output electric field in time, $\mathrm{E}(x, y, t)_{\mathrm{ref}}$ is the reference solution in time, and $\mathrm{E}_{\mathrm{ref}_{\mathrm{max}}}$ is the maximum value of the reference solution.

We then investigate the frequency dependence of optimal CFS-PML parameters, by doing a similar grid search parameter test as for the previous tests, but this time using an impulse source type followed by a convolution with a Ricker wavelet with central wavelength λ_c. We limit frequencies used to $20 < \lambda_c/dx < 100$, as this is the most commonly used range of λ/dx for efficient FDTD modelling, also noting the dispersion limit of $dx < \lambda_{min}/10$ (Giannopoulos, 1998) and that for a Gaussian waveform, the minimum significant wavelength considered for dispersion ($error < -40$ dB) is $\lambda_{min} \approx \frac{\lambda_c}{3}$. Using grid sizes of 0.01 and 0.1 m this allows testing in the range 100-700 and 10-70 MHz respectively. For this experiment, we use a 5-cell domain width with 15-cell PML.

Finally, we repeat our experiment of investigating domain width sensitivity to confirm that an improvement in error is observed using an optimised CFS-PML, before comparing the performance of an optimised first order PML with

those previously published in the literature, including Feng et al., 2017, which was developed for computational seismology but follows similar theory, along with Gedney and Zhao, 2010 and as outlined previously. For this case we use a model discretisation of 0.005 m and free space ($\epsilon_r = 1$).

5.5 Numerical Results

5.5.1 Impact of domain size

Figure 5.2 shows the results of reducing domain size for homogeneous and layered models. Thin models (3 cell model domain size) show significant ($<$ $t - 20$dB) noise levels at signal arrival, followed by low-frequency ringing as a result of evanescent energy from the model-PML interface. Figure 5.3 shows the error for both x- and z- polarisations for the homogeneous ice model. We estimate an error of -40 dB (1%) to be a feasible target to reduce the errors below the signal-to-noise ratio of a typical radargram which, from figure 5.3, would require a domain width of 60 cells. At small domain sizes, the effect of evanescent energy is significant, whereby low frequency and high amplitude errors are introduced following the direct arrival (arrivals in Figure 5.2, marked 'B'). Thickening the PML has minimal impact on this error as it is induced by the model/PML boundary.

5.5.2 1st order PML optimisation

The optimum values for α and κ were estimated through a brute-force grid search approach, producing error contour plots exemplified by Figure 5.4. The grid search shows minimum error bounds of -65 dB and -45 dB for 25 and 50 MHz, respectively. A clear frequency dependence of the optimum parameters can be seen, indicating that optimum κ_{max} decreases with increasing frequency, and that the sensitivity of error to the α value decreases with increasing frequency. This is intuitive as κ dictates the real coordinate stretch of the PML

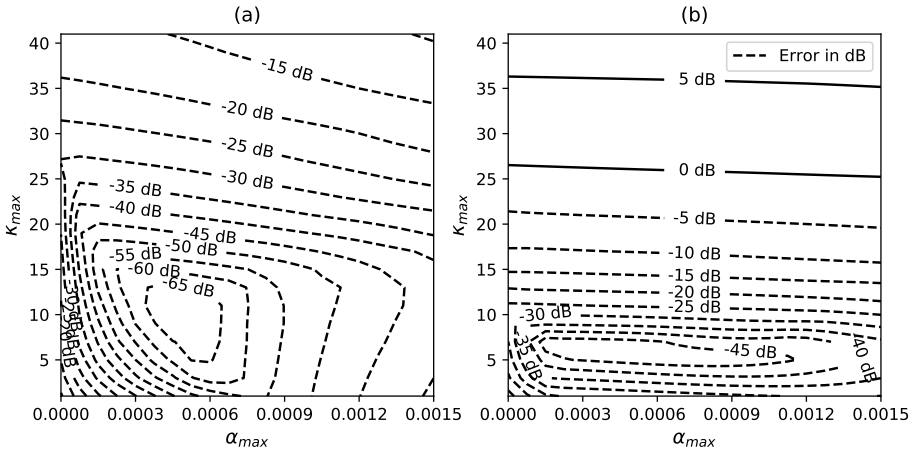

Figure 5.4: Contour plot of maximum error as a function of α_{max} (frequency shift factor, equation 5.5) and κ_{max} (stretching factor) for a homogeneous ice model with a 5 cell width model domain, 15 cell first-order PMLs, with $dx = 0.1$m. A Gaussian waveform with central frequency (a) 25 MHz and (b) 50 MHz is used.

- a higher value results in a higher stretch, such that the maximum $\frac{\lambda}{dx}$ within the stretched coordinates of the PML is minimised. The optimum value of α is approximately the same for both experiments, but has a much lower sensitivity in the high frequency.

5.5.3 Impact of Polynomial Order

Figure 5.5 shows the minimum error for each grid search as a function of order of polynomial scaling. It is clear that, for this example, a constant α scaling function is the most efficient, with a maximum -80 dB error. Higher orders of α result in an error of at least -50 dB. A quadratic κ scaling function is shown to provide the optimum attenuation for all orders of α. This result contrasts with Taflove and Hagness, 2005, where it is suggested that $\alpha = 0$ at the outermost grid boundary to enable sufficient travelling wave energy attenuation. Our optimal parameter setting is therefore minimising the effect of evanescent energy, with the remaining noise being primarily as a result of normal-incidence energy at the source point.

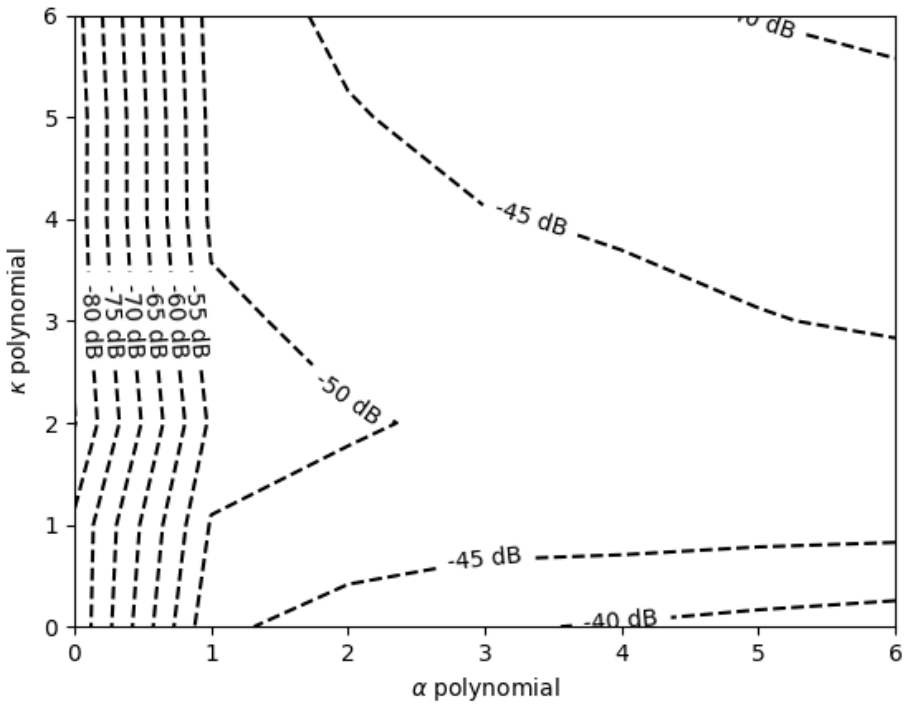

Figure 5.5: Minimum error for all combinations of polynomial scaling. This is found through repeating the results of Figure 5.4 for each combination of polynomials in α and κ. The optimum value is shown to be 0 for α and 2 for κ.

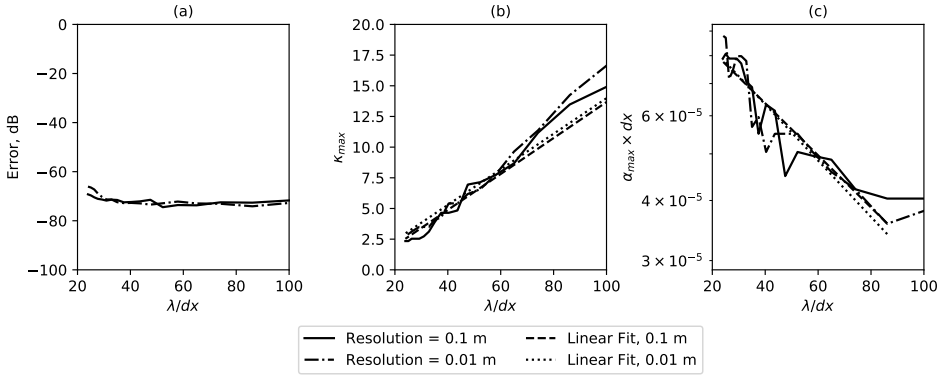

Figure 5.6: Frequency dependence of the 1st order CFS-PML parameters using a discretisation of 0.1 m and 0.01 m for the homogeneous model (Figure 5.2a). (a) shows the error as a result of the optimum parameters. (b) shows optimum κ_{max} as a function of $\frac{\lambda}{dx}$. A positive linear trend is observed as expected as a larger κ_{max} is expected for larger wavelengths. (c) shows $\alpha \times dx$ plotted as a function of $\frac{\lambda}{dx}$. This plot is scaled by discretisation on a lin-log plot, demonstrating that optimum α shows a slight negative trend with λ/dx and a scaling with resolution

5.5.4 Frequency Dependence

Figure 5.6 shows minimum error, optimum α and optimum κ as a function of $\frac{\lambda}{dx}$, firstly demonstrating (Figure 5.6 (a)) that error is relatively constant at approximately -70 dB for all values of $\frac{\lambda}{dx}$ tested. Figure 5.6 (b) shows the optimum selection of κ is linear with $\frac{\lambda}{dx}$, with a linear relationship of

$$\kappa_{max} = 0.14\frac{\lambda}{dx} - 1. \tag{5.16}$$

In Figure 5.6 (c), α_{max} is plotted as $\log_{10}\alpha_{max}dx$ as a function of $\frac{\lambda}{dx}$. A negative linear relationship can be plotted for the range $20 < \frac{\lambda}{dx} < 70$, of form

$$log_{10}(dx\alpha) = -0.005\frac{\lambda}{dx} - 4, \tag{5.17}$$

which reduces to

$$\alpha = \frac{10^{-4-0.005\frac{\lambda}{dx}}}{dx}. \tag{5.18}$$

Together with equation 5.13, these values can be readily used as a guideline

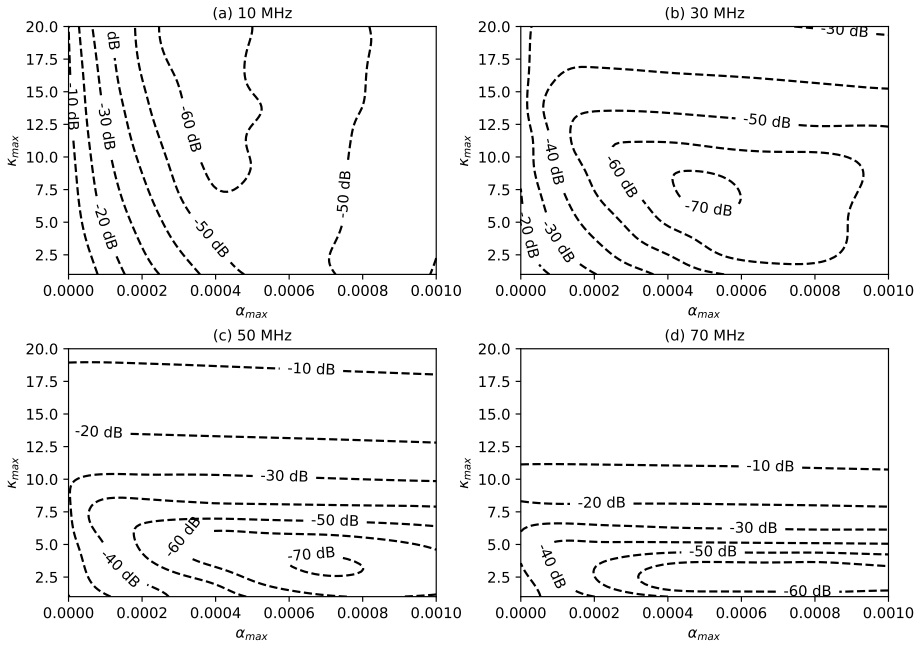

Figure 5.7: The error surface as a function of κ and α for a range of frequencies for dx=0.01 using the same experimental setup as in Figure 5.6 (a).

for 1st order CFS-PML parameters in the frequency range suggested as they only require calculation of a central wavelength λ and the discretisation. As such, they can be readily calculated in the FDTD implementation. Figure 5.7 additionally shows that at higher frequencies (i.e. lower values of λ/dx), the error is much more sensitive to the value of κ_{max} than to the value of α_{max}, and this provides a more stable linear regression result in Figure 5.6.

5.5.5 Domain width revisited

With our new understanding of optimum CFS-PML parameters, we now revisit signal error as a function of domain width (Figure 5.8). The optimised PML gives a consistent result of -38 dB for an x-polarised source type, and -45 dB for a z-polarised source type. The error increases slightly at a domain width of 10 cells for a z-polarised source, but remains under -40 dB down to a 3-cell domain width. In the following examples, we use a 5-cell domain width as a

balance between computational requirements and accuracy.

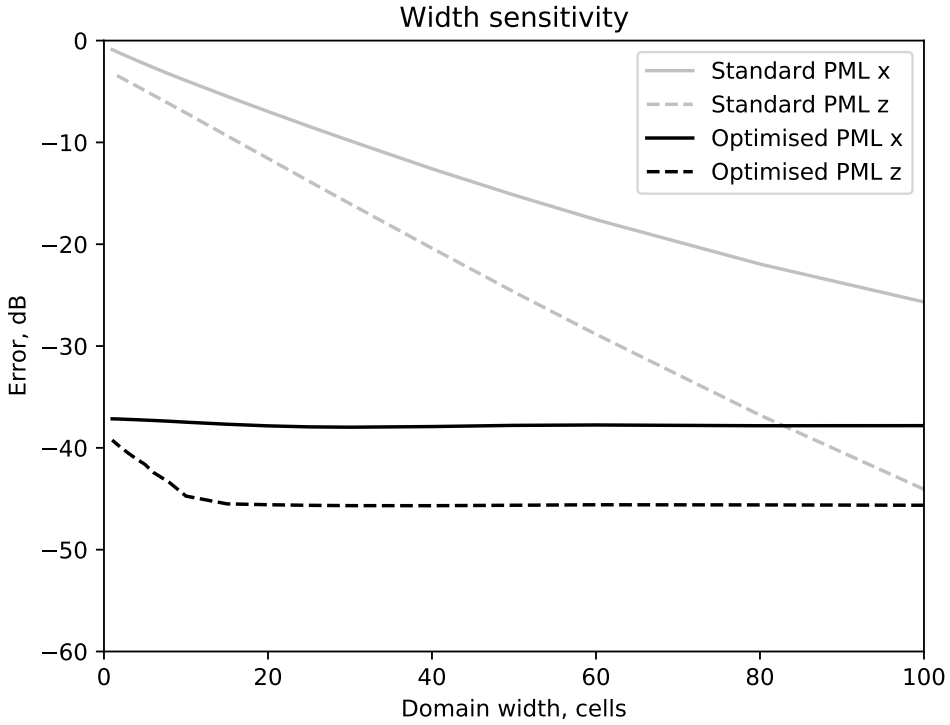

Figure 5.8: Comparison of the signal error as a function of domain width, as in Figure 5.3, but including results with an optimised CFS-PML, using the horizontally layered model as in Figure 5.2c) and d). A consistent -38 dB can be achieved for the x-polarised result and -45 dB for the z-polarisation using our recommendations for CFS PML parameters.

5.5.6 Comparison of implementations

The performance of differing implementations is compared in Figure 5.9 using a sliced-3D homogeneous ice model as in Figure 5.2 (a), now using 60 receivers in the positive x direction, representing a common source point experiment. The difference between each result and the reference solution in Figure 5.9 (a) is shown in panels (b) to (e). This demonstrates that a correctly optimised 1^{st}-order CFS-PML can produce synthetic data with no evanescent energy in a sliced-3D model domain. There is a slight error close to the source point in panel (c), as a result of the CFS-PML's reduced ability to attenuate normal-

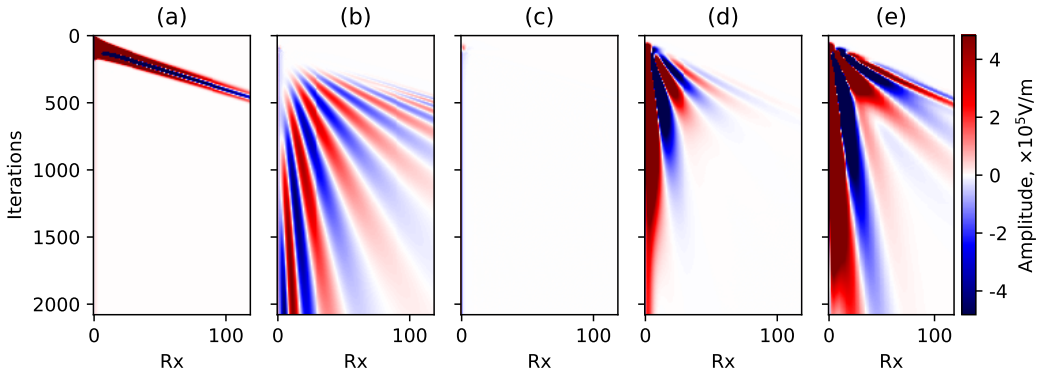

Figure 5.9: Error plots as a function of receiver offset and time for a 5-cell width sliced 3D domain with a z-polarised source at 50 MHz. Error is the difference between the result and a reference 3D solution. Colour scale is clipped at 1% of the maximum. (a) Reference solution from a 3D model showing direct arrival (b) a sliced-3D domain with no PML parameter optimisation (c) the same model with optimum parameters selected from equations 5.16 and 5.18, (d) with parameters selected from the results of Feng et al., 2017 and (e) with parameters recommended by Gedney and Zhao, 2010. This comparison demonstrates that a well-optimised 1st order CFS-PML, using recommendations from this study, can show an improvement for grazing-wave interactions over generic parameters chosen for both 1st and 2nd order PMLs, which are often developed for different applications.

incidence energy. Other recommendations (panels (d) and (e)) for CFS-PML parameters show strong evanescent energy, showing that while these have been recommended for a general case for 1st-order and 2nd-order CFS-PMLs, they are not suitable in this application.

5.6 Examples

We now demonstrate the performance of sliced-3D FDTD modelling in two applications for which error levels and model computational demand are important considerations. We first use a cross-borehole survey configuration in the presence of a heterogeneous soil with ϵ_r ranging between 8 and 18. This is similar to the cross-borehole FWI experiment configurations of Klotzsche et al., 2010 and the computational configuration of Mozaffari et al., 2016. We use a single z-polarised source point with a 200 MHz central frequency Ricker wavelet, with an array of receivers located in a second borehole (see Figure

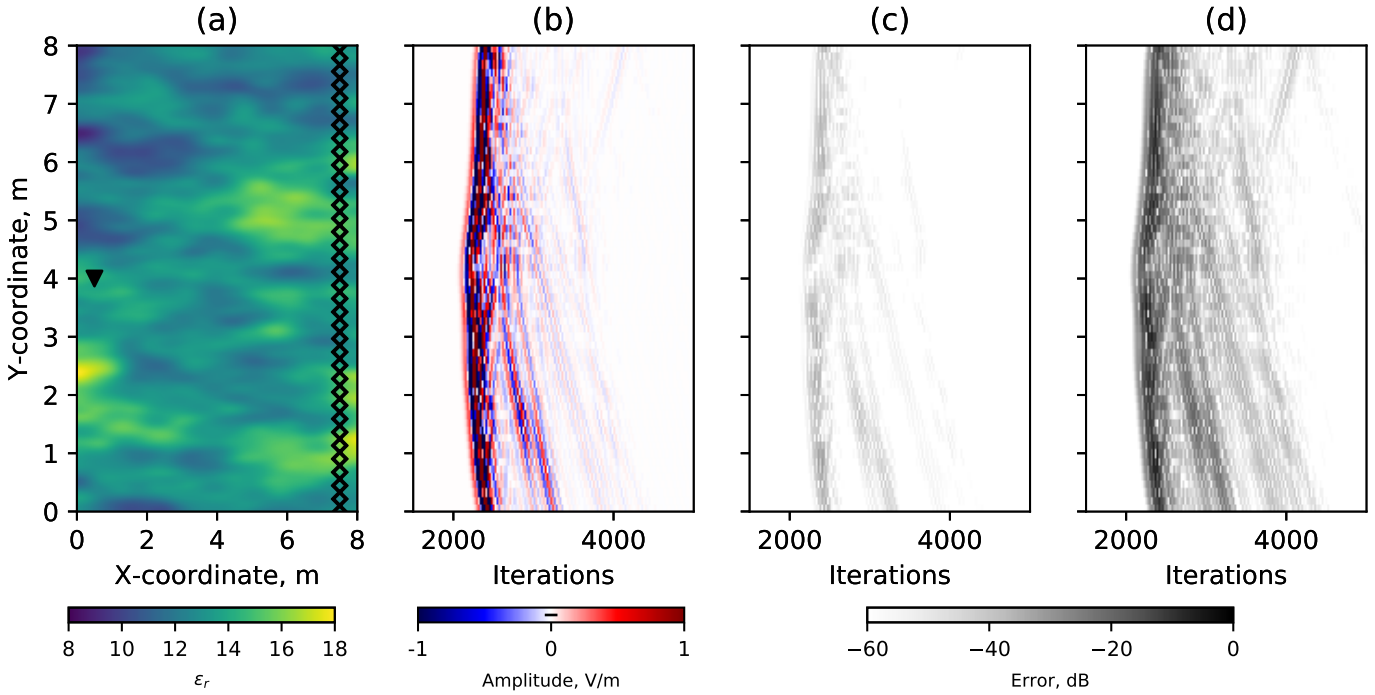

Figure 5.10: Cross-borehole GPR experiment example. (a) Model domain showing random variations in dielectric constant, overlaid with source point (triangle) and receiver locations (crosses). (b) Results of a full 3D modelling experiment using a z-polarised source. (c) Error plot (in dB) using a sliced-3D domain with parameters recommended in this paper. (d) Error plot (in dB) of 3D-to-2D transformed data using a Bleistein filter

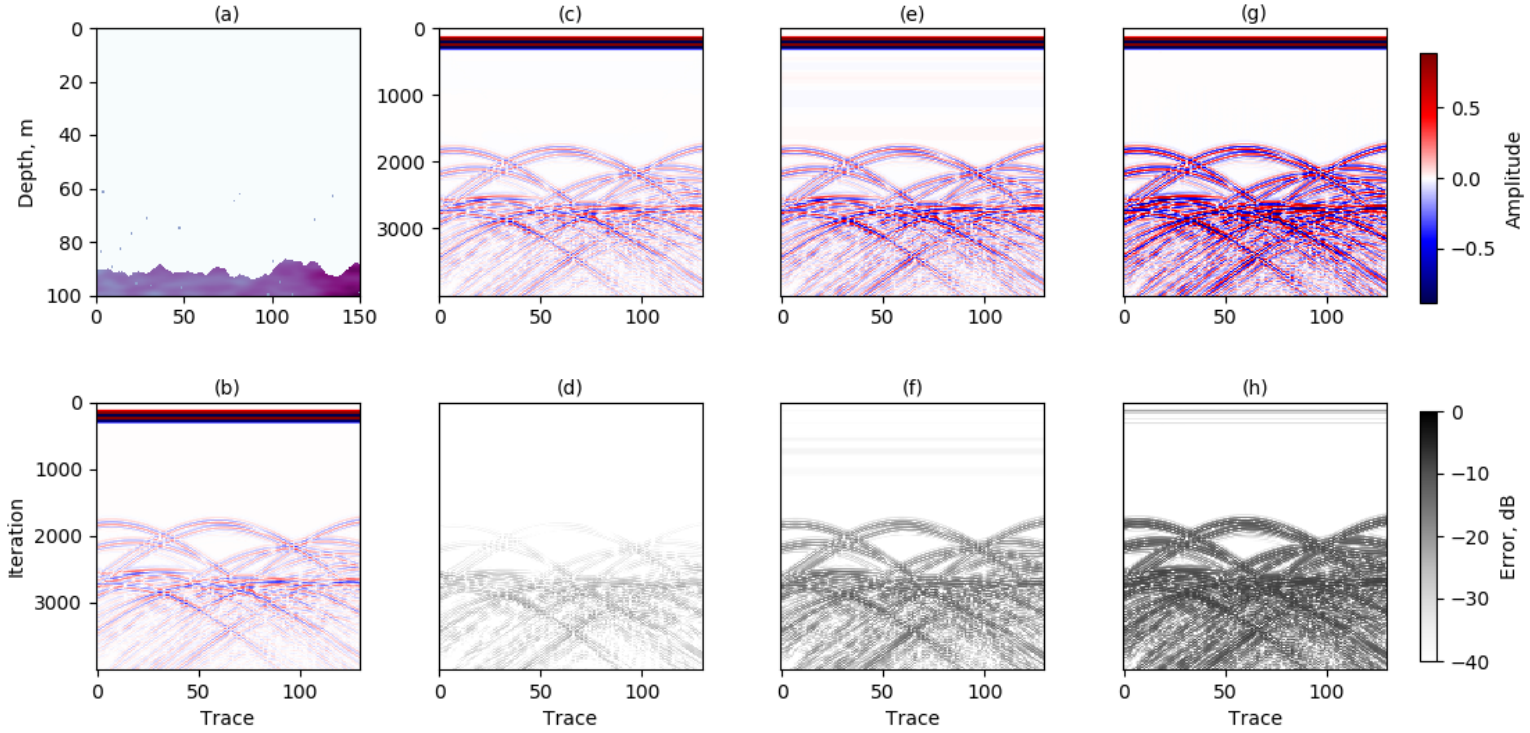

Figure 5.11: Synthetic representing a glacier bed with internal scattering points within the ice. (a) Initial model with homogeneous ice and a rough bed. (b) Reference model response from full 3D simulation. (c) Model response and (d) error with a sliced-3d domain and an optimised CFS-PML, using the recommendations from section 5.5.4. (e) Model response and (f) error for a sliced-3d domain with no optimised CFS-PML, using $\alpha_{max} = 0$, $\kappa_{max} = 1$ and $\sigma_{max} = \sigma_{opt}$. (g) Model response and (h) error for a 2D model followed by 2D-to-3D Bleistein filter transformation. A significant improvement in error can be observed when the correct source polarisation is used in a sliced-3D approach.

5.10a). The source and receiver boreholes are separated by 6 m. Using a discretisation of 0.02 m, the recommended parameters from equations 5.16 and 5.18 are $\alpha = 0.00397$ and $\kappa_{max} = 1.80$. We undertake the simulations in 3D, sliced-3D and in 2D. The sliced-3D model domain consisted of 1 cell width, with PMLs extended to 15 cells to minimise noise from normal-incidence energy.

All simulations are undertaken with a z-polarised source to enable like-for-like polarisation comparison with the 2D implementation. We apply a frequency-domain Bleistein 2D-to-3D filter to the 2D data (equation 5.1), with r equal to the straight line raypath between source and receiver for each trace and c calculated from the RMS value of ϵ_r from the model. We compare the results in figure 5.10 (c) and (d), which shows a significantly lower error field for the sliced-3D approach.

We then apply this approach to a model of a simple glacier with a rough bed and several internal scattering points. We use model dimensions of 150 x 100 x 3.5 m with a 15 cell PML thickness and resolution 0.1 m to demonstrate the low noise level achievable with our recommendations. A dipole source with a Ricker wavelet of central frequency of 25 MHz is used. Given these model parameters, CFS-PML parameters are chosen to be $\alpha = 0.00046$ and $\kappa_{max} = 3.70$, following Figure 5.6 and equations 5.16 and 5.18. We use a single-channel, common offset survey acquisition with source and receiver separated by 5 m to represent a typical survey with low-frequency dipole antennas. Several scattering points with $\epsilon_r = 80$ are imposed to simulate scattering bodies found within polythermal ice (Barrett et al., 2008). We use 130 source/receiver locations along the surface of a freespace/ice interface.

The results of the model are presented in Figure 5.11, along with error in dB in the second row (d), (f) and (h). Figure 5.11 (c) shows the solution for a sliced-3D model with optimised CFS-PML parameters with error compared to a 3D reference. This shows that optimisation of PML parameters can lower the error for scattering bodies to be consistently below -40 dB, with only

some later arrivals close to the bed with an error greater -40 dB. Figure 5.11 (e) shows the response and (f) the error for a sliced-3D model with no PML optimisation. Low-frequency noise is prevalent throughout and errors at the bed are significant. (g) and (h) show the response for a 2D model with 2D-to-3D transformation with the Bleistein filter assuming a first break time of 1μs for the bed return (2600 iterations Figure 5.11), and fails to replicate well the amplitudes for any of the scattering or bed returns

5.7 Discussion

The numerical results from the examples above show that the errors caused by near-grazing wave interactions with a bounding PML region can be significantly attenuated through optimisation of the first order CFS-PML parameters. We have suggested relationships between optimal parameters and model parameters to attenuate such low-frequency energy significantly as a function of λ/dx, which can be readily calculated using model parameters and source frequency used.

In practice, the effect of κ in the CFS-PML formulation is a real stretching of the cells within the PML region. Higher values of κ result in increasing cell size within the PML region. As such, κ_{max} is a balance between larger stretch and non-attenuated dispersive effects. For larger stretch coefficients, low frequency energy is more effectively attenuated, although large cell sizes can result in numerical dispersion at the outermost bounds of the PML introducing high frequency noise that the PML is not effective at attenuating.

While there have been significant developments in PML implementations through increasingly complex and higher order stretching functions, this study represents the first numerically-based approach to optimise 1st order CFS-PML parameters for a broad range of low frequency geophysical applications. We have compared our results to values published in the literature (Figure 5.9), although it must be noted that the previous values have been derived

and estimated for different applications, and as such the performance cannot always be expected to match those derived for this application.

We have suggested that our parameter choices can be applied for radio-glaciological survey, but the effects of a wider range of dielectric materials have not been explored. Regions of higher ϵ_r result in increased numerical dispersion in the propagation, resulting in the requirement of a higher resolution model. In such a case, we require improved attenuation of lower $\frac{\lambda}{dx}$ values, shown in Figure 5.6 to result in a higher sensitivity of error on κ_{max}. This may be a limitation of the technique in applications to wider geoscientific applications of sliced-3D FDTD modelling.

Further work in this area could explore the improvements that may be attained through optimisation of higher order CFS-PMLs, or through optimisation of recently developed multi-pole PML (Giannopoulos, 2018) However such approaches will necessarily be more complex due to the higher degrees of freedom implicit in these approaches.

5.8 Conclusions

We have shown through numerical modelling that optimisation of a 1st order CFS-PML can be undertaken to minimise domain size to obtain full 3D polarisation synthetics in the case of strictly 2D geometries. Such an approach is required to reduce the impact of grazing-angle evanescent energy close to the model and PML boundary. For a 5-cell domain size with a 15 cell PML, we can reach a maximum amplitude error of -70 dB (or 0.03%) over the typical range of $\frac{\lambda_c}{dx}$ used for efficient numerical modelling. We have suggested relationships between CFS-PML parameters α, κ and $\frac{\lambda}{dx}$ which demonstrate the suitability of such an approach for wider applications of GPR FDTD modelling where consideration of waveform polarisation is important. These recommendations mean this approach is readily applicable in iterative processing algorithms, as parameters can be automatically estimated using the defined model.

Chapter 6

Discussion

In this chapter, I will review the three thesis aims (TA1-3) as described in Chapter 2, and discuss how the research presented in Chapters 3, 4, and 5 has developed on these original aims. For each chapter, the limitations of the study and future opportunities for development will be discussed, considering how the research contributes to the wider field of radioglaciology. The chapter finishes with a wider discussion on future priorities of the research field.

6.1 Review of thesis aim 1

TA1: ***To develop methods for quantifying the internal structure and refining the approach to bed topography retrieval in polythermal glaciers.***

This aim was motivated by Section 2.3.3, which discussed the approach to estimating englacial radar velocity using multi-offset radar surveys. The shortcomings of such surveys were discussed, with issues arising in both the logistical difficulties hampering extensive acquisition, and geometric assumptions in the CMP method, often violated over temperate ice. Chapter 3 presented an approach to deriving the englacial radar velocity and water content over

a polythermal glacier in Svalbard using common-offset radar. I proposed a reconstruction of bed topography depth by the use of a diffraction focussing-derived velocity field and compared it to the bed topography derived from the commonly-used assumption of constant velocity.

6.1.1 Limitations

Due to limitations with logistics available in the field, the radar data for this study were collected as a standalone dataset, hence validation of the retrieved bed topography using diffraction focussing-derived radar wave velocity was not possible. In an ideal case, validation would be undertaken using a series of boreholes across the glacier, which would allow a ground-truth of retrieved bed topography; however, there is a significant cost associated with such work. A borehole would also have provided opportunities for intercomparison of the water content retrieved from backscatter approaches of Hamran et al. (1996) and Pettersson et al. (2003).

Boreholes with down-borehole video would also give further insight into the nature of internal scatterers, as demonstrated by Fountain et al. (2005). The estimation of water content from englacial radar velocity relies on the use of a correct mixing model. In the study, I used a CRIM relationship, which assumes scattering bodies are spherical and isotropic in nature. Numerous studies have previously used isotropic mixing methods (Murray et al., 2000; Bradford, 2005; Bradford et al., 2009; Brown et al., 2017). In this study, the approach was justified through comparison of the two-way travel time to the bed for survey lines intersecting at 90° angles. Additionally, no clear dipping features which could represent subglacial crevasses or surge-related thrusting were identified in the data, for example as observed in other radar data (Woodward et al., 2003; Fountain et al., 2005). Barrett et al. (2008) and Bradford et al. (2013) inferred englacial water to be held within sub-vertical englacial crevasses close to the bed, with Bradford et al. (2013) using a

mixing model incorporating anisotropic and non-spherical scatterers to derive a modified water content. The upper scattering layer interface is likely to consist of more random orientations of englacial voids as a result of well-rotted ice (Fountain et al., 2005; West et al., 2007). The transition between such macroscale pore spaces and deeper crevassing is not well-defined but is likely to be a function of the stress regime from basal drag dictating propagation of crevasses from the bed, enabling drainage to the bed from the upper temperate ice region. Co-located, multi-polarised data would allow further inference of englacial scatter character (Barrett et al., 2008).

6.1.2 Future Development

The processing flow I developed for Chapter 3 is, in theory, applicable to any low-frequency, common-offset data acquired across temperate and polythermal glaciers. Higher frequency surveys will, in general, result in a more chaotic signal character within temperate ice (Björnsson et al., 1996) and hence are unlikely to produce the coherent diffraction hyperbolas on which this approach depends. Challenges may be encountered where survey platforms are less stable (e.g. using helicopter-mounted GPR, Langhammer et al., 2019) which may result in non-hyperbolic moveout curves as a result of variable platform velocity and two-way travel time, although precise picking of the surface reflection and precise GPS data acquisition should allow for processing to compensate for such variations.

The presence of water within ice exerts a significant softening effect on glacier ice (lowering viscosity), which is accounted for in Glen's relationship in the rate factor (Duval, 1977). Hubbard et al. (2003) demonstrated the importance of understanding the relative contributions of cold and temperate ice for modelling polythermal glaciers, showing significant variations in the long-term evolution of temperate glacier extent as a function of ice viscosity. This approach uses a simplified block model to represent temperate and cold

ice regions, which is the most common approach as it makes use of the uppermost scattering layer (e.g. Schannwell et al., 2014; Sevestre et al., 2015). Diffraction focussing produces a spatially-continuous model of englacial water content, which I show in section 3.5.1 is able to differentiate between cold and temperate regions of ice and may be used for initiation of a polythermal glacier model. Furthermore, mass-conservation approaches are now commonly used for subglacial topography reconstruction (e.g. Farinotti et al., 2017; Fürst et al., 2018). Farinotti et al. (2017) undertook an intercomparison of several implementations to assess the associated accuracy and sources of errors for several approaches, noting however that most models assume a flow rate factor associated with temperate ice and fail to consider the relative contributions of cold and temperate ice. This applies not only to relatively small, High Arctic glaciers as demonstrated in this study but also to more extensive regions of temperate ice, such as the margins of the Greenland Ice Sheet, which often include extensive regions of temperate ice close to the bed (Iken et al., 1993; Funk et al., 1994).

6.2 Review of thesis aim 2

TA2. ***To investigate and develop methods to enable tracking of englacial stratigraphy and structure across polar ice sheets.***

Chapter 4 presented a comparison of previously-published automated algorithms for extracting internal stratigraphy from airborne RES data over Antarctica. I developed a formal mechanism by which automated tracking algorithms can be compared which translates directly to their application in ice-sheet age-depth relationship and englacial layer-dip extraction. Three automated approaches to extracting both the geometry and the dip of internal stratigraphy were implemented and compared to a manually-derived reference

pick on two test datasets. I identify that, while most layer autotracking approaches are generally successful in tracking individual line segments, linking of stratigraphy is a weakness in current implementations which precludes application of such algorithms over regional or ice-sheet scales.

6.2.1 Limitations

The reliable extraction of internal layer geometries using automated approaches on an ice-sheet scale is a challenging prospect. The research presented in Chapter 4 is an approach to quantifying errors and their implications of extracting an ice-sheet wide age-depth relationship over the scale of a radargram, yet does not cover the full extent of complexities encountered in IPR data. There are a range of contributing factors that are likely to result in errors or challenges, including (but not limited to):

1. Dip-induced internal-layer-amplitude degradation, as a result of incoherent stacking (Holschuh et al., 2014); Castelletti et al. (2019) present a method of overcoming this issue by a phase-tracking approach to coherent stacking.
2. Processing artefacts, for example transitions in amplitude where blended products of near-surface and depth-sounding radars are generated, or where ringing in the near-surface due to signal clipping at the surface reflection.
3. Basal freeze-on units, which manifest in a radargram as a non-layered structure close to the bed (Bell et al., 2011), although a degree of automated identification has been developed for these (Goldberg et al., 2020).
4. Anisotropic response of fabric-derived internal layers to survey line orientation (e.g. Ross et al., 2020).

A key consideration not encountered in the study is the spatial picking order, or how tracking progresses through a survey with multiple survey lines,

most likely away from seed points at dated ice-core sites. This is tackled in some seismic approaches through a metric of confidence in the picked horizon (Hoyes and Cheret, 2011); for each location, the subsequent pick is made at the location of maximum confidence in the picks already made. Areas of significant internal layer disruption, associated with fast ice flow or shear margins (Bingham et al., 2015) may provide a form of barrier to tracking, relying on another path to be used to link the full ice sheet. Ashmore et al. (2020) highlighted that the internal layer continuity index may be used as a predictor of picking success; such a confidence metric may be useful in guiding dating strategy in any future efforts and even future data acquisition.

6.2.2 Future developments

This study was motivated by the AntArchitecture project, an action group of the Scientific Committee on Antarctic Research (SCAR) which aims to generate an Antarctica-wide model of internal layer geometry, and hence age-depth structure, through combining the results of multiple Antarctic radar surveys from international collaborators. Much work focusing on the geometry internal stratigraphy has been undertaken using CReSIS (Panton, 2014), PASIN data (Karlsson et al., 2014; Ashmore et al., 2020) UTIG/TUD (Bingham et al., 2007; Cavitte et al., 2016), and the extensive SPRI/NSF/TUD data sources (Siegert et al., 1998), yet systematic integration of layer geometries between surveys has been limited. Given the scale of the project, automated and semi-automated approaches will no doubt contribute to these efforts, and, as discussed in the chapter, improved linking of picked isochrones across discontinuities and between surveys will be a major and necessary step.

Machine learning and probabilistic algorithms present a promising avenue for future internal layer autotracking, yet there has been limited development beyond auto-tracking of the bed return in CReSIS data (Berger et al., 2019). Progress is being made in this area, for example using convolutional neural

networks applied to radar-observed stratigraphy in near-surface layers representing successive snowfall events (Rahnemoonfar et al., 2020), which will likely guide development of future algorithms for deeper ice-sheet internal stratigraphy as explored in this study. It is possible that a combined approach using the image-processing techniques described in this study, combined with machine learning approaches yet to be developed, may provide an optimum solution to the problem.

Radar systems are becoming increasingly high-resolution, with the AWI-CReSIS developed ultra-wideband system operating over a 450 MHz bandwidth (150 - 600 MHz, Hale et al., 2016). Fully exploiting the internal structure revealed in these higher-resolution radargrams, with an increased overall number of resolvable layers, over regional survey scales, will further necessitate automated approaches to internal stratigraphy, although improvements of SNR may reduce the ambiguity of internal layer picking.

Ice-sheet modelling is often limited to geometrical considerations of bed topography, derived from a ice-sheet-scale collection (e.g. BEDMAP2/BedMachine collections Fretwell et al., 2013; Morlighem et al., 2020). Further model parameters such as basal traction or internal rheology required for successful modelling are either derived during an initialisation ('spin-up') stage or through direct use of observations as a model initialisation, which are then held as constant throughout the experiment (Goelzer et al., 2018). Basal traction is often estimated by the fitting of model spin-up to observed surface velocities (Pollard and DeConto, 2012), and short-wavelength lateral variations in ice rheology and basal traction, such as those observed at ice streams, are often poorly represented and do not well-reflect RES observations (e.g. in the Weddell Sea Sector, Jeofry et al., 2020). Systematically exploiting the full potential of isochrones in ice sheets will require developments in model-observation assimilation. While estimations of isochrone geometries from 3D rheology, basal traction, and basal freeze-on anomalies in ice-sheet models have been widely studied to aid interpretation (Hindmarsh et al., 2006; Leysinger Vieli et al.,

2007; Hindmarsh et al., 2009; Wolovick and Creyts, 2016; Leysinger Vieli et al., 2018), the inverse step of quantitative derivation of model parameters from observations has been limited to palaeoaccumulation estimation (Koutnik et al., 2016) and vertical velocity (Eisen, 2008). Future work may look to generate a more complete assimilation of such deep radiostratigraphy to tune ice-sheet model parameters from collections of isochrones, where current progress is limited. Holschuh et al. (2017) presents a development in reconciling data and model by matching layer-dip with a selection of model-derived isochrones to estimate basal traction; extension of such efforts to ice rheology may be possible in the future and aid in ice-sheet model initialisation.

6.3 Review of thesis aim 3

TA3: ***To improve approaches to generating full-polarisation and true-amplitude models from the FDTD techique to aid development in near-surface geophysics and radioglaciology.***

In Chapter 3 I developed a sliced-3D approach to full-waveform, 3D-polarisation modelling using the FDTD algorithm. The ultimate goal of this was to reduce the computational requirements of full-polarisation FDTD modelling, avoiding the need for post-processing of model outputs to obtain correct amplitudes, as would be the case for a 2D implementation of the Yee algorithm. Two examples were presented in the chapter as a demonstration of the approach, using a glaciological and a cross-borehole example.

6.3.1 Limitations

As discussed in the background chapter, the application of FDTD modelling in a glaciological context is limited due to the computational demands of the ap-

proach. Where large-scale models are required for ice-sheet radar studies with planar layers, a more common approach is the use of matrix methods (Fujita et al., 2006). The sliced-3D approach may enable wider uptake of FDTD modelling for glaciology through minimising the computational requirements through minimising cross-line dimension size, although the approach retains the assumption of model cross-line invariance as in a 2D modelling approach, which may not be truly representative of the 3D distribution of scatterers encountered in temperate ice (Barrett et al., 2008). The study was limited to a 1st order implementations of the CFS-PML, which enabled parameters to be derived using a brute-force approach to estimate the error minimum. Higher-order CFS-PMLs would in theory enable attenuation of both evanescent and travelling waves in the PML region. The use of higher-order implementations was discussed and discounted from the study due to cross-terms in the CFS-PML stretch factor, which would introduce a more complex response to the optimisation. Giannopoulos (2018) introduced the concept of the multipole PML (MPML) which aims to attenuate both evanescent and travelling energy while removing the cross-terms in the stretch function by using a summation of stretch factor S rather than a product. The 1st order CFS-PML enabled sufficient attenuation of noise (in general, -70 dB) to enable sliced-3D modelling, yet improvements may be made through optimisation of the MPML in the sliced-3D application.

6.3.2 Future Development

An immediate application of the sliced-3D approach is in cross-borehole and near-surface FWI. Cross-borehole applications currently use a 2D forward model for computational efficiency. Klotzsche et al. (2019) noted that use of 3D-to-2D transformations in the processing of synthetic data results in a quantitative bias in conductivity estimates derived from applications of FWI to borehole problems due to errors of the transformation in complex models

highlighted by Auer et al. (2013). This issue is overcome by Mozaffari et al. (2020) by using what is described as a 2.5D model, in effect a large 3D model with lateral invariance as in the presented sliced-3D approach, using 300 cells in the cross-line orientation to avoid grazing-wave interactions with the PML. This has an associated increase in the computational requirement of 300 times the previously-used 2D approach. By modifying PML parameters, the sliced-3D approach enabled the use of a 35-cell cross-line model size. This approach, therefore, presents an opportunity to improve FWI results while minimising the computational demand of the approach. Cross-borehole techniques have previously been used in radioglaciology as an approach of deriving englacial water content (e.g. Gusmeroli et al., 2010), and future work may look to apply FWI to such settings to further investigate the character and distribution of water, in more detail than can be achieved from surface techniques.

6.4 Future Prospects

Future directions in radioglaciology should look to build on and exploit the numerous recent developments in coherent radar systems, which have enabled the acquisition of swath radar data (Paden et al., 2010; Al-Ibadi et al., 2017) involving larger-scale acquisition of 3D bed topography than currently available using common-offset, ground-based techniques (Holschuh et al., 2020). Such high-resolution bed topography may lessen the uncertainty of basal roughness parameterisations in modern ice-sheet models, which currently incorporate assumptions of fine-scale topography not captured in typical 2D radargrams across the polar ice-sheets (Durand et al., 2011; Bingham et al., 2017). Swath data acquisition will reduce reliance on interpolation routines typically used to in-fill data gaps. Such systems may enable determination of 3D isochrone geometries; such a development would allow retrieval of internal surfaces as opposed to the modern-day internal layers, (e.g. Young et al., 2018).

The development of low-power and phase-sensitive radars operating in ac-

tive and passive time-lapse modes (e.g. ApRES Brennan et al., 2014; Kingslake et al., 2014; Young et al., 2018; Peters et al., 2019), and generation of opportunistic phase-sensitive data (Castelletti et al., 2020) enables precise observations of englacial strain regime through enabling seasonal and long-term monitoring of internal layer deformation. Phase-sensitive systems have additionally enabled polarimetric observations over ice sheets to assess depth-dependant ice-fabric anisotropy (Matsuoka et al., 2012b; Jordan et al., 2020), knowledge of which can be used to constrain ice palaeo-dynamics at specific locations (Brisbourne et al., 2019). The imaging products generated from IPR data will only increase with these opportunities, enabling further tuning of ice-sheet models with improved data assimilation.

The above discussion highlighted that polarimetric data across polythermal glaciers would have improved the ability to determine the nature and orientation of sub- and englacial fractures and voids. Helicopter-mounted systems have been developed for the purposes of improving imaging the bed of temperate glaciers (Langhammer et al., 2019), yet developments for ground-based towed systems is limited. To constrain the orientation of voids, at least 3 orientations of source/receiver pairs may be required (Bradford et al., 2013), hence this approach would likely require development of low-cost rugged antennas to make this approach feasible.

Chapter 7

Conclusions

This thesis set out to develop novel approaches to radar processing and imaging techniques to contribute to the wider understanding of the internal structure of glaciers and ice sheets. The key research findings are as follows:

1. This thesis has for the first time applied a diffraction focussing-based approach to velocity analysis using common-offset GPR data collected on a polythermal glacier. While previous approaches to understanding the englacial radar wave velocity within glaciers generally required the acquisition of logistically challenging and spatially limited multi-offset surveys, the diffraction focussing approach enables estimation of englacial radar velocity, and hence an estimate of internal water content, continuously across the full extent of the common-offset radar survey.
2. Application of the diffraction focusing algorithm to Von Postbreen, a polythermal glacier in Svalbard, reveals that in general, the englacial radar velocities differentiate between cold and temperate regions of ice well and that the velocity within the temperate ice region has significant variations along a centreline profile. Regions of low velocity in the lower ablation zone coincide with surface features which may represent access of water to the glacier interior and bed during the preceding summer melt season.

3. Chapter 4 developed an approach to comparing automated approaches to extracting internal stratigraphy and internal-layer dip from airborne RES data collected over Antarctica. While numerous approaches to automated interpretation have been developed, this is the first attempt to quantify and compare errors in internal layer interpretation, with the goal of quantifying the resultant error when extracting an age-depth relationship across ice sheets. Of the three algorithms tested, the ARESELP procedure (Xiong et al., 2018) was best at retrieving substantial lengths of isochrones, yet can be prone to deviations in dip, and while the Steger algorithm (Ferro and Bruzzone, 2013) shows a greater uncertainty in propagated ages, it shows an improvement in tracking general dip and a lower error in propagated age profile. The chapter makes recommendations on future developments for internal-layer interpretation algorithms, which are likely to exploit machine learning approaches, by improving linking of stratigraphy to enable age-depth relationship propagation over larger survey scales.
4. The final aspect of this thesis developed a sliced-3D approach to FDTD modelling. The goal of this was to enable the generation of 3D polarisation and amplitude-correct synthetic GPR data for strictly 2D geometries by minimising the size of the cross-line model domain. Such an approach required optimisation of perfectly matched layers, for which I investigate and develop a simple frequency-dependent relationship for optimum CFS-PML parameters. The resultant implementation is shown to enable a maximum error of -70 dB for over the typical range of $\frac{\lambda_c}{dx}$ used for efficient numerical modelling. Examples were given to show that this approach is readily applicable in near-surface cross-borehole model applications of full-waveform inversion and may readily be implemented with such algorithms as parameters can be automatically estimated using the defined model.

Bibliography

Anandakrishnan, S., D. D. Blankenship, R. B. Alley, and P. L. Stoffa (1998). "Influence of subglacial geology on the position of a West antarctic ice stream from seismic observations". In: *Nature* 394.6688, pp. 62–65. DOI: 10.1038/27889.

Annan, A. P. and S. R. Jackson (2017). "The WARR machine". In: *2017 9th International Workshop on Advanced Ground Penetrating Radar, IWAGPR 2017 - Proceedings*. Institute of Electrical and Electronics Engineers Inc., pp. 1–4. ISBN: 9781509054848. DOI: 10.1109/IWAGPR.2017.7996106.

Anschütz, H., D. Steinhage, O. Eisen, H. Oerter, M. Horwath, and U. Ruth (2008). "Small-scale spatio-temporal characteristics of accumulation rates in western Dronning Maud Land, Antarctica". In: *Journal of Glaciology* 54.185, pp. 315–323. DOI: 10.3189/002214308784886243.

Arcone, S. A., D. E. Lawson, and A. J. Delaney (1995). "Short-pulse radar wavelet recovery and resolution of dielectric contrasts within englacial and basal ice of Matanuska Glacier, Alaska, USA". In: *Journal of Glaciology* 41.137, pp. 68–86. DOI: 10.1017/S0022143000017779.

Arcone, S. A., V. B. Spikes, and G. S. Hamilton (2005). "Stratigraphic variation within polar firn caused by differential accumulation and ice flow: Interpretation of a 400 MHz short-pulse radar profile from West Antarctica". In: *Journal of Glaciology* 51.174, pp. 407–422. DOI: 10.3189/172756505781829151.

Arnold, E., C. Leuschen, F. Rodriguez-Morales, J. Li, J. Paden, R. Hale, et al. (2019). "CReSIS airborne radars and platforms for ice and snow sounding". In: *Annals of Glaciology*, pp. 1–10. DOI: 10.1017/aog.2019.37.

Ashmore, D. W., R. G. Bingham, R. C. A. Hindmarsh, H. F. J. Corr, and I. R. Joughin (2014). "The relationship between sticky spots and radar reflectivity beneath an active West Antarctic ice stream". In: *Annals of Glaciology* 55.67, pp. 29–38. DOI: 10.3189/2014AoG67A052.

Ashmore, D. W., R. G. Bingham, N. Ross, M. J. Siegert, T. A. Jordan, and D. W. F. Mair (2020). "Englacial Architecture and Age-Depth Constraints Across the West Antarctic Ice Sheet". In: *Geophysical Research Letters* 47.6. DOI: 10.1029/2019GL086663.

Auer, L., A. M. Nuber, S. A. Greenhalgh, H. Maurer, and S. Marelli (2013). "A critical appraisal of asymptotic 3D-to-2D data transformation in full-waveform seismic crosshole tomography". In: *GEOPHYSICS* 78.6, R235–R247. DOI: 10.1190/geo2012-0382.1.

Augustin, L., C. Barbante, P. R. Barnes, J. M. Barnola, M. Bigler, E. Castellano, et al. (2004). "Eight glacial cycles from an Antarctic ice core". In: *Nature* 429.6992, pp. 623–628. DOI: 10.1038/nature02599.

Baelum, K. and D. I. Benn (2011). "Thermal structure and drainage system of a small valley glacier (Tellbreen, Svalbard), investigated by ground penetrating radar". In: *Cryosphere* 5.1, pp. 139–149. DOI: 10.5194/tc-5-139-2011.

Bailey, J., S. Evans, and G. d. Q. Robin (1964). "Radio Echo Sounding of Polar Ice Sheets". In: *Nature* 204.4957, pp. 420–421. DOI: 10.1038/204420a0.

Baker, G. S. (1998). "Applying AVO analysis to GPR data". In: *Geophysical Research Letters* 25.3, pp. 397–400. DOI: 10.1029/97GL03773.

Baldwin, D. J., J. L. Bamber, A. J. Payne, and R. L. Layberry (2003). "Using internal layers from the Greenland ice sheet, identified from radio-echo sounding data, with numerical models". In: *Annals of Glaciology* 37, pp. 325–330. DOI: 10.3189/172756403781815438.

Bamber, J. L., J. A. Griggs, R. T. W. L. Hurkmans, J. A. Dowdeswell, S. P. Gogineni, I. Howat, et al. (2013). "A new bed elevation dataset for Greenland". In: *The Cryosphere* 7, pp. 499–510. DOI: 10.5194/tc-7-499-2013.

Bamber, J. L. (1987). "Internal Reflecting Horizons in Spitsbergen Glaciers". In: *Annals of Glaciology* 9, pp. 5–10. DOI: 10.3189/S0260305500200682.

Barrett, B. E., T. Murray, and R. Clark (2007). "Errors in Radar CMP Velocity Estimates Due to Survey Geometry, and Their Implication for Ice Water Content Estimation". In: *Journal of Environmental & Engineering Geophysics* 12.1, pp. 101–111. DOI: 10.2113/JEEG12.1.101.

Barrett, B. E., T. Murray, R. A. Clark, and K. Matsuoka (2008). "Distribution and character of water in a surge-type glacier revealed by multifrequency and multipolarization ground-penetrating radar". In: *Journal of Geophysical Research* 113.F4, F04011. DOI: 10.1029/2007JF000972.

Behrendt, J. C., D. D. Blankenship, C. A. Finn, R. E. Bell, R. E. Sweeney, S. M. Hodge, et al. (1994). "CASERTZ aeromagnetic data reveal late Cenozoic flood basalts(?) in the West Antarctic rift system". In: *Geology* 22.6, pp. 527–530. DOI: 10.1130/0091-7613(1994)022<0527:CADRLC>2.3.CO;2.

Bell, R. E., D. D. Blankenship, C. A. Finn, D. L. Morse, T. A. Scambos, J. M. Brozena, et al. (1998). "Influence of subglacial geology on the onset of a West Antarctic ice stream from aerogeophysical observations". In: *Nature* 394.6688, pp. 58–62. DOI: 10.1038/27883.

Bell, R. E., F. Ferraccioli, T. T. Creyts, D. Braaten, H. Corr, I. Das, et al. (2011). "Widespread Persistent Thickening of the East Antarctic Ice Sheet by Freezing from the Base". In: *Science* 331.6024, pp. 1592–1595. DOI: 10.1126/science.1200109.

Benjumea, B., Y. Y. Macheret, F. J. Navarro, and T. Teixido (2003). "Estimation of water content in a temperate glacier from radar and seismic sounding data". In: *Annals of Glaciology* 37, pp. 317–324. DOI: 10.3189/172756403781815924.

Berenger, J.-P. (1999). "Evanescent waves in PML's: origin of the numerical reflection in wave-structure interaction problems". In: *IEEE Transactions on Antennas and Propagation* 47.10, pp. 1497–1503. DOI: 10.1109/8.805891.

Berenger, J.-P. (2002). "Application of the CFS PML to the absorption of evanescent waves in waveguides". In: *IEEE Microwave and Wireless Components Letters* 12.6, pp. 218–220. DOI: 10.1109/LMWC.2002.1010000.

Berger, V., M. Xu, M. Al-Ibadi, S. Chu, D. Crandall, J. Paden, et al. (2019). "Automated Ice-Bottom Tracking of 2D and 3D Ice Radar Imagery Using Viterbi and

TRW-S". In: *IEEE Journal of Selected Topics in Applied Earth Observations and Remote Sensing* 12.9, pp. 3272–3285. DOI: 10.1109/JSTARS.2019.2930920.

Bindschadler, R. (1983). "The Importance of Pressurized Subglacial Water in Separation and Sliding at the Glacier Bed". In: *Journal of Glaciology* 29.101, pp. 3–19. DOI: 10.3189/S0022143000005104.

Bingham, R. G., A. L. Hubbard, P. W. Nienow, and M. J. Sharp (2008). "An investigation into the mechanisms controlling seasonal speedup events at a High Arctic glacier". In: *Journal of Geophysical Research* 113.F2, F02006. DOI: 10.1029/2007JF000832.

Bingham, R. G., D. M. Rippin, N. B. Karlsson, H. F. J. Corr, F. Ferraccioli, T. A. Jordan, et al. (2015). "Ice-flow structure and ice dynamic changes in the Weddell Sea sector of West Antarctica from radar-imaged internal layering". In: *Journal of Geophysical Research: Earth Surface* 120.4, pp. 655–670. DOI: 10.1002/2014JF003291.

Bingham, R. G., M. J. Siegert, D. A. Young, and D. D. Blankenship (2007). "Organized flow from the South Pole to the Filchner-Ronne ice shelf: An assessment of balance velocities in interior East Antarctica using radio echo sounding data". In: *Journal of Geophysical Research: Earth Surface* 112.3. DOI: 10.1029/2006JF000556.

Bingham, R. G., D. G. Vaughan, E. C. King, D. Davies, S. L. Cornford, A. M. Smith, et al. (2017). "Diverse landscapes beneath Pine Island Glacier influence ice flow". In: *Nature Communications* 8.1, p. 1618. DOI: 10.1038/s41467-017-01597-y.

Björnsson, H., Y. Gjessing, S.-E. Hamran, J. O. Hagen, O. LiestøL, F. Pálsson, et al. (1996). "The thermal regime of sub-polar glaciers mapped by multi-frequency radio-echo sounding". In: *Journal of Glaciology* 42.140, pp. 23–32. DOI: 10.3189/S0022143000030495.

Blankenship, D. D., C. R. Bentley, S. T. Rooney, and R. B. Alley (1986). "Seismic measurements reveal a saturated porous layer beneath an active Antarctic ice stream". In: *Nature* 322.6074, pp. 54–57. DOI: 10.1038/322054a0.

Blankenship, D. D., D. L. Morse, C. A. Finn, R. E. Bell, M. E. Peters, S. D. Kempf, et al. (2001). "Geologic Controls on the Initiation of Rapid Basal Motion for West Antarctic Ice Streams: A Geophysical Perspective Including New Airborne Radar Sounding and Laser Altimetry Results". In: *The West Antarctic Ice Sheet: Behavior and Environment*. Ed. by R. B. Alley and R. A. Bindschadler. American Geophysical Union (AGU), pp. 105–121. DOI: 10.1029/AR077p0105.

Blankenship, D. D., R. E. Bell, S. M. Hodge, J. M. Brozena, J. C. Behrendt, and C. A. Finn (1993). "Active volcanism beneath the West Antarctic ice sheet and implications for ice-sheet stability". In: *Nature* 361.6412, pp. 526–529. DOI: 10.1038/361526a0.

Blatter, H. and K. Hutter (1991). "Polythermal conditions in arctic glaciers". In: *Journal of Glaciology* 37.126, pp. 261–269. DOI: 10.3189/s0022143000007279.

Bleistein, N. (1986). "Two-and-one-half dimensional in-plane wave propagation". In: *Geophysical Prospecting* 34.5, pp. 686–703. DOI: 10.1111/j.1365-2478.1986.tb00488.x.

Bogorodskiy, V., G. Trepov, and B. Federov (1970). "On measuring dielectric properties of glaciers in the field". In: *Proceedings of the intenational meeting on*

radioglaciology, Lyngby, May 1970. Ed. by P. Gudmandsen. Technical University of Denmark, Laboratory of Electromagnetic Theory, pp. 20–31.

Booth, A., R. Clark, and T. Murray (2008a). "Waveform Corrections to Improve the Accuracy of GPR Velocity Analyses". In: *Processing* 1.

Booth, A. D., N. T. Linford, R. A. Clark, and T. Murray (2008b). "Three-dimensional, multi-offset ground-penetrating radar imaging of archaeological targets". In: *Archaeological Prospection* 15.2, pp. 93–112. DOI: 10.1002/arp.327.

Booth, A. D., R. Clark, and T. Murray (2010). "Semblance response to a ground-penetrating radar wavelet and resulting errors in velocity analysis". In: *Near Surface Geophysics* 8.3, pp. 235–246. DOI: 10.3997/1873-0604.2010008.

Booth, A. D., R. A. Clark, and T. Murray (2011). "Influences on the resolution of GPR velocity analyses and a Monte Carlo simulation for establishing velocity precision". In: *Near Surface Geophysics* 9.1802, pp. 399–411. DOI: 10.3997/1873-0604.2011019.

Booth, A. D. and J. K. Pringle (2016). "Semblance analysis to assess GPR data from a five-year forensic study of simulated clandestine graves". In: *Journal of Applied Geophysics* 125, pp. 37–44. DOI: 10.1016/j.jappgeo.2015.11.016.

Bradford, J. H. (2005). "Wave field migration as a tool for estimating spatially continuous radar velocity and water content in glaciers". In: *Geophysical Research Letters* 32.8, p. L08502. DOI: 10.1029/2004GL021770.

Bradford, J. H., J. Nichols, T. D. Mikesell, and J. T. Harper (2009). "Continuous profiles of electromagnetic wave velocity and water content in glaciers: an example from Bench Glacier, Alaska, USA". In: *Annals of Glaciology* 50.51, pp. 1–9. DOI: 10.3189/172756409789097540.

Bradford, J. H., J. Nichols, J. T. Harper, and T. Meierbachtol (2013). "Compressional and EM wave velocity anisotropy in a temperate glacier due to basal crevasses, and implications for water content estimation". In: *Annals of Glaciology* 54.64, pp. 168–178. DOI: 10.3189/2013AoG64A206.

Brennan, P. V., K. Nicholls, L. B. Lok, and H. Corr (2014). "Phase-sensitive FMCW radar system for high-precision Antarctic ice shelf profile monitoring". In: *IET Radar, Sonar & Navigation* 8.7, pp. 776–786. DOI: 10.1049/iet-rsn.2013.0053.

Brisbourne, A. M., C. Martín, A. M. Smith, A. F. Baird, J. M. Kendall, and J. Kingslake (2019). "Constraining Recent Ice Flow History at Korff Ice Rise, West Antarctica, Using Radar and Seismic Measurements of Ice Fabric". In: *Journal of Geophysical Research: Earth Surface* 124.1, pp. 175–194. DOI: 10.1029/2018JF004776.

Brown, J., J. Harper, and N. Humphrey (2017). "Liquid water content in ice estimated through a full-depth ground radar profile and borehole measurements in western Greenland". In: *The Cryosphere* 11.1, pp. 669–679. DOI: 10.5194/tc-11-669-2017.

Busch, S., J. van der Kruk, J. Bikowski, and H. Vereecken (2012). "Quantitative conductivity and permittivity estimation using full-waveform inversion of on-ground GPR data". In: *Geophysics* 77.6, H79–H91. DOI: 10.1190/geo2012-0045.1.

Carter, S. P., D. D. Blankenship, D. A. Young, and J. W. Holt (2009). "Using radar-sounding data to identify the distribution and sources of subglacial water: appli-

cation to Dome C, East Antarctica". In: *Journal of Glaciology* 55.194, pp. 1025–1040. DOI: 10.3189/002214309790794931.

Castelletti, D., D. M. Schroeder, E. Mantelli, and A. Hilger (2019). "Layer optimized SAR processing and slope estimation in radar sounder data". In: *Journal of Glaciology*, pp. 1–6. DOI: 10.1017/jog.2019.72.

Castelletti, D., D. M. Schroeder, T. M. Jordan, and D. Young (2020). "Permanent Scatterers in Repeat-Pass Airborne VHF Radar Sounder for Layer-Velocity Estimation". In: *IEEE Geoscience and Remote Sensing Letters*, pp. 1–5. DOI: 10.1109/LGRS.2020.3007514.

Catania, G. A., H. Conway, C. F. Raymond, and T. A. Scambos (2006). "Evidence for floatation or near floatation in the mouth of Kamb Ice Stream, West Antarctica, prior to stagnation". In: *Journal of Geophysical Research* 111.F1, F01005. DOI: 10.1029/2005JF000355.

Catania, G. A., T. A. Neumann, and S. F. Price (2008). "Characterizing englacial drainage in the ablation zone of the Greenland ice sheet". In: *Journal of Glaciology* 54.187, pp. 567–578. DOI: 10.3189/002214308786570854.

Cavitte, M. G. P., F. Parrenin, C. Ritz, D. A. Young, B. Van Liefferinge, D. D. Blankenship, et al. (2018). "Accumulation patterns around Dome C, East Antarctica, in the last 73 kyr". In: *The Cryosphere* 12.4, pp. 1401–1414. DOI: 10.5194/tc-12-1401-2018.

Cavitte, M. G. P., D. D. Blankenship, D. A. Young, D. M. Schroeder, F. Parrenin, E. Lemeur, et al. (2016). "Deep radiostratigraphy of the East Antarctic plateau: connecting the Dome C and Vostok ice core sites". In: *Journal of Glaciology* 62.232, pp. 323–334. DOI: 10.1017/jog.2016.11.

Chu, W., D. M. Schroeder, and M. R. Siegfried (2018). "Retrieval of Englacial Firn Aquifer Thickness From Ice-Penetrating Radar Sounding in Southeastern Greenland". In: *Geophysical Research Letters* 45.21, pp. 770–11. DOI: 10.1029/2018GL079751.

Church, G. J., A. Bauder, M. Grab, S. Hellmann, and H. Maurer (2018). "High-resolution helicopter-borne ground penetrating radar survey to determine glacier base topography and the outlook of a proglacial lake". In: *2018 17th International Conference on Ground Penetrating Radar (GPR)*. IEEE, pp. 1–4. ISBN: 978-1-5386-5777-5. DOI: 10.1109/ICGPR.2018.8441598.

Copland, L. and M. Sharp (2001). "Mapping thermal and hydrological conditions beneath a polythermal glacier with radio-echo sounding". In: *Journal of Glaciology* 47.157, pp. 232–242. DOI: 10.3189/172756501781832377.

Copland, L., M. J. Sharp, P. Nienow, and R. G. Bingham (2003). "The distribution of basal motion beneath a High Arctic polythermal glacier". In: *Journal of Glaciology* 49.166, pp. 407–414. URL: https://www.geos.ed.ac.uk/homes/rbingha2/03_2003_Copland.pdf.

CReSIS (2016). *CReSIS Radar Depth Sounder Data*. Lawrence, Kansas, USA. URL: http://data.cresis.ku.edu/..

Cuffey, K. and W. Paterson (2010). *The physics of glaciers*. Fourth. ISBN: 9780123694614.

Dabov, K., A. Foi, V. Katkovnik, and K. Egiazarian (2007). "Image denoising by sparse 3-D transform-domain collaborative filtering". In: *IEEE Transactions on Image Processing* 16.8, pp. 2080–2095. DOI: 10.1109/TIP.2007.901238.

Daniels, J. J., L. Wielopolski, S. Radzevicius, and J. Bookshar (2003). "3D GPR Polarization Analysis for Imaging Complex Objects". In: *Symposium on the Application of Geophysics to Engineering and Environmental Problems 2003*. Environment and Engineering Geophysical Society, pp. 585–597. DOI: 10.4133/1.2923205.

De Geer, G. (1910). "A geological excursion to central Spitzbergen". In: *XIe Congrès Géologique International, Stockholm, 1910 guide de l'excursion au Spitzberg*. Stockholm: Norstedt.

De Vries, D. and A. J. Berkhout (1984). "Velocity analysis based on minimum entropy". In: *Geophysics* 49.12, pp. 2132–2142. DOI: 10.1190/1.1441629.

Delf, R., A. Giannopoulos, R. G. Bingham, N. R. Hulton, and A. Curtis (2017). "A Sliced-3D FDTD approach as an alternative to 2D Ground Penetrating Radar modelling". In: *2017 9th International Workshop on Advanced Ground Penetrating Radar, IWAGPR 2017 - Proceedings*. IEEE, pp. 1–5. ISBN: 9781509054848. DOI: 10.1109/IWAGPR.2017.7996038.

Deregowski, S. M. and S. M. Brown (1983). "A theory of acoustic diffractors applied to 2-D models". In: *Geophysical Prospecting* 31.2, pp. 293–333. DOI: 10.1111/j.1365-2478.1983.tb01055.x.

Dix, C. (1955). "Seismic Velocities from Surface Measurements". In: *Geophysics* 20.1, pp. 68–86. DOI: 10.1190/1.1438126.

Dou, Q., L. Wei, D. R. Magee, and A. G. Cohn (2017). "Real-Time Hyperbola Recognition and Fitting in GPR Data". In: *IEEE Transactions on Geoscience and Remote Sensing* 55.1, pp. 51–62. DOI: 10.1109/TGRS.2016.2592679.

Dowdeswell, J. A., D. Drewry, O. Liestøl, and O. Orheim (1984a). "Radio Echo-Sounding of Spitsbergen Glaciers: Problems in the Interpretation of Layer and Bottom Returns". In: *Journal of Glaciology* 30.104, pp. 16–21. DOI: 10.1017/S0022143000008431.

Dowdeswell, J., D. Drewry, O. Liestøl, and O. Orheim (1984b). "Airbourne Radio Echo Sounding of Sub-Polar Glaciers in Spitsbergen". In: *Norsk Polarinstitutt Skrifter*. Oslo: Norsk Polarinstitutt.

Dowdeswell, J. A., G. S. Hamilton, and J. O. Hagen (1991). "The duration of the active phase on surge-type glaciers: contrasts between Svalbard and other regions". In: *Journal of Glaciology* 37.127, pp. 388–400. DOI: 10.3189/S0022143000005827.

Drewry, D. J., O. Liestøl, C. S. Neal, O. Orheim, and B. Wold (1980). "Airborne radio echo sounding of glaciers in Svalbard". In: *Polar Record* 20.126, p. 261. DOI: 10.1017/S0032247400003405.

Drewry, D. J. and O. Liestøl (1985). "Glaciological investigations of surging ice caps in Nordaustlandet, Svalbard, 1983". In: *Polar Record* 22.139, p. 359. DOI: 10.1017/S0032247400005611.

Drewry, D., S. Jordan, and E. Jankowski (1982). "Measured Properties of the Antarctic Ice Sheet: Surface Configuration, Ice Thickness, Volume and Bedrock Characteristics". In: *Annals of Glaciology* 3, pp. 83–91. DOI: 10.1017/S0260305500002573.

Drewry, D. (1983). *Antarctica, glaciological and geophysical folio*. Cambridge, United Kingdom: University of Cambridge, Scott Polar Research Institute. URL: https

://scholar.google.co.uk/scholar?cluster=13537211287156198640&hl=en&as_sdt=2005&sciodt=0,5.

Drossaert, F. H. and A. Giannopoulos (2007). "A nonsplit complex frequency-shifted PML based on recursive integration for FDTD modeling of elastic waves". In: *GEOPHYSICS* 72.2, T9–T17. DOI: 10.1190/1.2424888.

Durand, G., O. Gagliardini, L. Favier, T. Zwinger, and E. Le Meur (2011). "Impact of bedrock description on modeling ice sheet dynamics". In: DOI: 10.1029/2011GL048892.

Duval, P. (1977). "The role of the water content on the creep rate of polycrystalline ice". In: *IAHS Publ* 118, pp. 29–33. URL: http://hydrologie.org/redbooks/a118/iahs_118_0029.pdf.

Eisen, O., I. Hamann, S. Kipfstuhl, D. Steinhage, and F. Wilhelms (2007). "Direct evidence for continuous radar reflector originating from changes in crystal-orientation fabric". In: *The Cryosphere* 1.1, pp. 1–10. DOI: 10.5194/tc-1-1-2007.

Eisen, O., F. Wilhelms, U. Nixdorf, and H. Miller (2003). "Revealing the nature of radar reflections in ice: DEP-based FDTD forward modeling". In: *Geophysical Research Letters* 30.5, n/a–n/a. DOI: 10.1029/2002GL016403.

Eisen, O., M. Frezzotti, C. Genthon, E. Isaksson, O. Magand, M. R. Van Den Broeke, et al. (2008). "Ground-based measurements of spatial and temporal variability of snow accumulation in East Antarctica". In: *Reviews of Geophysics* 46.2. DOI: 10.1029/2006RG000218.

Eisen, O. (2008). "Inference of velocity pattern from isochronous layers in firn, using an inverse method". In: *Journal of Glaciology* 54.187, pp. 613–630. DOI: 10.3189/002214308786570818.

Esmersoy, C. and M. Oristaglio (1988). "Reverse-time wave-field extrapolation, imaging, and inversion". In: *GEOPHYSICS* 53.7, pp. 920–931. DOI: 10.1190/1.1442529.

Evans, S. (1963). "Radio techniques for the measurement of ice thickness". In: *Polar Record* 11.73, p. 406. DOI: 10.1017/S0032247400053523.

Fahnestock, M., W. Abdalati, S. Luo, and S. Gogineni (2001). "Internal layer tracing and age-depth-accumulation relationships for the northern Greenland ice sheet". In: *Journal of Geophysical Research: Atmospheres* 106.D24, pp. 33789–33797. DOI: 10.1029/2001JD900200.

Farinotti, D., D. J. Brinkerhoff, G. K. C. Clarke, J. J. Fürst, H. Frey, P. Gantayat, et al. (2017). "How accurate are estimates of glacier ice thickness? Results from ITMIX, the Ice Thickness Models Intercomparison eXperiment". In: *The Cryosphere* 11.2, pp. 949–970. DOI: 10.5194/tc-11-949-2017.

Farnsworth, W. R., Ó. Ingólfsson, M. Retelle, and A. Schomacker (2016). "Over 400 previously undocumented Svalbard surge-type glaciers identified". In: *Geomorphology* 264, pp. 52–60. DOI: 10.1016/J.GEOMORPH.2016.03.025.

Feng, H., W. Zhang, J. Zhang, and X. Chen (2017). "Importance of double-pole CFS-PML for broadband seismic wave simulation and optimal parameters selection". In: *Geophysical Journal International*. DOI: 10.1093/gji/ggx070.

Ferro, A. and L. Bruzzone (2013). "Automatic Extraction and Analysis of Ice Layering in Radar Sounder Data". In: *IEEE Transactions on Geoscience and Remote Sensing* 51.3, pp. 1622–1634. DOI: 10.1109/TGRS.2012.2206078.

Fisher, E., G. A. McMechan, and A. P. Annan (1992a). "Acquisition and processing of wide-aperture ground-penetrating radar data". In: *GEOPHYSICS* 57.3, pp. 495–504. DOI: 10.1190/1.1443265.

Fisher, E., G. A. McMechan, A. P. Annan, and S. W. Cosway (1992b). "Examples of reverse-time migration of single-channel, ground-penetrating radar profiles". In: *GEOPHYSICS* 57.4, pp. 577–586. DOI: 10.1190/1.1443271.

Flink, A. E., R. Noormets, N. Kirchner, D. I. Benn, A. Luckman, and H. Lovell (2015). "The evolution of a submarine landform record following recent and multiple surges of Tunabreen glacier, Svalbard". In: *Quaternary Science Reviews* 108, pp. 37–50. DOI: 10.1016/J.QUASCIREV.2014.11.006.

Fomel, S. (2002). "Applications of plane-wave destruction filters". In: *GEOPHYSICS* 67.6, pp. 1946–1960. DOI: 10.1190/1.1527095.

Fomel, S. (2003). "Time-migration velocity analysis by velocity continuation". In: *Geophysics* 68.5, pp. 1662–1672. DOI: 10.1190/1.1620640.

Fomel, S., E. Landa, and M. T. Taner (2007). "Poststack velocity analysis by separation and imaging of seismic diffractions". In: *Geophysics* 72.6, U89–U94. DOI: 10.1190/1.2781533.

Forieri, A., L. Zuccoli, A. Bini, A. Zirizzotti, F. Remy, and I. E. Tabacco (2004). "New bedrock map of Dome C, Antarctica, and morphostructural interpretation of the area". In: *Annals of Glaciology* 39, pp. 321–325. DOI: 10.3189/172756404781814456.

Forster, R. R., J. E. Box, M. R. van den Broeke, C. Miège, E. W. Burgess, J. H. van Angelen, et al. (2014). "Extensive liquid meltwater storage in firn within the Greenland ice sheet". In: *Nature Geoscience* 7.2, pp. 95–98. DOI: 10.1038/ngeo2043.

Forte, E., M. Dossi, M. Pipan, and R. R. Colucci (2014). "Velocity analysis from common offset GPR data inversion: theory and application to synthetic and real data". In: *Geophysical Journal International* 197.3, pp. 1471–1483. DOI: 10.1093/gji/ggu103.

Forte, E. and M. Pipan (2017). "Review of multi-offset GPR applications: Data acquisition, processing and analysis". In: *Signal Processing* 132, pp. 210–220. DOI: 10.1016/J.SIGPRO.2016.04.011.

Foss, F. J., N. E. Putzig, B. A. Campbell, and R. J. Phillips (2017). "3D imaging of Mars' polar ice caps using orbital radar data". In: *The Leading Edge* 36.1, pp. 43–57. DOI: 10.1190/tle36010043.1.

Fountain, A. G., R. W. Jacobel, R. Schlichting, and P. Jansson (2005). "Fractures as the main pathways of water flow in temperate glaciers". In: *Nature* 433.7026, pp. 618–621. DOI: 10.1038/nature03296.

Freire, S. L. M. and T. J. Ulrych (1988). "Application of singular value decomposition to vertical seismic profiling". In: *Geophysics* 53.6, pp. 778–785. DOI: 10.1190/1.1442513.

Fretwell, P., H. D. Pritchard, D. G. Vaughan, J. L. Bamber, N. E. Barrand, R. Bell, et al. (2013). "Bedmap2: Improved ice bed, surface and thickness datasets for Antarctica". In: *Cryosphere* 7.1, pp. 375–393. DOI: 10.5194/tc-7-375-2013.

Frezzotti, M. (2002). "Snow megadunes in Antarctica: Sedimentary structure and genesis". In: *Journal of Geophysical Research* 107.D18, p. 4344. DOI: 10.1029/2001JD000673.

Frezzotti, M., M. Pourchet, O. Flora, S. Gandolfi, M. Gay, S. Urbini, et al. (2005). "Spatial and temporal variability of snow accumulation in East Antarctica from traverse data". In: *Journal of Glaciology* 51.172, pp. 113–124. DOI: 10.3189/172756505781829502.

Fudge, T., N. F. Humphrey, J. T. Harper, and W. Tad Pfeffer (2008). "Diurnal fluctuations in borehole water levels: configuration of the drainage system beneath Bench Glacier, Alaska, USA". In: *Journal of Glaciology* 54.185, pp. 297–306. DOI: 10.3189/002214308784886072.

Fujita, S. and S. Mae (1994). "Causes and nature of ice-sheet radio-echo internal reflections estimated from the dielectric properties of ice". In: *Annals of Glaciology* 20, pp. 80–86. DOI: 10.3189/172756494794587311.

Fujita, S., H. Maeno, and K. Matsuoka (2006). "Radio-wave depolarization and scattering within ice sheets: A matrix-based model to link radar and ice-core measurements and its application". In: *Journal of Glaciology* 52.178, pp. 407–424. DOI: 10.3189/172756506781828548.

Funk, M., K. Echelmeyer, and A. Iken (1994). "Mechanisms of fast flow in Jakobshavns Isbræ, West Greenland: Part II. Modeling of englacial temperatures". In: *Journal of Glaciology* 40.136, pp. 569–585. DOI: 10.3189/S0022143000012466.

Fürst, J. J., F. Navarro, F. Gillet-Chaulet, M. Huss, G. Moholdt, X. Fettweis, et al. (2018). "The Ice-Free Topography of Svalbard". In: *Geophysical Research Letters* 45.21, pp. 760–11. DOI: 10.1029/2018GL079734.

Gades, A. M., C. F. Raymond, H. Conway, and R. W. Jacobel (2000). "Bed properties of Siple Dome and adjacent ice streams, West Antarctica, inferred from radio-echo sounding measurements". In: *Journal of Glaciology* 46.152, pp. 88–94. DOI: 10.3189/172756500781833467.

Gamba, P. and S. Lossani (2000). "Neural detection of pipe signatures in ground penetrating radar images". In: *IEEE Transactions on Geoscience and Remote Sensing* 38.2, pp. 790–797. DOI: 10.1109/36.842008.

Gasson, E., R. DeConto, and D. Pollard (2015). "Antarctic bedrock topography uncertainty and ice sheet stability". In: *Geophysical Research Letters* 42.13, pp. 5372–5377. DOI: 10.1002/2015GL064322.

Gedney, S. (1996). "An anisotropic perfectly matched layer-absorbing medium for the truncation of FDTD lattices". In: *IEEE Transactions on Antennas and Propagation* 44.12, pp. 1630–1639. DOI: 10.1109/8.546249.

Gedney, S. D. and B. Zhao (2010). "An Auxiliary Differential Equation Formulation for the Complex-Frequency Shifted PML". In: *IEEE Transactions on Antennas and Propagation* 58.3, pp. 838–847. DOI: 10.1109/TAP.2009.2037765.

Giannakis, I., A. Giannopoulos, and C. Warren (2019). "A Machine Learning-Based Fast-Forward Solver for Ground Penetrating Radar With Application to Full-Waveform Inversion". In: *IEEE Transactions on Geoscience and Remote Sensing* 7, pp. 4417–4426. DOI: 10.1109/tgrs.2019.2891206.

Giannopoulos, A. (1998). "The investigation of transmission-line matrix and finite-difference time-domain methods for the forward problem of ground probing radar." PhD thesis. University of York.

Giannopoulos, A. (2008). "An Improved New Implementation of Complex Frequency Shifted PML for the FDTD Method". In: *IEEE Transactions on Antennas and Propagation* 56.9, pp. 2995–3000. DOI: 10.1109/TAP.2008.928789.

Giannopoulos, A. (2012). "Unsplit Implementation of Higher Order PMLs". In: *IEEE Transactions on Antennas and Propagation* 60.3, pp. 1479–1485. DOI: 10.1109/TAP.2011.2180344.

Giannopoulos, A. (2018). "Multipole Perfectly Matched Layer for Finite-Difference Time-Domain Electromagnetic Modeling". In: *IEEE Transactions on Antennas and Propagation* 66.6, pp. 2987–2995. DOI: 10.1109/TAP.2018.2823864.

Giordano, S. (2005). "Order and disorder in heterogeneous material microstructure: Electric and elastic characterisation of dispersions of pseudo-oriented spheroids". In: *International Journal of Engineering Science* 43.13-14, pp. 1033–1058. DOI: 10.1016/j.ijengsci.2005.06.002.

Glen, J. W. (1955). "The creep of polycrystalline ice". In: *Proceedings of the Royal Society of London. Series A. Mathematical and Physical Sciences* 228.1175, pp. 519–538. DOI: 10.1098/rspa.1955.0066.

Glen, J. W. and J. G. Paren (1975). "The Electrical Properties of Snow and Ice". In: *Journal of Glaciology* 15.73, pp. 15–38. DOI: 10.1017/S0022143000034249.

Goelzer, H., S. Nowicki, T. Edwards, M. Beckley, A. Abe-Ouchi, A. Aschwanden, et al. (2018). "Design and results of the ice sheet model initialisation experiments initMIP-Greenland: an ISMIP6 intercomparison". In: *The Cryosphere* 12.4, pp. 1433–1460. DOI: 10.5194/tc-12-1433-2018.

Goff, J. A., E. M. Powell, D. A. Young, and D. D. Blankenship (2014). "Conditional simulation of Thwaites Glacier (Antarctica) bed topography for flow models: Incorporating inhomogeneous statistics and channelized morphology". In: *Journal of Glaciology* 60.222, pp. 635–646. DOI: 10.3189/2014JoG13J200.

Gogineni, S., D. Tammana, D. Braaten, C. Leuschen, T. Akins, J. Legarsky, et al. (2001). "Coherent radar ice thickness measurements over the Greenland ice sheet". In: *Journal of Geophysical Research: Atmospheres* 106.D24, pp. 33761–33772. DOI: 10.1029/2001JD900183.

Goldberg, M. L., D. M. Schroeder, D. Castelletti, E. Mantelli, N. Ross, and M. J. Siegert (2020). "Automated detection and characterization of Antarctic basal units using radar sounding data: demonstration in Institute Ice Stream, West Antarctica". In: *Annals of Glaciology* 61.81, pp. 242–248. DOI: 10.1017/aog.2020.27.

Golledge, N. R., E. D. Keller, N. Gomez, K. A. Naughten, J. Bernales, L. D. Trusel, et al. (2019). "Global environmental consequences of twenty-first-century ice-sheet melt". In: *Nature* 566.7742, pp. 65–72. DOI: 10.1038/s41586-019-0889-9.

Grab, M., A. Bauder, F. Ammann, L. Langhammer, S. Hellmann, G. J. Church, et al. (2018). "Ice volume estimates of Swiss glaciers using helicopter-borne GPR - An example from the Glacier de la Plaine Morte". In: *2018 17th International Conference on Ground Penetrating Radar, GPR 2018*. Institute of Electrical and Electronics Engineers Inc. ISBN: 9781538657775. DOI: 10.1109/ICGPR.2018.8441613.

Greaves, R. J., D. P. Lesmes, J. M. Lee, and M. N. Toksöz (1996). "Velocity variations and water content estimated from multi-offset, ground-penetrating radar". In: *Geophysics* 61.3, pp. 683–695. DOI: 10.1190/1.1443996.

Green, C. H. (1938). "Velocity Determinations by means of Reflection Profiles". In: *Geophysics* 3.4, pp. 295–305. DOI: 10.1190/1.1439508.

Gudmandsen, P. (1975). "Layer echoes in polar ice sheets". In: *Journal of Glaciology* 15.73, pp. 95–101. DOI: 10.3189/s0022143000034304.

Gusmeroli, A., T. Murray, P. Jansson, R. Pettersson, A. Aschwanden, and A. D. Booth (2010). "Vertical distribution of water within the polythermal Storglaciären, Sweden". In: *Journal of Geophysical Research* 115.F4, F04002. DOI: 10.1029/2009JF001539.

Gusmeroli, A., P. Jansson, R. Pettersson, and T. Murray (2012). *Twenty years of cold surface layer thinning at Storglaciären, sub-Arctic Sweden, 1989-2009*. DOI: 10.3189/2012JoG11J018.

Hale, R., H. Miller, S. Gogineni, J. B. Yan, F. Rodriguez-Morales, C. Leuschen, et al. (2016). "Multi-channel ultra-wideband radar sounder and imager". In: *International Geoscience and Remote Sensing Symposium (IGARSS)*. Vol. 2016-Novem. Institute of Electrical and Electronics Engineers Inc., pp. 2112–2115. ISBN: 9781509033324. DOI: 10.1109/IGARSS.2016.7729545.

Hambrey, M. J., T. Murray, N. F. Glasser, A. Hubbard, B. Hubbard, G. Stuart, et al. (2005). "Structure and changing dynamics of a polythermal valley glacier on a centennial timescale: Midre Lovenbreen, Svalbard". In: *Journal of Geophysical Research: Earth Surface* 110.1, F01006. DOI: 10.1029/2004JF000128.

Hambrey, M. J. and N. F. Glasser (2011). "Sediment Entrainment, Transport, and Deposition". In: *Encyclopedia of Earth Sciences Series*. Vol. Part 3. Springer Netherlands, pp. 984–1003. DOI: 10.1007/978-90-481-2642-2_475.

Hamran, S., E. Aarholt, J. O. Hagen, and P. Mo (1996). "Estimation of relative water content in a sub-polar glacier using surface-penetration radar". In: *Journal of Glaciology* 42.142, pp. 533–537. DOI: 10.3189/S0022143000003518.

Harlan, W. S., J. F. Claerbout, and F. Rocca (1984). "Signal/noise separation and velocity estimation". In: *GEOPHYSICS* 49.11, pp. 1869–1880. DOI: 10.1190/1.1441600.

Harrigan, E., J. R. Kroh, W. A. Sandham, and T. S. Durrani (1992). "Seismic horizon picking using an Artificial Neural Network". In: *ICASSP, IEEE International Conference on Acoustics, Speech and Signal Processing - Proceedings*. Vol. 3. Institute of Electrical and Electronics Engineers Inc., pp. 105–108. ISBN: 0780305329. DOI: 10.1109/ICASSP.1992.226265.

Hélière, F., C. C. Lin, H. Corr, and D. Vaughan (2007). "Radio echo sounding of Pine Island Glacier, West Antarctica: Aperture synthesis processing and analysis of feasibility from space". In: *IEEE Transactions on Geoscience and Remote Sensing*. Vol. 45. 8, pp. 2573–2582. DOI: 10.1109/TGRS.2007.897433.

Hindmarsh, R. C. A., G. J.-M. C. Leysinger Vieli, M. J. Raymond, and G. H. Gudmundsson (2006). "Draping or overriding: The effect of horizontal stress gradients on internal layer architecture in ice sheets". In: *Journal of Geophysical Research* 111.F2, F02018. DOI: 10.1029/2005JF000309.

Hindmarsh, R. C., G. Leysinger Vieli, and F. Parrenin (2009). "A large-scale numerical model for computing isochrone geometry". In: *Annals of Glaciology* 50.51, pp. 130–140. DOI: 10.3189/172756409789097450.

Hodson, A., J. Kohler, M. Brinkhaus, and P. Wynn (2005). "Multi-year water and surface energy budget of a high-latitude polythermal glacier: evidence for overwinter water storage in a dynamic subglacial reservoir". In: *Annals of Glaciology* 42, pp. 42–46. DOI: 10.3189/172756405781812844.

Holschuh, N., K. Christianson, J. Paden, R. B. Alley, and S. Anandakrishnan (2020). "Linking postglacial landscapes to glacier dynamics using swath radar at Thwaites glacier, Antarctica". In: *Geology* 48.3, pp. 268–272. DOI: 10.1130/G46772.1.

Holschuh, N., K. Christianson, and S. Anandakrishnan (2014). "Power loss in dipping internal reflectors, imaged using ice-penetrating radar". In: *Annals of Glaciology* 55.67, pp. 49–56. DOI: 10.3189/2014AoG67A005.

Holschuh, N., B. R. Parizek, R. B. Alley, and S. Anandakrishnan (2017). "Decoding ice sheet behavior using englacial layer slopes". In: *Geophysical Research Letters* 44.11, pp. 5561–5570. DOI: 10.1002/2017GL073417.

Holt, J. W., D. D. Blankenship, D. L. Morse, D. A. Young, M. E. Peters, S. D. Kempf, et al. (2006). "New boundary conditions for the West Antarctic Ice Sheet: Subglacial topography of the Thwaites and Smith glacier catchments". In: *Geophysical Research Letters* 33.9. DOI: 10.1029/2005GL025561.

How, P., D. I. Benn, N. R. J. Hulton, B. Hubbard, A. Luckman, H. Sevestre, et al. (2017). "Rapidly changing subglacial hydrological pathways at a tidewater glacier revealed through simultaneous observations of water pressure, supraglacial lakes, meltwater plumes and surface velocities". In: *The Cryosphere* 11.6, pp. 2691–2710. DOI: 10.5194/tc-11-2691-2017.

How, P., K. M. Schild, D. I. Benn, R. Noormets, N. Kirchner, A. Luckman, et al. (2019). "Calving controlled by melt-under-cutting: detailed calving styles revealed through time-lapse observations". In: *Annals of Glaciology*, pp. 1–12. DOI: 10.1017/aog.2018.28.

Hoyes, J. and T. Cheret (2011). "A review of "global" interpretation methods for automated 3D horizon picking". In: *The Leading Edge* 30.1, pp. 38–47. DOI: 10.1190/1.3535431.

Hubbard, B. P., A. Hubbard, H. M. Mader, J.-L. Tison, K. Grust, and P. W. Nienow (2003). "Spatial variability in the water content and rheology of temperate glaciers: Glacier de Tsanfleuron, Switzerland". In: *Annals of Glaciology* 37, pp. 1–6. DOI: 10.3189/172756403781815474.

Al-Ibadi, M., J. Sprick, S. Athinarapu, T. Stumpf, J. Paden, C. Leuschen, et al. (2017). "DEM extraction of the basal topography of the Canadian archipelago ICE caps via 2D automated layer-tracker". In: *2017 IEEE International Geoscience and Remote Sensing Symposium (IGARSS)*. IEEE, pp. 965–968. ISBN: 978-1-5090-4951-6. DOI: 10.1109/IGARSS.2017.8127114.

Iken, A., H. Röthlisberger, A. Flotron, and W. Haeberli (1983). "The Uplift of Unteraargletscher at the Beginning of the Melt Season—A Consequence of Water Storage at the Bed?" In: *Journal of Glaciology* 29.101, pp. 28–47. DOI: 10.3189/s0022143000005128.

Iken, A., Echelmeyer, W. Harrison, and M. Funk (1993). "Mechanisms of fast flow in Jakobshavns Isbræ, West Greenland: Part I. Measurements of temperature and water level in deep boreholes". In: *Journal of Glaciology* 39.131, pp. 15–25. DOI: 10.3189/S0022143000015689.

Irvine-Fynn, T., B. J. Moorman, J. L. Williams, and F. S. Walter (2006). "Seasonal changes in ground-penetrating radar signature observed at a polythermal glacier, Bylots Island, Canada". In: *Earth Surface Processes and Landforms* 31.7, pp. 892–909. DOI: 10.1002/esp.1299.

Irvine-Fynn, T., A. J. Hodson, B. J. Moorman, G. Vatne, and A. L. Hubbard (2011). "Polythermal glacier hydrology: a review". In: *Reviews of Geophysics* 49.4, RG4002. DOI: 10.1029/2010RG000350.

Jacobel, R. and C. Raymond (1984). "Radio echo-sounding studies of englacial water movement in Variegated Glacier, Alaska." In: *Journal of Glaciology* 30.104, pp. 22–29.

Jacobel, R. W., T. A. Scambos, N. A. Nereson, and C. F. Raymond (2000). "Changes in the margin of Ice Stream C, Antarctica". In: *Journal of Glaciology* 46.152, pp. 102–110. DOI: 10.3189/172756500781833485.

Jania, J., Y. Macheret, F. Navarro, A. Glazovsky, E. Vasilenko, J. Lapazaran, et al. (2005). "Temporal changes in the radiophysical properties of a polythermal glacier in Spitsbergen". In: *Annals of Glaciology* 42, pp. 125–134. DOI: 10.3189/172756405781812754.

Jania, J., D. Mochnacki, and B. Gdek (1996). "The thermal structure of Hansbreen, a tidewater glacier in southern Spitsbergen, Svalbard". In: *Polar Research* 15.1, pp. 53–66. DOI: 10.3402/polar.v15i1.6636.

Jazayeri, S., A. Klotzsche, and S. Kruse (2018). "Improving estimates of buried pipe diameter and infilling material from ground-penetrating radar profiles with full-waveform inversion". In: *Geophysics* 83.4, H27–H41. DOI: 10.1190/geo2017-0617.1.

Jeofry, H., N. Ross, and M. J. Siegert (2020). "Comparing numerical ice-sheet model output with radio-echo sounding measurements in the Weddell Sea sector of West Antarctica". In: *Annals of Glaciology* 61.81, pp. 188–197. DOI: 10.1017/aog.2019.39.

Jezek, K. C., J. W. Clough, C. R. Bentley, and S. Shabtaie (1978). "Dielectric Permittivity of Glacier Ice Measured In Situ by Radar Wide-Angle Reflection". In: *Journal of Glaciology* 21.85, pp. 315–329. DOI: 10.3189/S0022143000033505.

Jiracek, G. R. and C. R. Bentley (1971). "Velocity of Electromagnetic Waves in Antarctic Ice". In: *Antarctic snow and ice studies II*. Ed. by A. Crary. Washington DC: American Geophysical Union, pp. 199–208. DOI: 10.1029/AR016p0199.

Johari, G. P. and P. A. Charette (1975). "The Permittivity and Attenuation in Polycrystalline and Single-Crystal Ice Ih at 35 and 60 MHz". In: *Journal of Glaciology* 14.71, pp. 293–303. DOI: 10.3189/S002214300002178X.

Jordan, T. A., C. Martin, F. Ferraccioli, K. Matsuoka, H. Corr, R. Forsberg, et al. (2018a). "Anomalously high geothermal flux near the South Pole". In: 8, p. 16785. DOI: 10.1038/s41598-018-35182-0.

Jordan, T. M., D. M. Schroeder, C. W. Elsworth, and M. R. Siegfried (2020). "Estimation of ice fabric within Whillans Ice Stream using polarimetric phase-sensitive radar sounding". In: *Annals of Glaciology*, pp. 1–10. DOI: 10.1017/aog.2020.6.

Jordan, T. M., C. N. Williams, D. M. Schroeder, Y. M. Martos, M. A. Cooper, M. J. Siegert, et al. (2018b). "A constraint upon the basal water distribution and thermal state of the Greenland Ice Sheet from radar bed echoes". In: *The Cryosphere* 12.9, pp. 2831–2854. DOI: 10.5194/tc-12-2831-2018.

Kanagaratnam, P., S. P. Gogineni, N. Gundestrup, and L. Larsen (2001). "High-resolution radar mapping of internal layers at the North Greenland Ice Core Project". In: *Journal of Geophysical Research: Atmospheres* 106.D24, pp. 33799–33811. DOI: 10.1029/2001JD900191.

Karlsson, N. B., R. G. Bingham, D. M. Rippin, R. C. Hindmarsh, H. F. Corr, and D. G. Vaughan (2014). "Constraining past accumulation in the central Pine Island Glacier basin, West Antarctica, using radio-echo sounding". In: *Journal of Glaciology* 60.221, pp. 553–562. DOI: 10.3189/2014JoG13J180.

Karlsson, N. B., D. M. Rippin, R. G. Bingham, and D. G. Vaughan (2012). "A 'continuity-index' for assessing ice-sheet dynamics from radar-sounded internal layers". In: *Earth and Planetary Science Letters* 335-336, pp. 88–94. DOI: 10.1016/J.EPSL.2012.04.034.

Keisling, B. A., K. Christianson, R. B. Alley, L. E. Peters, J. E. M. Christian, S. Anandakrishnan, et al. (2014). "Basal conditions and ice dynamics inferred from radar-derived internal stratigraphy of the northeast Greenland ice stream". In: *Annals of Glaciology* 55.67, pp. 127–137. DOI: 10.3189/2014AoG67A090.

King, E. C., R. C. A Hindmarsh, and C. R. Stokes (2009). "Formation of mega-scale glacial lineations observed beneath a West Antarctic ice stream". In: DOI: 10.1038/ngeo581.

King, E. (2009). "Flow dynamics of the Rutford Ice Stream ice-drainage basin, West Antarctica, from radar stratigraphy". In: *Annals of Glaciology* 50.51, pp. 42–48. DOI: 10.3189/172756409789097586.

King, E. C., H. D. Pritchard, and A. M. Smith (2016). "Subglacial landforms beneath Rutford Ice Stream, Antarctica: detailed bed topography from ice-penetrating radar". In: *Earth Syst. Sci. Data* 8, pp. 151–158. DOI: 10.5194/essd-8-151-2016.

King, E. C., J. Woodward, and A. M. Smith (2007). "Seismic and radar observations of subglacial bed forms beneath the onset zone of Rutford Ice Stream, Antarctica". In: *Journal of Glaciology* 53.183, pp. 665–672. DOI: 10.3189/002214307784409216.

Kingslake, J., R. C. A. Hindmarsh, G. Aðalgeirsdóttir, H. Conway, H. F. J. Corr, F. Gillet-Chaulet, et al. (2014). "Full-depth englacial vertical ice sheet velocities measured using phase-sensitive radar". In: *Journal of Geophysical Research: Earth Surface* 119.12, pp. 2604–2618. DOI: 10.1002/2014JF003275.

Klotzsche, A., J. van der Kruk, G. Angelo Meles, J. Doetsch, H. Maurer, and N. Linde (2010). "Full-waveform inversion of cross-hole ground-penetrating radar data to characterize a gravel aquifer close to the Thur River, Switzerland". In: *Near Surface Geophysics* 8.6, pp. 635–649. DOI: 10.3997/1873-0604.2010054.

Klotzsche, A., H. Vereecken, and J. Van Der Kruk (2019). "Review of crosshole ground-penetrating radar full-waveform inversion of experimental data: Recent developments, challenges, and pitfalls". In: DOI: 10.1190/GEO2018-0597.1.

Koenig, L. S., A. Ivanoff, P. M. Alexander, J. A. MacGregor, X. Fettweis, B. Panzer, et al. (2016). "Annual Greenland accumulation rates (2009-2012) from airborne snow radar". In: *The Cryosphere* 10, pp. 1739–1752. DOI: 10.5194/tc-10-1739-2016.

König, M., C. Nuth, J. Kohler, G. Moholdt, and R. Pettersen (2014). "A digital glacier database for svalbard". In: *Global Land Ice Measurements from Space*. Berlin, Heidelberg: Springer Berlin Heidelberg, pp. 229–239. DOI: 10.1007/978-3-540-79818-7_10.

Koutnik, M. R., T. J. Fudge, H. Conway, E. D. Waddington, T. A. Neumann, K. M. Cuffey, et al. (2016). "Holocene accumulation and ice flow near the West Antarc-

tic Ice Sheet Divide ice core site". In: *Journal of Geophysical Research: Earth Surface* 121.5, pp. 907–924. DOI: 10.1002/2015JF003668@10.1002/(ISSN)1944-9186.WAISDIV.

Langhammer, L., L. Rabenstein, L. Schmid, A. Bauder, M. Grab, P. Schaer, et al. (2019). "Glacier bed surveying with helicopter-borne dual-polarization ground-penetrating radar". In: *Journal of Glaciology* 65.249, pp. 123–135. DOI: 10.1017/jog.2018.99.

Langhammer, L., L. Rabenstein, A. Bauder, and H. Maurer (2017). "Ground-penetrating radar antenna orientation effects on temperate mountain glaciers". In: *GEOPHYSICS* 82.3, H15–H24. DOI: 10.1190/geo2016-0341.1.

Lapazaran, J., J. Otero, A. Martín-español, and F. Navarro (2016). "On the errors involved in ice-thickness estimates I: ground-penetrating radar measurement errors". In: *Journal of Glaciology* 62.236, pp. 1008–1020. DOI: 10.1017/jog.2016.93.

Legarsky, J. J., S. P. Gogineni, and T. L. Akins (2001). "Focused synthetic aperture radar processing of ice-sounder data collected over the Greenland ice sheet". In: *IEEE Transactions on Geoscience and Remote Sensing* 39.10, pp. 2109–2117. DOI: 10.1109/36.957274.

Leong, W. J. and H. J. Horgan (2020). "DeepBedMap: Using a deep neural network to better resolve the bed topography of Antarctica". In: *The Cryosphere Discussions*, pp. 1–27. DOI: 10.5194/tc-2020-74.

Leuschen, C. and R. Plumb (2001). "A matched-filter-based reverse-time migration algorithm for ground-penetrating radar data". In: *IEEE Transactions on Geoscience and Remote Sensing* 39.5, pp. 929–936. DOI: 10.1109/36.921410.

Leysinger Vieli, G., M. J. Siegert, and A. J. Payne (2004). "Reconstructing ice-sheet accu-mulation rates at ridge B, East Antarctica". In: *Annals of Glaciology* 39.1, pp. 326–330. DOI: 10.3189/172756404781814519.

Leysinger Vieli, G., R. Hindmarsh, and M. Siegert (2007). "Three-dimensional flow influences on radar layer stratigraphy". In: *Annals of Glaciology* 46, pp. 22–28. DOI: 10.3189/172756407782871729.

Leysinger Vieli, G., R. C. Hindmarsh, M. J. Siegert, and S. Bo (2011). "Time-dependence of the spatial pattern of accumulation rate in East Antarctica deduced from isochronic radar layers using a 3-D numerical ice flow model". In: *Journal of Geophysical Research: Earth Surface* 116.2. DOI: 10.1029/2010JF001785.

Leysinger Vieli, G. J.-M. C., C. Martín, R. C. A. Hindmarsh, and M. P. Lüthi (2018). "Basal freeze-on generates complex ice-sheet stratigraphy". In: *Nature Communications* 9.1, p. 4669. DOI: 10.1038/s41467-018-07083-3.

Lliboutry, L. (1968). "General Theory of Subglacial Cavitation and Sliding of Temperate Glaciers". In: *Journal of Glaciology* 7.49, pp. 21–58. DOI: 10.3189/s0022143000020396.

Lomas, A. and A. Curtis (2019). "An introduction to Marchenko methods for imaging". In: *GEOPHYSICS* 84.2, F35–F45. DOI: 10.1190/geo2018-0068.1.

Looyenga, H. (1965). "Dielectric constants of heterogeneous mixtures". In: *Physica* 31.3, pp. 401–406. DOI: 10.1016/0031-8914(65)90045-5.

Lythe, M. B. and D. G. Vaughan (2001). "BEDMAP: A new ice thickness and subglacial topographic model of Antarctica". In: *Journal of Geophysical Research: Solid Earth* 106.B6, pp. 11335–11351. DOI: 10.1029/2000jb900449.

Maas, C. and J. Schmalzl (2013). "Using pattern recognition to automatically localize reflection hyperbolas in data from ground penetrating radar". In: *Computers & Geosciences* 58, pp. 116–125. DOI: 10.1016/j.cageo.2013.04.012.

MacGregor, J. A., D. P. Winebrenner, H. Conway, K. Matsuoka, P. A. Mayewski, and G. D. Clow (2007). "Modeling englacial radar attenuation at Siple Dome, West Antarctica, using ice chemistry and temperature data". In: *Journal of Geophysical Research* 112.F3, F03008. DOI: 10.1029/2006JF000717.

MacGregor, J. A., J. Li, J. D. Paden, G. A. Catania, G. D. Clow, M. A. Fahnestock, et al. (2015a). "Radar attenuation and temperature within the Greenland Ice Sheet". In: *Journal of Geophysical Research: Earth Surface* 120.6, pp. 983–1008. DOI: 10.1002/2014JF003418.

MacGregor, J. A., M. A. Fahnestock, G. A. Catania, J. D. Paden, S. Prasad Gogineni, S. K. Young, et al. (2015b). "Radiostratigraphy and age structure of the Greenland Ice Sheet". In: *Journal of Geophysical Research: Earth Surface* 120.2, pp. 212–241. DOI: 10.1002/2014JF003215.

MacGregor, J. A., W. T. Colgan, M. A. Fahnestock, M. Morlighem, G. A. Catania, J. D. Paden, et al. (2016). "Ice sheets: Holocene deceleration of the Greenland Ice Sheet". In: *Science* 351.6273, pp. 590–593. DOI: 10.1126/science.aab1702.

Macheret, Y. Y. and A. B. Zhuravlev (1982). "Radio Echo-Sounding of Svalbard Glaciers". In: *Journal of Glaciology* 28.99, pp. 295–314. DOI: 10.3189/s0022143000011643.

Macheret, Y. Y., M. Y. Moskalevsky, and E. Vasilenko (1993). "Velocity of radio waves in glaciers as an indicator of their hydrothermal state, structure and regime". In: *Journal of Glaciology* 39.132, pp. 373–384. DOI: 10.3189/S0022143000016038.

MacKie, E. J., D. M. Schroeder, J. Caers, M. R. Siegfried, and C. Scheidt (2020). "Antarctic Topographic Realizations and Geostatistical Modeling Used to Map Subglacial Lakes". In: *Journal of Geophysical Research: Earth Surface* 125.3. DOI: 10.1029/2019JF005420.

Masolov, V. N., S. V. Popov, V. V. Lukin, A. N. Sheremetyev, and A. M. Popkov (2006). "Russian Geophysical Studies of Lake Vostok, Central East Antarctica". In: *Antarctica*. Berlin/Heidelberg: Springer-Verlag, pp. 135–140. DOI: 10.1007/3-540-32934-X_16.

Matsuoka, K., D. Morse, and C. F. Raymond (2010a). "Estimating englacial radar attenuation using depth profiles of the returned power, central West Antarctica". In: *Journal of Geophysical Research: Earth Surface* 115.F2. DOI: 10.1029/2009jf001496.

Matsuoka, K., J. A. MacGregor, and F. Pattyn (2010b). "Using englacial radar attenuation to better diagnose the subglacial environment: A review". In: *Proceedings of the XIII Internarional Conference on Ground Penetrating Radar*. IEEE, pp. 1–5. ISBN: 978-1-4244-4604-9. DOI: 10.1109/ICGPR.2010.5550161.

Matsuoka, K. (2011). "Pitfalls in radar diagnosis of ice-sheet bed conditions: Lessons from englacial attenuation models". In: *Geophysical Research Letters* 38.5, n/a–n/a. DOI: 10.1029/2010GL046205.

Matsuoka, K., J. A. MacGregor, and F. Pattyn (2012a). "Predicting radar attenuation within the Antarctic ice sheet". In: *Earth and Planetary Science Letters* 359-360, pp. 173–183. DOI: 10.1016/j.epsl.2012.10.018.

Matsuoka, K., D. Power, S. Fujita, and C. F. Raymond (2012b). "Rapid development of anisotropic ice-crystal-alignment fabrics inferred from englacial radar polarimetry, central West Antarctica". In: *Journal of Geophysical Research: Earth Surface* 117.F3, n/a–n/a. DOI: 10.1029/2012JF002440.

Medley, B., I. Joughin, B. E. Smith, S. B. Das, E. J. Steig, H. Conway, et al. (2014). "Constraining the recent mass balance of Pine Island and Thwaites glaciers, West Antarctica, with airborne observations of snow accumulation". In: *The Cryosphere* 8, pp. 1375–1392. DOI: 10.5194/tc-8-1375-2014.

Medley, B., I. Joughin, S. B. Das, E. J. Steig, H. Conway, S. Gogineni, et al. (2013). "Airborne-radar and ice-core observations of annual snow accumulation over Thwaites Glacier, West Antarctica confirm the spatiotemporal variability of global and regional atmospheric models". In: *Geophysical Research Letters* 40.14, pp. 3649–3654. DOI: 10.1002/grl.50706.

Meles, G. A., J. Van Der Kruk, S. A. Greenhalgh, J. R. Ernst, H. Maurer, and A. G. Green (2010). "A new vector waveform inversion algorithm for simultaneous updating of conductivity and permittivity parameters from combination crosshole/borehole-to- surface GPR data". In: *IEEE Transactions on Geoscience and Remote Sensing* 48.9, pp. 3391–3407. DOI: 10.1109/TGRS.2010.2046670.

Mercer, J. H. (1978). "West Antarctic ice sheet and CO2 greenhouse effect: A threat of disaster". In: *Nature* 271.5643, pp. 321–325. DOI: 10.1038/271321a0.

Mertens, L., R. Persico, L. Matera, and S. Lambot (2016). "Automated Detection of Reflection Hyperbolas in Complex GPR Images With No <italic>A Priori</italic> Knowledge on the Medium". In: *IEEE Transactions on Geoscience and Remote Sensing* 54.1, pp. 580–596. DOI: 10.1109/TGRS.2015.2462727.

Millar, D. H. M. (1982). "Acidity Levels in Ice Sheets from Radio Echo-Sounding". In: *Annals of Glaciology* 3, pp. 199–203. DOI: 10.3189/s0260305500002779.

Moghaddam, M., E. J. Yannakakis, W. C. Chew, and M. Moghaddam (1991). "Modeling of the subsurface interface radar". In: *Journal of Electromagnetic Waves and Applications* 5.1, pp. 17–39. DOI: 10.1163/156939391X00455.

Moore, J. C. (1988). "Dielectric Variability of a 130 m Antarctic Ice Core: Implications for Radar Sounding". In: *Annals of Glaciology* 11, pp. 95–99. DOI: 10.3189/s026030550000639x.

Moore, J., A. Pälli, F. Ludwig, H. Blatter, J. Jania, B. Gadek, et al. (1999). "High-resolution hydrothermal structure of Hansbreen, Spitsbergen, mapped by ground-penetrating radar". In: *Journal of Glaciology* 45.151, pp. 524–532. DOI: 10.3189/S0022143000001386.

Moran, M. L., R. J. Greenfield, S. A. Arcone, and A. J. Delaney (2000). "Delineation of a complexly dipping temperate glacier bed using short-pulse radar arrays". In: *Journal of Glaciology* 46.153, pp. 274–286. DOI: 10.3189/172756500781832882.

Morlighem, M., C. N. Williams, E. Rignot, L. An, J. E. Arndt, J. L. Bamber, et al. (2017). "BedMachine v3: Complete Bed Topography and Ocean Bathymetry Mapping of Greenland From Multibeam Echo Sounding Combined With Mass Conservation". In: *Geophysical Research Letters* 44.21, pp. 051–11. DOI: 10.1002/2017GL074954.

Morlighem, M., E. Rignot, T. Binder, D. Blankenship, R. Drews, G. Eagles, et al. (2020). "Deep glacial troughs and stabilizing ridges unveiled beneath the margins of the Antarctic ice sheet". In: *Nature Geoscience* 13.2, pp. 132–137. DOI: 10.1038/s41561-019-0510-8.

Mozaffari, A., A. Klotzsche, G. He, H. Vereecken, J. van der Kruk, C. Warren, et al. (2016). "Towards 3D full-waveform inversion of crosshole GPR data". In: *2016 16th International Conference on Ground Penetrating Radar (GPR)*. IEEE, pp. 1–4. ISBN: 978-1-5090-5181-6. DOI: 10.1109/ICGPR.2016.7572687.

Mozaffari, A., A. Klotzsche, C. Warren, G. He, A. Giannopoulos, H. Vereecken, et al. (2020). "2.5D crosshole GPR full-waveform inversion with synthetic and measured data". In: DOI: 10.1190/GEO2019-0600.1.

Murray, T., A. Booth, and D. M. Rippin (2007). "Water-content of Glacier-ice: Limitations on Estimates from Velocity Analysis of Surface Ground-penetrating Radar Surveys". In: *Journal of Environmental & Engineering Geophysics* 12.1, pp. 87–99. DOI: 10.2113/JEEG12.1.87.

Murray, T., H. Corr, A. Forieri, and A. M. Smith (2008). "Contrasts in hydrology between regions of basal deformation and sliding beneath Rutford Ice Stream, West Antarctica, mapped using radar and seismic data". In: *Geophysical Research Letters* 35.12, n/a–n/a. DOI: 10.1029/2008GL033681.

Murray, T. and G. K. C. Clarke (1995). "Black-box modeling of the subglacial water system". In: *Journal of Geophysical Research: Solid Earth* 100.B6, pp. 10231–10245. DOI: 10.1029/95JB00671.

Murray, T., D. L. Gooch, and G. W. Stuart (1997). "Structures within the surge front at Bakaninbreen, Svalbard, using ground-penetrating radar". In: *Annals of Glaciology* 24, pp. 122–129. DOI: 10.3189/S0260305500012040.

Murray, T., G. W. Stuart, M. Fry, N. H. Gamble, and M. D. Crabtree (2000). "Englacial water distribution in a temperate glacier from surface and borehole radar velocity analysis". In: *Journal of Glaciology* 46.154, pp. 389–398. DOI: 10.3189/172756500781833188.

Murray, T. and A. D. Booth (2010). "Imaging glacial sediment inclusions in 3-D using ground-penetrating radar at Kongsvegen, Svalbard". In: *Journal of Quaternary Science* 25.5, pp. 754–761. DOI: 10.1002/jqs.1351.

Nanda, N. C. (2016). *Seismic Data Interpretation and Evaluation for Hydrocarbon Exploration and Production*. Springer International Publishing. DOI: 10.1007/978-3-319-26491-2.

Navarro, F. J., A. Martín-Español, J. J. Lapazaran, M. Grabiec, J. Otero, E. V. Vasilenko, et al. (2014). "Ice Volume Estimates from Ground-Penetrating Radar Surveys, Wedel Jarlsberg Land Glaciers, Svalbard". In: *Arctic, Antarctic, and Alpine Research* 46.2, pp. 394–406. DOI: 10.1657/1938-4246-46.2.394.

Navarro, F. J., Y. Y. Macheret, and B. Benjumea (2005). "Application of radar and seismic methods for the investigation of temperate glaciers". In: *Journal of Applied Geophysics* 57.3, pp. 193–211. DOI: 10.1016/j.jappgeo.2004.11.002.

Neidell, N. S. and M. T. Taner (1971). "Semblance and other coherency measures for multichannel data". In: *Geophysics* 36.3, pp. 482–497. DOI: 10.1190/1.1440186.

Nereson, N. A., C. F. Raymond, R. Jacobel, and E. D. Waddington (2000). "The accumulation pattern across Siple Dome, West Antarctica, inferred from radar-

detected internal layers". In: *Journal of Glaciology* 46.152, pp. 75–87. DOI: 10.3189/172756500781833449.

Neumann, T. A., A. J. Martino, T. Markus, S. Bae, M. R. Bock, A. C. Brenner, et al. (2019). "The Ice, Cloud, and Land Elevation Satellite – 2 mission: A global geolocated photon product derived from the Aadvanced Ttopographic Llaser Aaltimeter Ssystem". In: *Remote Sensing of Environment* 233, p. 111325. DOI: 10.1016/j.rse.2019.111325.

Ng, F. and H. Conway (2004). "Fast-flow signature in the stagnated Kamb Ice Stream, West Antarctica". In: *Geology* 32.6, p. 481. DOI: 10.1130/G20317.1.

Nias, I., S. Cornford, and A. Payne (2016). "Contrasting the modelled sensitivity of the Amundsen Sea Embayment ice streams". In: *Journal of Glaciology* 62.233, pp. 552–562. DOI: 10.1017/jog.2016.40.

Nicolson, H., A. Curtis, and B. Baptie (2014). "Rayleigh wave tomography of the British Isles from ambient seismic noise". In: *Geophysical Journal International* 198.2, pp. 637–655. DOI: 10.1093/gji/ggu071.

Nye, J. F. (1963). "Correction Factor for Accumulation Measured by the Thickness of the Annual Layers in an Ice Sheet". In: *Journal of Glaciology* 4.36, pp. 785–788. DOI: 10.3189/s0022143000028367.

Ødegård, R. S., J. O. Hagen, and S. .-.-E. Hamranw (1997). "Comparison of radio-echo sounding (30–1000 MHz) and high-resolution borehole-temperature measurements at Finsterwalderbreen, southern Spitsbergen, Svalbard". In: *Annals of Glaciology* 24, pp. 262–267. DOI: 10.3189/S0260305500012271.

Orosei, R., S. E. Lauro, E. Pettinelli, A. Cicchetti, M. Coradini, B. Cosciotti, et al. (2018). "Radar evidence of subglacial liquid water on Mars". In: *Science (New York, N.Y.)* 361.6401, pp. 490–493. DOI: 10.1126/science.aar7268.

Paden, J., T. Akins, D. Dunson, C. T. Allen, and P. Gogineni (2010). "Ice-sheet bed 3-D tomography". In: 56.195, pp. 3–11.

Panton, C. (2014). "Automated mapping of local layer slope and tracing of internal layers in radio echograms". In: *Annals of Glaciology* 55.67, pp. 71–77. DOI: 10.3189/2014AoG67A048.

Panton, C. and N. B. Karlsson (2015). "Automated mapping of near bed radio-echo layer disruptions in the Greenland Ice Sheet". In: *Earth and Planetary Science Letters* 432, pp. 323–331. DOI: 10.1016/j.epsl.2015.10.024.

Parrenin, F., J.-M. Barnola, J. Beer, T. Blunier, E. Castellano, J. Chappellaz, et al. (2007). "The EDC3 chronology for the EPICA Dome C ice core". In: *Climate of the Past* 3.3, pp. 485–497. DOI: 10.5194/cp-3-485-2007.

Parrenin, F. and R. Hindmarsh (2007). "Influence of a non-uniform velocity field on isochrone geometry along a steady flowline of an ice sheet". In: *Journal of Glaciology* 53.183, pp. 612–622. DOI: 10.3189/002214307784409298.

Pasolli, E., F. Melgani, and M. Donelli (2009). "Automatic Analysis of GPR Images: A Pattern-Recognition Approach". In: *IEEE Transactions on Geoscience and Remote Sensing* 47.7, pp. 2206–2217. DOI: 10.1109/TGRS.2009.2012701.

Peters, M. E., D. D. Blankenship, and D. L. Morse (2005). "Analysis techniques for coherent airborne radar sounding: Application to West Antarctic ice streams". In: *Journal of Geophysical Research B: Solid Earth* 110.6, pp. 1–17. DOI: 10.1029/2004JB003222.

Peters, M. E., D. D. Blankenship, S. P. Carter, S. D. Kempf, D. A. Young, and J. W. Holt (2007). "Along-track focusing of airborne radar sounding data from west antarctica for improving basal reflection analysis and layer detection". In: *IEEE Transactions on Geoscience and Remote Sensing* 45.9, pp. 2725–2736. DOI: 10.1109/TGRS.2007.897416.

Peters, S. T., D. M. Schroeder, D. Castelletti, M. S. Haynes, and A. Romero-Wolf (2019). "Two Dimensional Image Formation with Passive Radar Using the Sun for Echo Detection". In: *International Geoscience and Remote Sensing Symposium (IGARSS)*. Institute of Electrical and Electronics Engineers Inc., pp. 10091–10094. ISBN: 9781538691540. DOI: 10.1109/IGARSS.2019.8897880.

Pettersson, R., P. Jansson, and P. Holmlund (2003). "Cold surface layer thinning on Storglaciären, Sweden, observed by repeated ground penetrating radar surveys". In: *Journal of Geophysical Research: Earth Surface* 108.F1, n/a–n/a. DOI: 10.1029/2003JF000024.

Pettersson, R., P. Jansson, and H. Blatter (2004). "Spatial variability in water content at the cold-temperate transition surface of the polythermal Storglaciären, Sweden". In: *Journal of Geophysical Research: Earth Surface* 109.F2, n/a–n/a. DOI: 10.1029/2003JF000110.

Phillips, R. J., M. T. Zuber, S. E. Smrekar, M. T. Mellon, J. W. Head, K. L. Tanaka, et al. (2008). *Mars North Polar Deposits: Stratigraphy, Age, and Geodynamical Response*. DOI: 10.2307/20054833.

Pollard, D. and R. M. DeConto (2012). "A simple inverse method for the distribution of basal sliding coefficients under ice sheets, applied to Antarctica". In: *The Cryosphere* 6.5, pp. 953–971. DOI: 10.5194/tc-6-953-2012.

Pourchet, M., O. Magand, M. Frezzotti, A. Ekaykin, and J.-G. Winther (2003). "Radionuclides deposition over Antarctica". In: *Journal of Environmental Radioactivity* 68, pp. 137–158. DOI: 10.1016/S0265-931X(03)00055-9.

Preine, J., S. Benjamin, A. Bauer, and C. Hübscher (2020). "When there is no offset - a demonstration of seismic diffraction imaging and depth-velocity model building in the southern Aegean Sea". In: *JGR Solid Earth* In product. DOI: https://doi.org/10.1029/2020JB019961.

Pritchard, H. D., E. C. King, D. J. Goodger, M. Mccarthy, C. Mayer, and R. Kayastha (2020). "Towards Bedmap Himalayas: development of an airborne ice-sounding radar for glacier thickness surveys in High-Mountain Asia". In: DOI: 10.1017/aog.2020.29.

Pritchard, H. D. (2014). "Bedgap: where next for Antarctic subglacial mapping?" In: *Antarctic Science* 26.6, pp. 742–757. DOI: 10.1017/S095410201400025X.

Putzig, N. E., I. B. Smith, M. R. Perry, F. J. Foss, B. A. Campbell, R. J. Phillips, et al. (2018). "Three-dimensional radar imaging of structures and craters in the Martian polar caps". In: *Icarus* 308, pp. 138–147. DOI: 10.1016/J.ICARUS.2017.09.023.

Rahnemoonfar, M., D. Varshney, M. Yari, and J. Paden (2020). "Deep Ice Layer Tracking and Thickness Estimation using Fully Convolutional Networks". In: URL: http://arxiv.org/abs/2009.00191.

Reinardy, B. T. I., A. D. Booth, A. L. C. Hughes, C. M. Boston, H. Åkesson, J. Bakke, et al. (2019). "Pervasive cold ice within a temperate glacier – implications

for glacier thermal regimes, sediment transport and foreland geomorphology". In: *The Cryosphere* 13.3, pp. 827–843. DOI: 10.5194/tc-13-827-2019.

Reine, C., R. Clark, and M. van der Baan (2012). "Robust prestack Q-determination using surface seismic data: Part 1 — Method and synthetic examples". In: *GEOPHYSICS* 77.1, R45–R56. DOI: 10.1190/geo2011-0073.1.

Rémy, F. and I. E. Tabacco (2000). "Bedrock features and ice flow near the EPICA Ice Core Site (Dome C, Antarctica)". In: *Geophysical Research Letters* 27.3, pp. 405–408. DOI: 10.1029/1999GL006067.

Retzlaff, R., N. Lord, and C. Bentley (1993). "Airborne-radar studies: Ice Streams A, B and C, West Antarctica". In: *Journal of Glaciology* 39.133, pp. 495–506. DOI: 10.3189/S0022143000016397.

Rippin, D., I. Willis, N. Arnold, A. Hodson, J. Moore, J. Kohler, et al. (2003a). "Changes in geometry and subglacial drainage of midre Lovénbreen, Svalbard, determined from digital elevation models". In: *Earth Surface Processes and Landforms* 28.3, pp. 273–298. DOI: 10.1002/esp.485.

Rippin, D. M., M. J. Siegert, and J. L. Bamber (2003b). "The englacial stratigraphy of Wilkes Land, East Antarctica, as revealed by internal radio-echo sounding layering, and its relationship with balance velocities". In: *Annals of Glaciology* 36, pp. 189–196. DOI: 10.3189/172756403781816356.

Rippin, D. M., M. J. Siegert, J. L. Bamber, D. G. Vaughan, and H. F. J. Corr (2006). "Switch-off of a major enhanced ice flow unit in East Antarctica". In: *Geophysical Research Letters* 33.15, p. L15501. DOI: 10.1029/2006GL026648.

Ritz, C., T. L. Edwards, G. Durand, A. J. Payne, V. Peyaud, and R. C. Hindmarsh (2015). "Potential sea-level rise from Antarctic ice-sheet instability constrained by observations". In: *Nature* 528.7580, pp. 115–118. DOI: 10.1038/nature16147.

Roberts, R. L. and J. J. Daniels (1996). "Analysis of GPR Polarization Phenomena". In: *Journal of Environmental and Engineering Geophysics* 1.2, pp. 139–157. DOI: 10.4133/jeeg1.2.139.

Robin, G. D. Q., S. Evans, and J. T. Bailey (1969). "Interpretation of Radio Echo Sounding in Polar Ice Sheets". In: *Philosophical transactions. Series A, Mathematical, physical, and engineering sciences* 265.1166, pp. 437–505. DOI: 10.1098/rsta.1969.0063.

Robin, G. D. Q. (1975). "Velocity of radio waves in ice by means of a bore-hole interferometric technique". In: *Journal of Glaciology* 15.73, pp. 151–159. DOI: 10.3189/S0022143000034341.

Robin, G. D. Q., C. W. M. Swithinbank, and B. M. E. Smith (1970). "Radio echo exploration of the Antarctic ice sheet". In: *International Symposium on Antarctic Glaciological Exploration (ISAGE), Hanover, New Hampshire, 3-7 September 1968*, pp. 97–115.

Roden, J. A. and S. D. Gedney (2000). "Convolution PML (CPML): An efficient FDTD implementation of the CFS-PML for arbitrary media". In: *Microwave and Optical Technology Letters* 27.5, pp. 334–339. DOI: 10.1002/1098-2760(20001205)27:5<334::AID-MOP14>3.0.CO;2-A.

Ross, N., H. Corr, and M. Siegert (2020). "Large-scale englacial folding and deep-ice stratigraphy within the West Antarctic Ice Sheet". In: *The Cryosphere* 14.6, pp. 2103–2114. DOI: 10.5194/tc-14-2103-2020.

Röthlisberger, H. (1972). "Water Pressure in Intra- and Subglacial Channels". In: *Journal of Glaciology* 11.62, pp. 177–203. DOI: 10.3189/S0022143000022188.

Ryser, C., M. Lüthi, N. Blindow, S. Suckro, M. Funk, and A. Bauder (2013). "Cold ice in the ablation zone: Its relation to glacier hydrology and ice water content". In: *Journal of Geophysical Research: Earth Surface* 118.2, pp. 693–705. DOI: 10.1029/2012JF002526.

Saintenoy, A., J.-M. Friedt, A. D. Booth, F. Tolle, E. Bernard, D. Laffly, et al. (2013). "Deriving ice thickness, glacier volume and bedrock morphology of Austre Lovénbreen (Svalbard) using GPR". In: *Near Surface Geophysics* 11.2, pp. 253–262. DOI: 10.3997/1873-0604.2012040.

Sandmeier, K. (2020). *ReflexW User Manual*. Karlsruhe.

Schannwell, C., T. Murray, B. Kulessa, A. Gusmeroli, A. Saintenoy, and P. Jansson (2014). "An automatic approach to delineate the cold–temperate transition surface with ground-penetrating radar on polythermal glaciers". In: *Annals of Glaciology* 55.67, pp. 89–96. DOI: 10.3189/2014AoG67A102.

Schroeder, D. M., D. D. Blankenship, D. A. Young, and E. Quartini (2014). "Evidence for elevated and spatially variable geothermal flux beneath the West Antarctic Ice Sheet". In: *Proceedings of the National Academy of Sciences* 111.25, pp. 9070–9072. DOI: 10.1073/pnas.1405184111.

Schroeder, D. M., J. A. Dowdeswell, M. J. Siegert, R. G. Bingham, W. Chu, E. J. MacKie, et al. (2019). "Multidecadal observations of the Antarctic ice sheet from restored analog radar records". In: *Proceedings of the National Academy of Sciences* 116.38, pp. 18867–18873. DOI: 10.1073/pnas.1821646116.

Schroeder, D. M., R. G. Bingham, D. D. Blankenship, K. Christianson, O. Eisen, G. E. Flowers, et al. (2020). "Five decades of radioglaciology". In: *Annals of Glaciology* 61.81, pp. 1–13. DOI: 10.1017/aog.2020.11.

Schwarz, B. and D. Gajewski (2017). "Accessing the diffracted wavefield by coherent subtraction". In: *Geophysical Journal International* 211.1, pp. 45–49. DOI: 10.1093/gji/ggx291.

Schwarz, B. (2019). "Coherent wavefield subtraction for diffraction separation". In: *Geophysics* 84.3, pp. V157–V168. DOI: 10.1190/geo2018-0368.1.

Scott, J. B., A. M. Smith, R. G. Bingham, and D. G. Vaughan (2010). "Crevasses triggered on Pine Island Glacier, West Antarctica, by drilling through an exceptional melt layer". In: *Annals of Glaciology* 51.55, pp. 65–70. DOI: 10.3189/172756410791392763.

Sevestre, H., D. I. Benn, N. R. J. Hulton, and K. Baelum (2015). "Thermal structure of Svalbard glaciers and implications for thermal switch models of glacier surging". In: *Journal of Geophysical Research: Earth Surface* 120.10, pp. 2220–2236. DOI: 10.1002/2015JF003517.

Shabtaie, S., I. M. Whillans, and C. R. Bentley (1987). "The morphology of ice streams A, B, and C, west Antarctica, and their environs". In: *Journal of Geophysical Research* 92.B9, p. 8865. DOI: 10.1029/JB092iB09p08865.

Shannon, C. E. (1948). "A Mathematical Theory of Communication". In: *Bell System Technical Journal* 27.3, pp. 379–423. DOI: 10.1002/j.1538-7305.1948.tb01338.x.

Siegert, M. J. (1999). "On the origin, nature and uses of Antarctic ice-sheet radio-echo layering". In: *Progress in Physical Geography* 23.2, pp. 159–179. DOI: 10.1177/030913339902300201.

Siegert, M., N. Ross, H. Corr, J. Kingslake, and R. Hindmarsh (2013). "Late Holocene ice-flow reconfiguration in the Weddell Sea sector of West Antarctica". In: *Quaternary Science Reviews* 78, pp. 98–107. DOI: 10.1016/j.quascirev.2013.08.003.

Siegert, M. J., A. J. Payne, and I. Joughin (2003). "Spatial stability of Ice Stream D and its tributaries, West Antarctica, revealed by radio-echo sounding and interferometry". In: *Annals of Glaciology* 37, pp. 377–382. DOI: 10.3189/172756403781816022.

Siegert, M. J., R. Hodgkins, and J. A. Dowdeswell (1998). "A chronology for the Dome C deep ice-core site through radio-echo layer correlation with the Vostok ice core, Antarctica". In: *Geophysical Research Letters* 25.7, pp. 1019–1022. DOI: 10.1029/98GL00718.

Siegert, M. J. and A. J. Payne (2004). "Past rates of accumulation in central West Antarctica". In: *Geophysical Research Letters* 31.12, n/a–n/a. DOI: 10.1029/2004GL020290.

Sime, L. C., R. C. Hindmarsh, and H. Corr (2011). "Automated processing to derive dip angles of englacial radar reflectors in ice sheets". In: *Journal of Glaciology* 57.202, pp. 260–266. DOI: 10.3189/002214311796405870.

Sime, L. C., N. B. Karlsson, J. D. Paden, and S. Prasad Gogineni (2014). "Isochronous information in a Greenland ice sheet radio echo sounding data set". In: *Geophysical Research Letters* 41.5, pp. 1593–1599. DOI: 10.1002/2013GL057928.

Smith, A. M. (1997). "Basal conditions on Rutford Ice Stream, West Antarctica, from seismic observations". In: *Journal of Geophysical Research: Solid Earth* 102.B1, pp. 543–552. DOI: 10.1029/96JB02933.

Sobel, I. (1990). "Generalized and separable Sobel operators". In: *Machine vision for three-dimensional scenes*. Ed. by P. Danielsson and O. Seger. Academic Press. Chap. Appendix. URL: https://www.researchgate.net/publication/239398674_An_Isotropic_3x3_Image_Gradient_Operator.

Steenson, B. O. (1951). "Radar Methods for the Exploration of Glaciers". PhD thesis, p. 53. URL: http://resolver.caltech.edu/CaltechTHESIS:10092014-103732963.

Steger, C. (1998). "An unbiased detector of curvilinear structures". In: *IEEE Transactions on Pattern Analysis and Machine Intelligence* 20.2, pp. 113–125. DOI: 10.1109/34.659930.

Steig, E. J., P. A. Mayewski, D. A. Dixon, S. D. Kaspari, M. M. Frey, D. P. Schneider, et al. (2005). "High-resolution ice cores from US ITASE (West Antarctica): development and validation of chronologies and determination of precision and accuracy". In: *Annals of Glaciology* 41, pp. 77–84. DOI: 10.3189/172756405781813311.

Storn, R. and K. Price (1997). *Differential Evolution-A Simple and Efficient Heuristic for Global Optimization over Continuous Spaces*. Tech. rep., pp. 341–359. URL: https://link.springer.com/content/pdf/10.1023%2FA%3A1008202821328.pdf.

Stoyer, C. H. and R. J. Greenfield (1976). "Numerical solutions of the response of a two-dimensional earth to an oscillatory magnetic dipole source". In: *GEOPHYSICS* 41.3, pp. 519–530. DOI: 10.1190/1.1440630.

Stuart, G. (2003). "Characterization of englacial channels by ground-penetrating radar: An example from austre Brøggerbreen, Svalbard". In: *Journal of Geophysical Research* 108.B11, p. 2525. DOI: 10.1029/2003JB002435.

Sweeting, M. and G. Groom (1956). "Notes on the Glacier Fluctuations in Bünsow Land, Central Vestspitsbergen". In: *Journal of Glaciology* 2.19, pp. 640–641. DOI: 10.3189/002214356793701875.

Taflove, A. and S. C. Hagness (2005). *Computational electrodynamics : the finite-difference time-domain method*. Artech House, p. 1006. ISBN: 9781580538329.

Taner, M. T. and F. Koehler (1969). "Velocity spectra - digital computer derivation applications of velocity functions". In: *Geophysics* 34.6, pp. 859–881. DOI: 10.1190/1.1440058.

Toldi, J. L. (1989). "Velocity analysis without picking". In: *Geophysics* 54.2, pp. 191–199. DOI: 10.1190/1.1442643.

Turchetti, S., K. Dean, S. Naylor, and M. J. Siegert (2008). "Accidents and opportunities: a history of the radio echo-sounding of Antarctica, 1958–79". In: *The British Journal for the History of Science* 41.03, pp. 417–444. DOI: 10.1017/S0007087408000903.

Ulaby, F. T., R. K. Moore, and A. K. Fung (1981). *Microwave remote sensing: Active and passive. Volume 1 - Microwave remote sensing fundamentals and radiometry*. URL: http://ntrs.nasa.gov/search.jsp?R=19820039342.

Van Vorst, D. G., M. J. Yedlin, J. Virieux, and E. S. Krebes (2014). "Three-dimensional to two-dimensional data conversion for electromagnetic wave propagation using an acoustic transfer function: application to cross-hole GPR data". In: *Geophysical Journal International Geophys. J. Int* 198, pp. 474–483. DOI: 10.1093/gji/ggu111.

Vaughan, D. G., H. F. J. Corr, C. S. M. Doake, and E. D. Waddington (1999). "Distortion of isochronous layers in ice revealed by ground-penetrating radar". In: *Nature* 398.6725, pp. 323–326. DOI: 10.1038/18653.

Versteeg, R. J. (1993). "Sensitivity of prestack depth migration to the velocity model". In: *GEOPHYSICS* 58.6, pp. 873–882. DOI: 10.1190/1.1443471.

Vidale, J., D. V. Helmberger, and R. W. Clayton (1985). *Finite-Difference seismograms for SH waves*. Tech. rep. 6, pp. 1765–1782.

Virieux, J. and S. Operto (2009). "An overview of full-waveform inversion in exploration geophysics". In: *Geophysics* 74.6, WCC1–WCC26. DOI: 10.1190/1.3238367.

Waddington, E. D., T. A. Neumann, M. R. Koutnik, H. P. Marshall, and D. L. Morse (2007). "Inference of accumulation-rate patterns from deep layers in glaciers and ice sheets". In: *Journal of Glaciology* 53.183, pp. 694–712. DOI: 10.3189/002214307784409351.

Waite, A. H. and S. J. Schmidt (1962). "Gross Errors in Height Indication from Pulsed Radar Altimeters Operating over Thick Ice or Snow". In: *Proceedings of the IRE* 50.6, pp. 1515–1520. DOI: 10.1109/JRPROC.1962.288195.

Walder, J. S. (2010). "Röthlisberger channel theory: its origins and consequences". In: *Journal of Glaciology* 56.200, pp. 1079–1086. DOI: 10.3189/002214311796406031.

Warren, C. and A. Giannopoulos (2016). "gprMax User Guide". In: 14.

Wearing, M. G. and J. Kingslake (2019). "Holocene Formation of Henry Ice Rise, West Antarctica, Inferred From Ice-Penetrating Radar". In: *Journal of Geophysical Research: Earth Surface* 124.8, pp. 2224–2240. DOI: 10.1029/2018JF004988.

Weertman, J. (1957). "On the Sliding of Glaciers". In: *Journal of Glaciology* 3.21, pp. 33–38. DOI: 10.3189/s0022143000024709.

Weertman, J. (1964). "The Theory of Glacier Sliding". In: *Journal of Glaciology* 5.39, pp. 287–303. DOI: 10.3189/s0022143000029038.

Welch, B. C. and R. W. Jacobel (2003). "Analysis of deep-penetrating radar surveys of West Antarctica, US-ITASE 2001". In: *Geophysical Research Letters* 30.8. DOI: 10.1029/2003GL017210.

West, L., D. M. Rippin, T. Murray, H. M. Mader, and B. Hubbard (2007). "Dielectric Permittivity Measurements on Ice Cores: Implications for Interpretation of Radar to Yield Glacial Unfrozen Water Content". In: *Journal of Environmental & Engineering Geophysics* 12.1, pp. 37–45. DOI: 10.2113/JEEG12.1.37.

Winter, A., D. Steinhage, E. J. Arnold, D. D. Blankenship, M. G. P. Cavitte, H. F. J. Corr, et al. (2017). "Comparison of measurements from different radio-echo sounding systems and synchronization with the ice core at Dome C, Antarctica". In: *The Cryosphere* 11.1, pp. 653–668. DOI: 10.5194/tc-11-653-2017.

Winter, A., D. Steinhage, T. T. Creyts, T. Kleiner, and O. Eisen (2019a). "Age stratigraphy in the East Antarctic Ice Sheet inferred from radio-echo sounding horizons". In: *Earth System Science Data* 11.3, pp. 1069–1081. DOI: 10.5194/essd-11-1069-2019.

Winter, K., J. Woodward, N. Ross, S. A. Dunning, R. G. Bingham, H. F. J. Corr, et al. (2015). "Airborne radar evidence for tributary flow switching in Institute Ice Stream, West Antarctica: Implications for ice sheet configuration and dynamics". In: *Journal of Geophysical Research: Earth Surface* 120.9, pp. 1611–1625. DOI: 10.1002/2015JF003518.

Winter, K., J. Woodward, N. Ross, S. A. Dunning, A. S. Hein, M. J. Westoby, et al. (2019b). "Radar-Detected Englacial Debris in the West Antarctic Ice Sheet". In: *Geophysical Research Letters* 46.17-18, pp. 10454–10462. DOI: 10.1029/2019GL084012.

Wolovick, M. J. and T. T. Creyts (2016). "Overturned folds in ice sheets: Insights from a kinematic model of traveling sticky patches and comparisons with observations". In: *Journal of Geophysical Research: Earth Surface* 121.5, pp. 1065–1083. DOI: 10.1002/2015JF003698.

Woodward, J., T. Murray, R. A. Clark, and G. W. Stuart (2003). "Glacier surge mechanisms inferred from ground-penetrating radar: Kongsvegen, Svalbard". In: *Journal of Glaciology* 49.167, pp. 473–480. DOI: 10.3189/172756503781830458.

Wright, A. and M. Siegert (2012). "A fourth inventory of Antarctic subglacial lakes". In: *Antarctic Science* 24.6, pp. 659–664. DOI: 10.1017/S095410201200048X.

Xiong, S., J. P. Muller, and R. C. Carretero (2018). "A new method for automatically tracing englacial layers from MCoRDS Data in NW Greenland". In: *Remote Sensing* 10.1, pp. 1–22. DOI: 10.3390/rs10010043.

Xu, T. and G. A. McMechan (1997). "GPR attenuation and its numerical simulation in 2.5 dimensions". In: *GEOPHYSICS* 62.2, pp. 403–414. DOI: 10.1190/1.1444151.

Yang, X., A. Klotzsche, G. Meles, H. Vereecken, and J. Van Der Kruk (2013). "Improvements in crosshole GPR full-waveform inversion and application on data measured at the Boise Hydrogeophysics Research Site". In: *Journal of Applied Geophysics* 99, pp. 114–124. DOI: 10.1016/j.jappgeo.2013.08.007.

Yee, K. (1966). "Numerical solution of initial boundary value problems involving maxwell's equations in isotropic media". In: *IEEE Transactions on Antennas and Propagation* 14.3, pp. 302–307. DOI: 10.1109/TAP.1966.1138693.

Yilmaz, Ö. (2001). *Seismic Data Analysis*. Society of Exploration Geophysicists. ISBN: 978-1-56080-094-1. DOI: 10.1190/1.9781560801580.

Young, D. A., A. P. Wright, J. L. Roberts, R. C. Warner, N. W. Young, J. S. Greenbaum, et al. (2011). "A dynamic early East Antarctic Ice Sheet suggested by ice-covered fjord landscapes". In: *Nature* 474.7349, pp. 72–75. DOI: 10.1038/nature10114.

Young, T. J., D. M. Schroeder, P. Christoffersen, L. B. Lok, K. W. Nicholls, P. V. Brennan, et al. (2018). "Resolving the internal and basal geometry of ice masses using imaging phase-sensitive radar". In: *Journal of Glaciology* 64.246, pp. 649–660. DOI: 10.1017/jog.2018.54.

Zemp, M., M. Huss, E. Thibert, N. Eckert, R. McNabb, J. Huber, et al. (2019). "Global glacier mass changes and their contributions to sea-level rise from 1961 to 2016". In: *Nature* 568.7752, pp. 382–386. DOI: 10.1038/s41586-019-1071-0.

Zeng, X., G. A. McMechan, and T. Xu (2000). "Synthesis of amplitude-versus-offset variations in ground-penetrating radar data". In: *Geophysics* 65.1, pp. 113–125. DOI: 10.1190/1.1444702.

Appendices

Appendix A

FDTD modelling and the Yee algorithm

Here I summarise the basis of the Yee algorithm, as used for the finite-difference time-domain modelling (FDTD) approach used in Chapter 5, along with several key considerations for modelling using the FDTD approach.

Faraday's and Ampere's laws can be writen in differential form as

$$\frac{\partial \mathbf{B}}{\partial t} = -\nabla \times \mathbf{E} - \mathbf{M} \tag{A.1}$$

$$\frac{\partial \mathbf{D}}{\partial t} = \nabla \times \mathbf{H} - \mathbf{J} \tag{A.2}$$

where the following symbols are

- $\mathbf{E}$: electric field (volts/metre)
- $\mathbf{H}$: magnetic field (amperes/metre)
- $\mathbf{D}$: electric flux density (coulombs/metre ^{2})
- $\mathbf{B}$: magnetic flux density (webers/metre^2)
- $\mathbf{J}$: electric current density (amperes/metre^2)
- $\mathbf{M}$: equivalent magnetic current density (volts/metre^2)

The mathematical operation $\nabla \times \mathbf{E}$ represents the curl operator, which in a 3-dimensional Cartesian coordinate system with unit vectors $\mathbf{i}, \mathbf{j}, \mathbf{k}$ expands to

the following

$$\nabla \times \mathbf{E} = \Big(\frac{\partial E_z}{\partial y} - \frac{\partial E_y}{\partial z}\Big)\mathbf{i} + \Big(\frac{\partial E_x}{\partial z} - \frac{\partial E_z}{\partial x}\Big)\mathbf{j} + \Big(\frac{\partial E_y}{\partial x} - \frac{\partial E_x}{\partial y}\Big)\mathbf{k} \tag{A.3}$$

For the case of a linear, isotropic material, **D** and **E**, and **B** and **H** are linked through

$$\mathbf{D} = \epsilon_r \epsilon_0 \mathbf{E} \tag{A.4}$$

$$\mathbf{B} = \mu_r \mu_0 \mathbf{H} \tag{A.5}$$

where:

- ϵ_r : relative permittivity (dimensionless)
- ϵ_0 : permittivity of free space (8.854×10^{-12} farads/metre)
- μ_r : relative permeability (dimensionless)
- μ_0 : permeability of free space ($4\pi \times 10^{-7}$ henrys/metre)

Current density **J** and **M** act as an input to the system. In attenuative media, we can consider the losses as a result of conversion to thermal energy

$$\mathbf{J} = \mathbf{J}_{\text{source}} + \sigma \mathbf{E} \tag{A.6}$$

$$\mathbf{M} = \mathbf{M}_{\text{source}} + \sigma^* \mathbf{H} \tag{A.7}$$

Combining equations A.4 - A.7 with A.1 and A.2 we can derive Maxwell's curl equations as

$$\frac{\partial \mathbf{H}}{\partial t} = -\frac{1}{\mu}\nabla \times \mathbf{E} - \frac{1}{\mu}\Big(\mathbf{M}_{\text{source}} + \sigma^* \mathbf{H}\Big) \tag{A.8}$$

$$\frac{\partial \mathbf{E}}{\partial t} = \frac{1}{\epsilon}\nabla \times \mathbf{H} - \frac{1}{\epsilon}\Big(\mathbf{J}_{\text{source}} + \sigma \mathbf{E}\Big) \tag{A.9}$$

.

These can now be written in Cartesian coordinates as

$$\frac{\partial \mathbf{H}_x}{\partial t} = \frac{1}{\mu}\Big[\frac{\partial \mathbf{E}_y}{\partial z} - \frac{\partial \mathbf{E}_z}{\partial y} - \mathbf{M}_{\text{source}_\mathbf{x}} + \sigma^* \mathbf{H}_\mathbf{x}\Big] \tag{A.10}$$

$$\frac{\partial \mathbf{H}_y}{\partial t} = \frac{1}{\mu}\left[\frac{\partial \mathbf{E}_z}{\partial x} - \frac{\partial \mathbf{E}_x}{\partial z} - \mathbf{M}_{\mathrm{source_y}} + \sigma^* \mathbf{H_y}\right] \tag{A.11}$$

$$\frac{\partial \mathbf{H}_z}{\partial t} = \frac{1}{\mu}\left[\frac{\partial \mathbf{E}_x}{\partial y} - \frac{\partial \mathbf{E}_y}{\partial x} - \mathbf{M}_{\mathrm{source_z}} + \sigma^* \mathbf{H_z}\right] \tag{A.12}$$

$$\frac{\partial \mathbf{E}_x}{\partial t} = \frac{1}{\mu}\left[\frac{\partial \mathbf{H}_z}{\partial y} - \frac{\partial \mathbf{H}_y}{\partial z} - \mathbf{J}_{\mathrm{source_x}} + \sigma^* \mathbf{E_x}\right] \tag{A.13}$$

$$\frac{\partial \mathbf{E}_y}{\partial t} = \frac{1}{\mu}\left[\frac{\partial \mathbf{H}_x}{\partial z} - \frac{\partial \mathbf{H}_z}{\partial x} - \mathbf{J}_{\mathrm{source_y}} + \sigma^* \mathbf{E_y}\right] \tag{A.14}$$

$$\frac{\partial \mathbf{E}_z}{\partial t} = \frac{1}{\mu}\left[\frac{\partial \mathbf{H}_y}{\partial x} - \frac{\partial \mathbf{H}_x}{\partial y} - \mathbf{J}_{\mathrm{source_z}} + \sigma^* \mathbf{E_z}\right] \tag{A.15}$$

The above set of equations constitute the differential form of equations A.1 and A.2, forming the basis of the FDTD method.

The FDTD formulation of these equations uses an discretisation approach (Fig. A.1) after Yee (1966) whereby **E** and **H** are modelled on a 3D grid. Finite differences are calculated using a 1st-order central-difference approach. The model is usually initialised using a current source ($\mathbf{J_{source}}$ in equations A.10 to A.15).

A.1 TMz reduction to 2D

To reduce the above equations (A.10 to A.15) to two dimensions, two steps are taken; first, all partial derivatives with respect to z are set to zero, followed by a grouping by sets of field vectors. The most common approach uses H_x, H_y and E_z, generating the following three equations:

$$\frac{\partial \mathbf{H}_x}{\partial t} = \frac{1}{\mu}\left[-\frac{\partial \mathbf{E}_z}{\partial y} - \mathbf{M}_{\mathrm{source_x}} + \sigma^* \mathbf{H_x}\right] \tag{A.16}$$

$$\frac{\partial \mathbf{H}_y}{\partial t} = \frac{1}{\mu}\left[\frac{\partial \mathbf{E}_z}{\partial x} - \mathbf{M}_{\mathrm{source_y}} + \sigma^* \mathbf{H_y}\right] \tag{A.17}$$

$$\frac{\partial \mathbf{E}_z}{\partial t} = \frac{1}{\mu}\left[\frac{\partial \mathbf{H}_y}{\partial x} - \frac{\partial \mathbf{H}_x}{\partial y} - \mathbf{J}_{\mathrm{source_z}} + \sigma^* \mathbf{E_z}\right] \tag{A.18}$$

The reduction to 2D significantly reduces the computational requirements

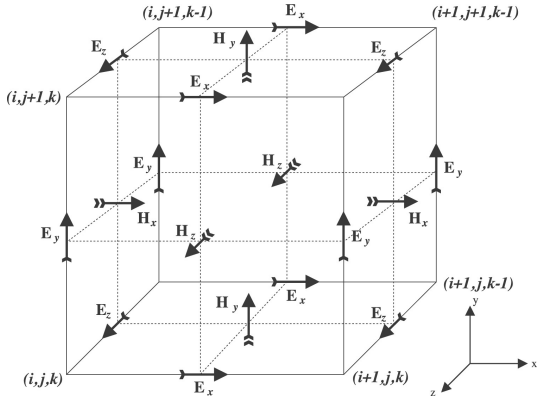

Figure A.1: 3D Yee cell used in FDTD modelling

of generating a model, yet results in a 2D scaling of amplitude, and a $\pi/4$ phase shift relative to the 3D model equivalent (Auer et al., 2013).

A.2 Spatial discretisation and dispersion

Spatial discretisation is an important consideration to avoid numerical dispersion. Numerical dispersion is caused by variations in phase velocity as a function of angle, due to the grid orientation of the Yee cell, and wavelength (Giannopoulos, 1998; Taflove and Hagness, 2005). Overcoming numerical dispersion requires use of a small discretisation ($\Delta l = \Delta x = \Delta y = \Delta z$), though this must be balanced against computational demands. While there is no formal approach to deciding spatial discretisation, a general rule of thumb, following (Giannopoulos, 1998) is as follows:

$$\Delta l = \frac{\lambda_c}{10} \tag{A.19}$$

where λ_c is the shortest wavelength associated with the source waveform.

A.3 Numerical stability

To ensure numerical stability, time step Δt must be sufficiently low to avoid numerical dispersion. The stability criterion follows the Courant, Freidrichs,

Lewy (CFL) condition whereby

$$\Delta t \leq \frac{1}{c\sqrt{\frac{1}{(\Delta x)^2} + \frac{1}{(\Delta y)^2} + \frac{1}{(\Delta z)^2}}} \tag{A.20}$$

where Δx, Δy, and Δz are the spatial discretisation of the model used.

Appendix B

Formatted *Annals of Glaciology* paper

Annals of Glaciology

Article

Cite this article: Delf R, Schroeder DM, Curtis A, Giannopoulos A, Bingham RG (2020). A comparison of automated approaches to extracting englacial-layer geometry from radar data across ice sheets. *Annals of Glaciology* **61** (81), 234–241. https://doi.org/10.1017/aog.2020.42

Received: 1 December 2019
Revised: 17 May 2020
Accepted: 18 May 2020
First published online: 17 June 2020

Key words:
Radio-echo sounding; glacier geophysics; Antarctic glaciology

Author for correspondence:
Richard Delf, E-mail: r.delf@ed.ac.uk

cambridge.org/aog

A comparison of automated approaches to extracting englacial-layer geometry from radar data across ice sheets

Richard Delf[1,2], Dustin M. Schroeder[3], Andrew Curtis[1], Antonios Giannopoulos[4] and Robert G. Bingham[1]

[1]School of GeoSciences, University of Edinburgh, Edinburgh, UK; [2]Department of Arctic Geology, University Centre in Svalbard, Longyearbyen, Norway; [3]Department of Geophysics, Stanford University, Stanford, CA, USA and [4]School of Engineering, University of Edinburgh, Edinburgh, UK

Abstract

Radar surveys across ice sheets typically measure numerous englacial layers that can often be regarded as isochrones. Such layers are valuable for extrapolating age–depth relationships away from ice-core locations, reconstructing palaeoaccumulation variability, and investigating past ice-sheet dynamics. However, the use of englacial layers in Antarctica has been hampered by underdeveloped techniques for characterising layer continuity and geometry over large distances, with techniques developed independently and little opportunity for inter-comparison of results. In this paper, we present a methodology to assess the performance of automated layer-tracking and layer-dip-estimation algorithms through their ability to propagate a correct age–depth model. We use this to assess isochrone-tracking techniques applied to two test case datasets, selected from CreSIS MCoRDS data over Antarctica from a range of environments including low-dip, continuous layers and layers with terminations. We find that dip-estimation techniques are generally successful in tracking englacial dip but break down in the upper and lower regions of the ice sheet. The results of testing two previously published layer-tracking algorithms show that further development is required to attain a good constraint of age–depth relationships away from dated ice cores. We recommend that auto-tracking techniques focus on improved linking of picked stratigraphy across signal disruptions to enable accurate determination of the Antarctic-wide age–depth structure.

Introduction

Ice-sheet englacial stratigraphy is prevalent throughout radar-sounding data collected over Antarctica and Greenland (e.g. Bailey and others, 1964; MacGregor and others, 2015; Schroeder and others, 2019). Due to the isochronous nature of most englacial layers (Siegert, 1999) such stratigraphy has been used to extrapolate age–depth relationships away from deep ice cores (Siegert and others, 2003; Siegert and Payne, 2004; MacGregor and others, 2015; Cavitte and others, 2016) to calculate palaeoaccumulation rates and variability (Fahnestock and others, 2001; Hindmarsh and others, 2009; Karlsson and others, 2014; Koutnik and others, 2016; Cavitte and others, 2018) and to make inferences concerning historical and contemporary ice dynamics (Nereson and others, 2000; Rippin and others, 2003; Siegert and others, 2003; Leysinger Vieli and others, 2007; Parrenin and Hindmarsh, 2007; Carter and others, 2009; Bingham and others, 2015; Holschuh and others, 2017).

To date, most studies exploiting ice-sheet englacial stratigraphy have employed manual tracing approaches, which can be prohibitively slow. After five decades of radioglaciology, and many thousands of radar profiles already in the archive and, in principle, available for ice-sheet modelling applications, it is imperative to develop automated and semi-automated approaches to trace englacial layers and/or characterise englacial-layer dip. This is far from straightforward, with surveys across Antarctica especially having been undertaken using a wide range of radar systems with different performance characteristics (Winter and others, 2017).

In this paper, we present a scheme for assessing the relative effectiveness of automated interpretation algorithms in a range of englacial stratigraphic settings. We apply each algorithm to a set of control radargrams from East Antarctica that cover the full range of englacial-layering geometries from continuous (typically associated with steady ice flow) to buckled/discontinuous (typically associated with fast or variable flow; Karlsson and others, 2012). We focus on two sets of algorithms: those that focus on tracing layers or layer continuity; and those that extract the slope, or dip, of englacial layers. The former are, in principle, of primary value for extracting age–depth information across ice sheets (e.g. MacGregor and others, 2015), while the latter have been advocated as a more practical alternative input for ice-sheet modelling (Holschuh and others, 2017). Our principal objective is to present a set of performance metrics for the intercomparison of algorithms as applied to future datasets. We use our results to highlight the principal shortcomings of current implementations of layer autotracking algorithms, and make recommendations for future development of automated interpretation algorithms to facilitate continent-scale interpretation.

Data and methodology

Reference data

We focus on two reference datasets from the CReSIS data archive (https://data.cresis.ku.edu/, accessed 04/09/19, CReSIS, 2016). The datasets were chosen to present variable levels of challenge to automated picking algorithms. Example 1 was acquired across the Vostok region of East Antarctica on 27/11/2013 (frames 01_034-036, 77.0825°S 111.1064°E to 76.4341°S 116.3196°E), and represents a set of relatively low-dip, continuous englacial layers throughout much of the ice depth (Fig. 1). Example 2 was obtained over Antarctica's Gamburtsev Mountain Province on 25/12/2008 (frames 04_002-005, 83.7551°S 75.0735°E to 82.4212°S 75.9330°E), and includes numerous reflector terminations and conflicting dips throughout. We begin with data lodged in the archive from processing stage L1B, after pulse compression, coherent channel averaging and SAR focusing through f-k migration (CReSIS, 2016). We firstly applied a simple high-pass filter by convolving the data with a Gaussian kernel in time and subtracting this from the original data to remove the trend of decreasing amplitude with depth, as in Panton (2014), which balances the amplitudes of near-surface, high amplitude reflections and deeper, low amplitude reflections. To generate reference englacial-layer picks, against which to test the further algorithms explored in this study, we imported the radargrams into Schlumberger Petrel, wherein we then traced layers using a combination of semi-automated local maxima peak tracking, guided tracking and fully manual tracking. For example 1, we were able to pick 33 layers, mostly continuously traversing the 147 km radar profile; for example 2, we picked 36 layers across a 145 km radar profile as a greater number of reflector terminations are observed.

Automated isochrone picking

To our reference radar datasets, we applied three algorithms designed to trace layers automatically, which, for simplicity, we will hereafter term the ARESELP, Steger and Sobel-Feldman algorithms. The Automated Radio-Echo Sounding Englacial Layer-tracing Package (ARESELP) autotracker algorithm was developed by Xiong and others (2018) to autotrace englacial layers. It uses a continuous wavelet transform (CWT) peak detection algorithm with an assumed Ricker or Morlet wavelet, combined with local Hough transform, to estimate local dip and propagate picks away from peak CWT response (seed) points. Initial tests showed that optimum performance was attained using a Morlet wavelet for the CWT and a block size of 20 pixels, ~50 m (depth) × 1500 m (along track) (assuming $v_{ice} = 1.68 \times 10^8$ ms^{-1}). We found that the Ricker wavelet applied by Xiong and others (2018), while suppressing noise in regions of high amplitude stratigraphy, failed to generate picks in lower amplitude regions (e.g.between 90 and 120 km in Fig. 2a).

The Steger algorithm is an image-processing technique that follows Ferro and Bruzzone (2013) in applying a pre-conditioning block-matching and 3D-filtering process (BM3D filter) (Dabov and others, 2007), followed by a Steger filter ridge detection algorithm (Steger, 1998) to enhance and detect englacial layering. In this image-processing context, the 'ridges' being detected equate to sets of amplitude peaks in adjacent traces, that represent englacial layers on radargrams. Ferro and Bruzzone (2013) applied this technique to extract layering in Mars' North Polar Ice Cap, but it has not previously been applied to terrestrial radar data. To our reference data, we firstly applied the BM3D filter followed by a stretch to the range [0,255] and application of the Steger ridge detector, filtering to a minimum line length of 50 pixels with an upper and lower threshold of 0.5 and 1, respectively.

Finally, the Sobel–Feldman algorithm is an image-processing edge-detection tool that identifies peak gradients in image brightness (Sobel, 1990). We apply this to the reference data wherein the edges equate to englacial layers, then skeletonise the results to binary images of the detected lines, filtered to remove lines below a minimum size of 50 pixels. This approach is the most simplistic but has the lowest computational cost.

Age–depth relationship propagation

One means of assessing layer-tracking performance is to test the effect each imposes on the propagation of an age–depth relationship through the ice sheet. To gauge this, we deployed a technique similar to MacGregor and others (2015), but using a synthetic age–depth profile. We generated a synthetic age–depth relationship using a 1-dimensional Nye model of reflector depth (Nye, 1963), as implemented in Leysinger Vieli and others (2011) by

$$A = \frac{H}{a}\ln\left(\frac{z-b}{H}\right), \quad (1)$$

where A is the age (years), H, z and b are ice thickness, elevation in the ice column and bed elevation respectively (all in m), and a is the mean accumulation rate (ma^{-1}). We use a representative average accumulation rate of 0.05 ma^{-1}, typical of East Antarctica (e.g. Leysinger Vieli and others, 2004), although only the relative amplitudes of errors reported here are of interest and the findings are independent of this rate. This approach makes the assumption of steady-state flow with zero horizontal advection and that all motion is due to basal sliding. We intersect picked isochrones (henceforth referred to as picks) at location A (Fig. 1a) with this age–depth relationship, which can be considered to be similar to a synthetically generated ice core with a known age–depth profile, and assign an age to each pick. We then propagate this age–depth relationship away from A. For each trace, we generate a 1-dimensional age–depth relationship from previously dated picks using a spline interpolation, then assign an age to each un-dated pick with the generated profile. All dated picks are then used to generate the age–depth relationship for the subsequent trace. We then extract the interpolated age–depth profile at a second location A' (Fig. 1a).

A principal benefit of manual interpretation is the ability to match layers through regions of discontinuous reflectors by recognising patterns or packages of reflections (see, e.g. Karlsson and others, 2014). For each picked isochrone, we calculate the degree of connectivity between that pick and the starting age–depth profile at A (Fig. 1a). Uninterrupted picks intersecting A are assigned a score of 0 as they present the lowest age uncertainty, assuming the pick is correctly aligned with an isochrone. For each interpolation required to assign a date to a new pick, the connectivity increases by one. The newly dated pick is assigned this score of connectivity, and used for subsequent pick dating. This approach to assessing uncertainty highlights when the interpretation consists of a high number of disconnected isochrones, potentially indicating a high sensitivity to low amplitude signal anomalies.

Englacial dip estimations

To extract dip fields through the reference data, we applied three approaches, which we will hereafter term Panton, ARESP and PWD. The Panton algorithm is described as Step 2 in Panton (2014). We convolve the radar data with a variably-slanted Gaussian kernel to derive the maximum stacking amplitude as a function of dip. The dip field is then filtered to remove noise caused by regions of low signal amplitude, characterised by

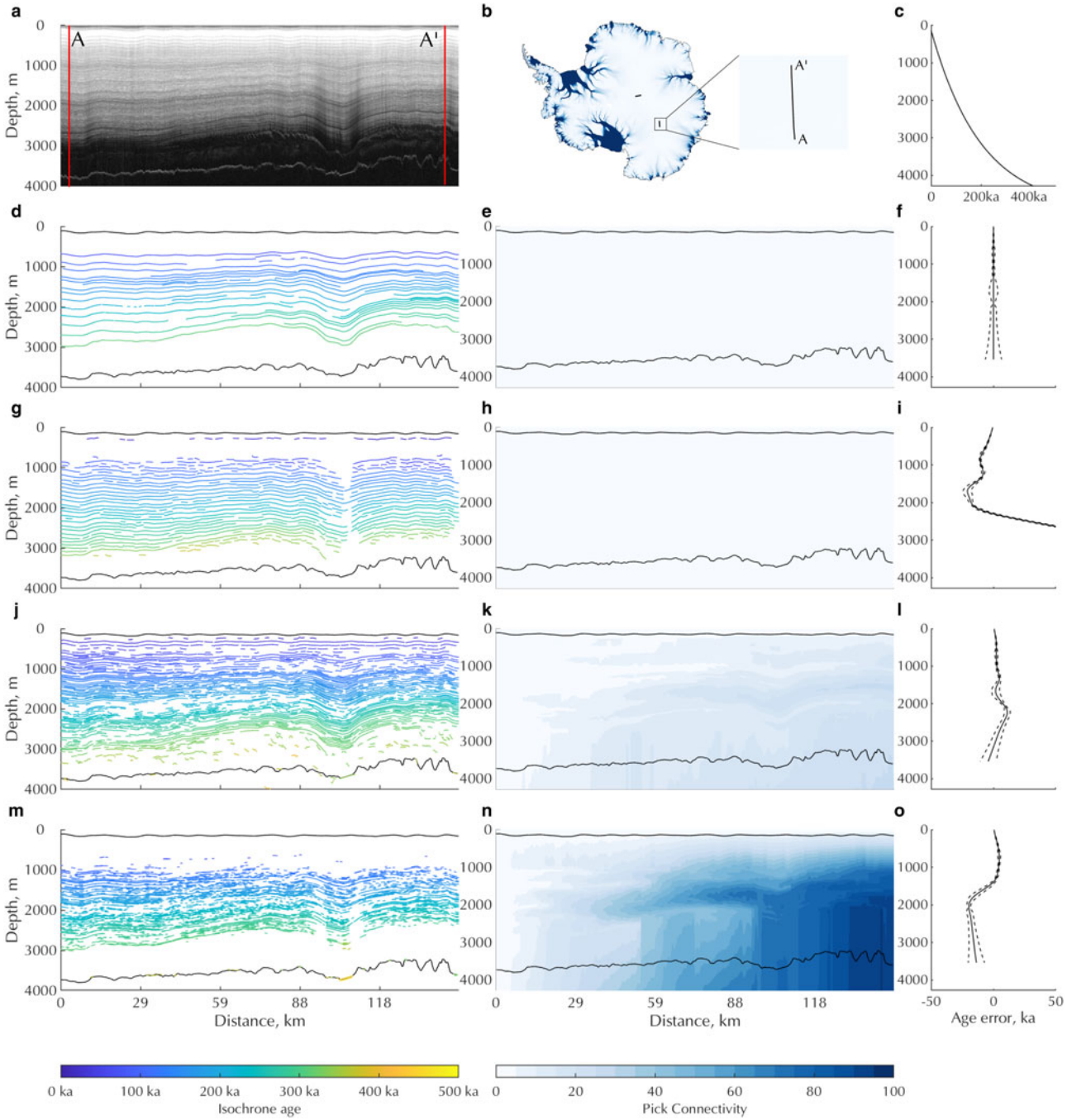

Fig. 1. Comparison of age propagation through auto-tracked isochrones. (a) The raw radar data showing coherent, low-dip layers. (b) Location within Antarctica. (c) Synthetic age–depth relationship applied at location A. (d) Manually-picked reference dataset with (e) isochrone connectivity metric and (f) profile of misfit between reference picks age–depth relationship with uncertainties propagated through the picks. (g) Englacial picks, (h) isochrone-connectivity metric and (i) misfit profile for ARESELP algorithm. (j) Englacial picks, (k) isochrone-connectivity metric and (l) misfit profile for Steger algorithm. (m) Englacial picks, (n) isochrone-connectivity metric and (o) misfit profile for Sobel–Feldman algorithm.

bands of dip noise between layers, by using an amplitude-weighed spline filter of dip. In Panton (2014), this procedure was presented mainly as pre-processing for englacial-layer tracing, but for this paper, we treat it as one of the direct methods that can be used to extract englacial-layer dip fields across wide swathes of ice sheets.

The Automated Radio Echo Sounding Processing (ARESP) algorithm (Sime and others, 2011) firstly applies horizontal stacking to reduce SNR, followed by a binarisation of layers and estimation of local dip of high amplitude signals using a moving window approach.

The plane wave destruction (PWD) algorithm follows Fomel (2002) in minimising the convolution of a predicted texture with the data to derive local slope. While the Panton and ARESP algorithms have previously been applied widely to radar surveys in Greenland (Sime and others, 2014; Panton and Karlsson, 2015), the PWD method, used routinely in seismic-data processing, is yet to be applied in radioglaciology.

To assess the performance of each algorithm in deriving englacial-layer dip, we use the synthetic age–depth profiles derived previously and consider that the dip of an isochronous reflector will be perpendicular to the angle of maximum gradient. The dip field relative to the surface can therefore be calculated as:

$$\theta = \tan^{-1}\frac{g_y}{g_x} - 90 \quad (2)$$

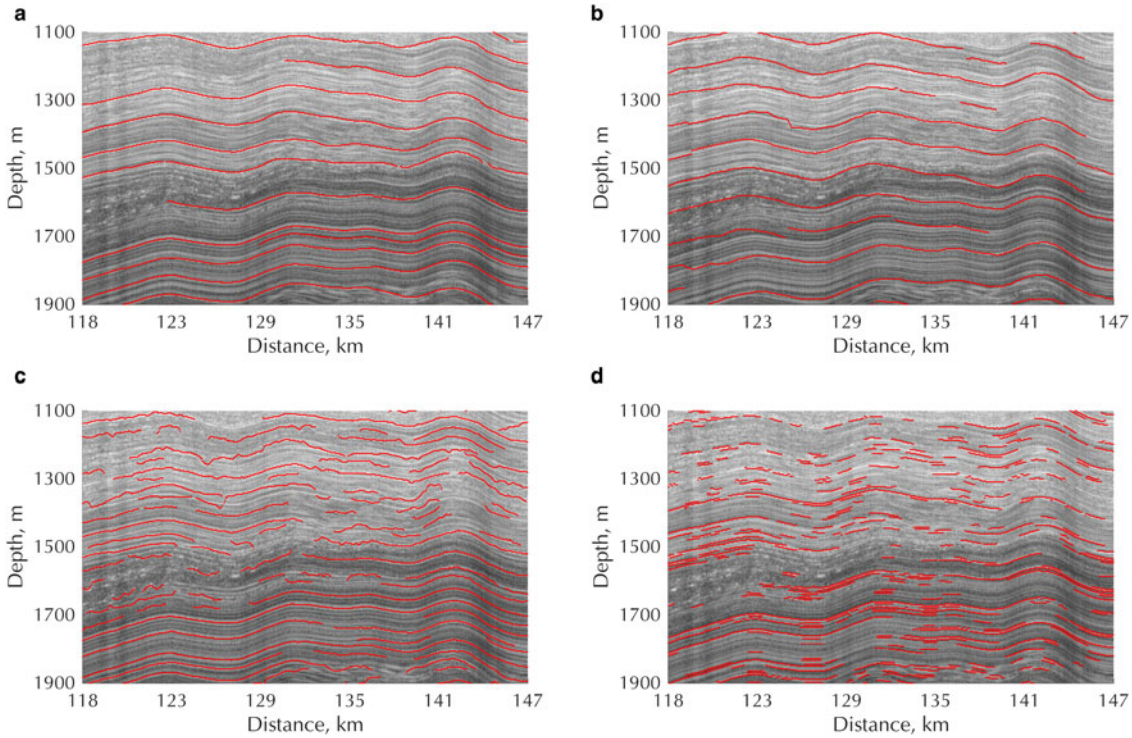

Fig. 2. Detail of each isochrone tracking methodology showing different failure points for each algorithm: (a) Manually-picked reference dataset, (b) ARESELP, (c) Steger filter and (d) Sobel edge detection.

where $g_x = \mathrm{d}A/\mathrm{d}x$ and $g_y = \mathrm{d}A/\mathrm{d}y$ and $A(x, y)$ is the inferred age–depth structure as a function of trace x and depth y. We then propagated a streamline through the data, which represents an integral across the dip field, starting from the location of the synthetic ice core described previously. This highlights the variation in algorithm performance as a function of depth through the radargram.

Results

Isochrone tracking

Figure 1 presents the application of our workflow to our reference data (frames 01_034-036 collected 27/11/2013, Fig. 1a), from East Antarctica's Vostok region, characterised by low dip, continuous reflectors. Parallel results for the more disrupted radar profiles across the Gamburtsev Mountains are presented in Supplementary Figure 1. The numerical results for isochrone tracking algorithms are summarised in Table 1. Englacial layers extracted using ARESELP indicated a high degree of continuity along the section (Fig. 1g). This approach took 4 min 56 s for the example 1 dataset. We extracted 66 individual elements, that in effect pick out most of the englacial layers that we had picked manually, yet the error between reference age–depth profiles at A' shows a significant deviation of up to − 25 ka in the upper 50% of the ice column with a significant swing to positive errors ~100 ka deeper in the ice column (Figs 1h and i). This error can be traced to breaks in the englacial layers in two ways. Firstly, the algorithm fails to constrain multiple isochrones crossing the amplitude low at 90–120 km, resulting in a region over which the age–depth profile is continued unconstrained in the deeper ice. Secondly, there are additional breaks in layer continuity in the upper layers across which the linking stage of the algorithm has mismatched wavelet peaks between seed points of the layers either side of the breaks.

The Steger approach shows improvements in some areas (Figs 1j–l) over the ARESELP algorithm. The retrieved age–depth profile shows a maximum error of 10 ka in the deepest regions of ice (Fig. 1l), but there is a greater degree of disconnectivity between A and A' than for ARESELP (compare Fig. 1l with Fig. 1i). This approach took 48 s per radargram for the BM3D filter, and 23 s for the picking and isochrone linking. We undertook parameter testing to increase the sensitivity to cross the amplitude low at 90–120 km, which led to an increase of picking success, but with an increase of false alarms in the deepest regions of ice. Overall, the Steger algorithm was able to identify 1076 elements in the radargram, compared with 66 from ARESELP, comparatively identifying more isochrones but with more disconnectivity. Up to 35 interpolations were required to constrain the age model throughout (Fig. 1k).

The Sobel–Feldman edge-detection algorithm extracted the highest number of individual elements (3210) throughout the data (Fig. 1m), showing a high sensitivity to low-amplitude signals. This is also highlighted through the degree of connectivity between A and A', where the maximum number of interpolations reaches 91 at the bed (Fig. 1n). This approach typically took under 1 s for each radargram. This experiment serves to highlight that although a good constraint on age–depth relationship can be achieved using simple edge-detection implementations, the uncertainties associated with propagating age between a high number of low-quality picks suggest that such approaches should be avoided.

Figure 2 shows a detailed sub-set of the data shown in Figure 1 to better highlight the relative strengths and weaknesses of each of the three tracing approaches. The ARESELP algorithm shows the most continuity and smoothest reflector dip throughout the data. In regions of good signal to noise ratio, the Hough transform approach to isochrone linking generally performs well, but dips deviate from the radargram structure for numerous internal layers (e.g. the layer starting at 1550 m depth). There are also numerous picks where the interpretation fails to trace reflector peaks successfully or, more significantly, jumps at a high angle (e.g. depth ≈ 1400 m in Fig. 2b). This can give rise to substantial

Table 1. Summary of quantitative assessment of auto-tracking algorithms. *N* is the number of elements (picks) generated by the algorithm, ⟨*L*⟩ is the average length of these picks in number of traces, *Median age error* and *Max age error* are the median and maximum difference between interpreted and reference age-depth profiles at A' (Fig. 1a), and *Max Conn.* is the maximum value of the connectivity index at A'

	Example 1					Example 2				
Method	*N*	⟨*L*⟩ (traces)	Median age error (ka)	Max age error (ka)	Max Conn.	*N*	⟨*L*⟩ (traces)	Median age error (ka)	Max age error (ka)	Max Conn.
Manual	33	2425	N/A	N/A	4	36	1222	N/A	N/A	5
ARESELP	66	1652	14.9	101.2	5	95	885	6.4	70.0	11
Steger filter	1076	185	2.7	11.1	35	641	134	19.3	92.4	34
Sobel-Feldman	3210	57	13.8	19.7	91	6391	28	97.1	207.0	127

deviations in the age–depth profile propagated along profiles. This behaviour reflects the results of Figures 1g–i, where the ARESELP algorithm shows that a low degree of connectivity (Fig. 1h) can be achieved between A and A', but large errors in age–depth relationship are obtained when compared to the reference dataset (Fig. 1i).

The Steger filter gives much more variability and a rougher pick as each ridge is picked independently of the previous one; there is only limited local directional guidance between traces. As such, in regions of strong signal with continuous isochrones the ridge tracking performs well in estimating the dip of structures within the radargram (in general, in the deeper regions of Fig. 2c). Increasing noise levels in the upper region of the figure (depths <1400 m) result in a larger number of noisy, conflicting-dip picks which do not track the radargram structure well. From Figures 1j–l, the general ability of the Steger filter to track the dip of continuous reflectors results in a better age–depth error compared to the ARESELP algorithm, but with more age interpolations required to connect A and A'.

The Sobel–Feldman edge detection algorithm is similar in that the linking is unguided by dip and shows similar variation and susceptibility to the variation of reflection amplitude to the Steger pick. The sensitivity of the Sobel–Feldman technique is higher to low-amplitude signals, resulting in the higher number of picks, but should be noted that despite this, the Sobel–Feldman shows a much lower susceptibility to crossing radargram layers in Figure 2d compared to both the Steger filter and ARESELP algorithms. This results in a much larger number of interpolations required to propagate the age–depth structure, which is reflected in Figure 1n.

Dip estimation techniques

Figure 3 presents englacial-dip fields along profile AA' derived directly from the manual englacial-layering picking (panel a) then from the three automated approaches. The Panton approach to dip estimation (Fig. 3b) shows a good agreement with the reference dataset. This approach includes a step to remove noise in regions of low amplitudes and applies an interpolation across such regions. There is also little differentiation between noise and englacial-layer dips, such that incorrect dips are propagated across the echo-free zone, shown for example by a reversal of the dip at the deepest regions of ice at ~110 km along the profile and small-scale variations close the lowest streamline in Figure 3b.

The ARESP approach exhibits higher sensitivity to lower-SNR regions, highlighted in the middle of the ice column at 110 km (Fig. 3c). Beneath the lowest traced englacial layer the average dip is zero, although slight noise in dip amplitude is observed.

Finally, the PWD method yields a higher degree of smoothing than ARESP, and has a flat streamline through the deepest ice. It is, however, sensitive to non-zero dips in the near surface that are not present or detected by the other techniques, and the uppermost streamlines deviate towards the surface as a result.

Discussion

Isochrone tracking intercomparison

Xiong and others (2018) compared their ARESELP results to the picks from the manually-constrained interpretation of MacGregor and others (2015) using a direct overlay of extracted isochrones, which enabled only a limited degree of inter-comparison and quantitative assessment. Ferro and Bruzzone (2013) similarly used a manually-picked dataset as a reference against which to compare their application of the Steger algorithm, but further compared their results in terms of false alarms and missed layers to guide optimal parameter selection. Critically, neither of these approaches facilitated quantitative insights into the glaciological implications of incorrect picking in an automated algorithm, which we can gain from the age–depth relationship propagation.

The results of this comparison show that significant errors in age–depth structure can result from isochrone tracking algorithms. On our least complex dataset, the best algorithm resulted in a 11.1 ka error, but with large uncertainties due to the low number of continuous reflections between A and A'. Cavitte and others (2016) model the age uncertainty from manual layer tracking as a combination of ice core age uncertainty and the radar range resolution and estimate an upper bound of uncertainty of 3.73 ka. Winter and others (2019) similarly estimate typical errors <2 ka, but up to 3.7 ka. Hence, none of the isochrone-tracking methods trialled in this study is yet able to rival the accuracy of picking englacial layers manually. However, manual interpretation of multiple layers takes of the order of days per 100 km, especially where the layering structure is disrupted or broken. Expanding this across the Antarctic data record, with ongoing surveys with ever-improving resolution rapidly becomes a considerable effort, which motivates the further development of auto-tracking algorithms.

The approach to age–depth propagation used here comprises a simpler implementation of the effective-strain estimation approach of MacGregor and others (2015), giving an interpolated fit rather than a physically-derived age–depth profile between isochrones. We found that due to the noisy and potentially converging layer picks from the automated approaches tested here, effective-strain estimations can be highly variable resulting in rapid deviations away from the expected ages. As algorithms improve, age propagation through a local strain estimation should be used. Despite ours being an approximate approach, it nonetheless gives insights into the performance of age-structure propagation through picked isochrones beyond a direct comparison of picked horizons.

Our approach to age–depth uncertainty using synthetic ice-core connectivity also highlights further issues that may be encountered with auto-tracking techniques. When manual picking is used, isochrones may be tracked across discontinuous regions in the absence of intersections with other interpreted profiles through recognising similar packages of reflections on either side of the noisy region (Cavitte and others, 2016; Ashmore and

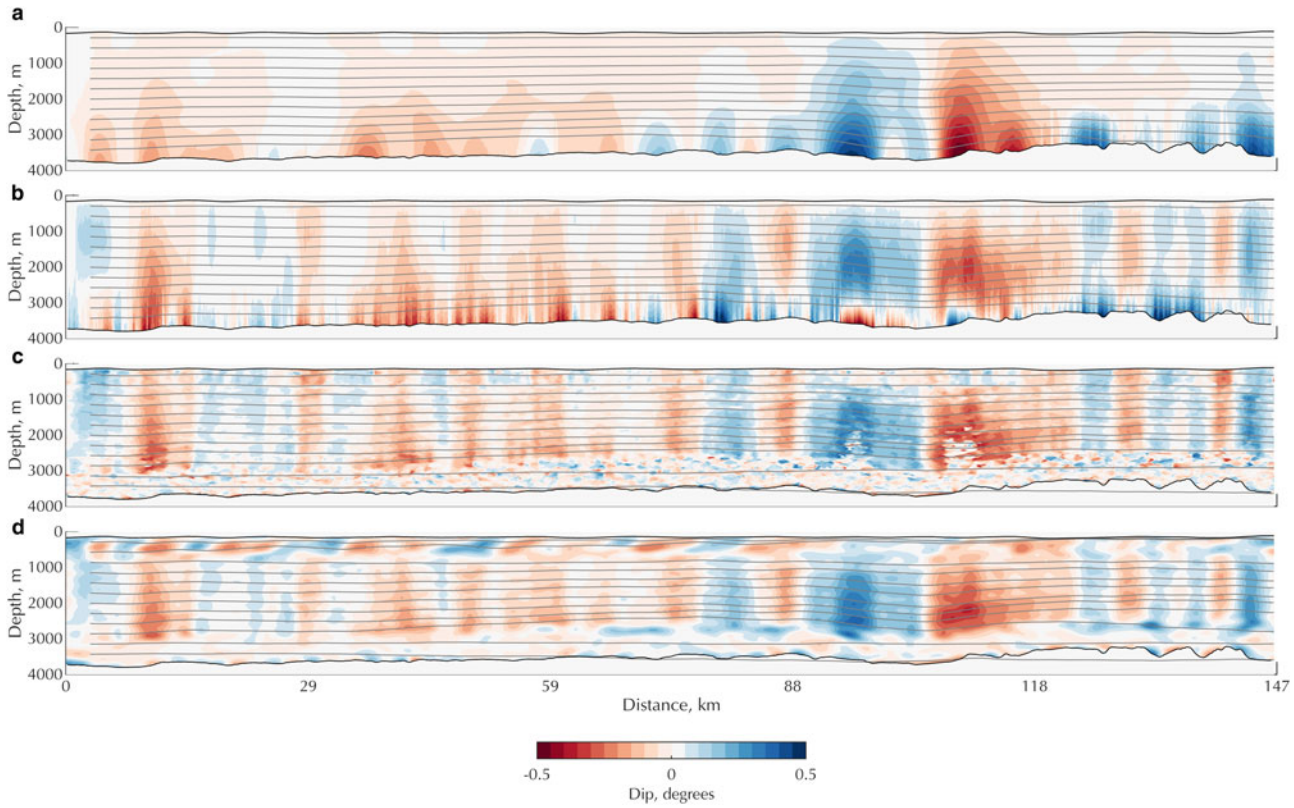

Fig. 3. Propagation of a streamline through dip fields derived from (a) reference picks, (b) Panton slope-extraction step, (c) ARESP and (d) using PWD.

others, 2020), similar to practice in the seismic interpretation workflow (Nanda, 2016). However, none of the automated layer-tracking algorithms investigated here have implementations that allow the recognition, and matching, of similar packages of layers across gaps in the records. Such shortcomings that have challenged wider layer-tracing efforts have indeed been one of the major motivations for developing dip tracking as an alternate approach. Matching layer packages has long been a challenge in the field of automated seismic interpretation, where discontinuities are prevalent as faults. Discontinuities could potentially be overcome using artificial neural networks (Harrigan and others, 1992) or through global interpretation (Hoyes and Cheret, 2011) but these approaches have yet to be applied to ice-sheet radiostratigraphy.

Future automated interpretation techniques need to target automated linking of interpreted horizons to match disconnected isochronal picks derived from the local peak tracking. The principal issue experienced with implementations tested here relates to trackers deviating from the target reflection. The ARESELP algorithm overcomes this to an extent as a result of the use of a Hough transform, yet still results in errors of age–depth profile as a result of deviations away from the data stratigraphy. Such linking may further be enhanced using correlation or artificial neural network approaches to signal matching, or through tracking along multiple trajectories using a confidence-based metric. The example and approach of age propagation testing presented here could be used to test these approaches.

Isochrone dip estimation

Each of the tested dip-retrieval algorithms worked well in the case of high-amplitude, high-SNR regions of the radargram. Failures occurred at three major locations: the deepest regions of ice with weaker or absent echoes; where englacial layers dip most steeply and SNR drops; and in the near surface. These are each where the signal power drops, or where local amplitudes vary rapidly as in the near surface. To combat this, operational use of algorithms could limit dip estimation to the middle of the ice column, following an approach commonly adopted for estimating layer continuity where the upper and lower 20% of the ice column are not used (Karlsson and others, 2012; Bingham and others, 2015). The Panton approach tested here did attempt to remove such low-amplitude regions by removing high spatial-frequency noise, but the drawback of this approach is the interpolation and associated loss of information from regions where dip is high, e.g. in the lower ice. This compares to Holschuh and others (2017), who used signal-amplitude thresholding within a moving window to reduce the impact of low-amplitude areas, returning a zero dip field in these regions.

Modern SAR processing of airborne phase-coherent data offers opportunities for direct estimation of englacial-layer dip. Castelletti and others (2019) presented a process to derive englacial-layer dips using retrieved phase before stacking to undertake in phase-coherent systems to reduce the effects of destructive stacking described in Holschuh and others (2014). Such an approach shows promising results in retrieving a dip field and enhancing layer coherence from complex data, but has yet to be applied to a larger region of Antarctica to aid a wider interpretation of ice-sheet stratigraphy.

Conclusions

We have undertaken an intercomparison of three isochrone auto-tracking and three englacial-dip estimation algorithms which may be used for wider exploration of the englacial radio-stratigraphic structure of the Antarctic Ice Sheet. We have presented a formal procedure for evaluating these approaches relative to a manually-picked reference dataset to give a reliable indication of the benefits

and shortcomings of each isochrone tracking technique. Of the automated isochrone trackers tested here, there is only limited success in linking the age–depth profile between two locations along a relatively simple isochrone geometry. Of the three algorithms tested, the ARESELP procedure (Xiong and others, 2018) is best at retrieving substantial lengths of isochrones, yet can be prone to deviations in dip. While the Steger algorithm (Ferro and Bruzzone, 2013) shows a greater uncertainty in propagated ages, it shows an improvement in tracking general dip and a lower error in propagated age profile. Supplementing this approach with more advanced pattern-matching using, for example, neural networks to improve isochrone pick continuity is recommended.

The three different approaches to dip estimation that we tested all performed relatively well on our reference datasets, although all are challenged in the deepest ice and at the near-surface. All have the potential for higher performance by adopting improved data preprocessing, application of tapered windows or thresholding (e.g. Holschuh and others, 2017). Future developments in automated tracking should focus on the ability to automate linking of interpreted isochrones and use a similar approach to age propagation to demonstrate successful implementation. We propose that the methodology developed here, and the two datasets from East Antarctica presented in this study, covering a range of englacial conditions, may be used as a standard validation approach for future algorithm developments.

Author contribution statement

RD, DMS and RGB designed the research. RD performed the analyses at Stanford University with DMS and at the University of Edinburgh with RGB, AC and AG. RD wrote the paper, and all authors contributed edits to the final paper.

Acknowledgments. This paper was stimulated by the AntArchitecture Action Group of the Scientific Committee for Antarctic Research. RD and RGB acknowledge funding from the U.K.'s Natural Environment Research Council via RD's scholarship in the Edinburgh E^3 Doctoral Training Partnership (NE/L002558/1) and the Scottish Alliance for Geoscience, Environment and Society (SAGES) via a Postdoctoral Early Career Research Exchange (PECRE) for RD to work with DMS at Stanford University. DMS was partially supported by an NSF CAREER award. We also acknowledge support from the Trans-Antarctic Association (Small Grant TAA-04-19) that allowed RD to present the work at the IGS Radioglaciology Symposium associated with this volume. We acknowledge the use of data and/or data products from CReSIS generated with support from the University of Kansas, NSF grant ANT-0424589, and NASA Operation IceBridge grant NNX16AH54G. We thank Martin Siegert, Hester Jiskoot and one anonymous reviewer for their comments on this paper.

Supplementary material. To view supplementary material for this article, please visit https://doi.org/10.1017/aog.2020.42

References

Ashmore DW and 5 others (2020) Englacial architecture and age-depth constraints across the West Antarctic ice sheet. *Geophysical Research Letters* **47** (6), e2019GL086663. doi: 10.1029/2019GL086663

Bailey J, Evans S and Robin GdQ (1964) Radio echo sounding of polar ice sheets. *Nature* **204**(4957), 420–421. doi:10.1038/204420a0

Bingham RG and 9 others (2015) Ice-flow structure and ice dynamic changes in the Weddell Sea sector of West Antarctica from radar-imaged internal layering. *Journal of Geophysical Research: Earth Surface* **120**(4), 655–670. doi:10.1002/2014JF003291

Carter SP, Blankenship DD, Young DA and Holt JW (2009) Using radar-sounding data to identify the distribution and sources of subglacial water: application to Dome C, East Antarctica. *Journal of Glaciology* **55**(194), 1025–1040. doi:10.3189/002214309790794931

Castelletti D, Schroeder DM, Mantelli E and Hilger A (2019) Layer optimized SAR processing and slope estimation in radar sounder data. *Journal of Glaciology* **65**(254), 983–988. doi:10.1017/jog.2019.72

Cavitte MGP and 7 others (2016) Deep radiostratigraphy of the East Antarctic plateau: connecting the Dome C and Vostok ice core sites. *Journal of Glaciology* **62**(232), 323–334. doi:10.1017/jog.2016.11

Cavitte MGP and 7 others (2018) Accumulation patterns around Dome C, East Antarctica, in the last 73 kyr. *The Cryosphere* **12**(4), 1401–1414. doi:10.5194/tc-12-1401-2018

CReSIS (2016) CReSIS Radar Depth Sounder Data. Lawrence, Kansas, USA. Digital Media. http://data.cresis.ku.edu.

Dabov K, Foi A, Katkovnik V and Egiazarian K (2007) Image denoising by sparse 3-D transform-domain collaborative filtering. *IEEE Transactions on Image Processing* **16**(8), 2080–2095. doi:10.1109/TIP.2007.901238

Fahnestock M, Abdalati W, Luo S and Gogineni S (2001) Internal layer tracing and age-depth-accumulation relationships for the northern Greenland ice sheet. *Journal of Geophysical Research: Atmospheres* **106**(D24), 33789–33797. doi:10.1029/2001JD900200

Ferro A and Bruzzone L (2013) Automatic extraction and analysis of ice layering in radar sounder data. *IEEE Transactions on Geoscience and Remote Sensing* **51**(3), 1622–1634. doi:10.1109/TGRS.2012.2206078

Fomel S (2002) Applications of plane-wave destruction filters. *Geophysics* **67** (6), 1946–1960. doi:10.1190/1.1527095

Harrigan E, Kroh JR, Sandham WA and Durrani TS (1992) Seismic horizon picking using an Artificial Neural Network. In *ICASSP, IEEE International Conference on Acoustics, Speech and Signal Processing - Proceedings*, vol. 3. Institute of Electrical and Electronics Engineers Inc, pp. 105–108.

Hindmarsh RC, Leysinger Vieli G and Parrenin F (2009) A large-scale numerical model for computing isochrone geometry. *Annals of Glaciology* **50**(51), 130–140. doi:10.3189/172756409789097450

Holschuh N, Christianson K and Anandakrishnan S (2014) Power loss in dipping internal reflectors, imaged using ice-penetrating radar. *Annals of Glaciology* **55**(67), 49–56. doi:10.3189/2014AoG67A005

Holschuh N, Parizek BR, Alley RB and Anandakrishnan S (2017) Decoding ice sheet behavior using englacial layer slopes. *Geophysical Research Letters* **44**(11), 5561–5570. doi:10.1002/2017GL073417

Hoyes J and Cheret T (2011) A review of global interpretation methods for automated 3D horizon picking. *The Leading Edge* **30**(1), 38–47. doi:10.1190/1.3535431

Karlsson NB and 5 others (2014) Constraining past accumulation in the central Pine Island Glacier basin, West Antarctica, using radio-echo sounding. *Journal of Glaciology* **60**(221), 553–562. doi:10.3189/2014JoG13J180

Karlsson NB, Rippin DM, Bingham RG and Vaughan DG (2012) A 'continuity-index' for assessing ice-sheet dynamics from radar-sounded internal layers. *Earth and Planetary Science Letters* **335–336**, 88–94. doi:10.1016/J.EPSL.2012.04.034

Koutnik MR and 7 others (2016) Holocene accumulation and ice flow near the West Antarctic ice sheet divide ice core site. *Journal of Geophysical Research: Earth Surface* **121**(5), 907–924. doi:10.1002/2015JF003668

Leysinger Vieli G, Hindmarsh R and Siegert M (2007) Three-dimensional flow influences on radar layer stratigraphy. *Annals of Glaciology* **46**, 22–28. doi:10.3189/172756407782871729

Leysinger Vieli G, Hindmarsh RC, Siegert MJ and Bo S (2011) Time-dependence of the spatial pattern of accumulation rate in East Antarctica deduced from isochronic radar layers using a 3-D numerical ice flow model. *Journal of Geophysical Research: Earth Surface* **116**(2), 00–00. doi:10.1029/2010JF001785

Leysinger Vieli G, Siegert MJ and Payne AJ (2004) Reconstructing ice-sheet accu-mulation rates at ridge B, East Antarctica. *Annals of Glaciology* **39**(1), 326–330. doi:10.3189/172756404781814519

MacGregor JA and 9 others (2015) Radiostratigraphy and age structure of the Greenland ice sheet. *Journal of Geophysical Research: Earth Surface* **120**(2), 212–241. doi:10.1002/2014JF003215

Nanda NC (2016) *Seismic Data Interpretation and Evaluation for Hydrocarbon Exploration and Production*. Springer International Publishing.

Nereson NA, Raymond CF, Jacobel R and Waddington ED (2000) The accumulation pattern across Siple Dome, West Antarctica, inferred from radar-detected internal layers. *Journal of Glaciology* **46**(152), 75–87. doi:10.3189/172756500781833449

Nye JF (1963) Correction Factor for Accumulation Measured by the thickness of the annual layers in an ice sheet. *Journal of Glaciology* **4**(36), 785–788. doi:10.3189/s0022143000028367

Panton C (2014) Automated mapping of local layer slope and tracing of internal layers in radio echograms. *Annals of Glaciology* **55**(67), 71–77. doi:10.3189/2014AoG67A048

Panton C and Karlsson NB (2015) Automated mapping of near bed radio-echo layer disruptions in the Greenland ice sheet. *Earth and Planetary Science Letters* **432**, 323–331. doi:10.1016/j.epsl.2015.10.024

Parrenin F and Hindmarsh R (2007) Influence of a non-uniform velocity field on isochrone geometry along a steady flowline of an ice sheet. *Journal of Glaciology* **53**(183), 612–622. doi:10.3189/002214307784409298

Rippin DM, Siegert MJ and Bamber JL (2003) The englacial stratigraphy of Wilkes Land, East Antarctica, as revealed by internal radio-echo sounding layering, and its relationship with balance velocities. *Annals of Glaciology* **36**, 189–196. doi:10.3189/172756403781816356

Schroeder DM and 9 others (2019) Multidecadal observations of the Antarctic ice sheet from restored analog radar records. *Proceedings of the National Academy of Sciences of the United States of America* **116**(38), 18867–18873. doi:10.1073/pnas.1821646116

Siegert MJ (1999) On the origin, nature and uses of Antarctic ice-sheet radio-echo layering. *Progress in Physical Geography* **23**(2), 159–179. doi:10.1177/030913339902300201

Siegert MJ and Payne AJ (2004) Past rates of accumulation in central West Antarctica. *Geophysical Research Letters* **31**(12), L12403. doi: 10.1029/2004GL020290.

Siegert MJ, Payne AJ and Joughin I (2003) Spatial stability of Ice Stream D and its tributaries, West Antarctica, revealed by radio-echo sounding and interferometry. *Annals of Glaciology* **37**, 377–382. doi:10.3189/172756403781816022

Sime LC, Hindmarsh RC and Corr H (2011) Automated processing to derive dip angles of englacial radar reflectors in ice sheets. *Journal of Glaciology* **57** (202), 260–266. doi:10.3189/002214311796405870

Sime LC, Karlsson NB, Paden JD and Prasad Gogineni S (2014) Isochronous information in a Greenland ice sheet radio echo sounding data set. *Geophysical Research Letters* **41**(5), 1593–1599. doi:10.1002/2013GL057928

Sobel I (1990) Generalized and separable Sobel operators. In Danielsson PE and Seger O (eds.), *Machine Vision for Three-Dimensional Scenes*. Academic Press.

Steger C (1998) An unbiased detector of curvilinear structures. *IEEE Transactions on Pattern Analysis and Machine Intelligence* **20**(2), 113–125. doi:10.1109/34.659930

Winter A and 9 others (2017) Comparison of measurements from different radio-echo sounding systems and synchronization with the ice core at Dome C, Antarctica. *The Cryosphere* **11**(1), 653–668. doi:10.5194/tc-11-653-2017

Winter A, Steinhage D, Creyts TT, Kleiner T and Eisen O (2019) Age stratigraphy in the East Antarctic Ice Sheet inferred from radio-echo sounding horizons. *Earth System Science Data* **11**(3), 1069–1081. doi:10.5194/essd-11-1069-2019

Xiong S, Muller JP and Carretero RC (2018) A new method for automatically tracing englacial layers from MCoRDS Data in NW Greenland. *Remote Sensing* **10**(1), 1–22. doi:10.3390/rs10010043

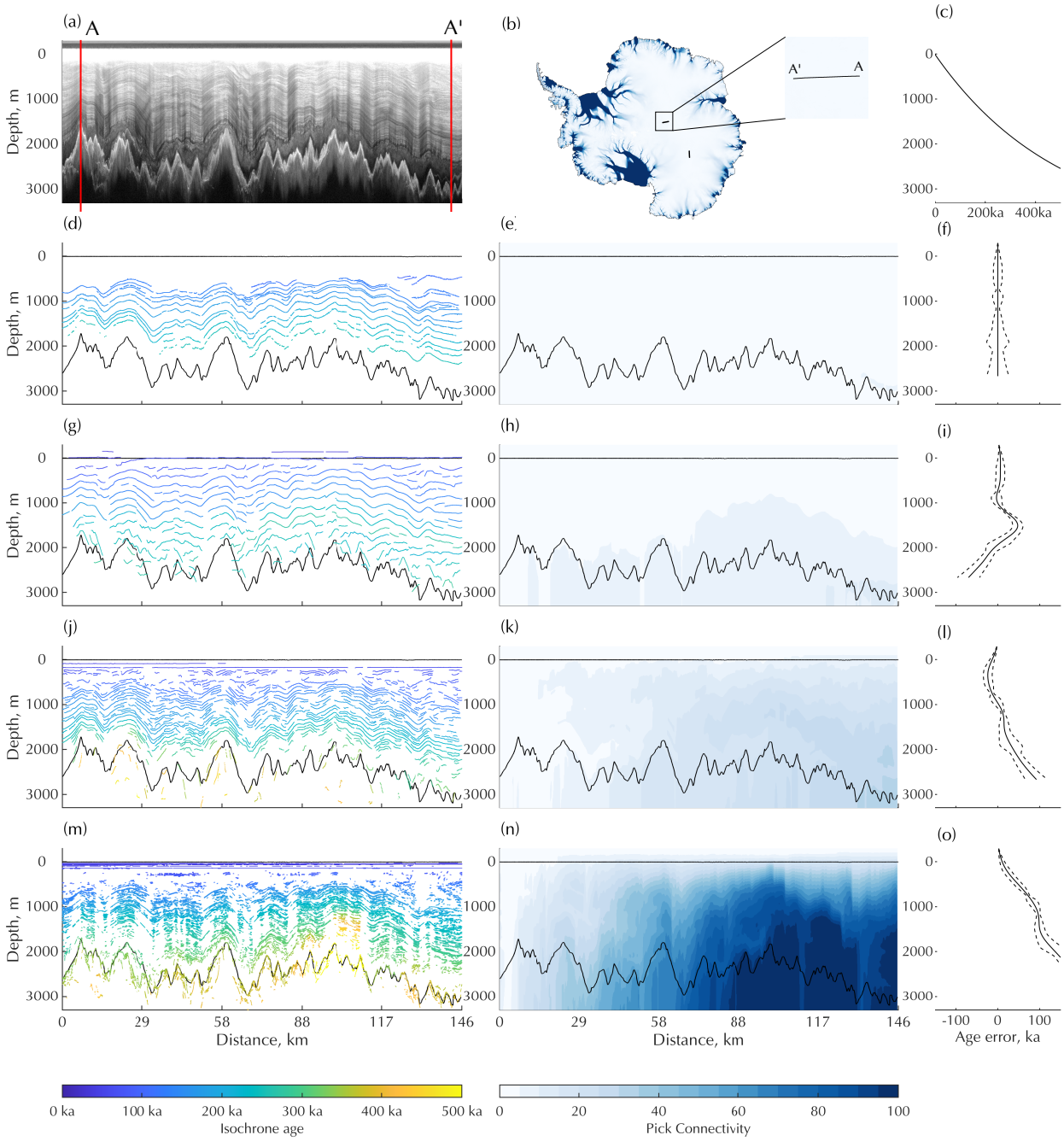

Supplementary Figure 1: Application of auto-tracking algorithms to the second of the example datasets, similar to Fig. 1 in the main text. (a) Profile from A to A', with (b) location in Antarctica and (c) starting age-depth profile at A. (d) Manually-picked reference dataset with (e) isochrone connectivity metric and (f) profile of misfit between reference picks age-depth relationship with uncertainties propagated through the picks. (g) Englacial picks, (h) isochrone-connectivity metric and (i) misfit profile for ARESELP algorithm. (j) Englacial picks, (k) isochrone-connectivity metric and (l) misfit profile for Steger algorithm. (m) Englacial picks, (n) isochrone-connectivity metric and (o) misfit profile for Sobel-Feldman algorithm.

Appendix C

Formatted *IWAGPR* Sliced-3D FDTD paper

This Appendix includes a conference paper with an early version of the work presented in Chapter 5, presented at the *International Workshop on Advanced Ground Penetrating Radar 2017*, hosted in Edinburgh.

A Sliced-3D FDTD approach as an alternative to 2D Ground Penetrating Radar modelling

Richard Delf*†, Antonios Giannopoulos‡, Robert G. Bingham*, Nicholas R.J. Hulton*† and Andrew Curtis*
* School of Geosciences, University of Edinburgh, Edinburgh, United Kingdom
† University Centre in Svalbard, PO Box 156 N-9171 Longyearbyen, Svalbard
‡School of Engineering, University of Edinburgh, Edinburgh, United Kingdom
Email: r.delf@ed.ac.uk, a.giannopoulos@ed.ac.uk, r.bingham@ed.ac.uk, nick.hulton@ed.ac.uk, andrew.curtis@ed.ac.uk

***Abstract*—Ground penetrating radar (GPR) is a powerful tool for characterisation of the subsurface in a range of applications. Finite-difference time-domain (FDTD) forward modelling is often used to gain a more quantitative understanding of the interaction between GPR systems and the region of interest. This can be undertaken in 2D, where simulations fail to model multiple polarisations and require a number of simplifying assumptions for both electromagnetic fields and for modelling the environment. Alternatively full 3D modelling may be used, but this can be very computationally expensive. Here we present an idea, in contrast to the more formal 2.5D FDTD GPR modelling approach, which is based on using a thin slice of a full 3D model in cases that we want full 3D fields but we have a 2D modelling environment. The key issue with this approach is minimising, if possible, the error introduced by the very close proximity of the perfectly matched layer (PML) absorbing boundaries of the model in the invariant direction of the modelled geometry. We use gprMax, an open source FDTD GPR modelling package, to check the viability of this idea. An assessment of domain size required is made considering the error produced and the computational demands. Optimising the PMLs will be key in making this approach viable for future GPR modelling that provides a full 3D field solution in cases where a 2D geometry is a reasonable assumption.**

Keywords: Ground Penetrating Radar, 3D FDTD modelling, polarisation, perfectly matched layers.

I. Introduction

Ground Penetrating Radar is a powerful tool in non-destructive investigation in a wide range of applications, including engineering, near-surface site surveys, archaeology and ice bed profiling in glaciology [1]. A typical common offset survey with appropriate data processing can be used as an excellent qualitative interpretation tool, and for a limited amount of quantitative interpretation. However, the complex interactions between the material properties in the area of interest, electromagnetic wave propagation, and radar system or wavelet properties, limit our ability to quantitatively interpret material properties of targets in a straightforward manner. To overcome such limitations, we can look to numerically simulate the response of a model of the area of interest. This provides an inexpensive method of testing processing techniques and interpretation methodologies in a controlled environment.

A. Forward Modelling of GPR

Finite-difference time-domain (FDTD) modelling of GPR datasets represents an opportunity to numerically obtain the response of a controlled environment to a synthetic survey. This is a simple, intuitive, and robust method allowing for a range of applications depending on the need of the user. FDTD modelling is generally undertaken using Yee's algorithm [2]. This algorithm is described in detail elsewhere [3]. In brief, the algorithm operates by discretising Maxwell's equations of electrodynamics by replacing the partial derivatives in Faraday's and Maxwell's-Ampere's laws with finite differences. At each step, the unknown "future" fields are calculated for every location in a discretised grid representing the model domain. This is repeated for the required duration of the simulation. The amplitude of any field at any location in the domain can be obtained directly without requiring any post-processing. This algorithm can be implemented in 3D, or in 2D if some key simplifications are made.

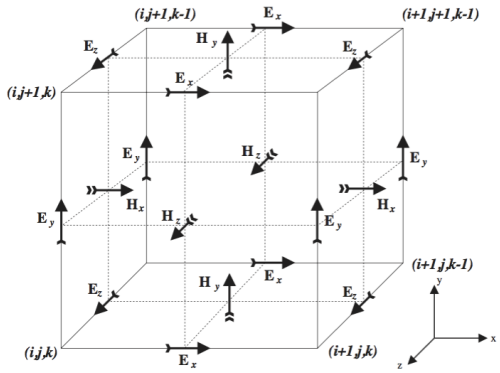

Fig. 1. The 3D FDTD Yee cell

2D simulations are a computationally quick and easy method of modelling but they provide the response of the model to an ideal 2D line source stretching to infinity in the cross line orientation. However, real-world sources are not solely polarised in a particular orientation and cannot be fully described by a simple line source model as needed by pure 2D modelling which obviously does not allow simulation of cross-polarisation antenna orientations. This is a limitation of the technique for survey design, as several authors have noted the significance of antenna orientation in both near-surface ap-

plications [4], [5] and glacial GPR surveys [6], [7]. In addition to this, the effects on polarisation from reflection or diffraction events cannot be simulated. 2D simulations additionally fail to account for realistic 3D spherical divergence and associated power loss [8], resulting in the need to apply a correction factor to represent true amplitude [9].

B. Sliced-3D vs 2.5D modelling

To simulate polarisation effects, a full 3D simulation is required. However, 3D models are computationally expensive and hence their use is limited where large domain sizes are required. For example, in glaciology, model domain size is dictated by ice thickness which can be approximately 2000m resulting often to unfeasibly high computational cost. This is particularly pressing when considering iterative processing and inversion algorithms, for example when considering full waveform inversion where many forward model runs are required to produce a solution [9].

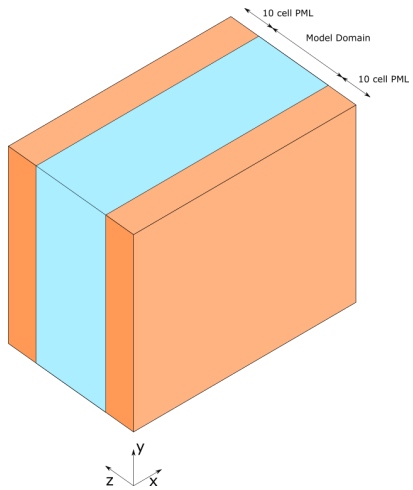

Fig. 2. Model domain showing PMLs in the positive and negative z directions. Additional PMLs are included in the x and y directions as in 2D modelling, but are not shown here.

A 2.5D model is an alternative approach allowing us to obtain full 3D field solution whilst the geometry of the model is assumed to be 2D and extending to infinity in the cross-plane dimension. Therefore, in a 2.5D model the electromagnetic fields are considered to be 3D and no assumption of a line source excitation is required. That is to say that it is essentially a 3D model of a laterally invariant 2D geometry. In developing a 2.5D appoach field components on the 3D Yee cell are projected in the 2D plane and the fields are transformed in the wavenumber domain along the invariance direction. The solution process produces 3D fields from a 2D geometry but requires a rather different FDTD algorithm - adjusted to take into account the solving in wavenumber domain of the fields - requiring a full 2D solution for every single wavenumber, with the final result being obtained using a post-processing step involving a spatial inverse Fourier transformation.

There have been limited previous attempts to undertake 2.5D modelling of GPR data. Moghaddam et al [12] developed a 2.5D algorithm by projecting a 3D formulation of Yee's grid onto a 2D domain and solving for the multiple effective wavelengths, based on the theory of [13]. It was found that approximately 55 2D simulations, each with a different wavenumber, were required for sufficient accuracy before the simulation outputs could be combined to produce the final result. A modification of this algorithm is implemented more recently by Xu et al [14] to include conductivity and hence attenuation effects in the wavelet response in a 2.5D model, at the same time showing that a reduced number of wavenumbers were required to produce a result similar to that produced by a full 3D model.

While these algorithms produce a computationally cheap and effective method of calculating the 2.5D response, they are developed by a rearrangement and using a special formulation of the FDTD equations and require post-processing of results to obtain the full result. Additionally, as far as the author is aware, codes are not available for general use. Developing alternative techniques in easily accessible and open source software would be of greater benefit to the wider GPR research community. From a computational perspective a 2.5D approach is not going to be significantly more efficient when compared to a full 3D model having a small number of cells along the invariance direction.

Here we propose that a similar result could be possibly obtained by using the full 3D implementation of Yee's algorithm by means of a thin slice of a 3D FDTD model.

To test the idea of what we call Sliced-3D modelling we use gprMax which is an open source numerical modelling software that simulates propagation of electromagnetic radiation, using Yee's implementation of the FDTD method in three dimensions [10]. In gprMax a simulation can be implemented both in 2D or 3D by defining a model through either explicitly placing objects with specified dielectric properties at locations throughout the domain, or by importing an array of data with a corresponding list of material properties. It includes many advanced features including anisotropic, and dispersive material modelling, as well as built in antenna models [11]. In addition, it has a flexible implementation of the perfectly matched player (PML) absorbing boundary condition used to truncate the model domain. A 2D model in gprMax is obtained from a single cell-thickness implementation of the 3D algorithm, therefore using the same codebase. This is achieved through a simplification of the 3D Yee cell to ignore any contributions to the electric and magnetic fields in the invariant direction of the model.

To implement the Sliced-3D FDTD model using gprMax a 2D model is replicated multiple times in the crossline direction of invariance to produce a 3D array. The number of cells required is a sum of those required for the model domain, and additional cells needed for the PML absorbing boundary conditions. The key is to be able to place the absorbing boundaries very close to the source requiring only a small number of 3D cells in the invariant direction. Additional computational resources are required for this implementation when compared to pure 2D modelling due to both the number

of cells increasing, and a decrease in the required time step. For a 3D problem, the associated time stability criterion must follow:

$$\Delta t \leq \frac{1}{\sqrt{\frac{1}{\Delta x^2} + \frac{1}{\Delta y^2} + \frac{1}{\Delta z^2}}} \tag{1}$$

where Δt is the time step and Δx, Δy and Δz are the spatial resolution. In the 2D case, the stability condition is obtained by letting $\Delta z \to \infty$, hence a smaller Δt is required for the 3D algorithm.

C. PML optimisation

gprMax utilises an efficient PML absorbing boundary condition. Specifically, it features a PML based on a recursive integration approach to the CFS PML [15]. Higher order CFS PMLs operate via an inclusive stretching function:

$$s_u = \prod_{i=1}^{N} s_{u_i} \tag{2}$$

where u is the orientation and N denote the order of the PML stretching function. The individual terms s_u are of the form

$$s_{u_i} = \kappa_{u_i} + \frac{\sigma_{u_i}}{\alpha_{u_i} + j\omega_{\epsilon_0}} \tag{3}$$

where κ represents the amount of real coordinate stretching. By default, gprMax uses a first order PML with $\alpha = 0, \kappa = 1$, and σ calculated internally based on the underlying material properties in the medium. Using such a formulation allows any order of PML to be defined by changing and optimising these parameters.

By changing parameters in equation 3, the performance of the PML can be optimised. Optimising the PML may result in the ability to use a thinner model domain for the Sliced-3D model approach as the source is required to be as close as possible to the PML.

II. Numerical experiments

Two independent numerical experiments have been performed to demonstrate the initial investigation. They showcase the potential of such an implementation, application of the Sliced-3D modelling approach, and more crucially allow us to study the effects of reducing the domain size. Initially, an empty model of free space will be compared to the analytical solution of a z-directed Hertzian dipole source. Following this, a simple model of a pipe embedded in a homogeneous medium will be used as a realistic example to demonstrate the implications of amplitude and polarisation errors on a GPR dataset.

A. Comparison to analytical solution in free space

The received waveform from a Hertzian dipole source is calculated for all locations throughout a two dimensional domain, using the theory of Ziolkowski [16]. This result has no effects of interference from adjoining PML layers and hence represents the full theoretical received waveform in a non-conductive free space environment. This is compared to the Sliced-3D grid approach of reducing the z-direction dimension, with an identical Hertzian dipole source. The spatial and temporal resolution of each simulation is kept identical throughout to remove any effects of the different simulation methods.

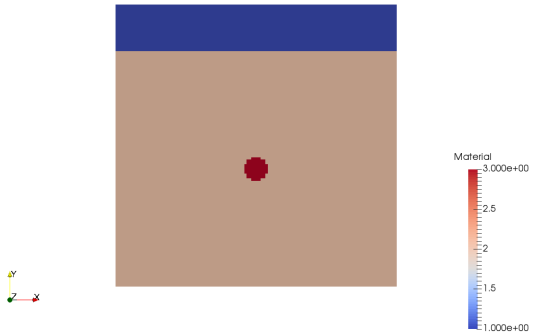

Fig. 3. z-projected view of simple pipe embedded in a homogeneous material. Sources are along the top sand/air interface.

B. B-scan pipe embedded in a homogeneous medium

A 3D model is constructed with a domain size of 0.26 m on all sides, with spatial resolution of 0.002 m. A perfectly electrical conductive (PEC) pipe of radius 0.01 m is placed in a homogeneous, non-dispersive subsurface of $\epsilon_r = 6$ and $\sigma = 0$. This subsurface is below an area of free space. The pipe extends across the full model in the z-direction. A common offset survey line with co-located source and receivers is orientated in the x-direction (perpendicular to the pipe orientation) in the middle of the survey, and in the z-direction at the interface between the air and subsurface. A standard 10 cell PML is used on all 6 sides of the domain.

After running a full domain 3D survey, the domain size is iteratively reduced in the z (cross-line) dimension. The reduction in domain size linearly reduces the run time required for each model. For each domain size, 70 shots are simulated to produce a GPR B-scan. The error is then calculated as a function of the size for (a) z-polarized source, and (b) x-polarized source using the model in Figure III-A. Errors are scaled relative to the maximum absolute value in the respective polarisations.

III. Results

A. Analytical solution comparison

The analytical solution allows a direct comparison to the true theoretical waveform received at a point. A comparison between two widths of the sliced 3D model and the analytical solution is presented in Figure 4. This clearly demonstrates that as the boundaries are brought closer to the source there is a significantly observable error. In order to reduce this error better performance of the PML boundaries will be required.

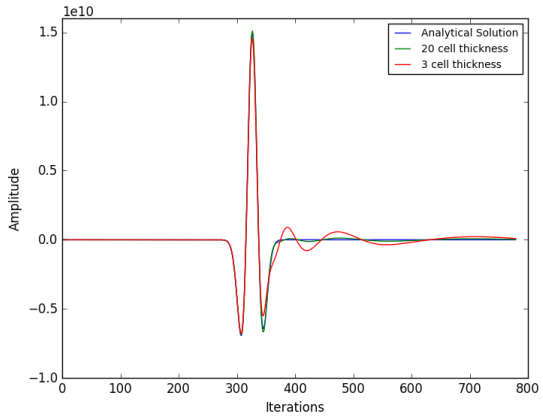

Fig. 4. Received wavelet at a point in free space compared to the analytical response. The point is located in the centre of the model such that the only PML influence should be in the z direction.

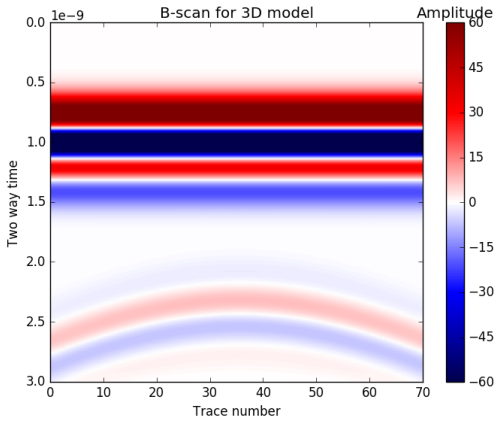

Fig. 5. Result from the full 3D scan, with clear direct arrival, and hyperbola from the embedded pipe.

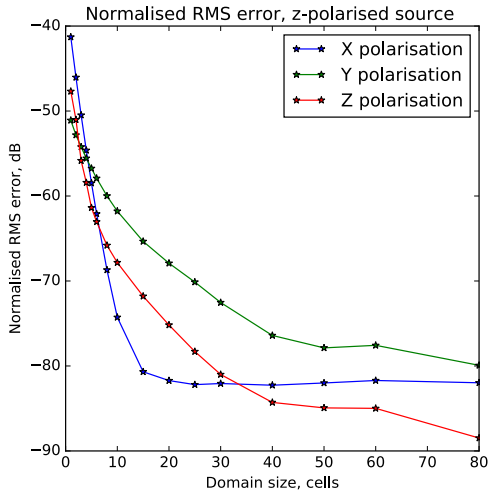

Fig. 6. Mean error across the B-scan for an z-polarised source.

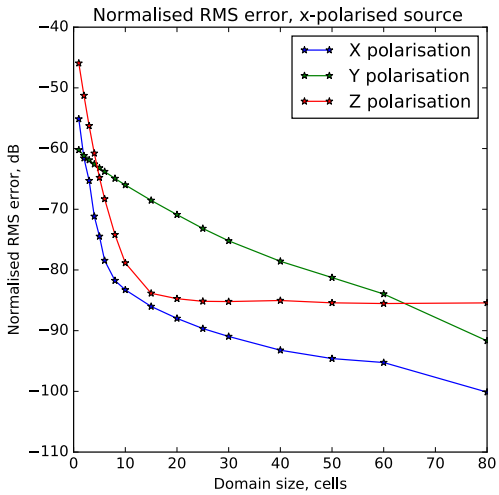

Fig. 7. Mean error across the B-scan for an x-polarised source.

B. Pipe embedded in a homogeneous medium

Figure 7 shows the results of the RMS error as a function of the z-coordinate domain size for the cylinder B-scan test using a z-polarised source. The error is calculated as an RMS error across the B-scan relative to the result of the full 3D model, and normalised to the maximum amplitude of the B-scan. The domain size does not include the number of cells taken by the PMLs. A single cell implementation gives a maximum error of -10 dB in the z-polarised response, with a rapid drop off as 10 more cells were added. At a 10 cells model domain width, the normalised RMS error is below -30 dB, and -40 dB at 30 cells width.

The overall error in the x and y polarisations is much less. The maximum error in the x polarisation is below 1% and in the y is 0.1%. This is to be expected as the initial polarisation was not in these projections. The error is again rather significant if a small slice of the full 3D model is to be used in a Sliced-3D modelling approach. This shows that a simple PML implementation is not really suitable for thin Sliced-3D modelling of GPR scenarios.

C. CFS-PML Parameters

As discussed, PML parameters can be optimised to improve performance of the absorbing boundaries. To demonstrate this, CFS PML parameters were altered for selected runs of the analytical solution comparison model. α was set as a constant 0.025, with $\kappa_{max} = 5$. The resultant residual error for the received waveform at a midpoint in the analytical solution test is shown in Figure 8.

The new PML parameters used show a significant improvement by reducing the amplitude of the residual error response throughout the arrival of the main wavelet but also significantly attenuated the ringing present later in the simulation after the main arrival.

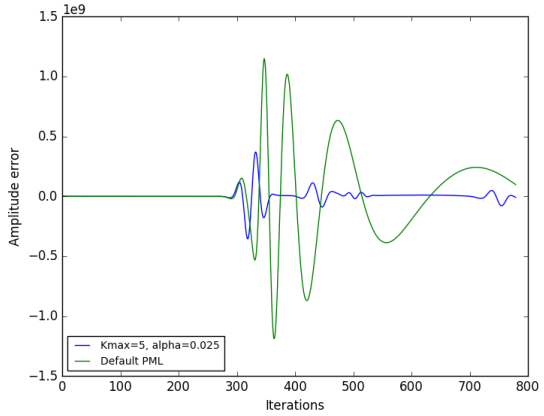

Fig. 8. Residual of modelled response in free space. A significant reduction in amplitude of the received waveform is observed by adjusting PML parameters. Further improvements may be possible through optimisation of PML parameters.

The parameters required for optimising PML performance and optimisation of PML performance is an area of active ongoing research especially if higher order PML formulations are to be used, as they have shown to improve performance [15]. Further optimisation of the Sliced-3D modelling technique requires a more in-depth optimisation of the PML parameters, including the possibility of higher order CFS PMLs. Using an analytical solution to compare results from this optimisation is likely to be the best approach.

IV. Discussion and Conclusions

The idea of using a method of modelling the 3D propagation of electromagnetic radiation using a reduced size or Sliced-3D domain has been demonstrated. Using such a model has several benefits over simple 2D modelling: it allows realistic polarisation effects to be investigated fully with realistic amplitude scaling; it results in a lower computational demand than full 3D simulations; and it allows polarisation effects to be investigated in a laterally inhomogeneous subsurface using openly available 3D GPR modelling software. It is clear that simple absorbing boundary conditions such is the standard PML formulation do not provide enough absorption for accurate solutions. However, some initial promising results have been obtained when simple optimisation of the CFS PML parameters was applied. Further research effort in properly optimising the PMLs will hopefully provide a viable solution and allow the use of this Sliced-3D GPR modelling approach. In practice, this means that further development is required to firstly optimise the PML parameters to maximise the performance of the PML layer, followed by repeating numerical experiments to establish acceptable reductions in domain size to minimise computational cost.

Acknowledgment

Richard Delf was supported by a NERC Scholarship hosted by the Edinburgh E3 Doctoral Training Programme.

References

[1] R. G. Bingham and M. J. Siegert, "Radio-echo sounding over polar ice masses," *Journal of Environmental & Engineering Geophysics*, vol. 12, no. 1, pp. 47–62, 2007.

[2] K. Yee, "Numerical solution of initial boundary value problems involving maxwell's equations in isotropic media," *IEEE Transactions on Antennas and Propagation*, vol. 14, no. 3, pp. 302–307, May 1966.

[3] A. Taflove and S. C. Hagness, *Computational electrodynamics*. Artech house, 2005.

[4] R. L. Roberts and J. J. Daniels, "Analysis of GPR polarization phenomena," *Journal of Environmental and Engineering Geophysics*, vol. 1, no. 2, pp. 139–157, 1996.

[5] J. J. Daniels, L. Wielopolski, S. Radzevicius, and J. Bookshar, "3D GPR polarization analysis for imaging complex objects," in *Symposium on the Application of Geophysics to Engineering and Environmental Problems 2003*. Society of Exploration Geophysicists, 2003, pp. 585–597.

[6] M. Moran, R. Greenfield, S. Arcone, and A. Delaney, "Delineation of a complexly dipping temperate glacier bed using short-pulse radar arrays," *Journal of Glaciology*, vol. 46, no. 153, pp. 274–286, 2000.

[7] L. Langhammer, L. Rabenstein, A. Bauder, and H. Maurer, "Ground-penetrating radar antenna orientation effects on temperate mountain glaciers," *Geophysics*, vol. 82, no. 3, pp. H15–H24, 2017.

[8] N. Bleistein, "Two-and-one-half dimensional in-plane wave propagation," *Geophysical Prospecting*, vol. 34, no. 5, pp. 686–703, 1986.

[9] A. Mozaffari, A. Klotzsche, G. He, H. Vereecken, J. van der Kruk, C. Warren, and A. Giannopoulos, "Towards 3D full-waveform inversion of crosshole GPR data," in *Ground Penetrating Radar (GPR), 2016 16th International Conference on*. IEEE, 2016, pp. 1–4.

[10] C. Warren, A. Giannopoulos, and I. Giannakis, "gprMax: Open source software to simulate electromagnetic wave propagation for ground penetrating radar," *Computer Physics Communications*, vol. 209, pp. 163–170, 2016.

[11] C. Warren and A. Giannopoulos, "Creating finite-difference time-domain models of commercial ground-penetrating radar antennas using Taguchis optimization method," *Geophysics*, vol. 76, no. 2, pp. G37–G47, 2011.

[12] M. Moghaddam, E. Yannakakis, W. Chew, and C. Randall, "Modeling of the subsurface interface radar," *Journal of Electromagnetic Waves and Applications*, vol. 5, no. 1, pp. 17–39, 1991.

[13] C. Stoyer and R. J. Greenfield, "Numerical solutions of the response of a two-dimensional earth to an oscillating magnetic dipole source," *Geophysics*, vol. 41, no. 3, pp. 519–530, 1976.

[14] T. Xu and G. A. McMechan, "GPR attenuation and its numerical simulation in 2.5 dimensions," *Geophysics*, vol. 62, no. 2, pp. 403–414, 1997.

[15] A. Giannopoulos, "Unsplit implementation of higher order pmls," *IEEE Transactions on Antennas and Propagation*, vol. 60, no. 3, pp. 1479–1485, March 2012.

[16] R. W. Ziolkowski, N. K. Madsen, and R. C. Carpenter, "Three-dimensional computer modeling of electromagnetic fields: A global lookback lattice truncation scheme," *Journal of Computational Physics*, vol. 50, no. 3, pp. 360–408, 1983.